Development of experimental methods to measure temperature fields and velocity fields in fluid flows using Magnetic Resonance Imaging

DISSERTATION
zur Erlangung des
Doktorgrades der Fakultät
für Mathematik und Physik
der
Albert-Ludwigs-Universität
Freiburg

vorgelegt von

Waltraud Buchenberg
aus Kempten im Allgäu

23. November 2016

Dekan:	Prof. Dr. G. Herten
Leiter der Arbeit:	Prof. Dr. J. Hennig
Referent:	Prof. Dr. J. Hennig
Koreferent:	Prof. Dr. M. Schumacher
Prüfer:	Prof. Dr. T. Filk
	Prof. Dr. G. Reiter

Datum der mündlichen Prüfung: 23.11.2016

Contents

Introduction

Magnetic resonance imaging (MRI) is a well established, non-invasive imaging technique. It is of high clinical importance due to its inherent high soft tissue contrast, allowing for the differentiation of many relevant pathologies without the use of ionizing radiation. Furthermore, organ function can be investigated. For example, MRI has been applied to assess the cardiac function by studying the velocities of the myocardium and the blood [1, 2, 3]. Velocity information can be obtained from the phase of the complex magnetic resonance (MR) signal using a technique known as phase contrast MRI. More recently, MRI has also been deployed in engineering as an imaging tool to measure velocity fields in fluid flows [4, 5, 6, 7, 8, 9]. Additionally, MRI is capable of non-invasively measuring temperature distributions [10]. Thus, MRI has great potential for an in-detail investigation of heat transfer processes in fluid flows. An additional asset is that compared to common conventional measurement techniques, no exchange of components in setups is needed when switching from velocity to temperature data acquisition, reducing the experimental effort. MRI even allows to measure velocity and temperature with a single measurement technique and one flow setup.

Clinical applications of temperature measurements using MRI are typically performed on static tissues to monitor thermal procedures guided by MRI [11, 12, 10]. Motion, which can potentially occur during the procedure, severely hampers temperature measurements [13]. However, in order to establish MRI as a measurement technique for temperature measurements in the field of fluid mechanics, temperature assessment needs to be accurately and precisely accomplished in fluid flows. The possibility to measure temperature and velocity in fluid flows using MRI has been investigated previously [14, 15]. The measurement of velocity fields in complex fluid flows is well established and accurately possible, while literature contains only a few studies about temperature distributions in fluid flows with low accuracy [16, 4].

The work described in this thesis aims to establish high spatially resolved 2D and 3D MR thermometry (MRT) in complex fluid flows. It studies in detail the accurate and precise measurement of temperature with MRT as well as MR velocimetry (MRV) in thermofluid applications (involving fluid mechanics and thermodynamics) simultaneously within a single measurement session. Experimental results using the newly developed methods and techniques demonstrate that MRI offers great potential to gain new insights into fundamental heat transfer phenomena, and that it can be of great interest as an additional non-invasive measurement modality.

The MRV method primarily established for in vivo applications had to be adapted to address the challenges arising from fluid flow or from components of the flow models.

Moreover, an MRT acquisition strategy was developed which is capable of accurately and precisely measuring 2D and 3D temperature distributions with high spatial resolution in

fluid flows. This involved the selection of an appropriate MRT method, its implementation and the corresponding data evaluation.
The method used for MRT and MRV to achieve high spatially resolved data are both based on phase information. Therefore, they use the same measurement parameter to extract velocity as well as temperature. It is thus of utmost importance to carefully separate the individual contributions to ensure accurate measurements. For this reason, velocity compensation was implemented in the MR sequence to perform MRT, whereas, temperature is kept constant during MRV. Extensive work was conducted to minimize or exclude possible degradations of the MRT results with respect to experimental stability (such as field drifts) or artifacts arising from susceptibility issues. Design rules were worked out to ensure maximum MR compatibility of the flow model with respect to MRT measurements, and thus to allow artifact free MRT. As an alternate approach, the feasibility of MRT in fluid flows using a spectroscopic method was successfully tested.
This thesis was part of an interdisciplinary project between the Technische Universität Darmstadt and the University Medical Center Freiburg (Grant of the Deutsche Forschungsgemeinschaft DFG: GR 3524/3-1 and JU 2687/10-1). The aim of this project was to establish MR methods and technologies to reliably measure 3D temperature distributions in in vitro flow models in addition to velocity fields.
The project partner (PhD Florian Wassermann) at the Technische Universität Darmstadt was responsible for the design and realization of the flow setups from a fluid mechanical as well as thermodynamic perspective. His contributions are available in his PhD thesis [17].
The author of this thesis at the University Medical Center Freiburg had all responsibilities for MRI and obtained studies and results are in this thesis.

This thesis is organized as follows:
Part 1 covers the principles of nuclear magnetic resonance and the methods to measure velocity and temperature with MRI. The various different methods to detect temperature are discussed with respect to their applicability to fluid flows. This part contains common conventional experimental methods to detect velocity and temperature. A summary is given for the most important engineering concepts with respect to this thesis. This part concludes with a literature search about the three thermofluid test cases (called case studies) investigated in this thesis.
Part 2 covers the methods examined, developed, and applied in this thesis. It begins with the MR sequence modifications and data analysis regarding the acquisition of temperature data in addition to velocity data. Furthermore, an extensive experimental groundwork had to be performed to lay the foundation for design rules regarding setup components and setup geometries in an MR system as a prerequisite for accurate velocity and temperature measurements. Additionally, a fiber optical temperature measurement system (providing a temperature reference) was investigated with respect to magnetic field dependency of the fiber optical probes. The experimental groundwork section already includes results, discussion and conclusions drawn from the individual experiments since this knowledge was required to establish and examine the thermofluid case studies.
Part 3 covers three investigated case studies: counter-current double pipe heat exchanger, pin fin array heat exchanger, and a horizontal cylinder with free convection inside. It includes case specific methods, results and discussions with a detailed analysis of measurement errors for each study.

Part 4 summarizes the major achievements of this thesis and gives an outlook to possible future work.

Part I

Principles of Nuclear Magnetic Resonance (NMR)

Chapter 1

Physics of Magnetic Resonance Imaging

In 1946, a phenomenon called nuclear magnetic resonance (NMR) was described [18, 19]. It relies on the magnetic property of the atomic nucleus. If certain nuclei are placed in an external magnetic field they absorb energy at a specific frequency (radiofrequency RF) which leads to a detectable signal [20]. NMR became an important tool for the examination of matter in a variety of different disciplines such as physics, chemistry, biology, medicine, and food science. With respect to clinical applications, R. Damadian [21] reported that malignant tumors possess different relaxation times T1 and T2 (no subscript numbers are used in this work to clearly distinguish relaxation time constants from temperature values) compared to healthy tissue.
However, it required several decades after the discovery of NMR until the foundation of spatially resolved magnetic resonance imaging (MRI) was laid by Paul Lauterbur [22]. He applied two magnetic fields and proposed a spatially resolved reconstruction of the imaged object. A few months later in that year, Peter Mansfield and P. K. Grannell published work where they applied a magnetic field gradient to study the structure in solids using NMR [23]. A few years later in vivo NMR images of mobile protons were conducted with comparable quality to X-ray tomography [24]. Later on the letter 'N' was dropped to avoid confusion with other assignments of nuclear such as in nuclear power plants or nuclear warfare [20]. Nowadays, MRI is frequently applied in medicine due to its high soft tissue contrast, the lack of ionizing radiation, and its three dimensional coverage of regions of interest. Furthermore, MRI is also applied in non-medical disciplines such as food science [25, 26], and in the engineering community [15] as an excellent measurement technique.
The following sections cover the theoretical background of NMR and MRI. This chapter is based on the books from references [27, 28, 29, 30, 31, 32].

1.1 Properties of the atomic nucleus

Mass, electric charge, magnetism and spin are physical properties which each atomic nucleus of an atom possesses [27].
The atomic nucleus consists of spin-1/2 particles (protons and neutrons) called nucleons. From the superposition of spin-1/2 particles [30] solely three possibilities for the nuclear spin quantum number I exist [27]:

- **odd number of nucleons:** An unpaired spin of either a proton or neutron remains and I is half-integer.
- **number of protons and neutrons are both even:** The ground state nuclear spin is given by I=0 since all spins are compensated. In NMR experiments these kind of nuclei do not contribute any signal.
- **number of protons and neutrons are both odd:** The ground state nuclear spin is given by $I \geq 1$ with I being an integer value.

1.2 Magnetism

The interaction of a substance with a magnetic field is described by its magnetic moment [27]. There are substances which have a permanent magnetic moment and others which obtain a magnetic moment induced if they are exposed to an external magnetic field. The latter scenario occurs in diamagnetism and paramagnetism, whereas the permanent magnetic moment is related to ferromagnetism. If a diamagnetic object is placed into a magnetic field classically a loop-current is induced resulting in a magnetic moment aligned antiparallel to the magnetic field [31]. Thus, the resultant force, acting on diamagnetic objects put into inhomogeneous magnetic fields, pushes them towards locations with smaller magnetic fields. Diamagnetism is mostly temperature independent [32]. The magnetic susceptibility χ (dimensionless quantity describing the magnetization of a substance in an external magnetic field) is smaller than zero. Dependent on the material, χ can be a tensor quantity. Generally, all materials are diamagnetic; however, it can be overwhelmed by the stronger paramagnetism or ferromagnetism. The atoms of a paramagnetic substance exhibit permanent magnetic moments which are randomly distributed without an external magnetic field. Thus, no resultant magnetic moment remains. However, in an external magnetic field the magnetic moments of the atoms align such that the resultant magnetic moment is aligned with the magnetic field. An object tends to align in an external magnetic field so that its magnetic energy is minimized [27]. The magnetic energy of the object is given by

$$E_{\mathrm{mag}} = -\vec{\mu} \cdot \vec{B}_0 \tag{1.1}$$

which is the dot product between the magnetic field $\vec{B}_0$ and the magnetic moment $\vec{\mu}$. Paramagnetic objects are attracted towards higher magnetic fields in contrast to diamagnetic objects. The alignment of the permanent magnetic moments depends on the strength of the external magnetic field and the temperature of the object. In stronger magnetic fields or at lower temperatures the number of aligned magnetic moments increases. The relationship between the magnetization, magnetic field and temperature is described by the law of Pierre Curie

$$M = C \cdot \frac{B_0}{T} = \chi \cdot B_0 \tag{1.2}$$

for small ratios of $\frac{B_0}{T}$ [31, 32]. The magnetization of the samples is a quantitative measure of the alignment of magnetic moments. If all magnetic moments are aligned the magnetization saturates. Paramagnetic materials have a χ larger than 0 which is temperature dependent (proportional to 1/T, see Eq. (1.2)); however, χ is independent of the magnetic field.

The sign of χ gives information about the distortion of a homogeneous magnetic field by an object. If χ is negative (diamagnetic objects), the magnetic field lines are pushed out of the object, whereas if χ is positive (paramagnetic objects), these field lines are pulled inside the object.
Ferromagnetic materials such as iron or alloys can have a strong permanent magnetic moment even without an external magnetic field since some of the magnetic moments of the atoms are aligned in so called domains [31]. In an external magnetic field further alignments occur and a strong magnetization aligned parallel with the external magnetic field arises if the temperature is not too high. This magnetization can partly remain after removing the external field [31]. χ values are large and dependent on the magnetic field as well as on the history of the material [32]. Furthermore χ is temperature dependent according to the law of Curie and Weiss,

$$\chi = \frac{C}{T - T_{\mathrm{C}}} \tag{1.3}$$

with T_{C} the Curie temperature and C the Curie constant. Above T_{C} the object becomes paramagnetic and χ is reduced by orders of magnitude. Ferromagnets are attracted to higher fields if they are located within an inhomogenous magnetic field.

1.3 Spin-1/2 particle in an external magnetic field

The hydrogen nucleus is the most relevant nucleus for MR imaging due to its high gyromagnetic ratio and its high abundance compared to other nuclei which are suited for MR imaging. This is in particular true for biological systems such as the human body [33]. The hydrogen nucleus consists only of a single proton which is a spin-1/2 particle. In the following a quantum mechanical description of this particle in an external magnetic field is given.

1.3.1 Energy eigenstates

Frequently, the static uniform magnetic field is aligned with the z-direction, $\vec{B}_0$=$B_0\vec{\mathrm{e}}_{\mathrm{z}}$ with B_0 denoting the strength of the field and $\vec{\mathrm{e}}_{\mathrm{z}}$ the unit vector in z-direction. Then, the interaction of a single proton with this magnetic field is given by the following Hamilton operator [30]

$$H = -\gamma B_0 I_{\mathrm{z}} = \omega_0 I_{\mathrm{z}}. \tag{1.4}$$

γ refers to the gyromagnetic ratio of the proton and ω_0 is its precession frequency (see next subsection). The operator I_{z} describes the spin angular momentum in z direction. There are $2I + 1$ eigenstates of I_{z} and the eigenequation of I_{z} is

$$I_{\mathrm{z}}|\alpha\rangle = m\hbar|\alpha\rangle \tag{1.5}$$

with the azimuthal quantum number m. For a spin-1/2 particle $m = \pm 1/2$. H and I_{z} just differ by a scalar. Thus, they commute with each other ([H,I_{z}] = 0) and the eigenstates of I_{z} are also energy eigenstates. There are two energy eigenstates for a spin-1/2 particle with the energy eigenvalues

$$\mathrm{E}_{lower/higher} = \pm \frac{1}{2}\hbar\omega_0. \tag{1.6}$$

The lower energy eigenstate corresponds to $m = 1/2$ for particles with a positive gyromagnetic ratio, and thus negative ω_0 (see Eq. (1.4)). The higher energy eigenstate corresponds to $m = -1/2$. Therefore, the energy eigenstates are no longer degenerate. This splitting of energy eigenstates is known as the Zeeman effect.

1.3.2 Spin dynamics

So far no time dependency of spin states has been considered. To determine the dynamics of a nuclear spin placed into $\vec{B}_0$ the time dependent Schrödinger equation,

$$\omega_0 I_z |\psi(t)\rangle = i\hbar \frac{d}{dt} |\psi(t)\rangle, \tag{1.7}$$

has to be solved [30]. A general solution is given by

$$|\psi(t)\rangle = a\, e^{-i\,\omega_0 \frac{t}{2}} |+\rangle + b\, e^{i\,\omega_0 \frac{t}{2}} |-\rangle. \tag{1.8}$$

The eigenvalues of the eigenvectors $|+\rangle$ and $|-\rangle$ are $\frac{\hbar}{2}$ and $-\frac{\hbar}{2}$, respectively. Calculating the norm $\langle\psi(t)|\psi(t)\rangle = 1$, leads to $|a|^2 + |b|^2 = 1$.

The following example was taken from reference [30]. What happens to the spin of a proton which points initially in the positive x-direction? The initial spin state given in the basis set of eigenvectors of I_z is $|S_x; +\rangle = \frac{1}{\sqrt{2}}|+\rangle + \frac{1}{\sqrt{2}}|-\rangle$ with $a = b = \frac{1}{\sqrt{2}}$. The probability of this spin state either pointing in the same direction or in the opposite direction at some later time is calculated by:

$$|\langle S_x; +|\psi(t)\rangle|^2 = \cos^2 \frac{\omega_0 t}{2} \tag{1.9}$$

$$|\langle S_x; -|\psi(t)\rangle|^2 = \sin^2 \frac{\omega_0 t}{2} \tag{1.10}$$

B_0 along z-direction causes the spin to rotate at a frequency ω_0. There is a finite probability that the spin will point along the negative x-direction at some later time.

The expectation value of the spin can be calculated using the spin operators S_x, S_y, S_z

$$S_x = \frac{\hbar}{2}\left(|+\rangle\langle -| + |-\rangle\langle +|\right) \tag{1.11}$$

$$S_y = \frac{\hbar}{2}\left(-i|+\rangle\langle -| + i|-\rangle\langle +|\right) \tag{1.12}$$

$$S_z = \frac{\hbar}{2}\left(|+\rangle\langle +| - |-\rangle\langle -|\right) \tag{1.13}$$

written again in the basis set of the eigenvectors of I_z.

The expectation value of the spin in x,y and z direction

$$\langle S_x \rangle = \langle \psi(\mathrm{t}) | S_x | \psi(\mathrm{t}) \rangle \tag{1.14}$$

$$= \left(\frac{\hbar}{2}\right) \cos^2\left(\frac{\omega_0 \mathrm{t}}{2}\right) + \left(-\frac{\hbar}{2}\right) \sin^2\left(\frac{\omega_0 \mathrm{t}}{2}\right) = \left(\frac{\hbar}{2}\right) \cos(\omega_0 \mathrm{t}), \tag{1.15}$$

$$\langle S_y \rangle = \left(\frac{\hbar}{2}\right) \sin(\omega_0 \mathrm{t}) \tag{1.16}$$

$$\langle S_z \rangle = 0 \tag{1.17}$$

describes a spin precession occurring in the xy-plane. Thus, a proton precesses inside B_0 at the *Larmor* frequency ω_0 with

$$\omega_0 = -\gamma B_0 \tag{1.18}$$

in units of rad/s. The proton gyromagnetic ratio is $42576375 \cdot 2\pi \, \frac{\mathrm{rad}}{\mathrm{s \cdot T}}$ [34]. In MRI, the dependency of the *Larmor* frequency on the magnetic field strength is exploited to obtain spatially resolved images (Section 2.1).
The same results as in Eq. (1.14) can be deduced using a semiclassical description with the proton being treated as a classical spinning top although with quantized energy levels.

1.3.3 Time dependent magnetic fields

The application of RF pulses (time dependent magnetic field $B_1(t)$) causes the Hamiltonian to be time dependent. A transformation from the laboratory frame into a rotating reference frame is conducted for simplification (RF pulse can be described with a component rotating in the same sense as the nuclear spin precession (resonant field) and another component rotating in the opposite sense (non-resonant field)) [27].
A transformation of the Hamiltonian given in Eq. (1.4) into the rotating frame results in

$$H_{\mathrm{rot}} = (\omega_0 - \omega_{\mathrm{ref}}) I_{\mathrm{z}} \tag{1.19}$$

containing the frequency difference between the *Larmor* frequency of the spins and the frequency of the rotating frame ω_{ref}. If an RF pulse is applied in addition to B_0, the Hamiltonian in the rotating frame can be approximated by

$$H_{\mathrm{rot,RF}} \approx (\omega_0 - \omega_{\mathrm{ref}}) I_{\mathrm{z}} + \omega_{\mathrm{nutation}} \left(I_{\mathrm{x}} \cos \Phi_p + I_{\mathrm{y}} \sin \Phi_p \right) \tag{1.20}$$

Overall, no time dependency remains in Eq. (1.20). The additional term in this equation (compared to Eq. (1.19)) contains the so called nutation frequency $\omega_{\mathrm{nutation}} = |\frac{1}{2}\gamma B_{1,\mathrm{max}}|$ which is directly proportional to the maximum amplitude of the RF pulse. The two operators I_{x} and I_{y} describe the spin angular momentums in x direction and y direction. The phase of the pulse is given by Φ_p. For example a x-pulse has $\Phi_p = 0$. If this pulse is applied on-resonance for a certain duration τ_{RF}, a parameter called flip angle of the pulse (Θ_{RF}) is defined as

$$\Theta_{\mathrm{RF}} = \omega_{\mathrm{nutation}} \, \tau_{\mathrm{RF}}. \tag{1.21}$$

A pulse is on-resonance if $\omega_0 - \omega_{\mathrm{ref}} = 0$. In this case the axis of the spin angular momentum is in the xy-plane. If a pulse is off-resonant ($\omega_0 - \omega_{\mathrm{ref}} \neq 0$), the spin angular momentum vector gets also a contributing component in z direction due to I_{z}. The further

off resonant a pulse is the more the axis of the spin angular momentum is aligned towards the z-direction. Hence, a pulse which is far off-resonance is quite ineffective and does not affect the longitudinal magnetization much (longitudinal magnetization is explained in subsection 1.4.2). On the other hand, if the RF pulse is resonant, the transition between spin states which is expected for that specific pulse occurs efficiently (transition probability reaches a value of one in this case). Therefore, RF pulses are frequency selective. Strong pulses having a large peak amplitude are less frequency selective than weak pulses. Since the differences between the *Larmor* frequencies of isotopes are usually much larger than the available nutation frequency and hence maximum RF pulse amplitudes, only one isotope can be substantially influenced by an RF field applied on-resonance. Therefore, multinuclear NMR spectrometer are designed which can be tuned to the resonance frequencies of different isotopes. This subsection 1.3.3 is a summary from the book of M. H. Levitt [27], and the reader is referred to this book for further details.

1.4 Spin-1/2 ensembles

In MR experiments, a huge number of protons as well as electrons are involved and the time dependent Schrödinger equations has to be solved for this multi particle system. Generally, this is not possible if all interactions are considered. Assumptions including time averaging and symmetry considerations simplify the equations to be solved. A detailed discussion on the simplification called spin Hamiltonian hypothesis and the remaining Hamiltonian operators describing different interaction mechanisms can be found in reference [27]. A brief summary of some spin interactions (magnetic interactions and electric interactions) is given below.

1.4.1 Spin interactions

Even if B_0 is homogeneous on a macroscopic scale, it is not on a microscopic scale due to the chemical environment of the atoms. The magnetic influence of electrons as well as of protons give rise to effects known as chemical shift and dipole-dipole coupling. Furthermore, electric interactions can arise. This subsection is based on reference [27].

Chemical shift

If the electrons are involved their impact on the *Larmor* frequency is known as *chemical shift* for diamagnetic substances. B_0 at the location of a nucleus is altered by the induced magnetic field of the electrons B_{induced}

$$B_{\mathrm{nucleus}} = B_0 + B_{\mathrm{induced}}. \tag{1.22}$$

Thus, its *Larmor* frequency $\omega_{\mathrm{nucleus}}$ is slightly changed compared to ω_0. The spectra of different compounds in a molecule for example are shifted on the frequency axis with respect to each other. Since this frequency shift is linearly dependent on B_0 and since ω_0 is also a linear function of B_0, a magnetic field independent quantity of the chemical shift δ is obtained by calculating the ratio

$$\delta = \left(\frac{\omega_0 - \omega_{\mathrm{TMS}}}{\omega_{\mathrm{TMS}}} \right). \tag{1.23}$$

ω_{TMS} refers to the *Larmor* frequency of the same substance in a reference compound such as tetramethylsilane (TMS) or 4,4-dimethyl-4-silapentane-1-sulfonic acid (DSS). Chemical shifts are usually denoted with ppm (a dimensionless unit meaning the same as 10^{-6}).

Dipole-dipole coupling

Dipole-dipole coupling is based on the mutual interaction of nuclear spins belonging to the same molecule (intramolecular dipole-dipole coupling) or belonging to different molecules (intermolecular dipole-dipole coupling). In isotropic liquids such as water dipole-dipole coupling essentially averages to zero. Thus, it is not directly observable in MRI; however, it plays a role in the relaxation of spin systems.
A detailed discussion and summary of spin interactions which are taking place within a sample placed into an NMR spectrometer is presented in reference [27]. As a result of the magnetic interactions, the NMR signal contains information about the electronic and nuclear environments of the spins [27].

Electric interactions

In addition, there are electric interactions which vanish for spin-1/2 particles. However, they can be of substantial strength for particles with $I > 1/2$ through electric quadrupole interactions.

1.4.2 Density operator

In isotropic liquids, the intermolecular interactions can be neglected (long range dipole-dipole interactions are very small and the short range dipole-dipole interactions average out due to motion) [27]. The spin angular momentums, and thus the magnetic moments of the proton spins, act independently in a sample of water (isolated spin-1/2 ensemble if additionally the rare isotopes are neglected). Generally, most of the spins are in superposition states of the two eigenstates $|+\rangle$ and $|-\rangle$. The method to describe this situation without considering each spin individually is called density operator method. It allows the results of macroscopic observation to be predicted.
The density matrix of a spin-1/2 ensemble (non-interacting spins) is given by [27]

$$\rho = \begin{pmatrix} \rho_{++} & \rho_{+-} \\ \rho_{-+} & \rho_{--} \end{pmatrix}. \tag{1.24}$$

The diagonal elements in this matrix represent the populations of the eigenstates $|+\rangle$ and $|-\rangle$. They are real numbers between 0 and 1. The difference in these populations is physically important. For example if a higher population occurs in the lower energy state (represented by $|+\rangle$) than in the higher energy state ($|-\rangle$), then a macroscopic net magnetization exists with its net spin angular momentum and thus magnetic moment aligned parallel to the external magnetic field. This refers to the longitudinal magnetization which is built up if a sample of water is placed into an MR system [27, 35]. The time scale to achieve this longitudinal magnetization is usually in the order of milliseconds or seconds. The longitudinal magnetization is very small; nevertheless, it can be used to generate an NMR signal.

The off diagonal elements of the density matrix are called coherences between the two eigenstates $|+\rangle$ and $|-\rangle$ and are complex numbers [27]. The coherence is an indicator if there exists any macroscopic transverse magnetization. This means if there is a non zero net spin angular momentum perpendicular to the magnetic field. This is of course not the case if the spin angular momentums are distributed equally in the xy-plane. The phase of the coherence gives information about the orientation of the transverse magnetization vector with respect to the x-axis in the rotating frame.

1.4.3 Occupation probability in thermal equilibrium

In thermal equilibrium, the coherences between the states are zero and the populations of the energy states are distributed according to the Boltzmann distribution [27]

$$\rho_{++,\text{equilibrium}} = \frac{e^{-\frac{\hbar\omega_0}{2\mathrm{k_B}T}}}{e^{-\frac{\hbar\omega_0}{2\mathrm{k_B}T}} + e^{\frac{\hbar\omega_0}{2\mathrm{k_B}T}}} \tag{1.25}$$

$$\rho_{--,\text{equilibrium}} = \frac{e^{\frac{\hbar\omega_0}{2\mathrm{k_B}T}}}{e^{-\frac{\hbar\omega_0}{2\mathrm{k_B}T}} + e^{\frac{\hbar\omega_0}{2\mathrm{k_B}T}}}. \tag{1.26}$$

At T=25 °C, the value of $\mathrm{k_B}T$ equals $4.1 \cdot 10^{-21}$ J. The energy difference ΔE between the two energy eigenstates of the proton in a high magnetic field of 11.74 T for example is four orders of magnitude smaller ($\hbar\gamma B_0 = 3.3 \cdot 10^{-25}$ J) [27].

Since $\mathrm{k_B}T \gg |\hbar\omega_0|$ (high temperature approximation), the exponential functions in equations Eq. (1.25), Eq. (1.26) can be expanded as a power series [27]

$$\rho_{++,\text{equilibrium}} \approx \frac{1 - \frac{1}{2}\frac{\hbar\omega_0}{\mathrm{k_B}T}}{\left(1 - \frac{1}{2}\frac{\hbar\omega_0}{\mathrm{k_B}T}\right) + \left(1 + \frac{1}{2}\frac{\hbar\omega_0}{\mathrm{k_B}T}\right)} = \frac{1}{2}\left(1 - \frac{1}{2}\frac{\hbar\omega_0}{\mathrm{k_B}T}\right) \tag{1.27}$$

$$\rho_{--,\text{equilibrium}} \approx \frac{1 - \frac{1}{2}\frac{\hbar\omega_0}{\mathrm{k_B}T}}{\left(1 - \frac{1}{2}\frac{\hbar\omega_0}{\mathrm{k_B}T}\right) + \left(1 + \frac{1}{2}\frac{\hbar\omega_0}{\mathrm{k_B}T}\right)} = \frac{1}{2}\left(1 + \frac{1}{2}\frac{\hbar\omega_0}{\mathrm{k_B}T}\right) \tag{1.28}$$

For $\gamma > 0$ follows $\omega_0 < 0$,and the population $\rho_{++,\text{equilibrium}}$ of the lower energy state is slightly larger than the population $\rho_{--,\text{equilibrium}}$ for the higher energy state at room temperature. NMR methods are based on this anisotropic occupation of energy states in thermal equilibrium.

The magnitude of this longitudinal magnetization in z-direction (parallel to B_0) is directly proportional to the population difference ($\rho_{++,\text{equilibrium}} - \rho_{--,\text{equilibrium}}$) times the total number of spin-1/2 particles N_{total} and given by [29]

$$M_{\text{z,equilibrium}} = -\frac{\hbar\omega_0}{2\mathrm{k_B}T}\, N_{\text{total}}\, \frac{\gamma\hbar}{2} = \frac{\hbar^2\gamma^2 B_0}{4\mathrm{k_B}T}\, N_{\text{total}}. \tag{1.29}$$

The term $\frac{\gamma\hbar}{2}$ equals the z-component of the magnetic moment vector for a spin-1/2 particle. Since the x-components and y-components of the spin magnetic moments are equally distributed between all angles (0 to 2π) within the xy-plane, no contributions to the macro-

scopic magnetization arises from x-components and y-components [29] and

$$\vec{M}_{\mathrm{macroscopic}} = M_{\mathrm{z,equilibrium}}\vec{\mathrm{e}}_{\mathrm{z}}. \tag{1.30}$$

1.4.4 Radio frequency pulses, population changes, creation of coherence

As for the case of a single spin-1/2 particle the interaction of a non-interacting spin-1/2 ensemble with an RF pulse is best described in a rotating frame [27]. The spin populations in the laboratory frame and rotating frame are equal. For the coherences an additional time dependent phase factor occurs in the rotating frame. A macroscopic net magnetization (net spin angular momentum) of the spin ensemble is described by the spin density operator of the non-interacting spin-1/2 particles in the rotating frame. A sufficiently strong RF pulse is considered such that off-resonance effects can be ignored (see section 1.3.3).
The z-magnetization pointing in positive z direction is rotated by an x-pulse, with a flip angle of π, to the negative z-axis. The population values between the low energy state and the high energy state are exchanged. No coherences are generated. Further examples and more details can be found in the book of M. H. Levitt [27]. An x-pulse with a flip angle of $\frac{\pi}{2}$ rotates the initial z-magnetization to the negative y-axis and coherent transverse magnetization is thus created. The populations of the two energy states become equal through the application of the pulse and coherences arise. Thus the z-magnetization becomes zero. After the end of the pulse the coherent transverse magnetization precesses in the xy-plane. Due to slightly different local magnetic fields at different instants of times (microscopic fluctuations) loss of coherence occurs and the free precessing magnetization in the xy-plane decreases as time evolves. This process is irreversible (entropy of the spin system increases) [27]. The time constant characterizing this relaxation process is called T2. T2 can be very small as for solids or large molecules in liquids in the order of microseconds. For most soft tissues T2 is in the order of tens of milliseconds, and in liquids T2 is in the order of seconds [28]. Due to field inhomogeneities of B_0 on a microscopic and a macroscopic scale the loss of coherence occurs actually faster than given by T2. This is considered in the overall relaxation time constant $\mathrm{T2}^*$ [28]. Another important time constant, called spin lattice relaxation time constant or longitudinal relaxation time constant (T1) [27], describes the return of the longitudinal magnetization to thermal equilibrium. For the latter the populations of the two energy states return to their initial values by exchange of energy between the spins and their molecular surroundings. The different time constants are related such that

$$\mathrm{T2}^* \leq \mathrm{T2} \leq \mathrm{T1}\ (\text{practical limit})\ [27]. \tag{1.31}$$

The values of T1, T2 and $\mathrm{T2}^*$ can be quite distinct for various types of tissue. Thus, MRI exhibits a variety of possibilities to generate image contrasts such as T1 weighting, T2 weighting, proton density weighting, susceptibility weighting and so on [36].
A full description of the spin-1/2 ensemble inside magnetic fields (including relaxation effects) was derived by F. Bloch. The so called Bloch equations are introduced in the subsequent subsection.
For further details regarding quantum mechanics and its application in NMR spectroscopy or imaging, the reader is referred to these books [27, 28, 30] or this journal article [35] for example.

1.4.5 Bloch equations

In 1946 Felix Bloch [18] introduced a formalism to describe the time dependency of the magnetization $\vec{M} = (M_\mathrm{x}, M_\mathrm{y}, M_\mathrm{z})$ of a spin-1/2 ensemble exposed to static magnetic fields and time varying magnetic fields such as radio frequency pulses. The relaxation of the spin system towards its equilibrium state after excitation are included in these equations.
For example for an external static magnetic field applied in z-direction, $\vec{B}_0 = (0, 0, B_0)$, the Bloch equations simplify to [28]

$$\frac{\mathrm{d}M_\mathrm{x}}{\mathrm{dt}} = \gamma M_\mathrm{y} B_0 - \frac{M_\mathrm{x}}{T_2} \tag{1.32}$$

$$\frac{\mathrm{d}M_\mathrm{y}}{\mathrm{dt}} = -\gamma M_\mathrm{x} B_0 - \frac{M_\mathrm{y}}{T_2} \tag{1.33}$$

$$\frac{\mathrm{d}M_\mathrm{z}}{\mathrm{dt}} = \frac{M_0 - M_\mathrm{z}}{T_1}. \tag{1.34}$$

T1 and T2 are the longitudinal and transverse relaxation times and M_0 denotes the thermal equilibrium magnetization. The precession of $\vec{M}_\mathrm{xy}$ in the x-y-plane is represented by the first term in Eq. (1.32) and in Eq. (1.33), respectively. The relaxation of $\vec{M}_\mathrm{xy}$ is given by the terms containing either T2 or T1.
The general solutions of the differential equation given above are [28]

$$M_\mathrm{x}(t) = e^{-\frac{t}{T2}} (M_\mathrm{x}(0)\cos(\omega_0 t) + M_\mathrm{y}(0)\sin(\omega_0 t)) \tag{1.35}$$

$$M_\mathrm{y}(t) = e^{-\frac{t}{T2}} (M_\mathrm{y}(0)\cos(\omega_0 t) - M_\mathrm{x}(0)\sin(\omega_0 t)) \tag{1.36}$$

$$M_\mathrm{z}(t) = M_\mathrm{z}(0) e^{-\frac{t}{T1}} + M_0 (1 - e^{-\frac{t}{T1}}). \tag{1.37}$$

In thermal equilibrium, $M_\mathrm{x}(\infty) = M_\mathrm{y}(\infty) = 0$ and $M_\mathrm{z}(\infty) = M_0$.
When considering the combination of static and time varying magnetic fields, a change of the reference system from the laboratory frame (static coordinate system) into a rotating frame is conducted to simplify the problem. Thus, a coordinate system rotating around the z-axis at a frequency ω is defined to describe the change of the magnetization during the signal generation process. A detailed introduction of the transformation into a rotating reference frame is given in Haacke *et al.*, Chapter 3 [28]. The axis of the rotating frame are denoted with x', y' and z'=z. For a left circularly polarized magnetic field B_1 as commonly applied in MR, the Bloch equations in the rotating frame are given by [28]

$$\left(\frac{\mathrm{d}M_\mathrm{x}}{\mathrm{dt}}\right)' = (\omega_0 - \omega)\, M_\mathrm{y'} - \frac{M_\mathrm{x'}}{T_2} \tag{1.38}$$

$$\left(\frac{\mathrm{d}M_\mathrm{y}}{\mathrm{dt}}\right)' = -(\omega_0 - \omega) M_\mathrm{x'} + \omega_1\, M_\mathrm{z} - \frac{M_\mathrm{y'}}{T_2} \tag{1.39}$$

$$\left(\frac{\mathrm{d}M_\mathrm{z}}{\mathrm{dt}}\right)' = -\omega_1\, M_\mathrm{y'} + \frac{M_0 - M_\mathrm{z}}{T_1}. \tag{1.40}$$

using the assumption $B_1 \ll B_0$. The precession frequency of the spins due to B_1 of the RF pulse is denoted with ω_1. Here, $\omega_0 \equiv \gamma B_0$ and ω refers to the frequency of the RF pulse in

the laboratory frame (non rotating system). If $\omega = \omega_0$ (on-resonance condition), B_1 is most effective in tipping the spins. The word *resonance* in the label *MR imaging* was inspired by this condition (see also subsection 1.3.3).

1.5 NMR signal generation

If a sample containing protons is placed into a static uniform external magnetic field, a longitudinal magnetization arises as described in the previous subsection. Frequently, the direction of B_0 and thus, of the longitudinal magnetization, is defined along the z-direction. The longitudinal magnetization obeys a cylindrical symmetry along z and no net magnetization results in the xy plane in thermal equilibrium. The application of an RF pulse can lead to a macroscopic transverse magnetization $\vec{M}_{\mathrm{xy}}$ which rotates in the x-y-plane. This freely rotating magnetic field induces an oscillating electric current (called free induction decay (FID) or NMR signal) in a wire coil properly placed next to the sample according to Faraday's law of induction and the principle of reciprocity. More details about nuclear induction and reciprocity can be found in [18, 28].
The complex NMR signal is related to the coherence $\rho_{-+}(t)$ with [27]

$$s(t) \sim 2i\rho_{-+}(t)\, e^{-i\Phi_{\mathrm{detect}}} = 2i\rho_{-+}(t=0)\, e^{-i\Phi_{\mathrm{detect}} + \left(i(\omega_0-\omega_{\mathrm{ref}}) - \frac{1}{\mathrm{T2}}\right)t}. \tag{1.41}$$

Φ_{detect} refers to possible phase shifting modes of the signal as it is detected. The coherence is time dependent in the rotating frame. Its amplitude at $t = 0$ (start of signal acquisition) is given by $\rho_{-+}(t = 0)$. Dependent on the kind of RF pulse applied, the amplitude of the signal can be complex.
The Fourier transformation of a complex NMR signal with real valued amplitude results in an absorption Lorentzian and dispersion Lorentzian for the real and imaginary part, respectively. This will be explained in more detail in the next section.

1.6 NMR spectroscopy

The acquired complex NMR signal over time oscillates due to the precessing transverse magnetization. The amplitude of the oscillations decrease exponentially with T2*. A Fourier transform of this signal results in a complex Lorentzian. The real part of the complex Lorentzian represents an absorption Lorentzian with the full width half maximum (FWHM) related to

$$\mathrm{FWHM}_{\mathrm{real}} = \frac{1}{\pi \cdot T2^*} \tag{1.42}$$

given in Hz [37]. Thus, the longer T2* (and therefore the slower the signal decays) the narrower the width of a spectral peak. Since most of the nuclear spins are related to a positive γ, their peaks are represented in the negative frequency range of the spectra (Eq. (1.18)). The imaginary part of the complex Lorentzian is called dispersion Lorentzian. It is a point-symmetric function. The real part of the spectrum is usually displayed since it provides a narrower and more symmetric representation than the imaginary part of the spectrum [38]. Due to spectral phase shifts the real part and the imaginary part of the complex Lorentzian can be a mixture of absorption and dispersion Lorentzians [27]. These phase shifts depend on features of the pulse sequence such as the timing of the

data acquisition. A phase correction of the spectrum is required to remove this 'out of phase' feature of the spectrum. However, accurate phase correction is not always possible. A possible representation of the spectrum is given by the magnitude of the spectrum since the phase shift is removed in this case. The disadvantage of the magnitude spectra is the increased width of the peaks compared to the absorption Lorentzian representation which may be problematic when peaks are overlapping ([38], page 104). The peak area of the magnitude mode is directly proportional to the number of nuclei. Since the peaks of the spectra considered in this work were clearly distinct and separate (see chapter 10), the magnitude of the spectrum was considered in this work to determine the temperature shift of the peaks. Another possibility of representation of the spectrum is the power spectra which is the square of the magnitude spectrum. The width of the power spectra is smaller than the magnitude spectrum by a factor of $\sqrt{3}$ [38].

Chapter 2

Magnetic Resonance Imaging (MRI)

The most important features to eventually obtain a spatially resolved MR images are summarized in this chapter. At first, selective excitation and spatial encoding as well as the concept of k-space are introduced. Subsequently, the main hardware components of an MR system and commonly applied software are explained. This chapter is based on the books from references [27, 28, 29].

2.1 Selective excitation and spatial encoding

In general, the acquired NMR signal contains information of the entire volume which was excited by the RF pulse. There is no intrinsic information about the spatial origin of the signal. As already briefly mentioned in the history section the key factor for the invention of MR imaging was to apply additional magnetic field gradients. These gradients were required to either spatially select a specific region of interest such as for slice selection or to encode the NMR signal with spatial information as in plane of a 2D slice for example.
Thus, to obtain additional information about the origin of the NMR signal so called selective excitation or spatial encoding can be conducted. The basic principle for the selection of a slice within an object and the spatial encoding in plane within the slice is introduced in the following.
The selection of a specific 2D imaging plane is conducted using an additional magnetic field gradient G_z superimposed on B_0. Hence, the precession frequency of the spin varies linearly along z according to Eq. (1.18). A narrow banded RF pulse with center frequency $\omega_{RF,0}$ is applied and interacts with the spin ensembles which precess at $\omega_0 = \omega_{RF,0}$ (resonance condition). In the low flip angle approximation the response profile of the RF pulse is given by the Fourier transform of its shape. Typically Gaussian shaped pulses or Hamming-filtered sinc-pulses are used.
The spins precessing at the resonance condition are located in a 2D plane perpendicular to the z-direction. Since the RF pulse consists of more than a single frequency, a 2D plane with a certain thickness d (called slice) is selected according to

$$\Delta z = d = \frac{\Delta\omega}{\gamma G_z} \tag{2.1}$$

with $\Delta\omega$ being the frequency bandwidth of the RF pulse. The bandwidth of the RF pulse is defined as $BW_{RF} = \frac{\Delta\omega}{2\pi}$. The slice selection gradient causes a dephasing of the spins

along the gradient direction within the slice. This reduces the signal. To compensate for this effect a second gradient along z with reversed sign is applied (gradient rephasing).

After the selection of the imaging slice of interest, the spatial origin of the signals within this slice is encoded. Additional magnetic field gradients are applied to modulate the *Larmor* frequency of the spins in the xy-plane according to

$$\omega_0(\vec{r}) = -\gamma \left(B_0 + B_{\text{grad}} \right) = -\gamma \left(B_0 + \vec{G}_{\text{r}} \cdot \vec{r} \right) = -\gamma \left(B_0 + G_{\text{x}} x + G_{\text{y}} y + G_{\text{z}} z \right) \tag{2.2}$$

with $\vec{r} = (x, y, z)$ denoting the spatial location. Chemical shifts are ignored in this equation. The gradients G_{x}, G_{y} and G_{z} are called frequency encoding gradient, phase encoding gradient, and slice selection gradients, respectively.

After slice selection, G_{y} is turned on for the time interval τ_{y} and turned off afterwards. Thus, the spins acquire a spatially dependent phase Φ_{penc} along G_{y} with

$$\Phi_{\text{penc}} = -\gamma G_{\text{y}} y \tau_{\text{y}}. \tag{2.3}$$

After G_{y} is turned off the spins precess again all at ω_0; however, each with a different phase. Therefore, G_{y} is called phase encoding gradient. After phase encoding and during data acquisition another gradient along the x-direction (perpendicular to the phase encoding direction) is applied. This G_{x} causes ω_0 of the signal $S(x, t)$ to vary along x-direction according to

$$S(x, t) \propto \int_{\text{sample volume}} \rho(x)\, e^{-i\gamma(B_0 + G_{\text{x}} x)t}\, dx. \tag{2.4}$$

Relaxation effects (T1, T2 or T2*) are neglected. In this 1D signal equation $\rho(x)$ denotes the spin density along x-direction. The local frequency is spatially dependent. Thus, the gradient causing this effect is called frequency encoding gradient.

By a superposition of the gradients in the three spatial directions x,y,z, images in arbitrary orientations can be acquired [29]. For convenience and without loss of generality the frequency encoding gradient, phase encoding gradient, and slice selection gradient are chosen to be aligned in x-direction, y-direction and z-direction, respectively.

Note, that only the component of the gradient along the z-direction $G_{\text{x,y,z}} = \frac{dB_{\text{x,y,z}}}{dz}$ is relevant for image encoding. The field components of the gradient coils in x and y direction are known as concomitant fields or Maxwell terms and lead to image distortions.

2.2 K-space and image space

Extending Eq. (2.4) to 3D, the spatially encoded, time dependent signal after demodulation (which removes the carrier signal oscillating at ω_0 [29]) is given by

$$S(t) \propto \int_{\text{sample volume}} \rho(\vec{r})\, e^{-i\gamma \vec{G}_{\text{r}}(t)\cdot\vec{r}\, t}\, d\vec{r} = \int_{\text{sample volume}} \rho(\vec{r})\, e^{-i2\pi \vec{k}(t)\cdot\vec{r}}\, d\vec{r} = S(\vec{k}) \tag{2.5}$$

neglecting relaxation (T1, T2 or T2*). The equation represents a Fourier transform of the spin density $\rho(\vec{r})$ in the sample volume. $\vec{r} = (x, y, z)$ refers to the location within the sample. Frequently, so called k-space coordinates or spatial frequency coordinates are

used and defined as

$$k_{\mathrm{r}}(t) = \frac{\gamma}{2\pi}\int_0^{\mathrm{t}} G_{\mathrm{r}}(\tau)\mathrm{d}\tau \qquad \text{and} \qquad \mathrm{r} = \{\mathrm{x},\mathrm{y},\mathrm{z}\}. \tag{2.6}$$

An inverse Fourier transformation of the measured signal distribution $S_{\mathrm{meas}}(\vec{k})$ reveals the desired reconstructed image

$$\hat{\rho}(\vec{r}) = \Im\{S_{\mathrm{meas}}\left(\vec{k}\right)\}^{-1}. \tag{2.7}$$

The more spins are located at a particular position (x,y,z) within the imaged object, the more spectral amplitudes add up [27]. So far, the image represents an accurate estimate of the spin density [28]. Since the data can only be sampled in a finite manner with respect to $\vec{k}$ (signal is acquired for a finite time during read out and signal acquisition is repeated with a finite number of phase encoding steps), ρ is not exactly equal to $\hat{\rho}$. Deviations between ρ and $\hat{\rho}$ such as aliasing or Gibbs ringing phenomenons can be related to the sampling process and specific properties of the Fourier transform. Overall, ρ is a real quantity whereas $\hat{\rho}$ can be real or complex.
The measured analogue signal which is sampled over a finite time is digitized by an analogue-digital converter. Thus, the digitized signal consists of N_{x} equidistant data points separated by the dwell time τ_{dwell}. Additionally, the acquisition of this signal was repeated N_{y} times with a different phase encoding gradient in each repetition to obtain a 2D encoded data set of a selected slice for example. The directions of the frequency encoding and the phase encoding are arbitrarily chosen to be in the x-direction and y-direction, respectively. A 2D resolved image is reconstructed by applying a discrete Fourier transformation to the discrete and finitely sampled data [36]

$$\hat{\rho}(j\Delta x, l\Delta y) = \frac{1}{N_{\mathrm{x}}N_{\mathrm{y}}}\sum_{m=0}^{N_{\mathrm{x}}-1}\sum_{n=0}^{N_{\mathrm{y}}-1} \mathrm{S}_{\mathrm{meas}}(m\Delta k_{\mathrm{x}}, n\Delta k_{\mathrm{y}})e^{i2\pi\left(\frac{jm\Delta k_{\mathrm{x}}\Delta x}{N_{\mathrm{x}}}+\frac{ln\Delta k_{\mathrm{y}}\Delta y}{N_{\mathrm{y}}}\right)} \tag{2.8}$$

with the continuous components of $\vec{r} = (x, y)$ and $\vec{k} = (\mathrm{k_x}, \mathrm{k_y})$ replaced by their discrete variables

$$x_j = j\Delta x,\ y_l = l\Delta y,\ k_{\mathrm{x},m} = m\Delta k_{\mathrm{x}}, \text{and } k_{\mathrm{y},n} = n\Delta k_{\mathrm{y}} \tag{2.9}$$

as well as

$$j = 0, 1, \ldots, N_{\mathrm{x}} - 1, \text{and } l = 0, 1, \ldots, N_{\mathrm{y}} - 1. \tag{2.10}$$

The number of data sampling points in x-direction and y-direction are related to Δx and Δk_{x} as well as to Δy and Δk_{y}

$$\Delta x\Delta k_{\mathrm{x}} = \frac{1}{N_{\mathrm{x}}}, \text{and } \Delta y\Delta k_{\mathrm{y}} = \frac{1}{N_{\mathrm{y}}}. \tag{2.11}$$

Thus, the product of the pixel size and the step size in k-space equals the inverse of the number of sampled points [36]. Furthermore, the total extent in k-space (e.g. $N_{\mathrm{x}}\Delta k_{\mathrm{x}}$) equals the inverse of the spatial pixel size in image space. Additionally, the field of view (FOV) given by $\mathrm{FOV_x} = N_{\mathrm{x}}\Delta x$ or $\mathrm{FOV_y} = N_{\mathrm{y}}\Delta y$ equals the inverse of the step size in k-space

$$\mathrm{FOV_x} = \frac{1}{\Delta \mathrm{k_x}}, \text{and } \mathrm{FOV_y} = \frac{1}{\Delta \mathrm{k_y}}. \tag{2.12}$$

The step size in k-space is related to the gradient and the time it is applied (see Eq. (2.6)),

$$\Delta k_{\mathrm{x}} = \frac{\gamma}{2\pi} G_{\mathrm{x}} \tau_{\mathrm{dwell}}, \text{and } \Delta k_{\mathrm{y}} = \frac{\gamma}{2\pi} \Delta G_{\mathrm{y}} \tau_{\mathrm{y}} \tag{2.13}$$

with τ_{y} the duration of ΔG_{y}. τ_{y} is kept the same for all N_{y} phase encoding steps. However, the amplitude of G_{y} is different for all N_{y} phase encoding steps. ΔG_{y} refers to this change in amplitude between two consecutive repetitions n and $n+1$.
The spatial resolution in image space in x-direction and y-direction can be rewritten using Eq. (2.13)

$$\Delta \mathrm{x} = \frac{2\pi}{\gamma G_{\mathrm{x}} \tau_{\mathrm{dwell}} N_{\mathrm{x}}} = \frac{1}{2k_{\mathrm{x,max}}} \quad \text{and} \quad \Delta y = \frac{2\pi}{\gamma \Delta G_{\mathrm{y}} \tau_{\mathrm{y}} N_{\mathrm{y}}} = \frac{1}{2k_{\mathrm{y,max}}} \tag{2.14}$$

with $k_{\mathrm{x,max}} = \frac{\gamma}{2\pi} G_{\mathrm{x}} \tau_{\mathrm{dwell}} \frac{N_{\mathrm{x}}}{2}$ and $k_{\mathrm{x,min}} = -k_{\mathrm{x,max}}$ as well as $k_{\mathrm{y,max}} = \frac{\gamma}{2\pi} \Delta G_{\mathrm{y}} \tau_{\mathrm{y}} \frac{N_{\mathrm{y}}}{2}$ and $k_{\mathrm{y,min}} = -k_{\mathrm{y,max}}$.
To define $\mathrm{FOV_x}$ the bandwidth of the receiver has to be adjusted. Note, the imaged object can be larger compared to the selected $\mathrm{FOV_x}$ since a hardware (bandpass) filter is applied (important feature of an MRI receiver) to avoid aliasing in the readout direction [36]. In contrast to the aliasing which occurs in the phase encoding direction when $\mathrm{FOV_y}$ is set too small compared to the extent of the object and cannot be removed via hardware filters.
The receiver bandwidth per pixel $BW_{\mathrm{receiver,pp}}$ and τ_{dwell} are related as [36]

$$BW_{\mathrm{receiver,pp}} \cdot \tau_{\mathrm{dwell}} = \frac{1}{N_{\mathrm{x}}}. \tag{2.15}$$

The total bandwidth of the receiver is then given by

$$BW_{\mathrm{receiver,total}} = BW_{\mathrm{receiver,pp}} N_{\mathrm{x}} = \frac{1}{\tau_{\mathrm{dwell}}}. \tag{2.16}$$

2.3 Magnetic Resonance (MR) system

The detection of NMR signals is challenging since these signals are weak. There is only a small surplus of spins in the thermal equilibrium in an external magnetic field which can be actually used for signal generation [27]. To increase this small amount of spins higher magnetic fields are applied. Nowadays, MR systems commonly operate at magnetic fields of several Tesla. For comparison the earth magnetic field is about 50μT at the surface of the earth [27].
The main components of a modern clinical MR system are:

1. a strong homogeneous static B_0 normally generated by a superconducting electromagnet
2. shim unit to sustain a homogeneous static B_0
3. gradient system providing additional magnetic fields in x-, y- and z-directions
4. radio transmitter section generating the RF pulse
5. Transmit and receive coil system:

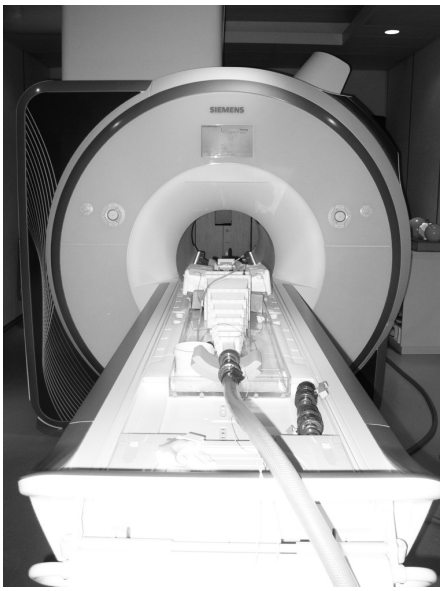

Figure 2.1: MR scanner with an in vitro setup on the patient table.

   (a) coil orientation: windings are not wrapped around B_0. Coil loop area vector is perpendicular to B_0.
   (b) transmit and receive coils (e.g. body volume coil) for RF signal emission and NMR signal detection
   (c) receive coils for NMR signal detection only (surface coils such as spine array coil, body array coil)

6. NMR signal receive section detecting a complex signal which is digitized via an analogue to digital converter (ADC)

7. a computer setup consisting of:

   (a) a host computer (MR-console)
   (b) a real time controller (called MPCU - measurement and physiologic control unit on a Siemens system)
   (c) an image reconstruction system

8. ancillary equipment such as the cooling system of the magnet

The superconducting electromagnet is cooled by liquid helium at a temperature of around 4 K. The gradient system, the shim unit and the body volume coil are incorporated into the housing of the MR system in Fig. 2.1. Characteristic parameters of the gradient system are the maximum gradient strength and the maximum slew rate. On the Siemens MR systems Tim-Trio and Prisma, which were used in this work, these values are 45 mT/m and 200 T/m/s (3 T, Tim-Trio, Siemens, Erlangen, Germany) and 80 mT/m and 200 T/m/s (3 T, Prisma, Siemens, Erlangen, Germany), respectively.
The gradient system is switched on and off, and the supply with electrical currents of these coils change. Lorentz forces act on the coils generating loud noises. Hence, ear protection

is required if people are in the vicinity of the running MR system or inside the bore of the magnet. The body volume coil is frequently used for emission of RF pulses. It is also applicable for NMR signal detection. However, to increase the signal to noise ratio of the detected NMR signal, surface coils are placed as closely as possible onto the subject to be imaged.
The MR imaging unit (MR scanner) is placed into an RF shielded room (Faraday cage) to avoid image distortions caused by external RF sources. Non conducting cables such as fiber optic cables can be fed through wave guides into the room of the MR system to sustain the Faraday cage.
At the MR-console, software (see pulse sequences in the following section) can be adjusted and run by the operator. Adjustments beyond the offered possibilities can be conducted in a special programming environment. The synchronization and timing of hardware components such as switching of gradient coils, RF amplifiers and so on is controlled by the real time computer. The acquired data is sent to the image reconstruction computer to process the MR images. All computers are connected via an Ethernet switch.

2.4 Pulse sequences

Pulse sequences are used at an MR system to control the timing of RF pulses, the gradient coils for spatial encoding, and the acquisition of k-space data. The FID signals can be manipulated such that so called spin echoes or gradient echoes are generated and detected. Pulse sequences based on spin echoes or gradient echoes are frequently used for MR acquisitions in clinical routine. Dependent on the timing of the individual components of a pulse sequence a variety of tissue contrasts can be generated which makes MRI an extremely powerful tool to address medical questions. The basic principles and key features of commonly applied MR pulse sequences are introduced in the following subsections. Two important parameters of an MR sequence are the echo time TE defining the time from the application of an RF pulse to the maximum amplitude of the echo, and the repetition time TR which gives the time interval between two consecutive sequence repetition intervals.

2.4.1 Spin echo sequence

In a spin echo sequence two RF pulses, a $\pi/2$ pulse and a π pulse, are applied consecutively (Fig. 2.2). The first pulse generates transverse magnetization as described in sections 1.5 and 2.1. After the first RF pulse and during the time interval $0 < t < \tau$, the transverse magnetization vector rotates in the xy-plane at ω_0. If there are local deviations from B_0 (denoted with $\Delta B(\vec{r})$ field inhomogeneities), precession frequencies of the spins deviate from ω_0. The corresponding phase offset is $\Phi_{\mathrm{xy}}(\vec{r},t) = -\gamma\Delta B(\vec{r})t$ [28]. The loss of coherence of the spin ensemble can be reversed by applying the second pulse with a flip angle of π. According to the Bloch equations 1.38–1.40, this second pulse rotates the transverse magnetization vector by $180°$ around the direction of the B_1-field of the pulse (For a $B_{1,y}$-pulse the y component of the vector remains the same whereas the x component changes its sign). This results in $\Phi_{\mathrm{xy,RF2}}(\vec{r},\tau) = \gamma\Delta B(\vec{r})\tau = -\Phi_{\mathrm{xy}}(\vec{r},\tau)$. During the consecutive time interval $\tau < t$ the phase offset becomes $\Phi_{\mathrm{xy2}}(\vec{r},t) = \gamma\Delta B(\vec{r})\tau - \gamma\Delta B(\vec{r})(t-\tau) = -\gamma\Delta B(\vec{r})(t-2\tau)$ [28]. At $t = 2\tau$ the phase offset becomes zero independently of the individual value of $\Delta B(\vec{r})$. Complete phase coherence is achieved and an echo signal occurs.

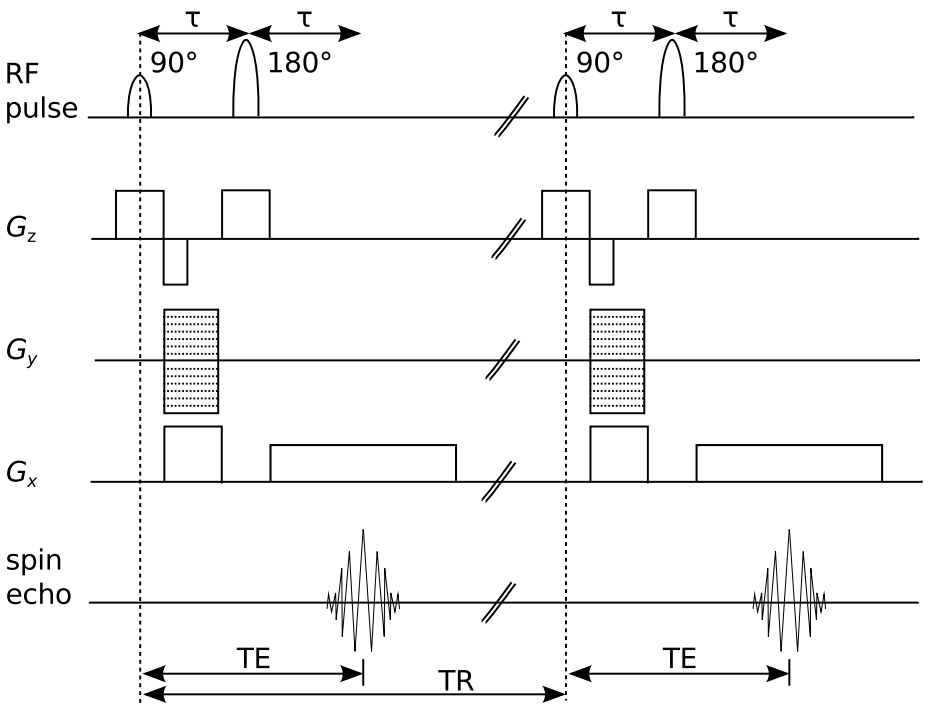

Figure 2.2: The schematics shows a spin echo sequence. The timing of the RF pulses ($\pi/2$ pulse and π pulse), the gradients for spatial encoding (G_x, G_y, G_z, see section 2.1), and the spin echo are indicated. The time interval τ between the $\pi/2$ pulse and π pulse and the time interval τ between the π pulse and the occurrence of the spin echo are equal. A spin echo occurs at $\mathrm{TE} \equiv 2\tau$. (Figure was adapted from reference [29].)

This signal acquired at $\mathrm{TE} \equiv 2\tau$ is called spin echo [39]. The key features here are that the time interval between the first and second RF pulse and the time interval between second RF pulse and the occurrence of the spin echo are equal and that the *Larmor* frequencies remain constant in time.
Since transverse magnetization undergoes T2-relaxation between excitation and echo formation (see subsection 1.4.4), the peak amplitude of the spin echo is given by [29]

$$s_{\mathrm{SE,ampl}} \propto e^{\left(-\frac{\mathrm{TE}}{\mathrm{T2}}\right)}. \tag{2.17}$$

In practice the flip angle of both excitation and refocusing pulse may deviate from $\pi/2$ and π, respectively. A more general equation considering arbitrary flip angles of the two pulses is given in [29]. The spin echo signal is a practically symmetric signal with its amplitude being T2 weighted [29].

2.4.2 Gradient echo sequence

Another way of generating an echo is by applying magnetic field gradients. If a gradient is applied, spins at different positions along the gradient acquire different phases. The longer the gradient is applied, the bigger the differences in their phases become. If the gradient is reversed (positive to negative sign or vice versa) the accumulated phases of the spins decrease according to their position in space. An echo signal (called gradient echo) occurs

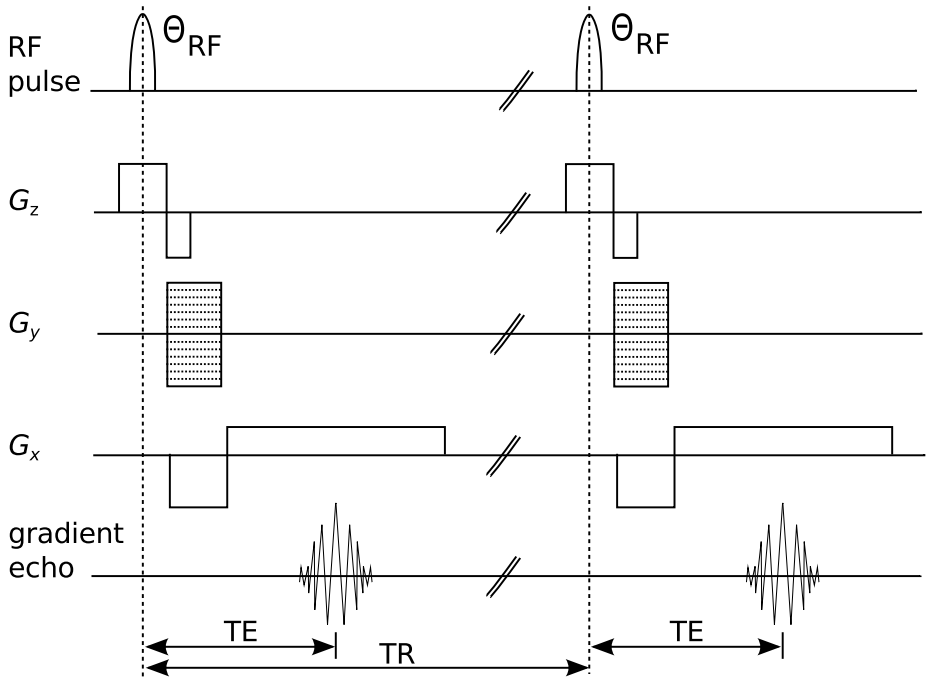

Figure 2.3: The schematics shows a gradient echo sequence. The timing of the RF pulse (with flip angle Θ_{RF}), the gradients for spatial encoding (G_{x}, G_{y}, G_{z}, see section 2.1), and the gradient echo are indicated. (Figure was adapted from reference [29].)

as the accumulated phases of the spins become zero (Fig. 2.3). All spins are rephased and phase coherence is regained. However, gradient reversal refocuses only the dephasing due to the gradient, dephasing due to other mechanisms (i.e., field inhomogeneities (see subsection 1.4.4)) remain. Thus, compared to spin echo formation the peak amplitude of the echo signal depends on T2* instead of T2 with

$$s_{\mathrm{gre,ampl}} \propto e^{\left(-\frac{\mathrm{TE}}{\mathrm{T2*}}\right)}. \tag{2.18}$$

Gradient echoes are frequently used in combination with the application of lower flip angles ($\Theta_{\mathrm{RF}} < 90°$) to reduce TR, and thus reduce the total acquisition time (denoted gre Fast Low Angle Shot (FLASH) sequences in the following). Due to the reduced TR, the longitudinal magnetization might not be fully recovered to its thermal equilibrium value before the next RF pulse is applied. Thus, a reduced amount of longitudinal magnetization is applicable for the conversion to coherence by the next RF pulse. After several RF pulses a steady state is reached between the recovery of the longitudinal magnetization and the generation of transverse magnetization. The optimum signal amplitude for a given TR and T1 is given by the so called 'Ernst'angle [40],

$$\cos(\Theta_{\mathrm{Ernst}}) = e^{\left(-\frac{\mathrm{TR}}{\mathrm{T1}}\right)}. \tag{2.19}$$

With Eq. (2.19) the optimum flip angle can be chosen to maximize the transverse magnetization of the steady state and hence, the measured signal.

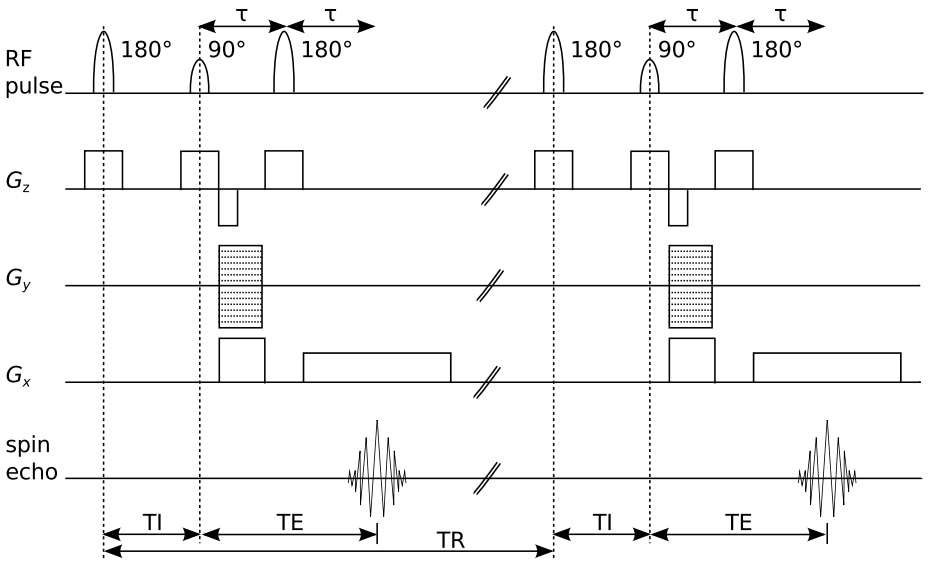

Figure 2.4: The schematics shows an inversion recovery spin echo sequence. The timing of the RF pulses (π pulse, $\pi/2$ pulse, and π pulse), the gradients for spatial encoding (G_x, G_y, G_z, see section 2.1), and the spin echo are indicated. The time interval between the first π pulse and the $\pi/2$ pulse of the spin echo sequence is called inversion time TI. (Figure was adapted from reference [29].)

2.4.3 Inversion recovery sequence

The relaxation time T1 is usually determined with an inversion recovery sequence. This type of sequence applies a π pulse to invert the longitudinal magnetization (magnetization preparation) as shown in Fig. 2.4. After waiting a time interval (called inversion time TI), the imaging sequence is played out starting with a $\pi/2$ pulse. During TI the inverted longitudinal magnetization (inverted populations) relaxes towards its equilibrium value. The population difference between the two energy levels for a spin-1/2 ensemble is converted into coherences as the $\pi/2$ pulse is applied. The resultant transverse magnetization generates an NMR signal. The NMR signal amplitude and with that (after Fourier transformation), the peak amplitude depends on T1 as follows [41, 21, 27]

$$s_{\mathrm{IR,ampl}} \propto \left(1 - 2\, e^{-\frac{\mathrm{TI}}{\mathrm{T1}}}\right). \tag{2.20}$$

To determine T1 the experiment has to be repeated several times applying each time a different value for TI.
If the pulses are repeated several times as it is commonly the case in MR imaging, the repetition time TR (this time defined as the time interval between the two consecutive π pulses) has to be considered according to [29]

$$s_{\mathrm{IR,ampl}} \propto \left(1 - 2\, e^{-\frac{\mathrm{TI}}{\mathrm{T1}}} + e^{-\frac{\mathrm{TR}}{\mathrm{T1}}}\right). \tag{2.21}$$

Chapter 3

Magnetic Resonance Velocimetry (MRV)

The ability to quantitatively measure velocities non-invasively in the human body is of great interest to study the progress of certain diseases in the vascular system. A frequently applied technique is Doppler ultrasound. However, in certain areas of the body the access with this technique is limited due to air or other constituents reflecting ultrasound waves. Thus, MR provides an excellent tool to study blood flow for example [3].

3.1 Velocity encoding

The sensitivity of the MR signal to motion was discovered in the 1950s [42, 41, 43, 44, 45]. However, it took several decades until velocity measurements were conducted in humans using magnetic resonance [46]. Different strategies were developed to extract velocity from the measured MR data. There are methods which rely on the change in signal intensity due to flow [43] or tagging of moving tissue using specific pulses [47, 48]. However, these methods have shortcomings such as difficulties in measuring velocity and vessel areas at once as stated in Pelc $et\ al.$[49]. Thus, they are not much used in clinical routine for measuring blood flow. In practice, so called phase shift methods are applied. They exploit the fact that the phase accumulation of spins traveling along a magnetic field gradient is different from static spins. Phase based methods (also known as phase contrast (PC) methods) are well suited for quantitative measurements [49]. PC MR velocimetry (MRV) is explained in more detail below since it was applied to acquire quantitative velocity images in this work.
The effective magnetic field B_{eff} seen by a spin ensemble inside the MR system providing an external static magnetic field B_0 is given by

$$B_{\text{eff}} = B_0 + \Delta B_0(\vec{r}) + \vec{G}(t) \cdot \vec{r}(t)). \tag{3.1}$$

Inhomogeneities of B_0, due to susceptibility differences of the object for example, are denoted by ΔB_0. The third term in Eq. (3.1) describes the contribution of the time dependent gradients applied during MR imaging. The effective frequency of the spin ensemble at a given location $\vec{r}$ is

$$\omega_{\text{eff}}(\vec{r}, t) = \gamma B_{\text{eff}}. \tag{3.2}$$

To obtain the phase accumulated by the spin ensemble within one excitation cycle the time integral of Eq. (3.2) has to be calculated,

$$\begin{aligned} \int_{t_0}^{t} \omega_{\text{eff}}(\vec{r},\tau)\,\mathrm{d}\tau &= \int_{t_0}^{t} \gamma\left(\Delta B_0 + \vec{G}(\tau)\cdot\vec{r}(\tau)\right)\,\mathrm{d}\tau \\ \Phi(\vec{r},t) - \Phi(\vec{r},t_0) &= \gamma\left(\Delta B_0(t-t_0) + \int_{t_0}^{t}\vec{G}(\tau)\cdot\vec{r}(\tau))\,\mathrm{d}\tau\right) \end{aligned} \tag{3.3}$$

with t_0 referring to the time when the RF pulse is applied and t denotes some later time such as the echo time TE, when the data is acquired. In a reference frame that is rotating at the *Larmor* frequency, γB_0 vanishes.
The vector variable $\vec{r}(\tau)$ in Eq. (3.3) can be rewritten in a Taylor series

$$\vec{r}(\tau) = \sum_{k=0}^{\infty} \frac{\vec{r}^{\,k}(t_0)}{k!}(\tau - t_0)^k \tag{3.4}$$

with $\vec{r}^{\,k}(t_0)$ being the k-th partial derivative of $\vec{r}(\tau)$ with respect to time evaluated at $\tau = t_0$. The combination of Eq. (3.4) with Eq. (3.3) results in

$$\Phi(\vec{r},t) = \Phi(\vec{r},t_0) + \gamma\Delta B_0(t-t_0) + \gamma\sum_{k=0}^{\infty}\frac{\vec{r}^{\,k}(t_0)}{k!}\cdot\int_{t_0}^{t}\vec{G}(\tau)(\tau-t_0)^k\,\mathrm{d}\tau \tag{3.5}$$

$$\Phi(\vec{r},t) = \Phi_0 + \sum_{k=0}^{\infty}\Phi_k(\vec{r}^{\,k},t). \tag{3.6}$$

The k-th gradient moment M^k is defined as [36]

$$M^k \equiv \int_{t_0}^{t}\vec{G}(\tau)(\tau-t_0)^k\,\mathrm{d}\tau. \tag{3.7}$$

The background phase Φ_0 includes the unknown initial phase of the spin ensemble at t_0 and additional phase contributions due to inhomogeneities of B_0. Note, the contributions of higher order gradient moments to $\Phi(\vec{r},t)$ are reduced by a factor of $\frac{1}{k!}$ (Eq. (3.5)).
The velocity is assumed to be approximately constant within the interval $[t_0 = 0, t]$. Therefore, higher orders of motion such as acceleration are negligible and the phase evaluation of the spin ensemble can be approximated by

$$\begin{aligned} \Phi(\vec{r},t) &\approx \Phi_0 + \gamma\,\vec{r}(0)\cdot\overbrace{\int_0^t\vec{G}(\tau)\,\mathrm{d}\tau}^{M^0} + \gamma\,\vec{v}(0)\cdot\overbrace{\int_0^t\vec{G}(\tau)\tau\,\mathrm{d}\tau}^{M^1} \\ &\approx \Phi_0 + \Delta\Phi_0 + \Phi_1. \end{aligned} \tag{3.8}$$

Typically, bipolar gradients are used to measure velocities. A bipolar gradient consists of a positive gradient lobe G_+ and a negative gradient lobe G_- (Fig. 3.1). These lobes have the same 0-th gradient moment. Stationary spins show a linear dephasing which is compensated by the second gradient lobe G_- after $2\Delta t$. Spins moving with a constant velocity along G follow a quadratic phase evolution leading to a non-zero phase $\Delta\Phi_1$ after

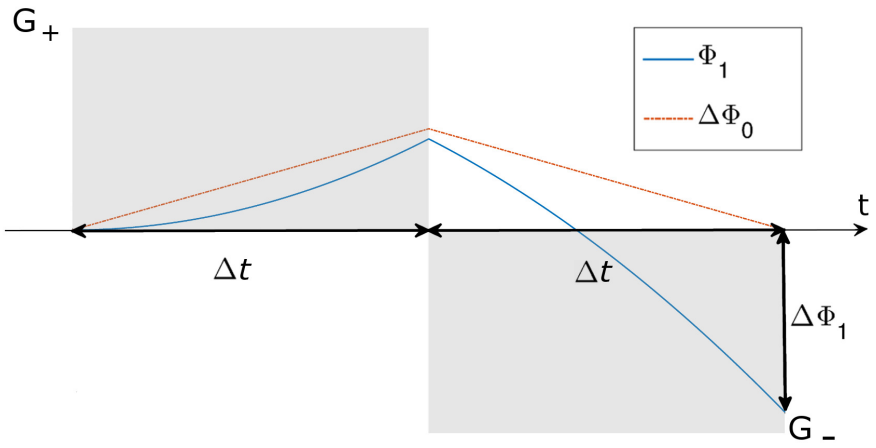

Figure 3.1: The schematics shows a point symmetric gradient G called bipolar gradient with a total duration of $2\Delta t$. Stationary spins show a linear dephasing which is compensated by the second gradient lobe G_- after $2\Delta t$. Spins moving with a constant velocity along G follow a quadratic phase evolution leading to a non-zero phase $\Delta\Phi_1$ after $2\Delta t$. (Figure was adapted from reference [36].)

$2\Delta t$.
The 0-th gradient moment M^0 of a bipolar gradient is zero, wheres its first gradient moment M^1 is nonzero. To null M^1 in addition to M^0, a tripolar gradient is required. It consists of three gradient lobes (G_+, two times G_-, and G_+ (Fig. 3.2)) leading to $\Delta\Phi_0 = 0$ and $\Phi_1 = 0$. Additional detailed information on gradient moment nulling can be found in Bernstein *et al.*[36].
Measurements once with a bipolar gradient (velocity encoded measurement) and once with a tripolar gradient (velocity compensated measurement) can be used to eliminate the unknown Φ_0 (Eq. (3.6)). These two measurements of $\Phi(\vec{r},t)$ with different M^1 are subtracted. Ideally, the remaining phase difference $\Delta\Phi(\vec{r},t)$ is only proportional to the velocity of the spin ensemble and all other effects affecting the phase are eliminated.
The phase difference between a velocity compensated and a velocity encoded measurement is given by

$$\begin{aligned} \Delta\Phi(\vec{r},t) &\approx \gamma v_{||} \Delta M^1 \\ \Longleftrightarrow v_{||} &\approx \frac{\Delta\Phi(\vec{r},t)}{\gamma\Delta M^1} = \Delta\Phi(\vec{r},t)\,\frac{v_{enc}}{\pi}. \end{aligned} \tag{3.9}$$

The maximum velocity which can be encoded with a certain value of M^1 and which leads to a phase shift of $\pm\pi$ is defined as v_{enc}

$$v_{enc} = \frac{\pi}{\gamma\Delta M^1}. \tag{3.10}$$

The v_{enc} is ideally chosen to be slightly higher than the maximum velocities occurring in the region of interest. If the v_{enc} is lower than the actual velocities measured, the phase difference exceeds the possible range of $-\pi$ to π and phase wrapping occurs. Phase wrap-

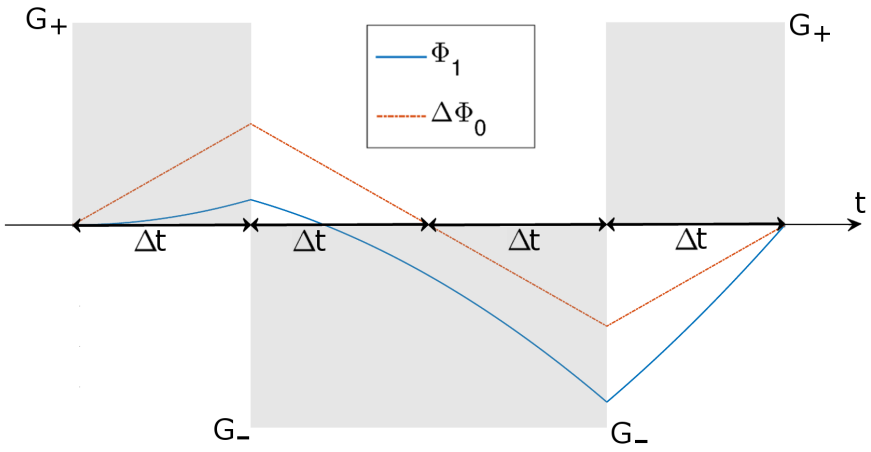

Figure 3.2: The schematics shows a tripolar gradient with a total duration of $4\Delta t$. The phase of the stationary spins and the phase of the non-stationary spins, moving with a constant velocity, are zero after $4\Delta t$ due to the specific combination of the gradient lobes G_+ and G_-. (Figure was adapted from reference [36].)

ping occurs since the phase and also the phase difference is a periodic function with a periodicity of 2π.

In contrast, choosing a too large v_{enc} compared to the maximum velocities within the region of interest causes an increase in the phase noise since [50]

$$\sigma_{\Phi \text{ noise}} \propto \frac{1}{SNR}. \tag{3.11}$$

SNR is the signal to noise ratio of the magnitude image. The phase noise of the phase difference images is given by

$$\sigma_{\Delta\Phi \text{ noise}} \propto \sqrt{\sigma^2_{\Phi \text{ noise}} + \sigma^2_{\Phi \text{ noise}}} = \frac{\sqrt{2}}{SNR} \tag{3.12}$$

if the noise of the two phase images is uncorrelated. Converting $\sigma_{\Delta\Phi \text{ noise}}$ to velocity units, results in the velocity phase noise [49]

$$\sigma_{\text{v}} = \frac{\sqrt{2}}{SNR}\frac{v_{enc}}{\pi}. \tag{3.13}$$

There are various different acquisition schemes to acquire velocity encoded data leading to different noise sensitivity of the measurement. Further information on this topic can be found in [51, 52].

A low v_{enc} measures low velocities more precisely than a high v_{enc} since the velocity phase shift is large compared to noise. However, increased flow ghosting can occur [53]. Generally, it is a trade-off between the adjustment of imaging parameters to the theoretically most suited value and imaging artifacts which may degrade the precision of quantitative analysis of the data.

3.2 Applications of MRV

Commonly, MRV is put into the medical context to study quantitatively the hemodynamics of the human body. Detailed reviews on currently available acquisition techniques and their possible clinical applications can be found in [3, 54, 55]. Data analysis strategies for flow visualization are presented and promising quantitative hemodynamic markers such as pulse wave velocity, pressure, turbulent kinetic energy, wall shear stress and so on are described.
Furthermore, MRV can be used to determine the physiologic boundary conditions required as data input in computational fluid dynamic (CFD) calculations [56]. Generally, the combination of these two methods offers a great potential for a variety of applications in engineering fields for example. An overview of disciplines which can benefit from MR imaging as an additional measurement device is presented in [57].
Additional to the medical application, MRV can be used in many other fields of science. An early application considered the measurement of fuel flow [58]. Recently, Wassermann $et\ al.$[8] presented MRV measurements conducted on a bi-stable fluidic oscillator. Good agreement was found between data acquired by MRV as well as laser Doppler anemometry. Another possible application of MRV was conducted in the field of biology. Goldstein $et\ al.$[59] studied the vacuolar flow in an acquatic plant using MRV. A comparison to theoretical calculations revealed excellent agreement. These examples just give a glimpse of the possibilities of MRV applied in fields other than medicine. A review on MRV with respect to engineering is given by Elkins and Alley [15].
In addition to MRV further parameters, describing scalar fields for example, could be investigated within the same MR measurement session. Benson $et\ al.$[6] studied 3D velocity fields and concentration fields to examine turbulent mixing of two streams in trailing edge regions of turbine blades.
There is a growing interest in different fields of engineering to determine both velocity fields and temperature fields using MRI. For example, in the context of biomedical engineering a laser heated shape memory polymer foam device was studied with MRI [60]. As the foam was thermally activated, the change in temperature as well as the change in the hemodynamics were of interest in this study.

Chapter 4

Magnetic Resonance Thermometry (MRT)

There are various temperature sensitive MR parameters which can be used for quantitative temperature assessment. The parameters are

1. proton resonance frequency (PRF) [61]
2. T1 and T2 relaxation times [62]
3. proton density [63]
4. diffusion coefficient [64]
5. magnetization transfer [65]

In addition, contrast agents have been developed which also exhibit a temperature dependency.
A brief summary about the basics of the above itemized parameters with respect to their applicability for temperature measurements is given in the following sections 4.2– 4.6. These sections are primarily based on the review article of Rieke and Pauly [10]. An overview over different applications of MRT reported in literature concludes this chapter.

4.1 MRT based on Proton Resonance Frequency (PRF)

The *Larmor* frequency of the hydrogen protons in the water molecule is altered due to the chemical shift (see Eq. (1.22)). An induced magnetic field (due to microscopic current distributions) partly screens the proton. Therefore, the local precession frequency of the proton is decreased,

$$\omega_{\mathrm{nucleus}} = \gamma\, B_0\, (1 - \sigma), \tag{4.1}$$

with σ denoting the screening constant of the hydrogen nuclei [10]. Hydrogen bonds influence this screening effect, and the formation of hydrogen bonds in water is temperature dependent. Fewer hydrogen bonds occur on average as the temperature increases. The screening becomes more effective. Therefore, σ increases with increasing temperature. This temperature dependency of $\omega_{\mathrm{nucleus}}$ is exploited in PRF thermometry.

The temperature dependency of σ can be linearly approximated as [10]

$$\sigma = \alpha\, T \tag{4.2}$$

within certain temperature ranges which depend on the substance under investigation. For instance, the temperature coefficient α is given by $\alpha_{\text{water}} = 1.03 \pm 0.02 \cdot 10^{-8}\,\text{K}^{-1}$ for pure water between -15 °C and 100 °C [66, 67] or $\alpha_{\text{water}} = 1.02 \pm 0.01 \cdot 10^{-8}\,\text{K}^{-1}$ over a temperature range between 13 °C and 36 °C [68]. Smaller values for water samples were determined by [69, 70], $\alpha_{\text{water}} = 0.970 \pm 0.003 \cdot 10^{-8}\,\text{K}^{-1}$ and $\alpha_{\text{water}} = 0.99 \pm 0.02 \cdot 10^{-8}\,\text{K}^{-1}$. The origin of the deviation to the value presented by Hindman [66] is not understood. Generally, variations of α for different tissue types containing water and no fat are typically sufficiently small such that a common value of $\alpha = 1.0 \cdot 10^{-8}\,\text{K}^{-1}$ is usually used in in vivo temperature measurements. In contrast to thermometry based on T1 (see section 4.2) no calibration for each tissue type is required for the PRF method.

In this work, α is defined to be positive because the screening effect increases with increasing temperature Eq. (4.2). In contrast, ω_{nucleus} decreases with increasing temperature. This temperature dependent change of ω_{nucleus} can be measured with MR techniques.

MRT based on PRF has been reported to be the most precise method [71] and the most sensitive method to detect small temperature changes [72]. There are two major acquisition strategies to detect temperature using PRF, one based on spectroscopy and one based on phase mapping.

4.1.1 Temperature sensitive spectroscopy

The temperature dependent chemical shift between two peaks of a spectrum can be used to determine absolute temperature values. For example, the spectrum contains a second temperature independent peak in addition to the water peak. The temperature dependent chemical shift of water can be determined in analogy to Eq. (1.23),

$$\delta_{\text{water,ref}} = \left(\frac{\omega_{\text{water}}(T) - \omega_{\text{reference peak}}(T)}{\omega_{\text{reference peak}}(T)} \right) \approx \left(\frac{\omega_{\text{water}}(T) - \omega_{\text{reference peak}}(T)}{\omega_{\text{spectrometer}}} \right). \tag{4.3}$$

with $\omega_{\text{spectrometer}}$ denoting the frequency of the spectrometer and T referring to the temperature [73]. $\delta_{\text{water,ref}}$ is related to the screening constants of water and the reference compound as follows,

$$\delta_{\text{water,ref}} \approx -\sigma_{\text{water}}(T) + \sigma_{\text{reference peak}} = \sigma_{\text{water,ref}} \tag{4.4}$$

with $\omega_{\text{water}}(T) = \gamma\, B_0\, (1 - \sigma_{\text{water}}(T) + \chi(T))$ and $\omega_{\text{reference peak}}(T) = \gamma\, B_0\, (1 - \sigma_{\text{reference peak}} + \chi(T))$. Note, the temperature dependent susceptibility $\chi(T)$ cancels.

If a linear relationship between $\delta_{\text{water,ref}}$ and temperature is present, the temperature change (slope of the linear regression) is given by $\alpha = \frac{\Delta\delta_{\text{water,ref}}}{\Delta T} = \frac{-\sigma_{\text{water}}(T_1) + \sigma_{\text{reference peak}} + \sigma_{\text{water}}(T_2) - \sigma_{\text{reference peak}}}{\Delta T} = \frac{\Delta\sigma_{\text{water}}}{\Delta T}$, and the absolute temperature can be obtained with [73]

$$T_{\text{abs}} = \frac{\delta_{\text{water,ref}}}{\alpha} + T_{\text{offset}} = \frac{\sigma_{\text{water,ref}}}{\alpha} + T_{\text{offset}}. \tag{4.5}$$

If solely a single peak is available in the spectrum, temperature differences can be determined (similarly to temperature phase mapping described in subsection 4.1.2), however, no absolute temperatures. A measurement needs to be conducted at two temperatures, T_{ref} and T for example. The shift in the resonance frequency at T_{ref} and T is determined and can be converted to a temperature change as [73]

$$\Delta T = \frac{\Delta\delta}{\alpha}. \tag{4.6}$$

Changes in the pH value might not directly affect the temperature coefficient. However, they influence the formation of hydrogen bonds, and thus the local resonance frequency of the protons causing difficulties in absolute temperature measurements [73]. Further factors which can influence the accuracy of the spectroscopic temperature measurements are the SNR, the duration for observing the decaying signal (spectral resolution), inhomogeneities of B_0 smaller than the voxel size, and eddy currents inducing transient changes of the resonance frequencies [73].

4.1.2 Temperature phase mapping

The acquisition of MR phase images with a gradient echo pulse sequence for example allows only the measurement of relative temperature changes (in contrast to the spectroscopic PRF method). Two consecutive measurements are performed: first, at temperature T_{ref} (serving as a reference scan), and second at a distinct temperature T achieved after cooling or heating of the sample.
During TE of the gradient echo sequence, the phase Θ_{PRF} of the acquired signal evolves as

$$\Theta_{\mathrm{PRF}} = \omega_{\mathrm{nucleus}}\,\mathrm{TE}. \tag{4.7}$$

A phase difference image is determined by subtracting the two phase images acquired at T_{ref} and T, respectively. The phase difference $\Delta\Theta_{\mathrm{PRF}}$ is directly proportional to the change in temperature ΔT between T and T_{ref},

$$\Delta T = \frac{\Theta_{\mathrm{PRF},T} - \Theta_{\mathrm{PRF},T_{\mathrm{ref}}}}{\gamma\, B_0\, \alpha\, \mathrm{TE}} = \frac{\Delta\Theta_{\mathrm{PRF}}}{\gamma\, B_0\, \alpha\, \mathrm{TE}}. \tag{4.8}$$

Eq. (4.8) results from the combination of Eq. (4.1),Eq. (4.2), and Eq. (4.7).
The phase sensitivity to temperature changes $\frac{\Delta\Theta_{\mathrm{PRF}}}{\Delta T}$ increases with increasing magnetic field strength and also with increasing TE. Generally, TE has to be adjusted to the expected range of temperature changes to avoid multi phase wraps ($\Delta\Theta_{\mathrm{PRF}} \gg 2\pi$) which cannot be corrected. However, there are also acquisition strategies available to make phase unwrapping of multi wrapped data possible by acquiring multi echo data using a multi echo gradient sequence for example. Furthermore, images acquired with longer TEs are more susceptible to inhomogeneities of B_0 and motion induced phase errors. For example, higher orders of motion add an additional phase which is not related to temperature. In addition, SNR can be decreased because of intra voxel dephasing and T2* relaxation.
The theoretical maximum of the temperature-dependent phase difference SNR is achieved if TE = T2* (see [10] for further details). If, however, PRF temperature phase mapping is conducted in fluid flows, TE smaller than T2* might need to be considered to reduce the displacement of spins during TE and possible phase contributions due to acceleration.

Thus, the best choice of TE depends on the flow conditions.
To estimate the uncertainty of the phase in the phase difference image, the phase noise which is related to SNR as shown in Eq. (3.12) for uncorrelated measurements is converted to temperature according to

$$\sigma_{\Delta \mathrm{T}} \approx \frac{\sqrt{2}}{SNR} \frac{1}{\gamma \, B_0 \, \alpha \, \mathrm{TE}}. \tag{4.9}$$

with the assumption $SNR_T \approx SNR_{T_{\mathrm{ref}}} = SNR$ since SNR changes with temperature. The factor $\sqrt{2}$ arises from Gaussian propagation of errors and disappears if the temperature uncertainty of a phase image acquired at a single temperature is considered as in referenceless PRF thermometry [74].
Furthermore, the accuracy of PRF temperature phase mapping is dependent on various effects arising from material properties (susceptibility, electrical conductivity) or temporal stability of the MR system (magnetic field drifts), and are discussed in the following.

Susceptibility effects

In addition to the temperature dependent chemical shift, the proton resonance frequency can be altered by the temperature dependence of the volume susceptibility [69]. In Eq. (4.1), the contributions to the screening by macroscopic currents occurring within the object was neglected. The macroscopic field of the object, $\vec{B}_{\mathrm{macro}}$, is altered by these currents. Hence, two effects [69], one microscopic (related to chemical shift) and one macroscopic, contribute to the total screening of a proton located at position $\vec{r}_{\mathrm{proton}}$. The total field at $\vec{r}_{\mathrm{proton}}$ is given by

$$\vec{B}_{\mathrm{local}}\left(\vec{r}_{\mathrm{proton}}\right) = \left(1 - \frac{2\chi_{\mathrm{object}}}{3} - \sigma\right) \vec{B}_{\mathrm{macro}}\left(\vec{r}_{\mathrm{proton}}\right) \tag{4.10}$$

with the susceptibility of the object χ_{object}. $\vec{B}_{\mathrm{macro}}$ is parallel to $\vec{B}_0$ for simple geometries such as a sphere or infinitely long cylinders whose axis are oriented parallel or perpendicular to B_0 [69]. This might not be the case for arbitrarily shaped objects. Generally, $\vec{B}_{\mathrm{macro}}$ can be calculated using Maxwell's equations. In the case of the infinitely long cylinders, the local fields inside are given by

$$B_{\mathrm{local,cyl,}\parallel} = \left(1 - \sigma + \frac{\chi_{\mathrm{object}}}{3} - \chi_{\mathrm{external}}\right) B_0 \tag{4.11}$$

$$B_{\mathrm{local,cyl,}\perp} = \left(1 - \sigma - \frac{\chi_{\mathrm{object}}}{6} - \frac{\chi_{\mathrm{external}}}{2}\right) B_0 \tag{4.12}$$

with χ_{external} denoting the susceptibility outside the object.
If the susceptibility were temperature independent, all susceptibility terms of $\vec{B}_{\mathrm{local}}\left(\vec{r}_{\mathrm{proton}}\right)$ would cancel when calculating the phase difference image. A conversion of the phase difference to a change in temperature using Eq. (4.8) with the corresponding α of the material is appropriate. However, the susceptibility of objects can be quite temperature dependent. For paramagnetic substances, the temperature dependency of the susceptibility is given by Curie's law Eq. (1.2), $\chi \propto \frac{1}{T}$, and thus $\frac{d\chi}{dT} \propto -\frac{1}{T^2}$. For diamagnetic substances there is no such general relationship. For example, the temperature

dependency of the susceptibility of water is given by $\frac{\Delta\chi_{\text{water}}}{\Delta T} = -0.26 \cdot 10^{-8}\,\text{K}^{-1}$ over a temperature range of 28 °C to 44 °C [69] or $\frac{\Delta\chi_{\text{water}}}{\Delta T} = -0.20 \pm 0.09 \cdot 10^{-8}\,\text{K}^{-1}$ covering a similar temperature range [70]. This means, a diamagnetic material like water becomes more diamagnetic with increasing temperature (see also [34, 75]).

For pure water and tissues with a high fraction of water the temperature dependency of the susceptibility is much smaller than the temperature dependent screening of the hydrogen nuclei $\left(\left|\frac{\Delta\chi_{\text{water}}}{\Delta T}\right| \ll |\alpha_{\text{water}}|\right)$ [10, 70]. The temperature dependencies in fat are different such that $\left|\frac{\Delta\chi_{\text{fat}}}{\Delta T}\right| \gg \left|\frac{\Delta\sigma_{\text{fat}}}{\Delta T}\right|$, for example $\frac{\Delta\chi_{\text{fat}}}{\Delta T} = -0.80 \pm 0.15 \cdot 10^{-8}\,\text{K}^{-1}$ and $\frac{\Delta\sigma_{\text{fat}}}{\Delta T} = 0.02 \pm 0.04 \cdot 10^{-8}\,\text{K}^{-1}$ for temperatures above 32 °C [70]. The temperature dependency of $\vec{B}_{\text{local}}\left(\vec{r}_{\text{proton}}\right)$ in fat is predominantly caused by changes in the susceptibility. Note the similar order of magnitude for $\left|\alpha_{\text{water}} = \frac{\Delta\sigma_{\text{water}}}{\Delta T}\right|$ and $\left|\frac{\Delta\chi_{\text{fat}}}{\Delta T}\right|$. As a consequence, accurate PRF temperature phase mapping in fatty tissue is quite challenging.

The phase change due to temperature is related to susceptibility changes in addition to the change in σ at a particular location in the object. Depending on the size of these susceptibility effects with respect to σ (thus, α), PRF thermometry results can be affected severely. For example, Streicher $et\ al.$ [76] found that a change in the air temperature from 23 °C to 69 °C caused an error of 2 K in the temperature difference maps. Whereas, if 100 % oxygen (paramagnetic gas) surrounded the object, the error increased up to 40 K. Additionally, the error was dependent in a nontrivial way on the experimental configuration.

In the configuration of the setup, the orientation and geometry of the heat source with respect to B_0 and the associated heat distribution need to be considered as demonstrated by Peters $et\ al.$ [77]. A radially symmetric temperature distribution surrounding a cylindrical heat source is deformed if the axis of the heat source is oriented perpendicular to B_0. In addition, α values determined once with the heat source oriented parallel and once oriented perpendicular to B_0 differ and are spatially dependent for the latter orientation. Errors up to $\pm 30\,\%$ can occur if this spatial variation of α is not considered.

In addition, the paramagnetic doping of the fluid used for cooling for example can affect the accuracy of the PRF temperature measurements [69]. High doping of the cooling fluid would be desirable to reduce flow artifacts in the region of interest due to the very short T2* relaxation times. Other ways to eliminate flow related artifacts are 1.) to turn the cooling flow off and wait until it settles down at the expense of temperature changes which can occur during the acquisition; 2.) using a copper pipe (as used in this work) which shields the RF pulse and prevents signal generation inside the pipe; 3.) circulating a proton free fluid such as fluorinert [16] which does not give any signal; 4.) to manipulate the geometry in a way that the temperature dependent field perturbations outside the cooling or heating system become very small, and a combination with high doped cooling fluids becomes feasible. For example, in the case investigated by De Poorter [69], an extension of the length of the cooling box would meet this condition.

In conclusion, the design of the setup (geometry and orientation with respect to B_0) and the material of the experimental setup need to be selected very carefully to minimize phase changes related with temperature dependent local B_0 inhomogeneities. The susceptibility of the materials and of the fluid should be matched as recommended in the review of Schenck on susceptibility in MRI [34].

Electrical conductivity dependence

Furthermore, Peters and Henkelman [78] observed the value of α to be dependent on the choice of TE. They propose that the corresponding phase shift offset is caused by a temperature dependent change of the electrical conductivity of the materials. The amplitude of the magnetic field component of an RF pulse will be attenuated and its phase will be retarded as it penetrates an electrically conducting object [79]. This interaction of the RF pulse and the material may result in a nonuniform flip angle distribution within the object and in a variation of the phase of the transverse magnetization with depth [78]. If the phase delay of the magnetic field component of an RF pulse differs for two measurements conducted at two distinct temperatures, a phase offset will remain in the phase difference image. However, this phase offset is actually not related to the temperature dependency of the screening effect. The phase retardation depends on object properties in particular the temperature dependent electrical conductivity. It was shown that the phase retardation effect is substantial in larger uniformly heated objects due to its depth dependency.

Magnetic field drift dependence

An additional source contributing to phase offsets is given by the temporal drifts of B_0. A variety of correction methods is proposed in literature to account for this error such as including thermally insulated reference phantoms [80, 81, 82] or more recently, using field probes [83, 84].

4.2 MRT based on T1 and T2 relaxation times

The relaxation time T1 is dependent on temperature [85]. The relaxation is caused by random field fluctuations which continuously vary the total local field. The motion of the molecules leading to those fluctuations is temperature dependent. T1 increases if the temperature of a non-viscous solution containing small molecules rises [27]. In contrast, T1 decreases if the temperature of a sample containing large molecules or a viscous solution rises [27]. For example, the value of the temperature dependency of T1 (called temperature dependent coefficient (TDC)) in light vegetable oils was determined to be $3.59 \pm 0.18\,\%/^{\circ}\mathrm{C}$ at 22 °C, and in copper sulfate solutions TDC was found to be $2.37 \pm 0.17\,\%/^{\circ}\mathrm{C}$ at 22 °C using a 0.15 T MR system [86]. Quantitative MRT based on T1 requires a calibration for each tissue type. Thus, in vivo, temperature mapping based on the temperature dependency of T1 is used as a qualitative measure due to unknown temperature dependencies of particular tissues or effects altering the tissue properties such that non linear dependencies occur [10].
The temperature dependency of T2 is similar to the T1 dependency. T2 of water increases with raising temperature, whereas T2 decreases with raising temperature in 0.5 % agarose gel [87]. The temperature dependence of T2 is relatively small [86]. Measurements in polypropylene revealed a non linear temperature dependency on T2 [88]. The temperature distribution within a polypropylene sample could be determined with an accuracy of approximately $\pm 2 - 3$K. In food science applications, the percentage temperature sensitivity of a starch-based sauce containing vegetables was determined to be $2.5\,\%/^{\circ}\mathrm{C}$ at 20 °C [89]. Further details on the relaxation mechanism of T1 and T2 as well as their dependencies on tissue type, NMR frequency, temperature and other parameters can be found in the

review of Bottomley $et\ al.$ [90].

A combination of T1 and T2 temperature dependencies can be exploited to conduct temperature monitoring as recently presented by Vesanen $et\ al.$ [87] at ultra low fields. The temperature dependencies of T1 and T2 relaxation times of water and agarose gel were studied for various field strength between 50 μT and 50 mT as well as at 3 T over a temperature range from 5 to 45 °C. In vitro temperature maps were reconstructed with previously determined T1 and T2 values.

Measurements of T1 are typically performed using inversion recovery sequences with different inversion times [89]. T2 values are measured by spin echoes sequences with various TE settings such as the Carr-Purcell-Meiboom-Gill (CPMG) multi-echo sequence [41, 91, 86, 89].

4.3 MRT based on proton density

The temperature sensitivity of the proton density of paramagnetic substances is based on the temperature dependency of the susceptibility of the object described by Eq. (1.2). The susceptibility is related to the equilibrium magnetization as $M_{\mathrm{z,equilibrium}} = \chi B_0$ [92], thus, $M_{\mathrm{z,equilibrium}} \propto \frac{1}{T}$. $M_{\mathrm{z,equilibrium}}$ and the proton density are directly proportional quantities. The temperature dependent signal change is -0.3±0.01 %/°C over a temperature range between 37 °C and 80 °C [10]. Relative temperatures can be determined by these signal changes in proton density-weighted images. To exclude changes related to T1 effects, long repetition times in the data acquisition are required. MR thermometry based on proton density has a low temperature sensitivity. Therefore, high SNR values are required to yield a sufficiently small temperature uncertainty. As shown by Chen $et\ al.$ [63], the standard deviation of the temperature is related to the fraction $\frac{T_{\mathrm{initial}}}{SNR}$. Therefore, a temperature uncertainty of 3 °C is achieved for an initial temperature of 300 K and an SNR value of 100 [63]. This level of uncertainty on the actual temperature value is very high e.g. for dynamic temperature imaging.

4.4 MRT based on diffusion coefficient

Spins traveling along a magnetic field gradient accumulate a phase. The encoding of velocities in MRV is based on this principle (see section 3.1). If random thermal motion (Brownian motion) of spins occurs along an imaging gradient, various phases are accumulated by the individual spins. A dispersion of their phases (loss of coherence) occurs which results in an attenuated signal [93]. Thus, the diffusion of molecules which is temperature dependent can be detected by MRI. If the corresponding diffusion coefficients are measured at two distinct temperatures, relative temperature change can be calculated. The temperature sensitivity of tissue is in the order of 2 %/°C [10, 94]. Thermometry based on the temperature dependency of the diffusion coefficient allows precise temperature measurements of small temperature changes (<1 °C) [64, 71]. However, it is very sensitive to any kind of motion and therefore, not used that often.

4.5 MRT based on magnetization transfer

Magnetization transfer techniques are used to obtain an additional tissue contrast in MR images [95]. These techniques are a combination of saturation transfer techniques and standard MRI sequences [96]. Hydrogen protons of biological systems can be assigned to two pools called free pool and bound pool. Hydrogen protons of the free pool are quite mobile. The free pool protons can be imaged using standard MRI methods due to the relatively long T2 times which are in the order of tens or hundreds of milliseconds [96]. The spectral line width of the free pool is narrow (see Eq. (1.42) for the correlation between line width and T2 or T2*). Hydrogen protons with restricted motion correspond to the bound pool. These kind of protons can be bound in macromolecules or cellular membranes [96]. Their very short T2 time (< 0.1 ms) [96] leads to broad line width in the spectrum. The bound pool is invisible with conventional MRI due to the very short T2.
The central frequencies of the spectral peaks for the free pool and bond pool are approximately the same. However, due to the quite different spectral line widths, frequency selective saturation of the bound pool can be conducted using off-resonance RF pulses. The saturated protons may transfer their magnetization to protons of the free pool [10]. Thus, the longitudinal magnetization (which is related to the number of protons of the free pool) available for imaging is reduced. Hence, a lower signal is detected at locations where magnetization transfer occurred [10]. The method based on selective saturation which substantially affects the bound pool while leaving the free pool almost entirely undistorted is one possible method to generate magnetization transfer contrast. A detailed description on the mechanism of magnetization transfer and its applications is given in references [65, 96].
The magnetization transfer effect is temperature dependent. Thus, it could be a potential mechanism to be used in MR thermometry. Possible drawbacks of this method are its limited sensitivity and strong dependence on the tissue type [10].

4.6 Temperature sensitive contrast agents

There are three main categories of temperature sensitive contrast agents [10].
The first category includes paramagnetic thermosensitive liposomes which provide the ability to access absolute temperature values [97]. They consist of a phospholipid membrane which encloses gadolinium for example. The membrane becomes more permeable for water at a particular temperature T_{perm} (called gel to liquid crystalline phase transition temperature). T_{perm} can be altered by changing the phospholipid layer accordingly. At T_{perm} the water exchange between the interior and exterior of the liposome is more efficient and a drastic increase in the longitudinal (T1) relaxivity occurs changing the signal intensity in MRI [97]. The enclosed paramagnetic molecule can be also released and contribute to increase the relaxivity such as in the case of Mn^{2+} ions. In general, however, the release of the paramagnetic molecule is not mandatory. The substantial change of the relaxivity at T_{perm} allows the assessment of absolute temperature values. However, no continuous mapping over a temperature range is possible due to strong nonlinear relationships. Besides the temperature assessment, thermosensitive lipsomes are important for specific drug delivery to reduce side effects for example. More details about the different kinds of thermosensitive lipsomes are given in the review of Lindner $et\ al.$ [97].
The second category includes paramagnetic lanthanide complexes. The temperature coef-

ficient of these substances is approximately one to two orders of magnitude higher than that of water. For example, the methyl group of $TmDOTMA^-$ corresponds to a coefficient of $\alpha_{\mathrm{TmDOTMA^-}} = 57 \cdot 10^{-8}\,\mathrm{K}^{-1}$ [98, 99, 100]. The methyl signal of $TmDOTMA^-$ can be used to conduct in vitro phase difference temperature mapping with a spatial resolution of about 1-2 mm at high field strengths (9.4 T) [98, 99, 100]. An excellent water suppression is required in such acquisitions. Another aspect of paramagnetic lanthanide complexes is that they have generally very short relaxation times T1 and T2 (in the order of up to a few milliseconds). Thus, the linewidth of the peaks in the spectrum are typically broad with a FWHM according to Eq. (1.42). This fact might cause difficulties in the determination of the peak's maxima and thus, affect the accuracy of the temperature measurement. The uncertainty of the determined temperature is dependent on the uncertainty for chemical shift determination which is related to the SNR of each individual peak [100]. Small T2 values lead to a reduction in the SNR. Additionally, short T2 times in the order of up to a few milliseconds can make spatial encoding in MR imaging experiments quite challenging.
The third category includes a specific kind of paramagnetic lanthanide complexes called PARACEST agents [101, 102]. These agents are measured in an indirect way. The signal intensity of the bulk water is changed due to a chemical exchange saturation transfer (CEST) process. The exchange rate is temperature dependent (given by the Arrhenius equation) [102]. If the concentration of the agent is known, the temperature can be determined. In particular in in vivo applications it is difficult to assess the correct local concentration of the contrast agent. The acquisition of a so called Z-spectra (intensity of a pixel plotted versus saturation frequency offset) in combination with the temperature dependent hyperfine shift of the lanthanide-bound water proton could be used to determine 2D temperature maps in this case [102]. Over a temperature range from 20-50 °C temperature sensitivities for $Dy(1)^{3+}$ and $Eu(2)^-$ vary linearly and are approximately 690-fold and 40-fold greater than α_{water} [102]. Since the signal of the bulk water is acquired, much higher spatial resolutions might be applicable than with current spectroscopic imaging methods [102].
Beyond these three main categories of contrast agents introduced above, other temperature dependent properties of contrast agents were investigated. Muller *et al.* [103] studied the temperature dependent spin transition of a system switching from a diamagnetic $S = 0$ state to a paramagnetic state $S = 2$. The latter state causes distortions in the MR image which are represented as arrowhead shaped artifacts for example. This kind of contrast agent could serve as an artifact switch which indicates that a particular temperature is reached. Another temperature sensitive contrast mechanism based on the Curie temperature was investigated by Settecase *et al.* [104]. Ferromagnetic substances lose their permanent magnetization and become paramagnetic at the Curie temperature. This temperature dependent transition involves a drastic change in its magnetic susceptibility, given by Eq. (1.3) above the Curie temperature. A calibration using the size of the susceptibility artifact in the MR image versus temperature could serve to detect absolute temperatures.

It is difficult to make general conclusions about which temperature sensitive parameter is the best one to use. The MRT method of choice strongly depends on the magnetic field strength and the experimental setup (materials, geometry, orientations of the objects with respect to B_0, presence of motion, kind of motion), temporal stability of the setup, and thus the acceptable acquisition time.
Temperature phase mapping is expected to be the most suitable for the acquisition of high spatially resolved temperature distributions in fluid flow. Other methods based on signal intensity changes such as T1 or based on diffusion coefficients are known to be less accurate and less sensitive to small temperature changes than PRF based methods [71, 72]. Furthermore, there are various effects beyond temperature changes which can alter signal intensity such as intra voxel dephasing due to motion. In addition, temperature measurements based on diffusion are very prone to motion, and thus not suited for temperature mapping in fluid flows. Therefore, temperature mapping based on temperature dependent changes in PRF is applied in this work. Compared to spectroscopic PRF methods much higher spatial and temporal resolutions are possible within less measurement time. Additionally, from a practical point of view the same imaging protocol with only minor adjustments of parameters such as TE or bandwidth per pixel can be applied to conduct either velocity or temperature measurements. Gradient echo pulse sequences are typically applied for velocity imaging instead of spin echo pulse sequences due to shorter minimum TRs. For example, shorter TRs reduce the sensitivity to displacement errors in the images and also the overall acquisition time.

4.7 Applications of MRT

Since the early 1980s MRI has been used in studies to non-invasively monitor spatial temperature distributions in vitro and in vivo [105]. The temperature dependence of intrinsic NMR parameters of a sample such as the relaxation times, however, was already recognized decades earlier [106, 107, 108] .
Compared to invasive local thermocouple measurements, MRI can provide spatially resolved 3D temperature maps within a few minutes. Thus, MRT is an excellent method to address questions in the field of medicine and act as a supporting imaging modality during patient treatments. MRT is frequently applied in MR safety studies [109, 110, 111, 112, 113] or in interventional MRI to guide in vivo thermal therapies of tumors [11, 12, 10]. The aim is to provide a minimally invasive treatment of the target volume without damaging the adjacent healthy surrounding tissues. Furthermore, the application of PRF thermometry allows non-invasive mapping of pH distributions in addition to the temperature distribution which is particularly useful to address medical questions or to investigate biological systems [114, 100].
In NMR spectrometers, the temperature of the sample is kept constant by a surrounding gas flow to ensure reproducibility of the spectra. Lutz *et al.* [115] proposed a method to calibrate the temperature in cell culture perfusion systems of NMR spectrometers. The temperature dependency of a sample on the flow rate was monitored using PRF spectroscopy. Appropriate adjustments of the flow rate can then be made to ensure constant temperature conditions. An internal temperature calibration for blood plasma and other biofluids was proposed by Farrant *et al.* [116] by using the temperature dependent chemical shift between water signal and a glucose signal. In addition, they investigated the

dependence of the linewidth on temperature. In capillary electrochromatography, online temperature monitoring with an accuracy of 0.2 °C was estabilshed using microcoil NMR and the temperature dependent proton resonance frequency of water [117].
Another field where MRT is applied includes food science and food engineering to ensure product quality or product safety such as monitoring sterilization processes [57, 118, 119]. For example, temperature distributions in food due to microwave heating were investigated with respect to different MRT methods. PRF was found to be the most robust one [89]. 2D PRF temperature phase maps of ohmically heated samples consisting of whey gel and NaCl solution were quantified by the group of Ye $et\ al.$ [120]. They conclude that this temperature mapping method is well suited for applications in dynamic food processes as well as for the development of an ohmic model and its validation. Temperature mapping based on T1 times were conducted in a carrot [121]. Furthermore, convective heat transfer coefficients were determined using MRT and finite element modeling [122], where the shape of the food particle was considered in the modeling. 2D temperature mapping based on the diffusion coefficient of water in a potato and using half Fourier transform MRI to reduce scan time were conducted by Sun $et\ al.$ [123]. An accuracy of the temperature measurements better than 0.84 °C and a resolution of 0.75 mm^2 was achieved.
MRT can also be extended to other engineering fields such as fluid mechanics to study temperature distributions in fluid flows. Of particular interest in fluid mechanics is the acquisition of both velocity fields and temperature fields. Sun and Hall [14] acquired 2D cross sectional planes of a water cooled circular cylinder (containing a flow of an opaque fluid) using MRV and velocity compensated MRT based on PRF temperature phase mapping. They demonstrated that MRI can provide quantitative temperature and velocity profiles which both can then be used to objectively assess and validate computational models. An inversion recovery tagging method was developed by Ogawa $et\ al.$ [16] to simultaneously measure velocity and temperature based on T1 relaxation in doped water flowing through a cooled pipe. The accuracy of the determined temperature was within 15 % of the temperature difference $\Delta T = 15$ °C. MRV and MRT was performed on a homogeneously heated turbulent pipe flow by Elkins $et\ al.$ [4]. Observed variations in the PRF temperature phase maps were up to about $\pm$20 %. No velocity compensation was used in the acquisitions of the temperature data.

Chapter 5

Velocity and temperature fields in fluid flows

The simultaneous examination of velocity and temperature fields in fluid flows are of great interest to the engineering community since both fields are mostly coupled. The investigation of both quantities can contribute fundamental information about heat transfer in fluids. Knowledge of the velocity and temperature field in flows enables the optimization of the performance and efficiency of devices. Furthermore, the experimental results of velocity and temperature distributions can provide ground truth in case studies to compare with numerical simulations such as CFD.
Currently, almost any kind of flow geometry can be manufactured with very high precision in a relatively short amount of time (in the order days) using rapid prototyping techniques. However, with increasing flow model complexity it becomes more difficult to examine the fluid mechanical and thermodynamic questions with the available conventional experimental methods described in section 5.1. This demonstrates the need for a quantitative non-invasive measurement techniques such as MRI.
After the introduction of conventional measurement techniques, the engineering concept of common dimensionless numbers is summarized in section 5.2. This concept for example allows to compare measurement results performed with different fluids (i.e. air used in wind tunnel experiments and water used to perform MRI acquisitions). Furthermore, the different types of convection flows are introduced since convection played an important role in the flow models considered in this work. This chapter concludes with the thermofluid test cases designed and studied in this work to allow accurate and precise MR measurements of velocity fields and temperature fields (5.3, 5.4).
The design of the flow models required a close collaboration with the project partner to address fluid mechanical requirements as well as to ensure MR compatibility such that accurate and precise MRV and MRT results could be obtained.

5.1 Conventional measurement techniques

State of the art flow measurements are laser-optical methods such as Particle Image velocitmetry (PIV) or Laser Doppler Velocimetry (LDV, frequently also called Laser Doppler Anemometry LDA) to measure velocities [124]. Both techniques are classified as semi-invasive since they require particles added to the fluid to track motion. Therefore, they

detect the flow in an indirect manner. Generally, the flow is not substantially altered by these particles in contrast to invasive techniques for example, by placing sensors directly into the flow. A detailed description about the principles of PIV and LDV is provided in Tropea *et al.* [124]. LDV was applied to the setup of a double pipe heat exchanger by the project partner to compare LDV data and MRV data. LDV allows to determine up to three velocity components at a single location within the flow, whereas PIV is typically applied to 2D planes measuring two velocity components. The measurement of a 3D velocity vector field with PIV enormously increases the complexity of the entire experimental procedure and are therefore seldomly performed.

The measurement of 2D or 3D temperature distributions in fluid flows is particularly challenging. Commonly applied techniques involve sensors which are inserted into the flow to detect local temperatures [125]. The alteration of the velocity distributions can lead to inaccurate temperature results, and the accuracy of the sensor may suffer from errors caused by heat conduction [126] as well as from positioning errors. Furthermore, the flow needs to be accessible for the sensor such that its impact on the flow is minimized (example described in section 8.1.3). This issue restricts the number of possible flow models to be investigated with this invasive method. The acquisition of a 2D field using pointwise measurement techniques is possible, however, time consuming. In particular, the acquisition of 3D volumes is practically impossible in most cases. Other possibilities for the measurement of temperature distributions in 2D include infrared thermography using an infrared camera and the application of temperature sensitive paint on the surface of the object [125]. However, both of these methods are only capable of detecting surface temperatures. Therefore, they are not suited to measure temperature distributions in fluid flows. To measure temperature fields in fluid flows particle image thermometry (PIT) can be performed by seeding the flow with thermochromic liquid crystals. These crystals have a temperature-dependent reflection. PIT counts similar as PIV to the semi-invasive techniques. A review on experiments based on PIT can be found in reference [127]. Recent experiments within the scope of microfluidics achieved the measurement of 3D temperature fields within a droplet using PIT [128].

To measure both velocity and temperature, a combination of PIT and PIV has been applied to acquire 2D resolved data in many experimental flow setups [127, 128]. However, these optical techniques require homogeneous illumination of the region of interest. This requires optical access to the flow and in many cases the required homogeneity is difficult to achieve. Difficulties can arise if surfaces of the model are not sufficiently optically smooth or due to a refractive index mismatch between the fluid and the flow model. In addition, the particles used in these techniques need to be distributed equally throughout the liquid and have to follow the flow. Generally, a complex and time-consuming calibration of the system is necessary, and different light sources are required to achieve optimum measurement conditions (PIV: monochromatic light, PIT: white light).

Due to these challenges and the fact that velocity and temperature are acquired in an indirect manner, which may introduce additional errors, MRI as a non-invasive imaging modality is attractive for the study of velocity and temperature.

To compare velocity and temperature data measured with different measurement techniques and potentially with differently sized flow models, the dimensionless numbers in fluid mechanics play an essential role and are discussed next.

5.2 Common dimensionless numbers in fluid mechanics

Dimensionless numbers are important parameters to compare similar fluid mechanical setups which can differ in flow parameters of the fluid such as velocity or density as well as in the size of the flow model. For example, experiments typically conducted in wind tunnels (air flow) can be transferred to water flow analogues such that the flow topology remains the same (see hydrodynamic similarity in reference [32]). Additionally, the geometry of the model can be scaled compared to the original model to fit into the desired experimental environment, e.g. of an MR system with a given FOV for data acquisition. The underlaying concept is covered by the theory of similitude.
The most important dimensionless number in fluid mechanics to characterize flow is the *Reynolds (Re)* number which represents the ratio of inertia forces to viscous forces. *Re* is small for laminar flows, and thus the internal friction in the flow is dominant. If *Re* is large the flow can be assumed as inviscid since inertia forces dominate the behavior of the fluid. Disturbances in the flow are weakly damped and the flow eventually becomes turbulent with increasing *Re* number.
Additional dimensionless numbers, which played a role to characterize the flows investigated in this work, are the Rayleigh number and the Richardson number. Both numbers characterize the influence of buoyancy forces. Detailed information about these parameters and how they are determined for the setups considered in this work can be found in the thesis of the project partner [17]. Moreover, the reader is referred to the books from references [129, 130] for a detailed discussion on the derivations of dimensionless numbers and its applications. In theory, the dimensionless numbers characterize the flow in a sufficient manner. By keeping these numbers the same, it is ensured that the flow behaves the same. Thus, the introduction of dimensionless numbers is convenient to transfer and generalize the outcome of measurements [130]. Furthermore, dimensionless numbers can reduce the number of variables involved in calculations.
Before the flow models of this work are introduced in the next sections, the three main categories of convective flows (forced, free, and mixed convection) which can be present in these models are explained. The term forced, free, or mixed refers to the mechanism which drives the convection.

- **Forced convection** requires bulk fluid motion induced by an external force such as from a pump. The *Re* number and frequently the *Nusselt (Nu)* number are considered in similarity considerations for forced convections [130]. The *Nu* number represents the ratio of convective heat transfer to conductive heat transfer, and thus describes how much more heat is transfered due the forced convection compared to a heat transfer solely occurring via conduction.

- **Free (or natural) convection** occurs when gravity acts upon a non-uniformly heated stationary fluid. The stationary temperature distribution results in a spatially varying density of the fluid. The fluid of higher density moves downwards due to the influence of a gravity, forcing the lower density fluid upwards. This produces a buoyancy force which generates a natural convection in the fluid. The resultant bulk fluid motion gives rise to a frictional force in the opposing direction. The *Grashof* number *Gr* as dimensionless numbers relates these two counteracting forces, and is defined as the ratio of buoyancy forces to viscous forces [130].

- **Mixed convection** occurs if substantially large contributions of free convection as well of forced convection are present simultaneously [131]. This type of convection was present in the double pipe heat exchangers examined in this work.

An explanation of the heat exchangers investigated in this work follows below.

5.3 Heat exchangers

Heat exchangers are frequently applied devices in technical applications to transfer heat. Various types can be designed using databases such as the VDI heat atlas [132]. Nevertheless, a deep understanding of the underlaying physics is desired for optimization of the performance of the devices. Two types of heat exchangers were studied in this work after the framework has been established to image velocities as well as temperature using MRI. One type consists of a double pipe (called double pipe heat exchanger). The other type (called pin fin array heat exchanger) contains multiple cylinders in an array which are arranged in a staggered manner. Their main features and applications are summarized in the following two subsections. Subsection 5.3.1 is partly based on the journal article Buchenberg *et al.* [133].

5.3.1 Double pipe heat exchanger

Convective transfer of heat and fluid flow are important mechanisms to be studied in engineering fields, for example, in the case of device performance optimization or computational fluid dynamic simulations. Forced, natural and mixed convection heat transfer and fluid flow in an annulus are of particular interest in the engineering community since they are involved in many technological applications such as heat exchangers, boilers, solar energy systems, cooling nuclear reactors cores or cooling of electronic devices and so on [131]. The study of buoyancy effects on the heat transfer in an annulus is of particular interest for double pipe heat exchangers which are applied e.g. in evaporators or coolers.
Generally, a double pipe heat exchanger consists of two pipes with different diameters which can be placed either concentrically or asymmetrically inside each other. Heating or cooling can be conducted through the inner pipe using either hot or cold fluid flow, respectively. Electrical heating could provide another possibility for heat transfer [134]. Laminar flow conditions inside the annulus between the inner and outer pipe can be obtained with a *Re* number below the critical value of approximately 2000 [135], walls which are hydraulically smooth, and an undistorted inflow. These prerequisites were present in the experimental setup studied in this work. To obtain mixed convection the flow rate and the temperature differences have to be adjusted accordingly. A stationary temperature distribution can be achieved showing a characteristic structure known as plume in literature [136].
Heat transfer in an annular passage was investigated in many numerical studies and fewer experimental studies [137, 131]. Hattori and Kotake [138] conducted one of the few experiments in horizontal tubes with concentric annuli and laminar flow characteristics. They measured the wall temperature at the inner and outer pipe for different tube diameter ratios. A numerical study of Nieckele and Patankar [139] examined mixed convection heat transfer in an annulus with axial laminar flow and heated inner cylinder. 2D axial representations of isotherms and streamlines are presented for various *Rayleigh* numbers

(*Ra* = *Pr*· *Gr*) and *Prandtl* numbers *Pr*. In conclusion, buoyancy forces have a substantial impact on the heat transfer which is highly nonuniform in the annulus. A stable temperature stratification inside the annulus is present and thin thermal boundary layers on the heated inner cylinder occur. Recently, a numerical simulation was conducted for 3D laminar mixed convection water flow in the annulus of two elliptically shaped concentric cylinders with temperature dependent physical properties [140]. Zerari $et\ al.$ [140] depicted 2D velocity fields and 2D temperature fields at different axial cross-sections along the main flow direction. They show that both fields are of a three-dimensional nature.
Thus far, to the author's knowledge, 3D resolved velocity and temperature data of experimental studies on a horizontal circular concentric counter-current double pipe heat exchanger [141, 137, 131] have not been previously presented in literature. For this reason and since it was expected that this style of flow model can provide a 3D velocity and temperature distribution inside the annulus, the double pipe heat exchanger is chosen as a test case in this work. 3D MRV and 3D MRT measurements are performed in the counter-current double pipe heat exchanger and compared to pointwise sampled data of common conventional measurement techniques to show that MRV and MRT are capable of accurately and precisely measuring 3D velocity and temperature distributions in fluid flows.
Details of the setup and MR acquisitions as well as results and discussion are given in chapter 8. Additional information about specific engineering parameters or engineering problems of the experimental setup can be found in the thesis of the project partner [17]. Furthermore, publications of the author on this topic are available in the Journal of Magnetic Resonance in Medicine, Buchenberg $et\ al.$ [133] as well as in the conference proceedings of the annual meetings of the International Society for Magnetic Resonance in Medicine (ISMRM), Buchenberg $et\ al.$ [142, 143].

5.3.2 Pin Fin array heat exchanger

The complexity of the double pipe setup is increased to a pin fin array heat exchanger which is the second test case studied in this work.
Multiple cylinders are arranged either in inline arrays or staggered arrays [141]. A pin fin array heat exchanger is frequently applied in industrial processes for cooling purposes to prevent electronic devices, e.g. from overheating [144]. In addition to cooling purposes, they can act as structural supports as in the case of a turbine blade [144]. Thus, pin fin arrays are interesting components for many industrial applications.
A deep understanding of the heat transfer is of great interest to maximize the effectiveness of cooling or to adjust the cooling performance to specific requirements which ensure the full functionality of the device. An empirical model to predict the performance of pin fin arrays was developed by Zografos and Sunderland [145]. An overview of heat transfer in staggered pin fin arrays applied for turbine cooling is given by the review of Armstrong and Winstanley [146]. Recently, design parameters of a staggered pin fin array were proposed such that they establish a benchmark case in CFD calculations [147]. Comprehensive experimental work on staggered pin fin arrays was performed by Ames $et\ al.$ [148, 149, 150] to gain a deeper understanding on the physics of the transport mechanisms. Their aim was to develop more physics-based models using computational tools as opposed to the more commonly applied empirical approach. Thus, designers of thermofluid devices for example can use these new models with more complex geometries or thermal boundary conditions, and not be restricted to those available only through an

empirical database. Ames *et al.* [148, 149, 150] investigated the turbulent transport in staggered pin fin arrays by measuring pressure, heat transfer and turbulence. Velocity distributions as well as turbulence measurements were acquired in a staggered pin fin array for different *Re* numbers using hot wire anemometry. Hot wire anemometry provides invasively measured pointwise data. Distributions of the heat transfer at the surface endwall were detected using an infrared (IR) camera. The endwalls of a pin fin array are the two plates holding the pins. The surface temperature measurement uncertainty of $\pm 2°$ was reduced to $\pm 0.7°$ by applying multiple correction methods [150]. Metzger and Harley [151] studied heat transfer and visualized flow patterns on the endwall surfaces in a pin fin array using a kerosene-lampblack method. Wassermann and Grundmann [152] visualized flow in a staggered pin fin array using MRV. Overall, there are few experimental works considering both velocity fields and temperature fields in a pin fin heat exchanger. The common approach using IR cameras allows a 2D coverage of surface temperatures. Generally, two distinct measurement setups are required for velocity and temperature acquisitions. MRI can overcome these restrictions.
MRV and MRT measurements were conducted in a staggered pin fin setup with continuously heated pins in this work (chapter 9). To the author's knowledge, similar data has not been previously presented.

5.4 Free convection inside a horizontal cylinder

Many processes involve the transport of energy and matter via free convection flows. The investigation of free convection flows in enclosed spaces is of interest for example to optimize the cooling of devices. For this reason temperature fields and velocity fields inside a horizontal cylinder were studied experimentally and simulated numerically by Martini and Churchill [153]. More recently, a deep understanding of free convection flows in enclosures gained attention in the fields of crystal growing such as the semiconductor production [154]. Numerous CFD simulations were performed to address questions regarding free convection in enclosures [155, 156, 157, 154, 158]. Generally, these kind of convection flows, where velocity fields and temperature fields are closely coupled, are difficult do be analyzed by means of conventional measurement techniques.
Because of the relevance of free convection in enclosures, a method of non-invasive examination would be of great interest to better understand the underlying processes. In this work free convection flow inside a closed horizontal cylinder heated on one end and cooled on the other end was investigated with respect to temperature distributions using PRF-spectroscopy (chapter 10). As an advantage the small volume of the closed horizontal cylinder compared to the heat exchanger setups (section 5.3) reduces the amount of necessary chemicals that are added to the fluid considerably, and thus reducing costs. Furthermore, this kind of setup could also represent a valuable test case for validation of numerical models.

Part II

Methods and setups for measurements and evaluation

Chapter 6

MR data acquisition and evaluation

In the following sections, considerations and pre-investigations regarding the design and components of the in vitro setups with respect to MR requirements are discussed.
Various parameters have to be considered in detail to assure the MR compatibility of the flow setup such as the conductivity, the susceptibility of the materials, and the shape of the flow model and its orientation to B_0. Several different materials were investigated with respect to MR image degradation. The findings led to design rules for the flow models.

6.1 Sequence modifications

MR measurements were conducted based on the in-house built 4D gre FLASH sequence [159]. In this sequence, TE is minimized as much as possible to reduce displacement issues and phase contributions due to higher orders of motion such as acceleration. Generally, the sequence settings are optimized for in vivo imaging of the heart such as aortic flow measurements or tissue phase mapping. However, sequence protocol settings of in vivo applications may not be directly transferable to in vitro flow setups. Hence, MRV imaging parameters were adjusted with respect to the in vitro setups studied in this work. The phase encoding direction needed to be chosen such that flow ghosting minimally affected the volume of interest. Furthermore, TE could not be adjusted generally to the minimum for all investigated in vitro setups. For example, 3D velocity data of the double pipe setup showed severe higher order distortions in the phase difference images. These kinds of

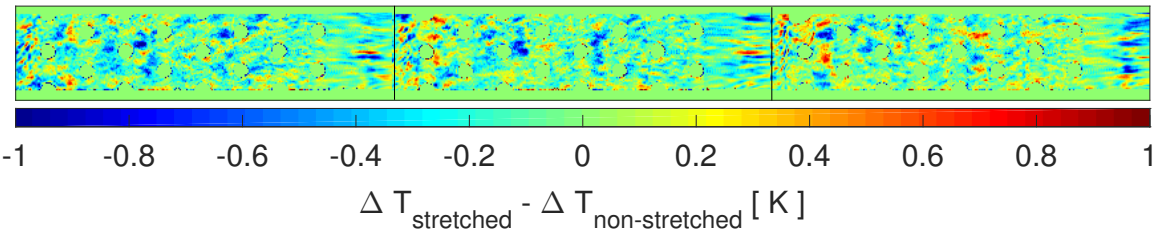

Figure 6.1: ΔT maps, acquired with the stretched and non-stretched gradient schemes, are subtracted. The remaining differences are presented for three different slices (slice 1 to slice 3 from left to right). Remark: Data corresponds to pin fin array heat exchanger experiments with $T_{\text{flow 1}} = T_{\text{flow 2}}$ (see chapter 9).

distortions may be caused by eddy currents. 3D background phase corrections did not provide an acceptable quality of the velocity maps. Approximately doubling TE resolved this issue in the MRV phase difference images. Errors due to displacement or acceleration are expected to remain sufficiently small, because of the slow laminar fluid flow (stream wise velocity $\lesssim 0.1\,\mathrm{m/s}$), and thus they are negligible. A comparative study between MRV data and LDV data (LDV measurements were conducted by the project partner) showed good agreements (see reference [17], section 5.3.2.7), and thus supports this assumption.
For the quantitative PRF temperature phase mapping in fluid flows, more adjustments and changes of the sequence were required. Typically, temperature mapping is conducted in vivo in different types of tissues. Temperature mapping in fluid flows in in vitro models faces different challenges and its acquisition and post-processing was built up from the scratch in this work. The MRT sequence needs to be velocity compensated to minimize effects of fluid motion. To be able to apply the in-house built 4D gre FLASH sequence also for MRT measurements, velocity compensation was inserted as an additional acquisition option. To adjust the temperature resolution to the expected temperature range, TE of an MRT sequence is not minimized in general. Additionally, since fluid flow is present, TE needs to be adapted to the underlaying flow conditions such that spin displacement or phase errors due to acceleration are not important. Hence, TE is fully adjustable in the sequence. Since a longer TE than the minimum possible value is typically applied, a low receiver bandwidth can be used to increase SNR without increasing the scan time. In addition, because of the prolonged TE, more time is available for the application of gradients. Hence, the gradients can be ramped up and down slower to a lower final amplitude compared to the maximum performance values of the MR system, which reduces eddy currents. Both times the same gradient moments are encoded. The two methods, one with the gradients applied as shortly as possible (non-stretched gradients) and one with the gradients stretched to the available time for the individual encoding direction, were implemented in this work. The phase encoding was kept as close as possible before the readout occurred to minimize in-plane spin displacement. Comparisons of resultant PRF ΔT maps revealed differences within 1 K (Figs. 6.1 and 6.2) and excellent correlations (Fig. 6.3). The stretched gradient scheme was chosen for MRT data acquisitions (see also chapter 9).
Generally, all MRV and MRT acquisitions were fully sampled since restrictions on the duration of the data acquisition are not as strict as in in vivo imaging. Moreover, a major requirement of engineering measurement techniques is that the accuracy of the measurements has to be as as high as possible. Hence, accelerated imaging methods such as GRAPPA [160] are expected to be less suitable in this case.
Furthermore, the option to apply dephasing (spoiler) gradients after readout of the data was implemented, to reduce off-resonance effects which may be caused by reference phantoms placed in the proximity of the flow model. The dephasing gradients can be applied in the slice, phase or readout direction separately or in all directions at once. The duration of these gradients is freely adjustable.

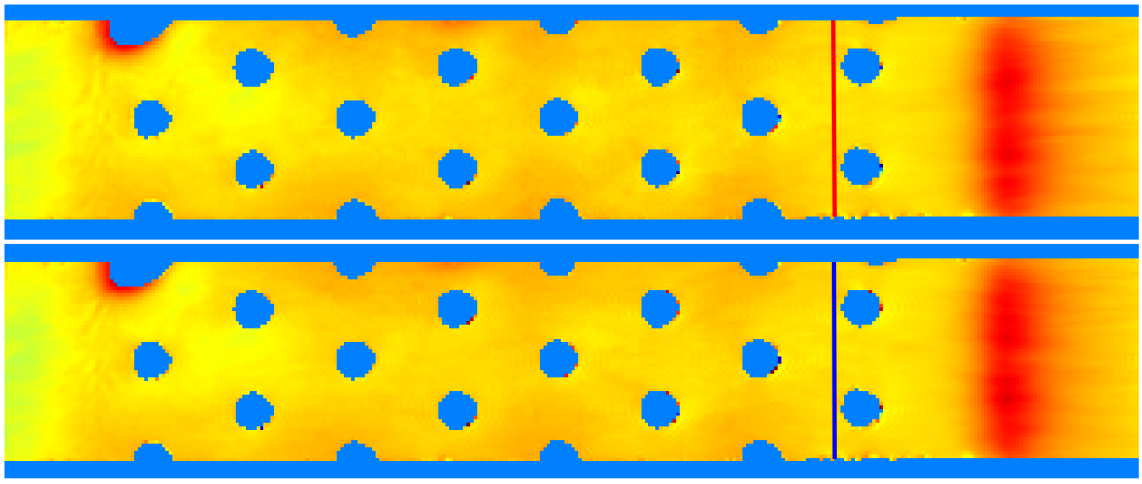

(a) ΔT maps (10 averages): stretched gradient scheme (top); non-stretched gradient scheme (bottom). Clearly visible are the impact of the flange connecting the pin fin model to the tubes on the left and right as well as air bubbles at the top, both mimicking local temperature increase or decrease.

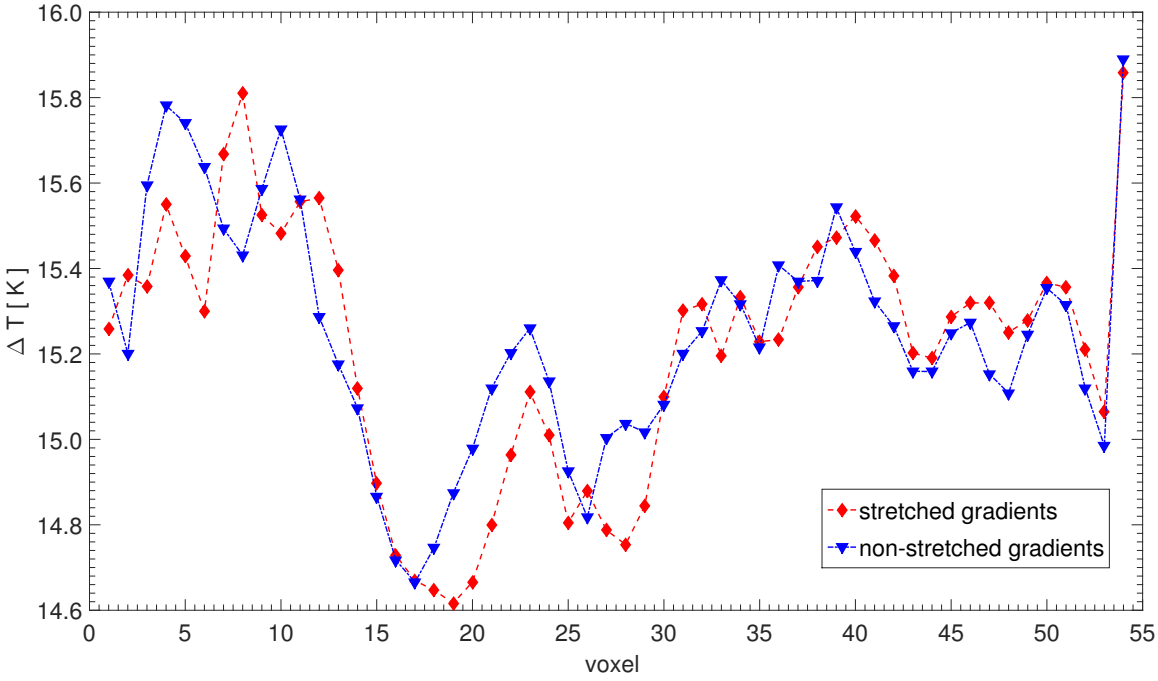

(b) Comparison of ΔT, acquired with stretched and non-stretched gradient schemes, along a vertical line (top to bottom) as depicted in Fig. 6.2a

Figure 6.2: Transverse ΔT maps are presented acquired with the stretched and non-stretched gradient schemes. The temperature in the bulk flow and inside the copper pins were the same and kept constant during the acquisitions. The direction of the flow is from right to left with a flow rate of 5.5 l/min. Remark: Data corresponds to pin fin array heat exchanger experiments with $T_{\text{flow 1}} = T_{\text{flow 2}}$ (see chapter 9).

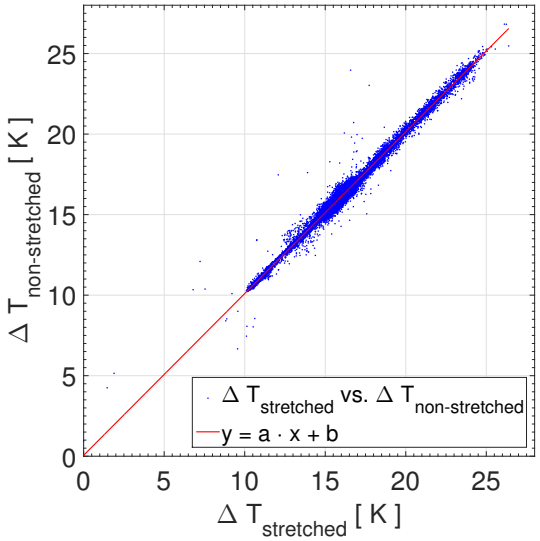

(a) slice 1: a=1.0040 ± 0.0007, b=0.057 ± 0.011, r^2 = 0.991

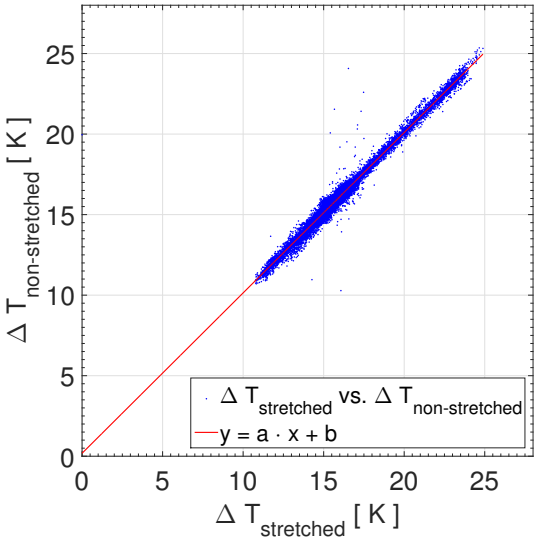

(b) slice 2: a=0.9956 ± 0.0007, b=0.184 ± 0.011, r^2 = 0.990

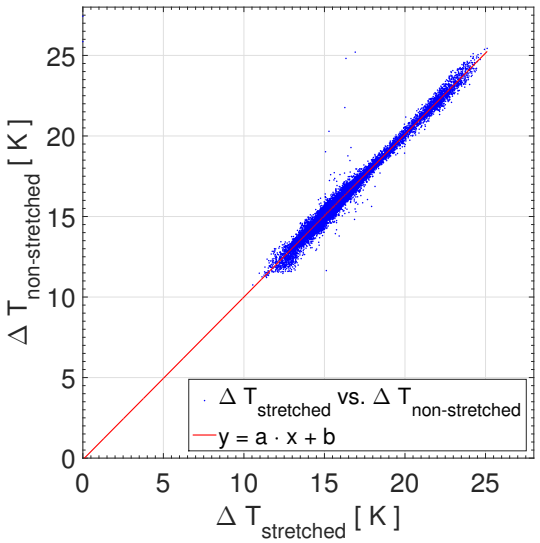

(c) slice 3: a=1.0097±0.0008, b=−0.098±0.013, r^2 = 0.988,

Figure 6.3: ΔT data of the non-stretched gradient scheme versus ΔT data of the stretched gradient scheme is depicted for three slices. The correlation of the ΔT values was determined with a linear regression $y = a \cdot x + b$. The slope a and the y-axis offset b as well as r^2 of the goodness-of-fit statistics is given. Remark: Data corresponds to pin fin array heat exchanger experiments with $T_{\text{flow 1}} = T_{\text{flow 2}}$ (see chapter 9).

6.2 Data post processing

The entire post processing pipeline to obtain PRF ΔT maps was implemented using matlab (The Mathworks, Massachusetts, USA).

6.2.1 PRF temperature phase maps (PRF ΔT maps)

One of the most important steps to correctly determine the phase difference maps requires the usage of single coil dicom data if the acquisition involved multiple receiver coils (typically used to increase SNR).
The signal phase measured by one of the receiver channels k contains a coil phase caused by receiver phase shifts, electronical configurations of the coil or positional and geometrical factors. If this unknown coil phase is temporally stable within the two equally acquired MR measurements, its contribution cancels when the phase difference of the k-th receiver channel is calculated. Thus, the phase difference for each receiver channel is calculated before actually combining them according to

$$\Delta\Theta = \measuredangle \sum_{k=1}^{L} \left(S_k^{T_{\mathrm{ref}}} \left(S_k^T \right)^* \right) \tag{6.1}$$

where L refers to the total number of coils used [36]. $S_k^{T_{\mathrm{ref}}}$ as well as S_k^T denote complex data acquired at temperatures T_{ref} and T, respectively. The asterisk denotes the complex conjugate of the complex data. Combining the multiple coils before calculating the angle (arctangent operation) has the advantage to determine ΔΘ values near aliasing boundaries ($\pm\pi$) correctly as illustrated in Bernstein *et al.* [36] at page 563. $S_k^{T_{\mathrm{ref}}}$ and S_k^T are combined using the single coil magnitude (mag) images and the single coil $phase$ images according to

$$S_k^{T_{\mathrm{ref}}} = mag_k^{T_{\mathrm{ref}}} \cdot \mathrm{e}^{i\, phase_k^{T_{\mathrm{ref}}}} \tag{6.2}$$

$$S_k^T = mag_k^T \cdot \mathrm{e}^{i\, phase_k^T}. \tag{6.3}$$

A comparison between PRF ΔT maps obtained with the above described reconstruction and PRF ΔT maps obtained from dicom phase data precombined by the MR system's reconstruction software (called precombined dicom phase data) is illustrated in Fig. 6.4. The phase difference of the precombined dicom phase data $\Delta\Theta_{\mathrm{PreComb}}$ occurring between the measurement conducted at T_{ref} and T was calculated according to

$$\Delta\Theta_{\mathrm{PreComb}} = \measuredangle \left(S^{T_{\mathrm{ref}}} \left(S^T \right)^* \right) = \measuredangle\, \mathrm{e}^{i\, \left(phase^{T_{\mathrm{ref}}} - phase^T \right)}. \tag{6.4}$$

The magnitude data was disregarded on the right side of this equation since it does not alter the outcome of the determination of the angle. The calculation of the phase difference between the data acquired at T_{ref} and T for each coil before combining them clearly reduces noise (Fig. 6.4). Additionally, areas suffering from high noise levels within the phantom, and thus within the region of interest are eliminated. Overall, the quality of the PRF ΔT map is highly improved if single dicom data is used. Additionally, a comparison between PRF ΔT maps provided from single dicom data and from raw data revealed

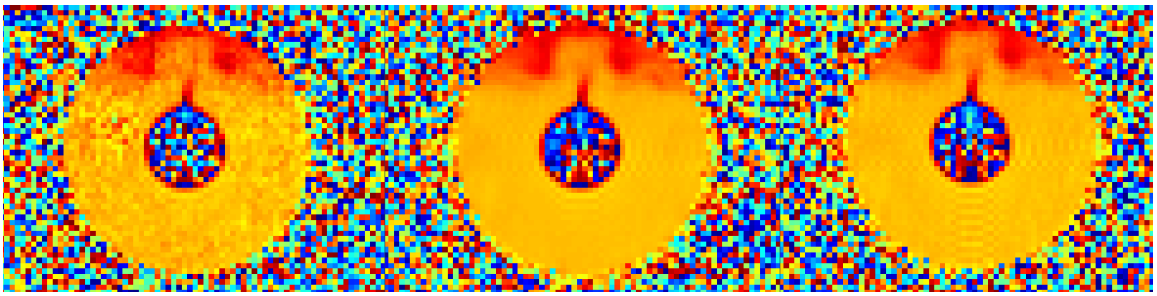

Figure 6.4: Phase difference maps (transverse views) of the double pipe heat exchanger (see chapter 8) were calculated using dicom phase data precombined by the MR system (left image), single coil dicom data (central image), and single coil raw data. Single coil phase data (either dicom or raw) results in similar phase difference maps. Whereas, the precombined phase data shows an inhomogeneously enhancement of noise.

similar image quality. Minor differences could be due to the filter which may be applied in the dicom reconstruction of the MR system, whereas no filtering was applied in the reconstruction of raw data. In summary, single coil phase data has to be used in the determination of PRF ΔT maps. To be able to apply additional post-processing of the data provided by the MR system such as a spatial distortion correction, dicom data of single coils was used throughout this work.

The calculated phase difference images $\Delta\Theta = \Theta_{T_{\mathrm{ref}}} - \Theta_T$ are then converted to temperature using Eq. (4.8).

If m acquisitions are acquired at T_{ref} and T, the complex data $S_{k,j}^{T_{\mathrm{ref}}}$ and $S_{k,j}^{T}$ is averaged over all acquisitions as follows

$$\Delta\Theta_{av} = \measuredangle \sum_{k=1}^{L} \left(\left(\sum_{j=1}^{m} S_{k,j}^{T_{\mathrm{ref}}} \right) \left(\sum_{j=1}^{m} S_{k,j}^{T} \right)^{*} \right). \tag{6.5}$$

Note, the magnitude of $S_{k,j}^{T_{\mathrm{ref}}}$ and the magnitude of $S_{k,j}^{T}$ (representing the length of a vector in the complex plane) act as weighting factors accounting for signal strength. The contribution of each vector to the phase is given by its length. Therefore, a measurement with low signal (which is equivalent to a low magnitude image, and thus results in a short complex vector) does not contribute with the same amount to the resultant phase. For this reason, the exclusion of coil data which mainly contributes noise, does not severely affect the PRF temperature phase maps as presented in Fig. 6.5. Note, the factor $\frac{1}{m}$ (to calculate mean values) can be neglected because only the angle between the two resultant complex vectors is of interest here and not the average length of the complex vectors.

Phase offsets caused by B_0 drifts for example, can contribute background phases which are not related to actual temperature changes in the fluid. Reference phantoms surrounding the flow model provide the ability to estimate these phase offsets [81]. In this work, thermally insulated reference phantoms (distilled water plus 5% hydroxyethylcellulose to increase viscosity and 1 g/l $CuSO_4$ to increase signal) were positioned within the FOV. If the reference phantoms sufficiently enclosed the flow model, first order 2D or 3D background corrections can be applied. Otherwise, the temperature difference maps were corrected for

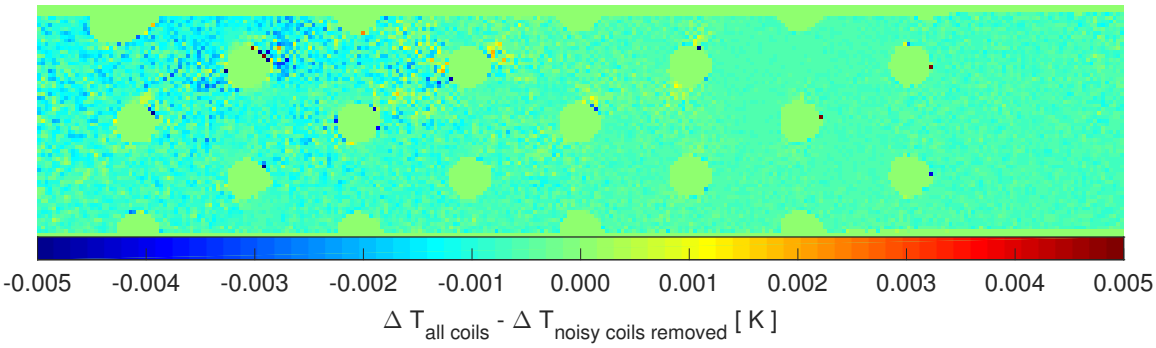

(a) PRF ΔT map difference of 50 averages

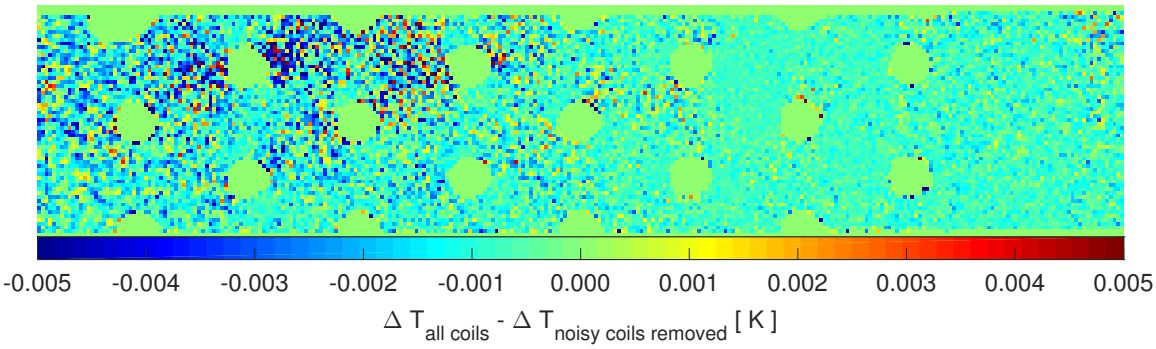

(b) PRF ΔT map difference of a single acquisition

Figure 6.5: The difference between PRF ΔT maps calculated by including all coils and PRF ΔT maps calculated by excluding coils which added mainly noise is shown. Remark: Data corresponds to pin fin array heat exchanger experiments with $T_{\text{flow 1}} > T_{\text{flow 2}}$ (see chapter 9).

a constant offset only.

6.2.2 Velocity phase maps

The conversion of the velocity encoded phase data to velocities was conducted using a home built matlab tool of the project partner. Afterwards, corrections e.g. for Eddy currents were applied by gaining estimations either through reference phantoms or an additional scan without fluid flow (if applicable). This estimation of the background phase was done using a 3D fit routine based on real-valued spherical harmonics [161] up to first order ($l = 1$).
3D visualization of the velocity or temperature data was performed using TecPlot software tools (Washington, USA).

6.3 Imaging parameter echo time

If the MR system and the measuring fluid are selected, the remaining parameter for adjusting the temperature resolution is TE (Eq. (4.8)). PRF ΔT maps acquired with different TEs of 4 ms, 10 ms, and 14 ms are shown in Fig. 6.6. Additionally, temperature maps with an TE of 14 ms and TE of 4 ms were subtracted revealing temperature maps with an effective

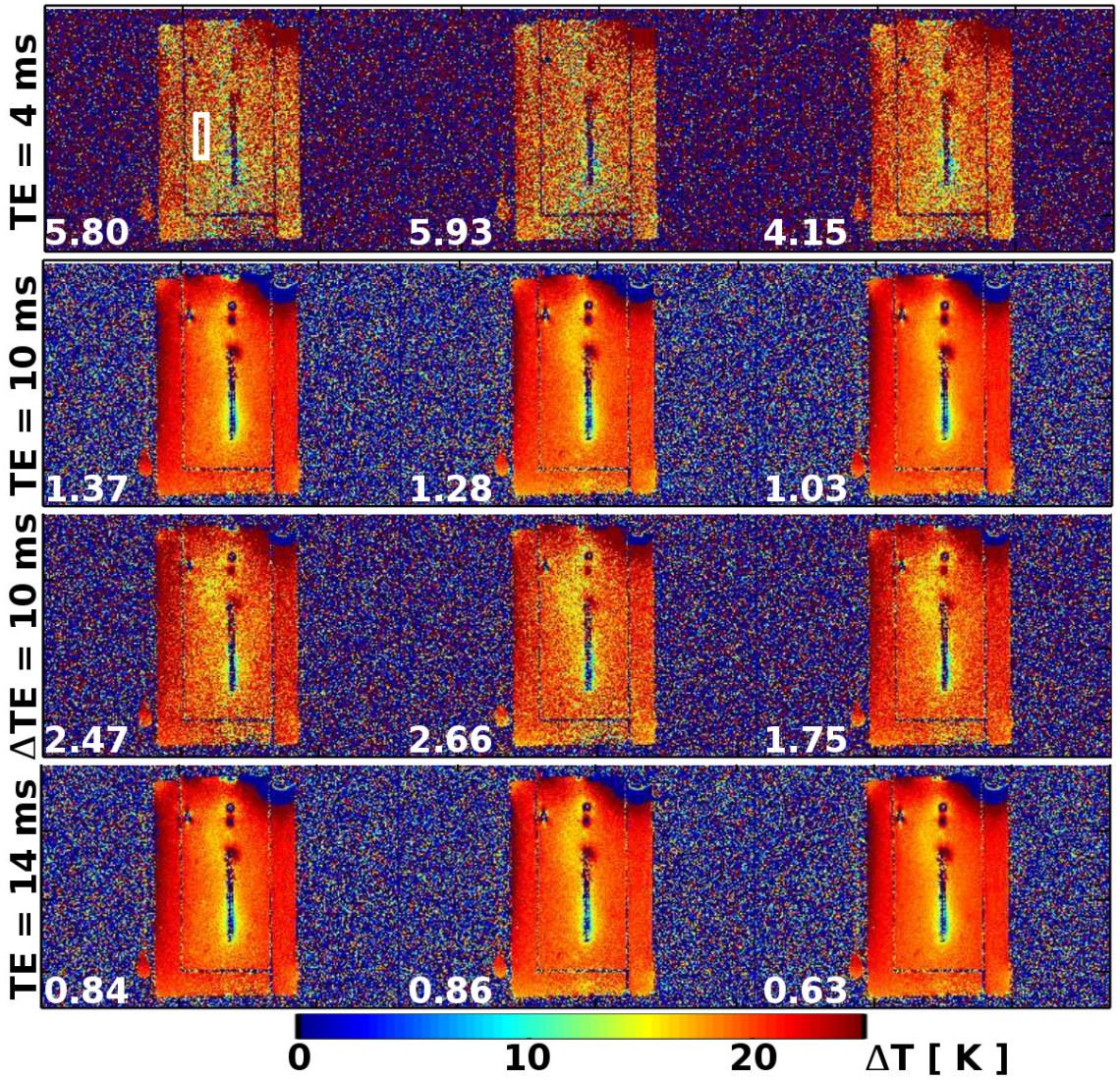

Figure 6.6: PRF temperature phase maps (transverse view) of a silicon nitride cuboid aligned perpendicular to B_0 are presented for two consecutively conducted experiments (left and central column) and their average (right column). White numbers represent the standard deviation of the temperature values within the white ROI. The experiments were performed using the double-wall heat exchanger shown in Fig. 7.1.

echo time of ΔTE = 10 ms. This is equivalent to a double-echo acquisition which is applied for in vivo MR thermometry [162] to reduce the impact of temperature related changes of the electrical conductivity [78] (see subsection 4.1.2).

Fig. 6.6 depicts two consecutively acquired PRF temperature phase maps in the left and middle column, respectively. The average of these temperature maps is shown in the right column for each individual TE. As a quantitative measure to compare the individual PRF temperature phase maps, the standard deviation within a ROI was calculated and is given in Fig. 6.6 as white number. Minor improvements with respect to noisiness of the PRF temperature phase maps are obtained by two averages. Performing more averages, how-

ever, may increase phase drifts. A clear improvement of the PRF temperature phase maps is achieved if longer TEs are used for data acquisition (Fig. 6.6). Note, the noise in the PRF temperature phase maps of the double echo method is clearly increased compared to the corresponding PRF temperature phase maps with TE = 10 ms. The coarse temperature resolution of the short TE has a clear adverse effect on the final result. Nevertheless, the PRF temperature phase maps with TE = 10 ms and ΔTE = 10 ms qualitatively agree with respect to the structural resolution within the temperature map. The necessity of conducting double echo acquisitions may become redundant for in vitro applications given the proper choice of the fluid and materials, in particular the ones located further to the outside in the FOV (e.g. use electrical insulators). Of course this option does not exist for in vivo studies.
Therefore, PRF temperature phase maps were performed with a single TE in this work. Given that the same temperature resolution is achieved using a single TE also reduces the total measurement time compared to a double echo acquisition. Finally, a TE = 20 ms was chosen which provided a sufficiently high temperature resolution and kept the spin displacement in the order of the spatial resolution of the temperature map.

Chapter 7

Experimental groundwork for MRT measurements

Beyond the mandatory adjustments of parameters for the MR data acquisition, different materials and components (required to design a model for thermofluid applications) were investigated in this work. This includes the fluid used to conduct MRV as well as MRT measurements. Results and the conclusions drawn from these results are presented in this chapter. This knowledge laid the foundation to develop the final setups such as the double pipe heat exchanger, the pin fin array heat exchanger as well as the horizontal cylinder with free convection inside. Furthermore, to monitor the temperature of the fluid during the MR data acquisitions without degrading the MR image quality, a fiber optical temperature measurement systems was used. However, the system suited and available for this work was affected by strong magnetic fields. Therefore, a detailed study of this system and an additional different fiber optical system was conducted for B_0 up to 9.4 T and published in the Journal of Magnetic Resonance in Medicine, Buchenberg $et\ al.$ [163]. Section 7.2 presented in this work is based on this journal article.

7.1 Measurement setup to study fluid flow

7.1.1 Flow model materials and components

Selection of materials

Materials to construct flow models or other in vitro phantoms for MR experiments have to be selected with care. Matching the susceptibility of the components and the fluid for example is of particular importance. The review of Schenck [34] gives an excellent overview on susceptibility effects in MRI and susceptibility values of various materials. The susceptibility of the components may change with temperature leading to a change in the local magnetic fields ultimately mimicking wrong local temperature distributions (see pp. 38 ff.). Due to the small value of the temperature coefficient α, PRF thermometry is highly sensitive to inhomogeneities of the magnetic field. The issue of temperature dependent susceptibility phase offsets can be eliminated in MRV if the temperature is kept constant during data acquisition. The two phase images required for velocity evaluation are acquired consecutively during the same data acquisition. Therefore, the phase contribution due to temperature cancels in the subtraction of the phase data. Stable temperature con-

ditions can typically be assumed in in vivo measurements. However, in in vitro setups an additional cooling or heating device may be required to ensure constant temperature conditions during the measurement.

Geometry and possible heat delivery options

In addition to the type of material its shape and orientation also have an important impact on the homogeneity of B_0 (see pp. 38 ff.). In the backward facing step (BFS) flow setup, susceptibility issues were clearly visible in the acquired PRF temperature phase maps, whereas the MRV results were not corrupted. This setup is discussed in detail in the Phd thesis of the project partner [17]. Electrical heating was conducted via silicon nitride ceramics included into the bottom of the flow model (rectangular shaped cubes with their long axis aligned perpendicular to B_0). The temperature of the ceramic elements during heating was just below the boiling point of the water. Hence, the temperature of the ceramics changed substantially between the acquisition of the PRF temperature reference data (e.g. at room temperature) and the acquisition of the PRF temperature data during heating. Changing from rectangular to circular shapes in combination with the long axis aligned parallel to B_0 may resolve this issue. However, this can result in different challenges. For example, circular shaped ceramic arrays do not align as perfect as cuboids to obtain an even surface which was required in the BFS experimental setup.
In summary, the kind of heat delivery as implemented in the BFS seems to be prone to cause susceptibility phase offsets in PRF temperature phase maps. Therefore, alternative ways for heating were considered such as water circuits integrated into the flow model for cooling or heating purposes. For this kind of heat transfer, materials with high thermal conduction coefficients such as copper are favored. Hence, copper tubes located in the FOV were investigated with respect to PRF thermometry since the susceptibility matching between copper and water is quite good (susceptibility χ [SI units]: $\chi_{\mathrm{copper}} = -9.63 \times 10^6$,$\chi_{\mathrm{water}} = -9.05 \times 10^6$ [34]).

Copper pipe

Measurements with a copper pipe (length: 7.19 cm, inner diameter 1.31 cm, wall thickness 1.1 mm) aligned perpendicular and parallel to B_0 were performed. The copper pipe was placed into a double-wall heat exchanger (Fig. 7.1) filled with a viscous liquid (glycerin) to prevent convective flows. The heat exchanger was connected to an immersion heating circulator (Julabo SE, class III, Seelbach, Germany) pumping distilled water. The circulator was turned off during the MR data acquisition to prevent flow artifacts of the water. No insulated reference phantoms were included since field drift corrections were not of interest in this test of materials.
3D acquisitions were conducted once at room temperature and once at approximately 20°C above room temperature (achieved $\Delta T \approx 20\,\mathrm{K}$) with a velocity compensated gre FLASH sequence (TE/TR = 10 ms/12.9 ms, spatial resolution = 1.2x1.2x1.2 mm^3, matrix = 256x176x120, FOV = 300x206 mm^2, flip angle of 8°, bandwidth/pixel = 454, acquisitions time = 4:34).
Example images with the copper pipe aligned perpendicular (bottom row) and parallel (top row) to B_0 are presented in Fig. 7.2. Magnitude images (left) and phase images (middle) acquired at room temperature as well as the resultant PRF ΔT maps (right) are

Figure 7.1: Double-wall heat exchanger. A sample inside the heat exchanger is heated by water flowing inside the double-wall.

shown. No temperature legends are included since the focus was on the local distortion of the copper pipe and the temperature coefficient of glycerin is unknown. The circular shape of the copper pipe is not visible and a dipole field occurs in the vicinity to the copper pipe in the perpendicular alignment. In contrast, the parallel alignment clearly resolves the shape of the cylinder and no dipole field is present.
Furthermore, RF pulses cannot penetrate the copper pipe and excite spins of the fluid such as water. Therefore, no artifacts are caused by fluid flow inside the pipe. Hence, any kind of flow can be applied for cooling or heating. Moreover, it is no longer necessary to dope this fluid to reduce artifacts, and the experimental setup becomes simpler and less expensive.
Overall, copper pipes aligned parallel to B_0 were used in the setups in this work (i.e., double pipe heat exchanger and pin fin array heat exchanger) since they provide a high thermal conductivity, good susceptibility matching, and prevent flow artifacts from the heating or cooling section.

Aluminum oxide cylinder

Next an aluminum oxide cylinder was examined. It is an electrical insulator, and thus its thermal conductivity is much smaller than the thermal conductivity of copper. Susceptibility matching between aluminum oxide (Al_2O_3) and water is not as good as for copper tubes (susceptibility χ [SI units]: $\chi_{Al_2O_3} = -18.1 \times 10^6$,$\chi_{water} = -9.05 \times 10^6$ [34]). Since the parallel orientation of the copper pipe did not degrade the quality of the PRF temperature phase maps, the parallel orientation of aluminum oxide cylinders were expected to reveal similar results. Therefore, the main focus was to determine possible local distortions of PRF temperature phase maps with the long axis of the cylinder aligned perpendicular to B_0.
The measurements with an aluminum oxide cylinder (length: 3.42 cm, inner diameter 1.70 cm, wall thickness 0.75 mm) aligned perpendicular to B_0 were performed in a similar manner as for the copper pipe. The same MR imaging parameters as for the copper pipe experiments were applied. A mixture of hydroxyethylcellulose (HEC) and double distilled water (25g HEC powder was desolved in 500g double distilled water) was filled inside the cylinder. A fiber optical probe (FOP) monitored a temperature increase of 22.7 ± 0.3°C

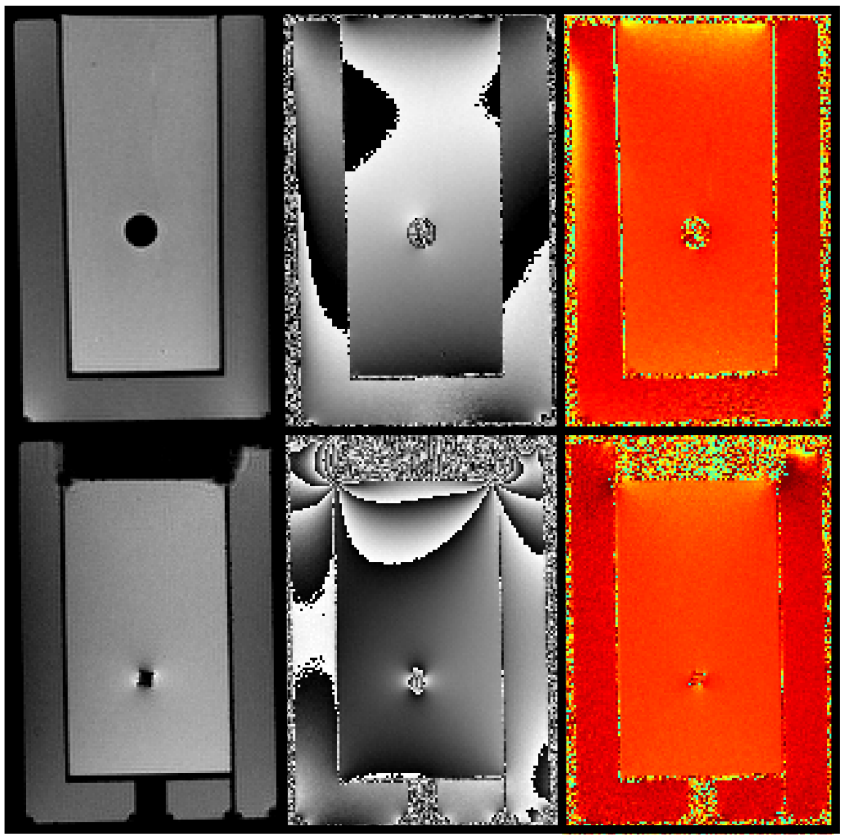

Figure 7.2: Magnitude images, phase images and PRF ΔT maps (column from left to right) are shown. The copper pipe (placed inside the double-wall heat exchanger 7.1) was aligned perpendicular (bottom row) and parallel (top row) to B_0.

between the reference data acquisition and the heated case.

For the conversion of the PRF phase difference maps to temperature (Eq. (4.8)), α_{water} was used. The ΔT measured in the PRF ΔT map within an ROI in the vicinity of the probe's tip revealed 23.6 ± 1.0°C. No field drift correction was applied. However, even without conducting a field drift correction, a comparison of the ΔT measured by the fiber optical probe and within an ROI in the vicinity of the probe's tip in the PRF ΔT map revealed a good agreement. Similar to the copper pipe a dipole pattern is observed in the phase data (Fig. 7.4, right). However, the magnitude data (Fig. 7.4, left) reveals the round shape of the cross section.

Examples of transverse and coronal views of the PRF temperature phase maps are shown in Fig. 7.3a. Outside the cylinder artificial increases of ΔT (dark red) and decreases of ΔT (yellow) occur in the vicinity of the outer wall. This behavior can be clearly seen in Fig. 7.3b at x ≈ 154.5 mm and x ≈ 167 mm. Furthermore, ΔT increases towards the inner wall of the double-wall heat exchanger indicating that a homogeneous stable temperature distribution within the viscous liquid was not reached. This may explain the variations of ΔT inside the aluminum oxide cylinder at location x=155.6 mm to x=165 mm. Inside

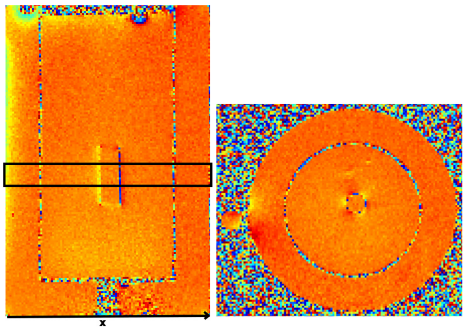

(a) Transverse (left) and coronal (right) views of PRF ΔT maps. The black rectangular box enclosed the ten horizontal lines used for calculating the average temperature data shown in Fig. 7.3b.

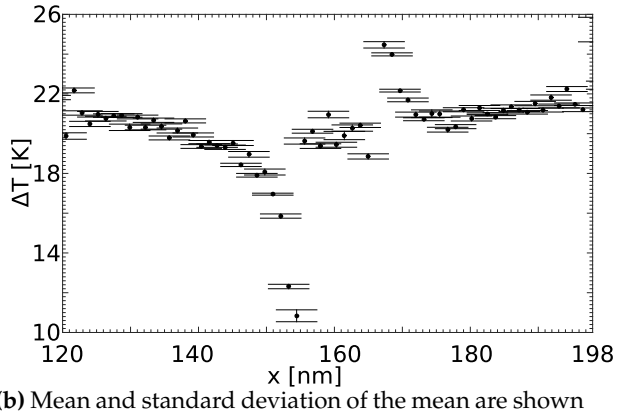

(b) Mean and standard deviation of the mean are shown for the temperature data highlighted with a black box in the transverse view in Fig. 7.3a.

Figure 7.3: PRF temperature phase maps of the aluminum oxide cylinder (placed inside the double-wall heat exchanger 7.1) are depicted. The aluminum oxide pipe was aligned perpendicular to B_0. Averaged temperature data along a horizontal line cutting approximately through middle of the cylinder's length are depicted in Fig. 7.3b.

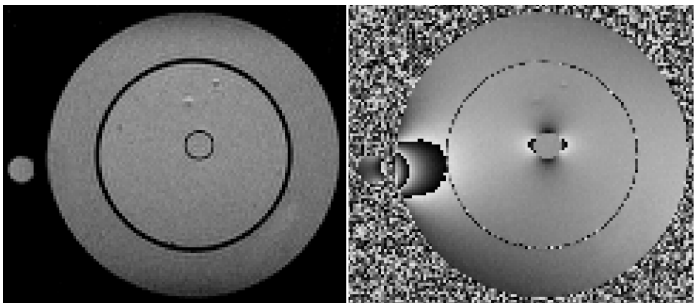

Figure 7.4: Coronal views of a magnitude image (left) and phase image (right) are shown. The aluminum oxide pipe (placed inside the double-wall heat exchanger 7.1) was aligned perpendicular to B_0.

the aluminum oxide cylinder no artifacts or shape distortions are visible. Thus, aluminum oxide cylinders may be used for setups where temperature fields of the heating or cooling circuits are of interest.

Fiber optical probe inlets

Fiber optical probe inlets were included into flow models to locally monitor temperature during the MRT acquisition for comparison. However, first experiments conducted with the double pipe heat exchanger showed substantial temperature changes in the PRF ΔT maps in the vicinity of the probe inlets which could not be traced back to actual changes due to the heating. A detailed investigation of the impact of probe inlets, with and without a fiber optical probe, on PRF ΔT maps was conducted. A double pipe heat exchanger with two probe inlets (model 1), one at the top and one at the bottom as indicated in Fig. 7.5b, and a similar double pipe heat exchanger without any probe inlets at the transparent pipe (model 2, Fig. 7.5a) were studied. The transparent pipe was made from acrylic

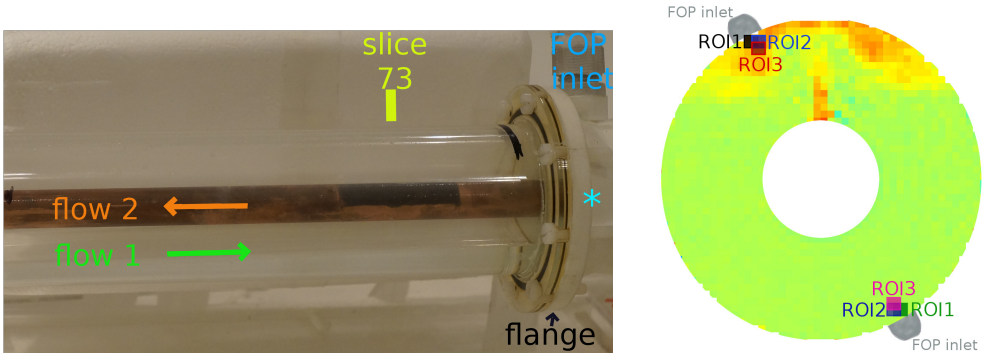

(a) Model 2. The direction of the two counter-current fluid flows is depicted. The location of the transverse slice, labeled with zero, is indicated by a star. The end nozzle containing a FOP inlet was connected via a flange to the double pipe.

(b) PRF ΔT map of a transverse slice. The location of the FOP inlets of model 1 are indicated. The position of three ROIs at the top part and the bottom part used for data evaluation are marked.

Figure 7.5: Counter current double pipe heat exchanger.

glass (PMMA). The measurement setup and data acquisition was similar as described in detail in section 8.1 (case with $T_{\text{flow 1}} < T_{\text{flow 2}}$). Only features relevant for this study are summarized in what follows.

The counter current flows (flow 1: flow inside the annulus between the PMMA pipe and the copper pipe; flow 2: flow inside the copper pipe) are indicated in Fig. 7.5a. A flange connects the PMMA pipe to the end nozzle containing an inlet for fiber optical probes to monitor the outlet temperature of flow 1. Model 1 differed from model 2 by two additional sensor inlets located at the PMMA pipe itself (approximately 8 cm to the left from the position indicated by the star in Fig. 7.5a, which coincided with slice number 73). Two cases were studied with model 1. Case 1: FOPs were inserted into the inlets such that their tips were just touching flow 1. Case 2: without any FOPs. Altogether, three cases were investigated: case 1 and case 2 with model 1 and case 3 with model 2. Note, local temperatures measured by fiber optical probes at two distinct positions, $\Delta T_{\text{FOP,top}}$ and $\Delta T_{\text{FOP,bottom}}$, are only available in case 1.

For model 1 and model 2 a 3D volume of the double pipe heat exchanger (including parts of the nozzle) was acquired by PRF MR thermometry (details see section 8.1; case with $T_{\text{flow 1}} < T_{\text{flow 2}}$). The PRF ΔT maps were obtained as described in section 6.2 and 8.1.

PRF temperature phase mapping required two acquisitions. The reference acquisition was performed with $T_{\text{flow 1}} = T_{\text{flow 2}}$, and the second acquisition was performed with $T_{\text{flow 1}} < T_{\text{flow 2}}$. During both MRT measurements the temperature of flow 1 and flow 2 was kept constant and monitored by FOPs. The temperature change ΔT_{FOP} inside flow 1 was then determined.

Locations next to the sensor inlets (three ROIs located at top left and bottom right, respectively (Fig. 7.5b) were analyzed in more detail in transverse slices of the PRF ΔT maps. Each individual ROI enclosed 4 voxels and its mean and standard deviation of the mean were computed for each slice. The slice labeled with zero coincided with the distal edge of the flange (marked by a star in Fig. 7.5a). Slices located to the left of this slice are labeled with positive numbers, whereas slices located to the right of this slice are labeled with

negative numbers. The sensor tips, and thus the center of the FOP inlets were located in slice number 73.
The results of the ROI evaluation are shown in Fig. 7.6. In 7.6, $\Delta T_{\mathrm{FOP,top}} = 7.1 \pm 0.3\,\mathrm{K}$ and $\Delta T_{\mathrm{FOP,bottom}} = -0.1 \pm 0.3\,\mathrm{K}$ are indicated by a green line and a dashed green line, respectively. The actual position of the probe is highlighted by an ellipse (Fig. 7.6a). The lines are included to aid visualization in all three cases shown in Fig. 7.6. However, the ΔT_{FOPs} values are measured simultaneously with MRT for case 1 only.
A temperature increase or decrease of several Kelvin at the vicinity of the probe inlets (approximately slices 60 to 90) is clearly observed for case 1 (Fig. 7.6a) and for case 2 (Fig. 7.6b). Whereas, this feature disappears for case 3 (Fig. 7.6c). For case 1 the FOPs lead to very local changes of the mean and its standard deviation compared to case 2 (slice 73). Additionally, an increase or decrease of ΔT_{ROI} is observed in the vicinity of the flange and the consecutively positioned FOP inlet (slices 20 to -20) in all three cases. Air bubbles of different size and numbers were located at the top part of the flange in all three cases. This may explain variations observed between the three cases at these locations. Highly varying values of ROI1 located at the top part (black circles) in slices with numbers larger than ~ 100 can be related to partial volume effects since this ROI had the outermost position compared to ROI2 and ROI3.
In conclusion, sensor inlets clearly altered temperature changes measured by the PRF method which were not related to actual changes in temperature due to heating. The FOP did locally alter ROI mean values and its standard deviation. The main source of this varying mean values is assumed to be from a combination of susceptibility effects and noise contributed by the probe since it does not provide any MR signal. Therefore, the mean and standard deviation of the ROI containing 4 voxels could be parameters to detect the tip of the probe in areas with not highly deviating temperature values.

7.1.2 Measuring fluid

The list of requirements on the fluid used for the MR experiments includes the following properties

- high MR signal (suitable relaxation times)
- chemically stable and no phase transitions within the temperature range of interest ($\sim$ 5°C to 60°C)
- viscosity such that fluid mechanically desired Reynolds numbers are achievable
- resonance frequency similar to water (most clinically used coils are resonant to the hydrogen proton signal; otherwise, x-nuclei coil required)
- high temperature sensitivity
- proper susceptibility matching between flow model and liquid
- durable (to be reused often)
- low costs
- easy to purchase and dispose

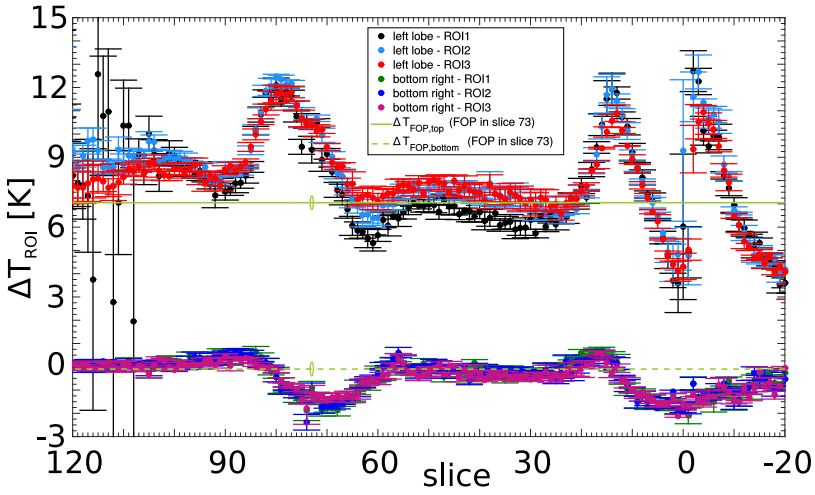

(a) Case 1, tip of fiber optical probes located in slice 73

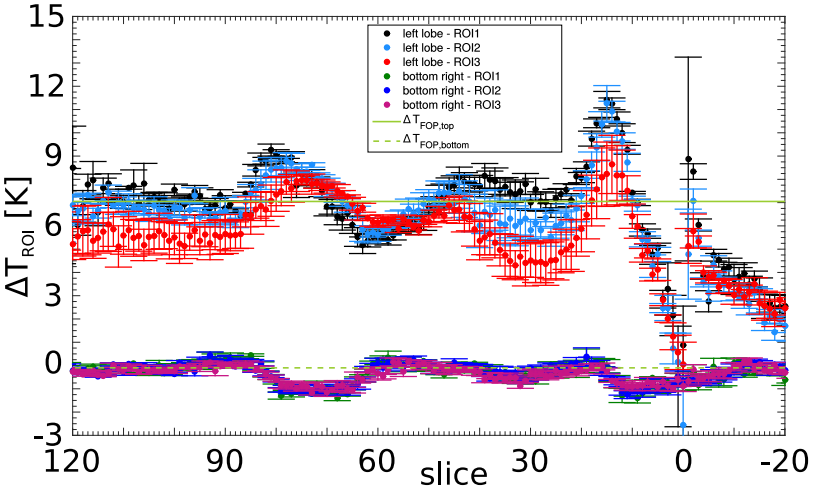

(b) Case 2, no fiber optical probes

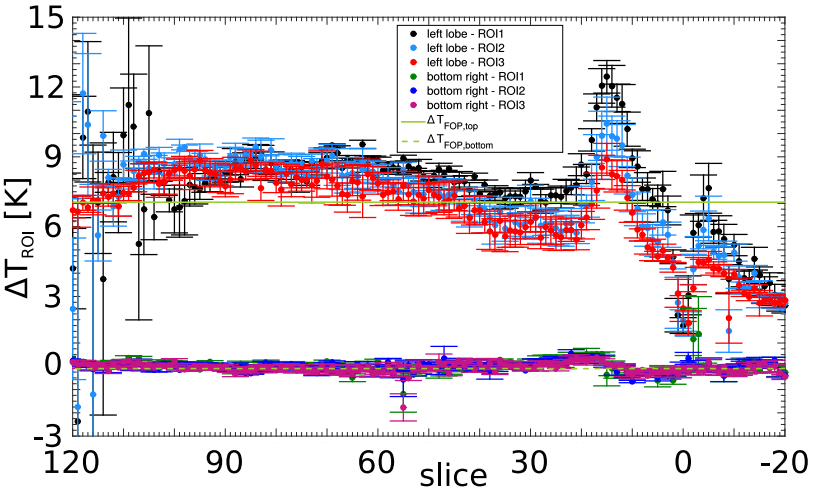

(c) Case 3, no inlets for fiber optical probes

Figure 7.6: ROI data evaluation of the PRF ΔT maps. The mean and the standard deviation of the mean are shown for each ROI at different slices. The temperature change determined by the FOPs for case 1, $\Delta T_{\mathrm{FOP,top}}$ and $\Delta T_{\mathrm{FOP,bottom}}$, are depicted in all figures to aid visualization.

- non-toxic
- non-corrosive (check the chemical resistivity of pumps, heaters and so on or establish a suitable cover layer)

Pure water is not practical to use due to its long relaxation times which can result in low signal to noise ratios in MR imaging or long data acquisition times. Thus, paramagnetic species are added to reduce the relaxation times (see Runge $et\ al.$[164]). Copper ions, Cu^{2+}, or MR contrast agents containing gadolinium are possible options.
A clinically used MR contrast agent (e.g. containing a gadolinium chelate complex) was added to de-ionized water to increase SNR. However, the life time of this aqueous solution was restricted (in the order of a few months) and had to be replaced frequently. Furthermore, the thermal stability of this complex is tested and adjusted for human applications ($T \approx 37$°C). Thus, it might not be applicable to heating experiments covering a wider temperature range from roughly 5°C to 60°C. Details about the thermal stability of the complex was not available from the manufacturer. Free gadolinium is toxic and would require additional precautions with respect to the construction and handling of the in vitro setups. Additionally, since MR contrast agents are medically approved for in vivo applications, they are very expensive. In particular, due to the large amount of the fluid (approximately 100 l) required for the flow experiments, copper sulfate was considered as an alternative option to MR contrast agents.

Copper sulfate

Paramagnetic chemical species are metallic ions such as Cu^{2+} [165]. Aqueous ionic solutions of water and copper sulphate pentahydrate ($CuSO_4 \cdot 5H_2O$) are frequently used for MR phantoms. Cu^{2+} reduces the relaxation times T1 and T2 of water [166, 34] and thus, affects the SNR of the MR measurement. However, if 1 g/l $CuSO_4 \cdot 5H_2O$ is added to the water, the increase in signal due to the reduction of T1 is much larger than the decrease in signal due to the reduction of T2. Using the values from the review article of Schenck [34], 1 g/l $CuSO_4$ reduces the T1 of water from ~ 3.6 s to ~ 0.3 s and T2 from ~ 2.2 s to ~ 0.3s at 1.5 T. A TE of 20 ms as applied for MRT in this work and considering the relaxation of the transverse magnetization $\vec{M}_{\mathrm{xy}}$ (Eq. (1.35) and Eq. (1.36)) for both T2 values reveals

$$\frac{M_{\mathrm{x,water}}}{M_{x,\mathrm{CuSO_4}}} = \frac{M_{\mathrm{y,water}}}{M_{y,\mathrm{CuSO_4}}} = \frac{e^{-\frac{0.02\ \mathrm{s}}{2.2\ \mathrm{s}}}}{e^{-\frac{0.02\ \mathrm{s}}{0.3\ \mathrm{s}}}} \approx \frac{0.99}{0.94} \approx 1.05 \tag{7.1}$$

for the effect of the change in T2 on the signal. Approximately 5% more transverse magnetization remains for signal generation at TE for the pure water sample than for the 1 g/l $CuSO_4$ sample. Meanwhile the effect of the change in T1 (assuming perfect spoiling and neglecting T2* effects) is

$$\frac{M_{\mathrm{z,water}}}{M_{z,\mathrm{CuSO_4}}} \propto \frac{\frac{1-e^{-\frac{0.0291\ \mathrm{s}}{3.6\ \mathrm{s}}}}{1-\cos\left(7°\frac{\pi}{180°}\right)e^{-\frac{0.0291\ \mathrm{s}}{3.6\ \mathrm{s}}}}}{\frac{1-e^{-\frac{0.0291\ \mathrm{s}}{0.3\ \mathrm{s}}}}{1-\cos\left(7°\frac{\pi}{180°}\right)e^{-\frac{0.0291\ \mathrm{s}}{0.3\ \mathrm{s}}}}} \approx \frac{0.52}{0.93} \approx 0.56 \tag{7.2}$$

using a flip angle = 7° and TR=29.1 ms. The result in Eq. (7.2) reveals a decrease of the signal of the pure water sample by approximately 44% compared to the 1 g/l $CuSO_4$ sample.

The desired relaxation times can be adjusted via the amount of copper sulfate added. However, regarding the concentration of copper ions there is another aspect to be considered. Since Cu^{2+} is paramagnetic, the susceptibility of the solution is altered. For concentrations of approximately 1 to 2 g/l, as commonly used in MR phantoms, the susceptibility of the solutions is similar to the susceptibility of water [34]. With increasing concentrations of copper sulfate the volume susceptibility of the solution increases and becomes even positive at very high concentrations (see Fig. 3 in the review of Schenck [34]). Thus, the susceptibility matching between the phantom and the fluid has to be adjusted accordingly. Furthermore, with increasing concentrations of copper sulfate the electrical conductivity of the fluid increases. However, PRF temperature phase mapping is sensitive to temperature induced changes of the electrical conductivity [78]. Therefore, it would be beneficial to use non-conducting materials for the setup. This represents another reason to prefer a low concentration of $CuSO_4 \cdot 5H_2O$. In addition, if the flow of an electrically conducting fluid is not aligned parallel to B_0, a physical phenomenon similar to the Hall effect in solid state materials occurs, the so called magnetohydrodynamic (MHD) effect [167, 168, 169]. This can cause alterations of the flow profile and flow retardation [169, 170]. These alterations, however, are expected to be negligible at the applied field strength of 3 T in combination with the low flow velocities compared to the aortic blood flow (typically used to simulate the altered flow profiles and flow retardations). A further advantage of copper is that it features antimicrobial properties [171, 172, 173], whereby the life time of the aqueous solutions can be prolonged when adding copper sulfate. Hence, the solution can be reused for many experiments if it was stored in a closed container to avoid evaporation which would change the concentration of the solution. Another aspect of economical nature is that it is much cheaper than using MR contrast agents. Important to note is that the copper sulfate solution is corrosive and the pumps as well as all other setup components have to be checked for the compatibility with this solution.

Considering all the former discussed dependencies and properties, a solution of deionized water and 1 g/l $CuSO_4 \cdot 5H_2O$ (4 mM copper sulfate solution) was expected to be appropriate. This fluid provided good signal to noise values, was cheap and kept the additional effort regarding personal safety within feasible limits. Furthermore, the desired fluid mechanical and thermodynamical requirements could be achieved as discussed by the project partner [17]. The electrical conductivity of this fluid (~ 0.066 S/m at 20°C) was an order of magnitude smaller than for blood (0.5 S/m) and tissue (0.2 S/m) [174].
T1 and $T2^*$ of this solution were determined using an inversion recovery sequence (subsection 2.4.3) and a multi gre sequence (subsection 2.4.2), respectively. The determination of the relaxation times provides the ability to select MR imaging parameters which are optimized with respect to SNR such as the flip angle using Eq. (2.19) or the temperature-dependent phase difference SNR which is dependent on $T2^*$ [10]. Data evaluation of T1 was performed using Eq. (2.21) (Fig. 7.7), and revealed $T1_{CuSO_4}$ = 327.71±0.11 ms. An artifact appeared as a series of ellipses with higher and lower signal intensities in the MR magnitude data when using higher flip angles of the order of 25° (corresponding to the Ernst angle). The origin of this artifact remained unclear after changing parameters such as TE, TR, phase encoding direction and applying high gradient spoiling as well as exchanging flow models. Generally, it could be greatly reduced using low flip angles ($\sim 7°$). Thus, in the case of severe image degradation due to this unknown artifact, reduced flip angles compared to the Ernst angle were applied still providing adequate SNR. Future work could include further investigation of this artifact.

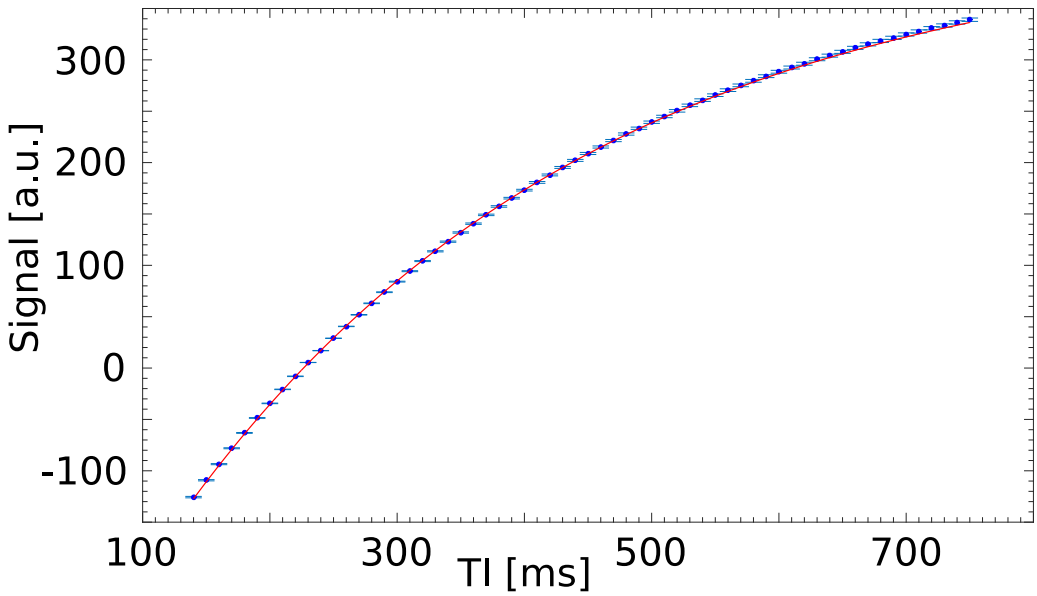

Figure 7.7: Determination of T1 of a 4 mM copper sulfate solution at a temperature of 21.2±0.2°C. Blue dot and error bar represent the mean and the standard deviation of the mean, respectively, which were determined within an ROI in the sample for different inversion times TI.

T2* data was determined in the double pipe heat exchanger for a transverse slice. However, it is dependent on local magnetic field variations, and thus may differ for differently arranged or differently shaped setups. T2* were determined within an region of interest in the reference phantoms (static viscous copper sulfate solution) as well as in the flow phantom as the pump was turned off (static copper sulfate solution). For T2* data evaluation Eq. (2.18) was used if no sinc modulation due to susceptibility effects occurred, otherwise the modified equation

$$s_{\mathrm{gre,ampl,mod}} \propto e^{\left(-\frac{\mathrm{TE}}{\mathrm{T2^*}}\right)} \cdot d \cdot \left| \frac{\sin\left(\frac{\gamma}{2} \cdot d \cdot G_{\mathrm{add}} \cdot \mathrm{TE}\right)}{\frac{\gamma}{2} \cdot d \cdot G_{\mathrm{add}} \cdot \mathrm{TE}} \right| \tag{7.3}$$

was applied with slice thickness $d = 0.005\,\mathrm{mm}$, $\gamma = 42576375 \cdot 2 \cdot \pi\,\mathrm{Hz/T}$ [34], and G_{add} an additional field gradient (background gradient) due to susceptibility effects which is perpendicular to the 2D slice (see [175] for details). The absolute value of the sinc function was considered in this work since magnitude data was used. Examples of fit results of T2* are shown in Fig. 7.8 for a region of interest positioned either inside a reference phantom or inside the annular passage of the double pipe. Within the reference phantom a clear exponential relaxation is observed, whereas, a modulation of the exponential function with a sinc function occurs in the flow phantom. However, since the additional field gradients due to susceptibility effects may not be perfectly aligned to the through plane direction, deviations from Eq. (7.3) are likely to occur [176], and may explain the deviations between the fitted function and the data. Values of T2* of the order of approximately 130 ms were obtained in the flow model and slightly lower ones in the reference phantoms (Figs. 7.8a

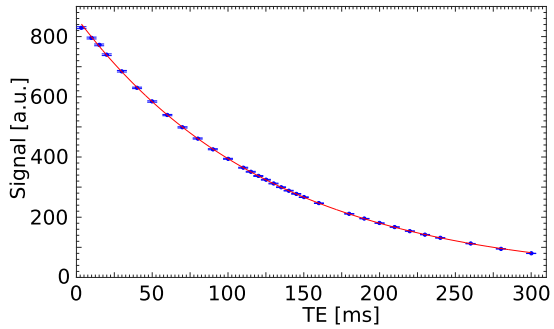

(a) Magnitude signal determined within an ROI of the left reference phantom versus TE. A fit using $y = a \cdot e^{\left(-\frac{\mathrm{TE}}{\mathrm{T2}^*}\right)}$ revealed $\mathrm{T2}^* = 127.61 \pm 0.11\,\mathrm{ms}$

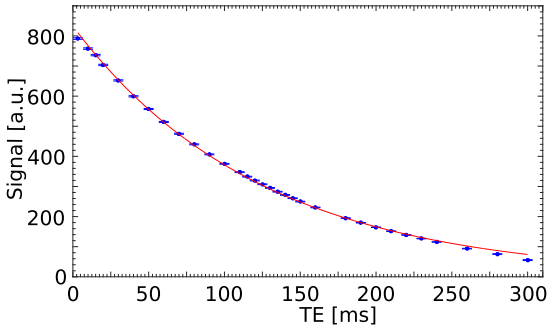

(b) Magnitude signal determined within an ROI of the right reference phantom versus TE. A fit using $y = a \cdot e^{\left(-\frac{\mathrm{TE}}{\mathrm{T2}^*}\right)}$ revealed $\mathrm{T2}^* = 124.0 \pm 0.6\,\mathrm{ms}$

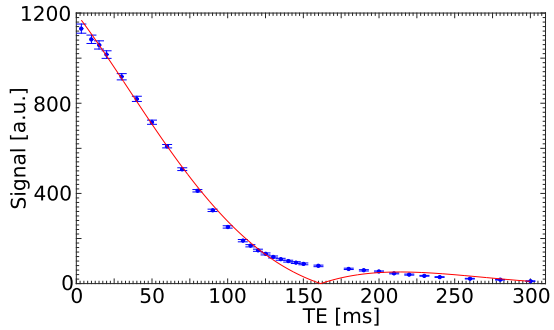

(c) Magnitude signal determined within an ROI inside the double pipe versus TE. A fit using $y = a \cdot e^{\left(-\frac{\mathrm{TE}}{\mathrm{T2}^*}\right)} \cdot d \cdot \left|\frac{\sin\left(\frac{\gamma}{2} \cdot d \cdot G_{\mathrm{add}} \cdot \mathrm{TE}\right)}{\frac{\gamma}{2} \cdot d \cdot G_{\mathrm{add}} \cdot \mathrm{TE}}\right|$ revealed $\mathrm{T2}^* = 137 \pm 8\,\mathrm{ms}$

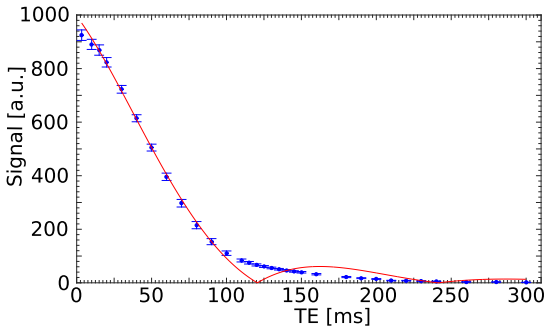

(d) Magnitude signal determined within an ROI inside the double pipe. A fit using $y = a \cdot e^{\left(-\frac{\mathrm{TE}}{\mathrm{T2}^*}\right)} \cdot d \cdot \left|\frac{\sin\left(\frac{\gamma}{2} \cdot d \cdot G_{\mathrm{add}} \cdot \mathrm{TE}\right)}{\frac{\gamma}{2} \cdot d \cdot G_{\mathrm{add}} \cdot \mathrm{TE}}\right|$ revealed $\mathrm{T2}^* = 132 \pm 4\,\mathrm{ms}$

Figure 7.8: Determination of T2* in one of the experimental setups (in this case, double pipe heat exchanger) using a multi gradient echo sequence. Two insulated cylindrical reference phantoms (long axis parallel to B_0, temperature of 21.5±0.2°C) were placed to the left and to the right side of the double pipe. The flows inside the double pipe were turned off and the temperature of the copper sulfate solution was at 20.5±0.3°C. Two distinct regions of interest were chosen in the annular passage as well as one in the left and right reference phantom. The mean and the standard deviation of the mean within the ROI were calculated (depicted as blue dot with error bar). This averaged signal data from magnitude images acquired with different TE was fitted and T2* determined.

to 7.8d). The decrease of homogeneity of B_0 towards the image borders can increase intra voxel dephasing, and thus may cause the reduction in T2*.

Determination of the temperature coefficient

An experiment is conducted to determine the conversion factor (temperature coefficient α) between phase differences and temperature changes of the used fluid.
A double-wall heat exchanger is designed such that it can hold common lab plastic bottles filled with the desired solution (Figs. 7.1 and 7.9). It is connected to an immersion heating

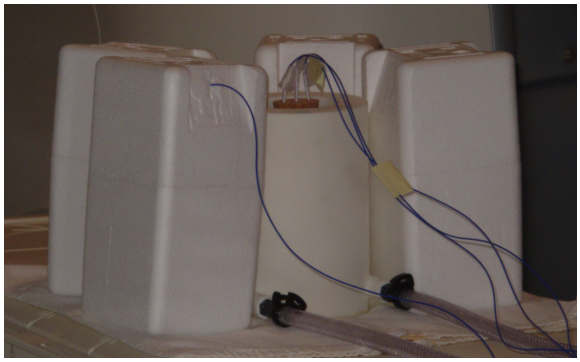

Figure 7.9: Experimental setup to measure the temperature coefficient α.

circulator (Julabo SE, class III, Seelbach, Germany) pumping water at the desired temperature. A fiber optical temperature measurement system is utilized (FOTEMP 4, probe TS2, Optocon AG, Dresden, Germany) to monitor and log temperature within the MR scanner. The probes are calibrated within B_0 as described in section 7.2. Three probes are placed within the solution and its temperature data is averaged during data evaluation. One probe is located inside a reference phantom to monitor its temperature stability during the whole measurement session. In total four insulated reference phantoms surround the heat exchanger. The reference phantoms are required to allow field drift corrections of the MR data.
To determine the temperature coefficient of the 1 g/l copper sulfate solution, 2D gre FLASH acquisitions were conducted. A temperature range between 21 °C and 47 °C was covered. At each temperature multiple acquisitions were conducted each with a different echo time. To avoid flow artifacts the immersion heating circulator was turned off during data acquisition.
The conversion factor was determined similarly as presented in the journal article of Peters $et\ al.$ [77]. The measured phase differences ($\Delta\Phi$) are plotted versus the averaged temperature change ΔT of the three fiber optical probes. A linear regression was performed for each individual TE (Fig. 7.10a). To obtain a general conversion factor the determined $\frac{\Delta\Phi}{\Delta T}$ are drawn versus the corresponding TE (Fig. 7.10b). A linear regression revealed α for the liquid to be $\alpha_{\mathrm{CuSO4}} = 0.9702 \pm 0.0018 \cdot 10^{-8}\,\mathrm{K}^{-1}$. This type of experiment was reassembled and repeated on another day to check reproducibility ($\alpha_{\mathrm{CuSO4}} = 0.971 \pm 0.002 \cdot 10^{-8}\,\mathrm{K}^{-1}$). Finally, the mean of the two α values, $\alpha_{\mathrm{CuSO4}} = 0.9706 \pm 0.0014 \cdot 10^{-8}\,\mathrm{K}^{-1}$, was used as the conversion factor for all MR temperature data evaluations in this work.

7.1.3 Flow apparatus

A pumping system has been established by the project partner to control and condition the flows required to carry out reproducible velocity and temperature field measurements. A summary of its components and features required to understand the concept of the experimental flow setups presented in sections 8.1 and 9.1 is provided in the following. This subsection is based on the journal article Buchenberg $et\ al.$ [133], and additional information can be found in the thesis of the project partner [17].
The pumping system maintains two independent flow circuits while simultaneously logging the conditions of the flow (Fig. 7.11). The closed primary circuit (flow 1, green lines)

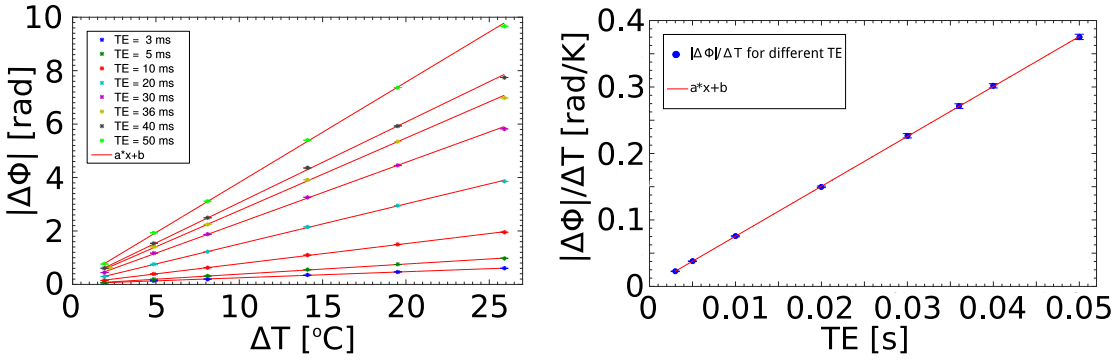

(a) Determine α for each individual TE. **(b)** Determine general α.

Figure 7.10: Linear regressions to determine α.

was established by connecting a 100 liter reservoir of deionized water with 1 g/liter $CuSO_4$ solution (tank cart, cyan box) to a pumping cart (light green box) and a flow model. The pumping cart includes a pump (Grundfos CME3-2 A-R-I-V-AQQE, nominal flow rate 3.7 m^3/h, Grundfos, Bjerringbro, Denmark), a flow meter (Bürkert 8030 DN15, range 5 - 30 l/min, Bürkert, Ingelfingen, Germany), a pressure sensor (Jumo Midas 401001, Jumo, Fulda, Germany) and a temperature sensor (pt100). An immersion cooler (Julabo FT402, Seelbach, Germany) or an ohmic heating foil (MINCO HK5600R25.5L12A, Minco, Minneapolis, Minnesota, USA) can be used to alter and maintain the temperature within the tank cart. Details about these components and the pumping cart can be found in the thesis of the project partner [17], section 3.3.
The closed secondary circuit (flow 2, orange lines) consists of either an external pump which includes the functionality of heating and cooling (HC-pump, Julabo FC1200T, Seelbach, Germany), or an immersion heating circulator which is only capable of heating (Julabo SE, class III, Seelbach, Germany). The HC-pump contains an internal reservoir which can hold 10 liters of water. The water can be cooled with 1.3 kW or heated with 1.2 kW. It provides a constant flow rate of $\approx$ 25 l/min (up to 3.5 bar pressure loss). The immersion heating circulator is placed on top of a self-built acrylic glass reservoir containing 10 liters of water. This pump offers 4 adjustment levels which reveal (dependent on the pump pressure in combination with the pressure loss) a constant flow rate between $\approx 13 - 19$ l/min. The heating power of the pump is 1.3 kW. Pure water without $CuSO_4$ can be used in either of the two pumps since no signal is received from the secondary circuit. Flow 2 is flowing within copper pipes (acting as a Faraday cage) in all flow models examined with the flow apparatus described in this section.
It is advantageous to have two pump systems for flow 2 since the water temperature of flow 2 can be quickly modified, thus, reducing the waiting time between MR acquisitions. This can help to minimize field drifts. Additionally, a prolonged use of water at higher temperatures generates air bubbles at the surface of copper pipes (see discussion about counter-current double pipe heat exchanger 8.3). Air bubble severely degrade PRF temperature phase mapping results.
The water temperature of the reservoirs of the pumps can be adjusted independently. The interchange of the two pump systems with distinct reservoir temperatures allows a quick alteration of the temperature in the secondary circuit instead of waiting for the water to be

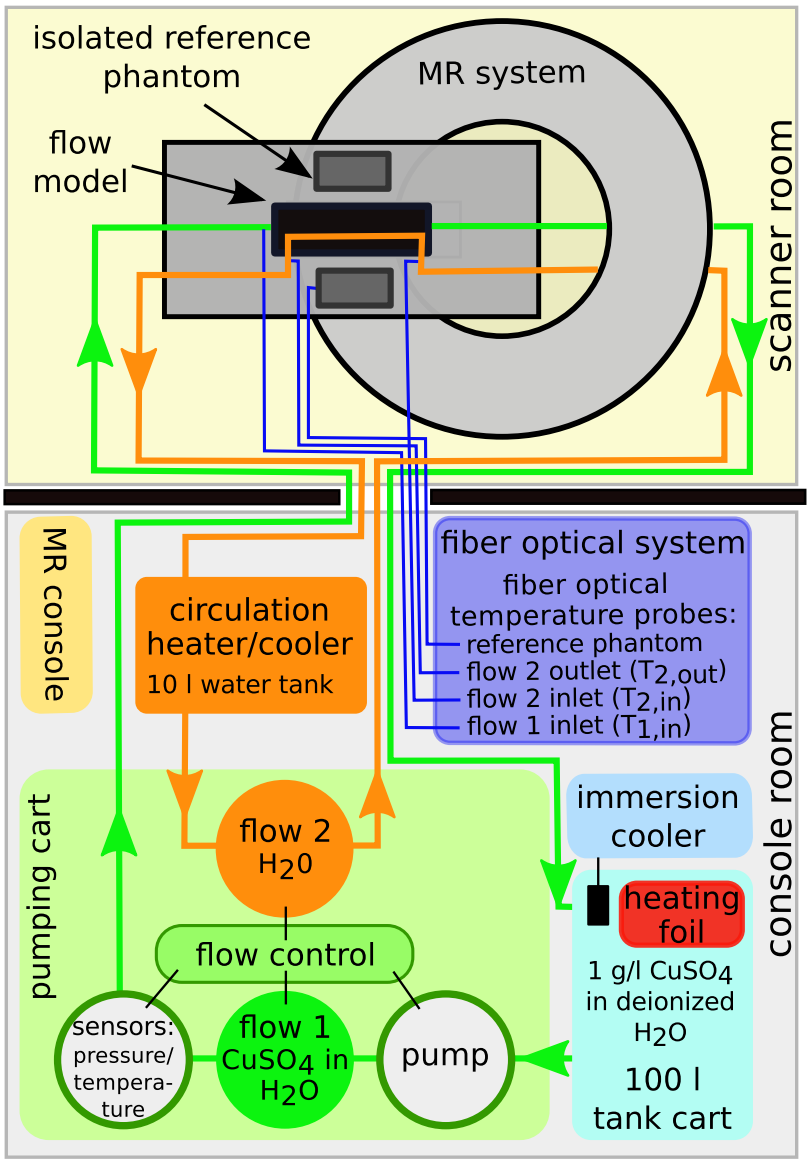

Figure 7.11: Flow apparatus used for measurements of the double pipe heat exchanger and of the pin fin array heat exchanger. Two independent flow circuit are maintained by the pumping system allowing reproducible velocity and temperature field measurements within the flow model. Flow 2 was applied for heating or cooling of the fluid flow 1. An immersion cooler or an ohmic heating foil maintained the temperature of flow 1 in the tank cart at a constant temperature. The flow rates of both flows were monitored by a flow control system including two flow meters. An A/D-converter (National Instruments DAQ USB-6009, National Instruments, Austin, Texas, USA) is connected to all sensors and the pump driving flow 1. The pump voltage can be adjusted via a Labview program (National Instruments, Austin, Texas, U.S.) installed on a laptop computer to provide the desired flow rate. In addition, the temperature and pressure of the water can be monitored at the pumping cart by the Labview program. The temperature of the flows as well as of an insulated reference phantom was monitored and logged by a fiber optical system. (Figure was adapted from the journal article Buchenberg *et al.* [133].)

heated or cooled.
The pumping system including all devices for heating and cooling as well as the fiber optical system is established in the console room of the MR system. The PVC hoses of flow 1 (inner diameter=25.4 mm) and flow 2 (inner diameter=19.05 mm), and the four MR compatible fiber optical probes (FOTEMP 4, probe TS2, Optocon AG, Dresden, Germany) are fed through waveguides into the MR scanner room. Altogether the functionality of the waveguides is preserved.
All in all this versatile pumping system can be connected to any appropriately designed flow model to either both of the flow circuits or either of them.

7.2 Static magnetic field dependency of fiber optical temperature probes

This section investigates the static magnetic field dependency of fiber optical temperature probes and is based on the journal article Buchenberg *et al.* [163].
A fiber optical system with fiber optical temperature probes was used to monitor and log temperature data of the fluid flows and reference phantoms inside the bore of the MR system. This type of temperature probes are typically nonmagnetic. Their cable is non electrically conductive in contrast to conventional temperature measuring devices such as thermocouples or resistance temperature detectors. Hence, the probes can be fed through the waveguide without degrading MR image quality due to RF interferences. In addition, they are not heated during MR imaging.
Accurate measurements of temperature in an MR environment are of particular importance for MR thermometry and MR safety studies to develop MR-safe devices or to ensure safety and effectiveness of MR guided thermal therapies. If fiber optical probes are placed in strong magnetic fields, there are indications found in literature for an underestimation of the actual absolute temperature [177, 178].
The temperature determination by FOPs is based on various measurement principles such as fiber optic displacement sensing [179], microfiber loop resonance [179], Brillouin scattering [179], fluorescence lifetime measurements in e.g. rare-earth-doped materials [179, 180], Fabry-Perot interferometry [181], fiber Bragg grating measurements [182], and optical translucence of semiconductors [183]. Currently, the fluorescence method and the semiconductor method are widely spread and either of them is applied in most commercially available temperature measurement systems.
A temperature-sensitive phosphor such as manganese-activated magnesium fluorogermanate is typically used in FOPs based on fluorescence. The fluorescent signal intensity decreases after the optical excitation of the phosphor ended. The corresponding decay time of the fluorescent signal is determined via curve fitting. This decay time is in the order of a few milliseconds and decreases as temperature of the probe increases. The temperature of the phosphor, and thus locally of the sample, is obtained by comparing the determined decay time to the system calibration values stored in an internal lookup table.
FOPs operating with a semiconductor often made from gallium-arsenide (GaAs) exploit the temperature sensitivity of the band gap. The light absorption of GaAs probes depends strongly on the wavelength of the photons. The semiconductor becomes optically transparent as the wavelength of the monochromatic light exceeds a threshold of approximately 900 nm at room temperature [184]. This threshold wavelength changes with temperature

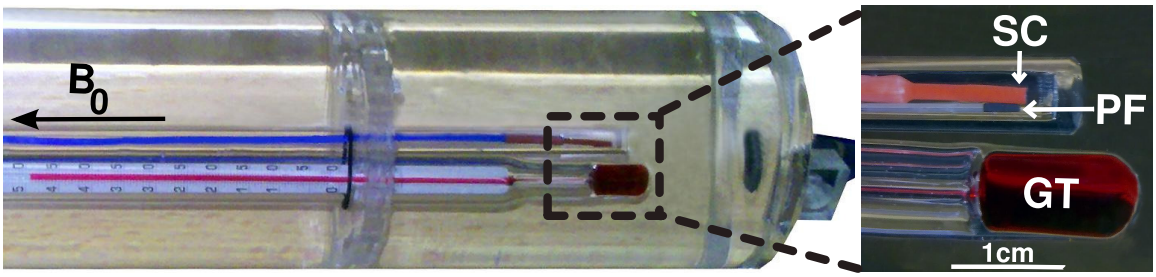

Figure 7.12: An image of the cylindrical flow phantom is shown which was used to compare temperature measurements conducted with two different fiber optical probes and a glass thermometer. The long axis of this phantom was aligned parallel to B_0 if not stated otherwise. The inset shows the positions of the PF-probe tip and the SC-probe tip located next to the glass thermometer GT. (This figure was taken from the journal article Buchenberg *et al.* [163].)

by approximately 0.35 nm/K [183] since the edge of the band-gap of the semiconductor is temperature dependent [185, 186, 187]. A built-in spectrometer in commercial GaAs systems analyzes the threshold wavelength which in turn can be converted to temperature values.
In this work temperature measurements of a phosphor fluorescence (PF) system and a GaAs semiconductor (SC) system were compared. They were conducted at magnetic field strengths up to 9.4 T covering a temperature range of 25°C to 65°C. The two commercial fiber-optical systems used to measure temperatures were: PF-system (Luxtron with probe SMM, sensor size: $0.3 \times 0.3 \times 0.3\,\mathrm{mm}^3$, Lumasense Technologies GmbH, Santa Clara, CA) and SC-system (FOTEMP 4 with probe TS2, sensor size: $0.75 \times 0.75 \times 0.75\,\mathrm{mm}^3$, Optocon AG, Dresden, Germany).

7.2.1 Measurement setup

An MR compatible cylindrical flow phantom was designed and constructed from acrylic glass as shown in Fig. 7.12 to hold two distinct fiber optical probes, one of the PF-system and one of the SC-system, and a glass thermometer (GT) with organic alcohol filling (#8098, L. Schneider GmbH&Co.KG, Wertheim, Germany). The two probes were placed into an acrylic glass capillary filled with distilled water. Their tips were positioned very closely together to allow a comparison between their performances of measuring temperature. One end of the capillary was closed to avoid any possible impact of flow on the temperature measurements. The fiber optical probes were aligned parallel to B_0 by either using the laser positioning system of the 3 T MR system or by using a ruler at the 7 T and 9.4 T MR systems. The tips of the probes were located next to the tip of the GT used to provide temperature reference values. The flow phantom was connected via flexible plastic tubes to an immersion heating circulator (Julabo SE, class III, Seelbach, Germany) sitting on a 10 l water reservoir. The circulator provided a stable temperature environment in the flow phantom at various different temperatures.
The measurement precision of the PF-system, the SC-system, and the glass thermometer were $\pm 0.5\,^{\circ}\mathrm{C}$, $\pm 0.2\,^{\circ}\mathrm{C}$, and $\pm 0.2\,^{\circ}\mathrm{C}$, respectively. These values were taken from the corresponding manufacturer's instruction manuals.

The flow phantom was placed into various static B_0 fields provided by the following three MR systems, a 3 T whole-body system (TRIO, Siemens, Erlangen, Germany), a 7 T small-animal system (Bio Spec 70/20, Bruker, Ettlingen, Germany), and a 9.4 T small-animal system (Bio Spec 94/21, Bruker, Ettlingen, Germany). Temperature measurements at the 7 T MR system were carried out at the isocenter and in the console room ($B_0 \approx 0$ T). At the 3 T and 9.4 T MR systems, they were conducted at the isocenter, the console room, and additionally at different distances from the isocenter to collect data at numerous distinct B_0 values. A Hall probe (digital Teslameter FM 210, Projekt Elektronik GmbH, Berlin) was used to determine the corresponding B_0 values in the magnetic fringe field at the 3 T system. It was positioned with the laser positioning system of the 3 T system and a ruler at the same locations as the optical probes were placed. The accuracy of the Hall probe given by the manufacturer was $< 0.5\% \pm 2$ digits. In the 9.4 T MR system, B_0 values within its magnetic fringe field were calculated by the manufacturer of the MR system using their simulation model for magnet construction. The accuracy of this simulation is better than the performance of measurements of B_0 with a Hall probe. Thus, the major impact on the precision of the B_0 values in this experimental setup is caused by positioning errors of the fiber optical probes within the strongly decreasing fringe field. Since the magnetic field changes most steeply at the bore entrance positioning errors are more pronounced at this location than close to the isocenter. A positioning offset of the probe tips of $\pm$0.5 cm (either decreasing or increasing the distance with respect to the isocenter) changes B_0 by less than 4% at all positions. The change of B_0 was less than 1% up to 30 cm away from isocenter. The maximum change of B_0, thus maximum error occurred close to the bore entrance. An off center displacement in the radial direction $\vec{r}$ with $\vec{r} \perp \vec{B}_0$ of even 1 cm caused only a small relative error on B_0 of up to 0.2% in the fringe field.

7.2.2 Experiments

Temperature measurements were performed at a total of 17 B_0 values and at 6 or 7 different temperatures $T = 25.0$ °C, 30.0 °C, (35.0 °C only at the 3 T MR system), 40.0 °C, 50.0 °C, 60.0 °C, and 65.0 °C. At each of these temperatures, the measurements were carried out in the order of increasing B_0 (i.e., moving towards the isocenter) first. After the isocenter was reached, they were conducted in a reversed order by moving away from the isocenter. The mean of the two measurement values obtained at each location was determined to reduce the error caused by inaccurate positioning within the steeply changing field away from the isocenter.
Temperature differences ΔT were calculated as the difference between each temperature measurement at $B_0 \approx 0$ T and the measurement at the same temperature with $B_0 > 0$ T,

$$\Delta T = T(B_0 > 0\,\mathrm{T}) - T(B_0 \approx 0\,\mathrm{T}). \tag{7.4}$$

ΔT was modeled using a second order Taylor expansion around B_0,

$$\Delta T = a \cdot B_0^2 + b \cdot B_0 + c, \tag{7.5}$$

to quantify the temperature shift of the SC probe, and to provide an empirical equation applicable to correct temperature measurements conducted with the SC probe in magnetic fields. Fitting of the data was done using the fitting toolbox of Matlab Version R2013a (The Mathworks, USA).

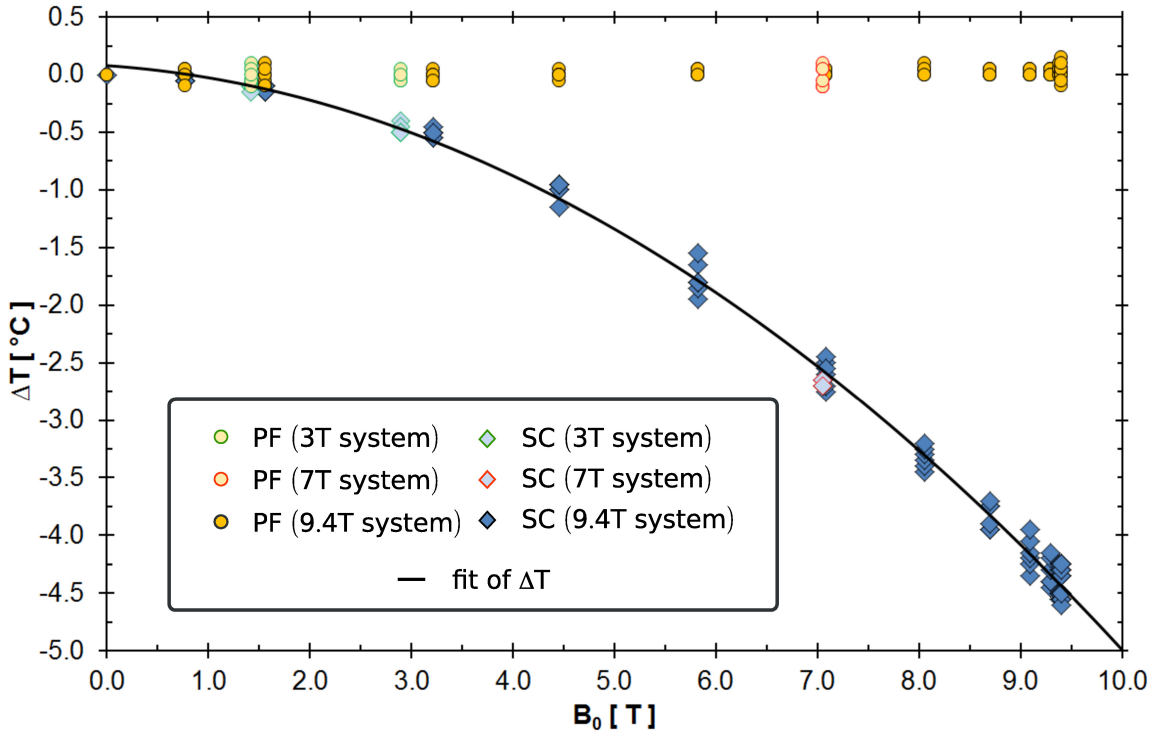

Figure 7.13: ΔT versus B_0 is depicted at all measured temperatures. Measurements which were performed at TRIO ($B_0 = 1.4\,\mathrm{T}$ and $B_0 = 2.9\,\mathrm{T}$; green marker borders) and at Bio Spec ($B_0 = 7\,\mathrm{T}$; red marker borders) are highlighted with pale yellow and pale blue colors for the PF-system and the SC-system, respectively. Errors on B_0 are within the marker size. (This figure was taken from the journal article Buchenberg *et al.* [163].)

The calibration of both systems was carried out at $B_0 \approx 0\,\mathrm{T}$ and at a temperature $T_{\mathrm{cal}} = 25.0°\mathrm{C}$. To investigate whether the calibration temperature affects the precision, an additional measurement was performed at 65.0 °C with calibration also performed at $T_{\mathrm{cal}} = 65.0°\mathrm{C}$.
Furthermore, to assess possible orientation effects, measurements with the fiber optical probes oriented perpendicular to B_0 (phantom rotated by 90°) were conducted at $B_0 = 3\,\mathrm{T}$ at three different temperatures $T = 25.0\,°\mathrm{C}$, 40 °C, and 65 °C. These measurements could only be performed at the 3 T whole-body MR system because of its sufficiently large bore size. For the comparison of results acquired with the probes oriented parallel and perpendicular to B_0, eight and four ΔT values were averaged, respectively.

7.2.3 Results

The dependence of ΔT on B_0 is depicted in Fig. 7.13 for all temperatures measured at the three different MR systems. Temperature measurements made with the PF probe and the SC probe agreed within $\pm 0.1°\mathrm{C}$ at $B_0 \approx 0\,\mathrm{T}$. ΔT values determined from the data of the PF probe varied within $0.2°\mathrm{C}$ for all B_0 values. This variation is within the measurement accuracy of the system. However, a systematic decrease of ΔT with increasing B_0 values was clearly observed for the data of the SC probe. A maximum deviation of $-4.6°\mathrm{C}$ at $B_0 = 9.4\,\mathrm{T}$ was determined (Tab. 7.1). The fit of the empirical Eq. (7.5) to quantify the

	ΔT [°C]	
T_{GT}	SC-system	PF-system
25.0	-4.6	-0.1
29.8	-4.6	0.0
39.5	-4.5	0.0
48.8	-4.3	0.2
58.4	-4.3	0.1
65.1	-4.3	0.0

Table 7.1: ΔTs obtained by the SC-system and PF-system at $B_0 = 9.4\,\mathrm{T}$ are listed. Additionally, the corresponding absolute temperatures of the glass thermometer T_{GT} are shown. (This table was taken from the journal article Buchenberg *et al.* [163].)

temperature shift of the SC probe data is represented by a black line in Fig. 7.13, and yielded the following parameters: $a = (-0.0447 \pm 0.0015)°\mathrm{C/T}^2$, $b = (-0.060 \pm 0.016)°\mathrm{C/T}$, $c = (0.08 \pm 0.03)°\mathrm{C}$, and $\mathrm{r}^2 = 0.9966$ (Goodness-of-Fit statistics). In addition, the mean values of $\Delta T \pm \mathrm{SD}_{\mathrm{mean},\Delta T}$ and standard deviations (SD) are listed in Tab. 7.2 for each single B_0 value to gain a better understanding on the measurement precision. The observed B_0 dependent temperature shift was independent of the MR system (see Fig. 7.13 pale yellow colored values with green borders at 1.4 T, 3 T, and with red borders at 7 T).
The measurements at $T_{\mathrm{cal}} = 25.0°\mathrm{C}$ and $T_{\mathrm{cal}} = 65.0°\mathrm{C}$ show that ΔT did not change for either of the fiber optical systems when they were recalibrated in the console room ($|\Delta T_{25°\mathrm{C}} - \Delta T_{65°\mathrm{C}}| \leq 0.2°\mathrm{C}$). Changing the alignment of the long axis of the flow phantom with respect to $\vec{B}_0$ from parallel to perpendicular (i.e. the orientation of the phosphorus or the semiconductor contained in the tip of the probes) also revealed no difference in the mean values of ΔT determined at the 3 T MR system (Tab. 7.3).
Fig. 3 compares temperature data of the glass thermometer measured in the console room with temperature data of both fiber-optical probes measured in the console room and additionally at 9.4 T. All data agrees well ($T_{\mathrm{SC-system}} \leq 0.2°\mathrm{C}$, $T_{\mathrm{PF-system}} \leq 0.7°\mathrm{C}$) except for the SC-probe measurements performed at the isocenter.

	SC-system		PF-system	
$\lvert\vec{B}_0\rvert$	$\overline{\Delta T} \pm \mathrm{SD}_{\mathrm{mean},\Delta T}$ [°C]	SD [°C]	$\overline{\Delta T} \pm \mathrm{SD}_{\mathrm{mean},\Delta T}$ [°C]	SD [°C]
1.42 [a]	-0.12±0.01	0.04	-0.02±0.02	0.07
2.89 [a]	-0.48±0.01	0.04	0.01±0.02	0.06
7.05 [b]	-2.68±0.01	0.03	-0.01±0.03	0.08
0.77	-0.036±0.009	0.02	0.01±0.02	0.06
1.56	-0.12±0.01	0.03	0.00±0.02	0.06
3.21	-0.51±0.01	0.03	-0.01±0.01	0.04
4.45	-0.99±0.03	0.07	0.00±0.01	0.03
5.83	-1.76±0.05	0.13	0.014±0.009	0.02
7.08	-2.58±0.04	0.11	0.014±0.009	0.02
8.05	-3.31±0.04	0.10	0.04±0.01	0.04
8.70	-3.81±0.05	0.12	0.014±0.009	0.02
9.09	-4.13±0.06	0.15	0.02±0.01	0.03
9.30	-4.29±0.05	0.13	0.02±0.01	0.03
9.38	-4.37±0.06	0.15	0.04±0.01	0.03
9.40 [c]	-4.39±0.05	0.13	0.014±0.009	0.02
9.40 [c]	-4.39±0.05	0.14	0.03±0.01	0.03
9.40	-4.40±0.06	0.15	0.03±0.03	0.09

[a] B_0 values of the 3 T MR system
[b] B_0 value of the 7 T MR system
[c] B_0 at distances of 4.8 cm and 9.8 cm from the isocenter of the 9.4 T MR system

Table 7.2: Measurements acquired at different temperatures and with different calibration temperatures were averaged for each individual B_0 value. The mean of ΔT and the standard deviation of the mean $\overline{\Delta T} \pm \mathrm{SD}_{\mathrm{mean},\Delta T}$ as well as the standard deviation (SD) are listed for each individual B_0 for both fiber optical systems (SC-system, PF-system). (This table was adapted from the journal article Buchenberg *et al.* [163].)

	$\overline{\Delta T}$ [°C]	
$\lvert\vec{B}_0\rvert = 3\,\mathrm{T}$	SC-system	PF-system
$\parallel$	-0.48±0.01	0.01±0.02
$\perp$	-0.44±0.03	0.00±0.02

Table 7.3: Orientation effect check for the SC-system and PF-system. The mean of ΔT and the standard deviation of the mean ($\overline{\Delta T} \pm \mathrm{SD}_{\mathrm{mean},\Delta T}$) are listed when the flow phantom was positioned parallel ($\parallel$) and perpendicular ($\perp$) to B_0 into the isocenter of TRIO. (This table was taken from the journal article Buchenberg *et al.* [163].)

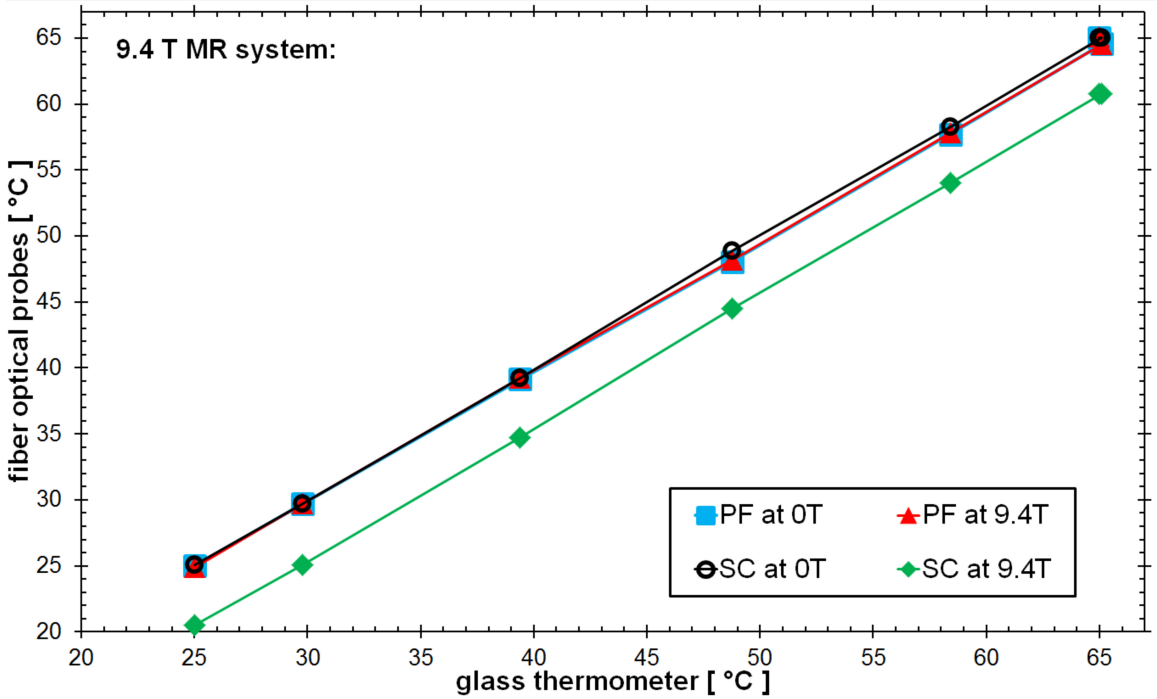

Figure 7.14: Temperature values of the glass thermometer acquired in the console room are drawn versus temperature values acquired with the two fiber optical probes in the console room ($B_0 \approx 0\,\mathrm{T}$) and at $B_0 = 9.4\,\mathrm{T}$. At $T = 65.0°\mathrm{C}$: measurements with $T_{\mathrm{cal}} = 25.0°\mathrm{C}$ and $T_{\mathrm{cal}} = 65.0°\mathrm{C}$ are both included, however, with this temperature scale not distinguishable. (This figure was taken from the journal article Buchenberg *et al.* [163].)

7.2.4 Discussion

The fiber optical systems investigated in this work are typically used to locally monitor absolute temperatures. These temperature measurements are taken as ground truth to validate MR thermometry acquisitions, to determine temperature coefficients or for MR safety studies in SAR measurements [188]. All of these applications require an accuracy better than $1°\mathrm{C}$. For example, in in vivo MR-guided thermal treatments the Sapareto thermal dose model [189] is used to control tissue damage. This model is very sensitive to small temperature changes, and thus requires a high precision of the temperature measurements. However, this work clearly demonstrated that the accuracy of the temperature measurements in magnetic fields critically dependents on the type of the fiber optical probe used. If the probe consists of a semiconductor and the connected fiber optical system is calibrated outside B_0, then, absolute temperature measurements performed inside B_0 will underestimate the actual temperature. This was partly described in earlier works [177, 178]. At 9.4 T mean temperature shifts of $-4.5°\mathrm{C}$ were measured by Roland *et al.* (see Tab.1 in reference [177]). On average $-4.4°\mathrm{C}$ (see Tab. 7.2) were determined in this work at the isocenter of the small animal MR imaging system ($B_0 = 9.4\,\mathrm{T}$). Both results show a very good agreement. In a 7 T whole-body system Groebner *et al.* [178] observed a decrease of $-2.6°\mathrm{C}$ which excellently agrees with the measurement results of this work, $-2.6°\mathrm{C}$ (measurements performed in the fringe field of the 9.4 T MR system, see Tab. 7.2) and $-2.7°\mathrm{C}$ (measurements performed at the small animal MR imaging system with $B_0 = 7.05\,\mathrm{T}$ at the

isocenter, see Tab. 7.2). This suggests that these measured temperature differences are not dependent on the MR system type and are purely related to the magnetic field strength.
The observed temperature shift is caused by an increase in the band gap of the semiconductor since the optical band gap width of GaAs increases with increasing magnetic field [190]. Aleshkin and Zakrevskiĭ [190] presented a theoretical description of the width of the band which is dependent on many parameters such as the polarization of the light or the direction of the light propagation with respect to $\vec{B}_0$, and those are unknown for the GaAs probe of the SC-system. Thus, an empirical model was introduced in this work to describe the relationship between B_0 and ΔT. It allows for retrospective correction of temperature data in the case that the system's calibration was carried out at a different B_0 than the actual temperature measurement. The correction applies for the specific temperature probe type examined in this work, however, it can also be done for other SC probes.
Interestingly, the temperature shift observed in measurements conducted with the GaAs probe was independent of the orientation of the probe with respect to $\vec{B}_0$. Orientation effects are known to exist for other semiconductor elements such as Metal-Oxide-Semiconductor Field Effect Transistors (MOSFET) since the induced Hall voltage in the inversion layers is dependent on the orientation of the magnetic field with respect to the drain current in MOS devices [191].
In summary, the PF-system allows precise field-strength-independent temperature measurements. A B_0 dependent temperature shift has to be considered during temperature measurements in magnetic fields for GaAs fiber optic probes. If it is accounted for, the SC-system allows also precise temperature measurements over a wide temperature range. The shift can be corrected either prospectively by calibrating the system at the desired B_0 or retrospectively using the empirical model determined in this work. Prospective correction was applied to the SC-system for the measurements presented in this work.

Part III

Case studies

Chapter 8

Counter-current double pipe heat exchanger

Details on heat exchangers were given in section 5.3. A case study with a counter-current double pipe heat exchanger will be laid out in this chapter which is partly based on the journal article Buchenberg *et al.* [133] as well as on the conference proceedings Buchenberg *et al.* [142, 143].

8.1 Methods

8.1.1 Flow model design

A double pipe heat exchanger was constructed based on the literature [141, 132] by the project partner. Further technical details can be found in his thesis [17]. Schematics of the corresponding CAD drawings provided by the project partner as well as a picture of the double pipe heat exchanger are depicted in Fig. 8.1.
To ensure MR compatibility of the flow model, results of experimental groundwork in this work (subsections 7.1.1, 7.1.2) as well as Schenck's review on susceptibility [34] were considered. The flow model was built of a copper pipe (outer diameter OD = 15 mm) inside a pipe made of acrylic glass (inner diameter ID = 50 mm, length of both pipes = 320 mm). Flow 2 refers to the flow inside the inner pipe, and flow 1 refers to the flow in the annulus between the inner pipe and outer pipe. The direction of the flows inside the flow model were chosen to be opposite (counter-current) to maximize heat transfer. The length axis of the flow phantom was oriented parallel to B_0. Fiber optical probes (in total four probes were available) can be inserted through the inlets to monitor the temperature of both flow circuits during the experiments.
Both pipes were fixed between a flow preparation system to achieve an undistorted inflow and an end nozzle. A wide-angle diffuser designed by the project partner after guidelines proposed by Mehta [192] expanded the flow from hose diameter to the settling chamber diameter. Internal grids induced a pressure loss to realize a steep opening angle of the diffuser and prevent unwanted flow separation from the walls. Flow 1 was further homogenized in the settling chamber which included an de-aeration hole for air removal. The connected nozzle accomplished three major tasks. It fixed both pipes, it accelerated flow 1 further reducing flow turbulence, and it comprises the outlet of flow 2 downstream

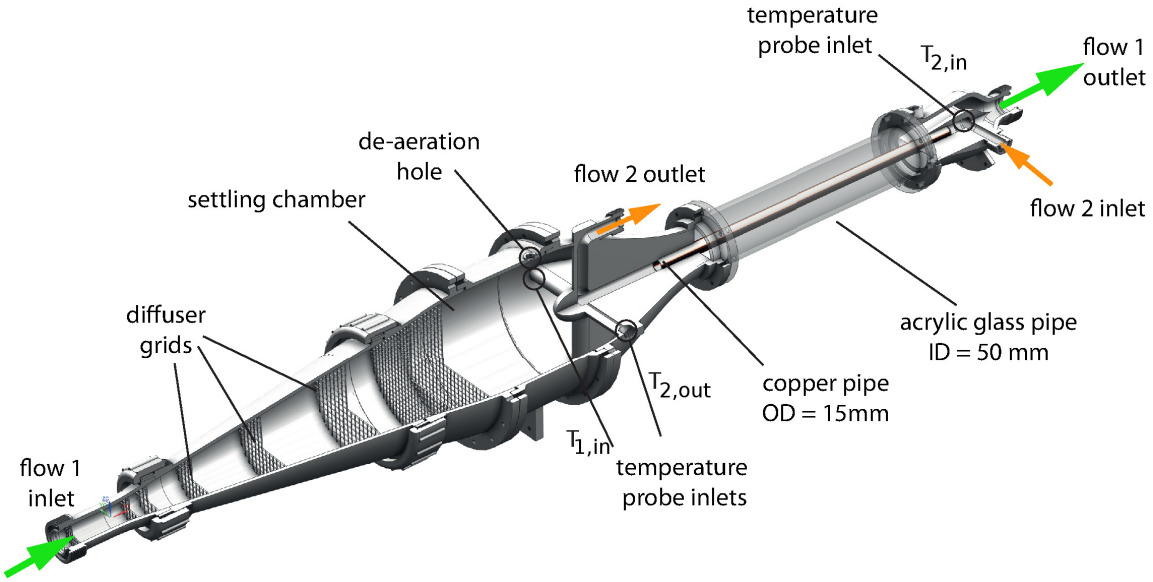

(a) Cross-sectional cut through the 3D CAD drawing

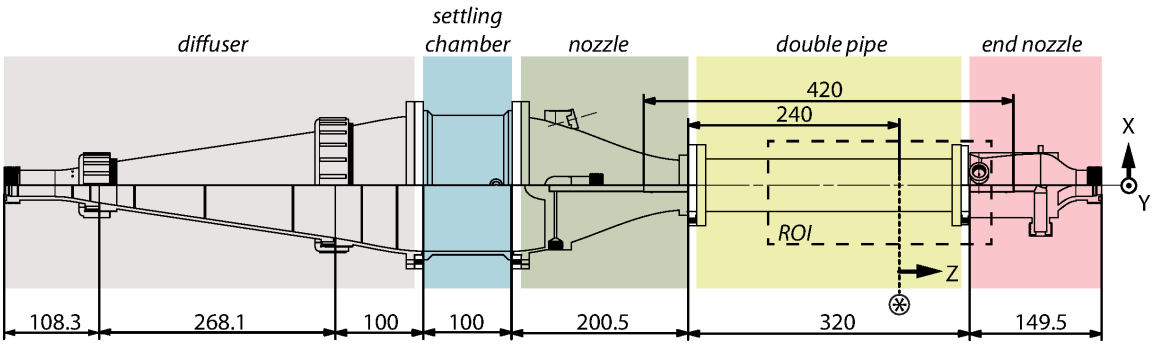

(b) Top view schematics of the flow model with the top half of the schematic depicting the outside of the model, and the bottom half depicting a cut through the model

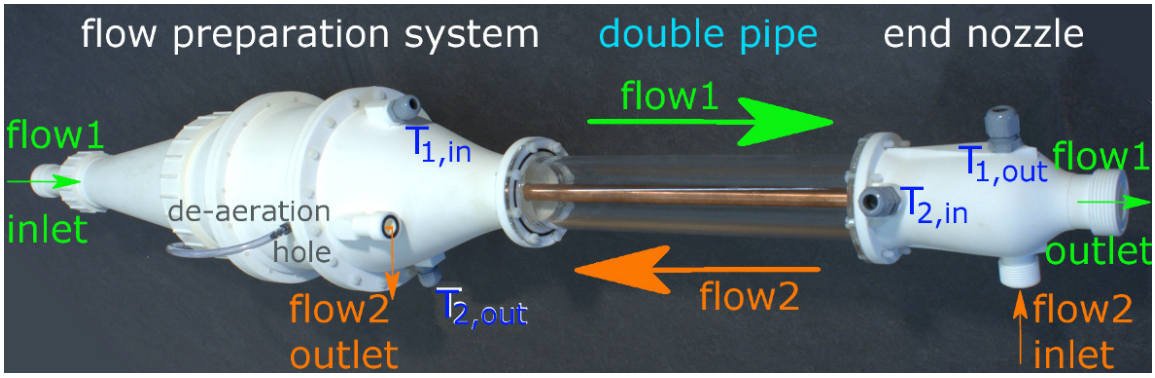

(c) Picture showing the main parts and features of the flow model

Figure 8.1: Various views of the counter current double pipe heat exchanger are depicted. Fiber optical probes were inserted into the inlets to measure the temperature of flow 1 ($T_{1,\mathrm{in}}$) as well as the inflow and outflow temperatures of flow 2 ($T_{2,\mathrm{in}}$, $T_{2,\mathrm{out}}$). The remaining fourth probe was used to monitor the temperature of the insulated reference phantom (not shown here). The different components and its dimensions (in units of mm) are presented. The axes of the coordinate system are depicted. The Z axes is aligned with B_0 and with the direction of flow 1. Flow 2 flows in opposed direction corresponding to negative Z direction. Figs. 8.1a, 8.1b were adapted from the journal article Buchenberg *et al.* [133].

MR imaging parameters	MRV	MRT
TE/TR [ms]	11.5/15.5	20.0/29.1
flip angle [°]	7	7
pixel bandwidth [Hz/pixel]	455	120
spatial resolution [mm^3]	$1.1 \times 1.1 \times 1.1$	$1.1 \times 1.1 \times 1.1$
Phase encoding (PE) lines/slices	280/64 (or: 270/72)	280/64 (or: 270/72)
Read out direction	Z	Z
In plane PE direction	X	X
Slice PE direction	Y	Y
v_{enc} [m/s]	0.05	—

Table 8.1: MR sequence parameters used for 3D MRV and 3D MRT acquisitions of the double pipe heat exchanger. MRT measurements were performed with velocity compensation. The number of phase encodings and slices was dependent on the location of the FOV and the position of the reference phantoms. The total acquisition times of an MRV measurement and an MRT measurement were 15 to 20 minutes and 8 to 9 minutes, respectively.

of the copper pipe. Upstream of the copper pipe the end nozzle provided the outlet of flow 1, the inlet of flow 2, and temperature probe inlets. The flow preparation system and the end nozzle were made of polyamide (PA) using direct laser-sintering. The components were connected via PolyVinyl Chloride (PVC) screws. O-rings were incorporated to avoid water leakage.

8.1.2 Experiments

All experiments were performed with the double pipe model connected to the flow apparatus described in subsection 7.1.3.
Firstly, PRF temperature data was acquired using model 1 (see pp. 69 ff.) and the sequence described in 6.1. The flow rate of flow 1 was held constant during the MR acquisitions, once at 5 l/min and once at 10 l/min. The flow rate of flow 2 was according to the maximum possible supply provided by the two Julabo systems (see section 7.1.3 for more details about the Julabo systems).
3D imaging volumes were acquired with TR/TE=24.9/16 ms, flip angle = 7°, pixel bandwidth = 120 Hz/pixel, spatial resolution = 1.2 mm isotropic, phase encoding (PE) lines = 96, and slices=120. The imaging was performed with both flow circuits at room temperature of 21 °C (heat off, T^{off}) and with $T_{\text{flow 1}} = 21\,^{\circ}\text{C}$, $T_{\text{flow 2}} = 50\,^{\circ}\text{C}$ (heat on, T^{on}). Local reference temperatures within model 1 were acquired during the MR data acquisitions using fiber optical probes positioned through inlets as indicated in Fig. 7.5b. The local temperature change ΔT_{loc} of the probes is defined as $\Delta T_{\text{loc}} = T^{\text{on}}_{\text{loc}} - T^{\text{off}}_{\text{loc}}$.
MRT data evaluation was conducted as described in the subsection 6.2, however, using precombined dicom phase data. Temperature results obtained with this kind of data can suffer from spatially dependent noise enhancement (see subsection 6.2).
Secondly, MRV and MRT were performed using model 2 (see pp. 69 ff.) and the sequence described in 6.1. Imaging parameters for these measurements are summarized in Tab. 8.1. PRF temperature phase mapping was conducted with three different pairs of acquisitions

with different temperatures for flow 1 ($T_{\text{flow 1}}$) and flow 2 ($T_{\text{flow 2}}$).

1. Homogeneous spatial temperature distribution i.e., $T_{\text{flow 1}} = T_{\text{flow 2}}$. A reference acquisition with flow 1 and flow 2 both at room temperature (21 °C) and an acquisition with flow 1 and 2 both at a higher temperature (31 °C) were performed. Flow 2 was provided by the HC-pump (see section 7.1.3).

2. Inhomogeneous spatial temperature distribution i.e., $T_{\text{flow 1}} < T_{\text{flow 2}}$. A reference acquisition with flow 1 and flow 2 both at room temperature (21 °C) and an acquisition with flow 1 at a lower temperature than flow 2 ($T_{\text{flow 1}} = 21\,°\text{C}$, $T_{\text{flow 2}} = 50\,°\text{C}$) were performed. Flow 2 was provided by the HC-pump during the reference acquisition. Meanwhile, water at a high temperature was prepared and maintained by the immersion heater. After the reference acquisition was finished the HC-pump was removed and replaced by the immersion heater. This approach allowed the two acquisitions to be performed as closely together in time as possible. It was of particular importance here, because the prolonged use of water at 50 °C generated air bubbles on the surface of the copper pipe.

3. Inhomogeneous spatial temperature distribution i.e., $T_{\text{flow 1}} > T_{\text{flow 2}}$. A reference acquisition with flow 1 and 2 both at the same temperature (31°C) and an acquisition with flow 1 at a higher temperature than flow 2 ($T_{\text{flow 1}} = 31\,°\text{C}$, $T_{\text{flow 2}} = 9\,°\text{C}$) were performed. Flow 2 was provided by the immersion heater during the reference acquisition. Meanwhile, water at a low temperature was prepared and maintained by the HC-pump. After the reference acquisition was finished the immersion heater was removed and replaced by the HC-pump.

Homogeneous spatial temperature distributions (first pair of acquisitions) can be used to show that the applied PRF temperature phase mapping method is able to accurately and precisely measure temperature changes in fluid flows. The second and third pairs of acquisitions (cases with $T_{\text{flow 1}} < T_{\text{flow 2}}$ and $T_{\text{flow 1}} > T_{\text{flow 2}}$, respectively) were performed to demonstrate that the applied PRF temperature phase mapping method is capable of measuring spatially inhomogeneous 3D temperature distributions in fluid flows. The 3D temperature distributions are assumed to remain constant during the MR data acquisition.

The flow rate for flow 1 was held constant at 5 l/min, whereas, the flow rate for flow 2 was according to the maximum possible supply provided by the two Julabo systems during all MR acquisitions (see section 7.1.3 for more details about the Julabo systems). Fiber optical probes were positioned into the inlets to measure $T_{1,\text{in}}$, $T_{2,\text{in}}$ and $T_{2,\text{out}}$ as well as into one of the reference phantoms (see Figs. 7.11 and 8.1). The thermally insulated reference phantoms (cylindric bottles with ID = 6 cm; filled with distilled water, 5% hydroxyethylcellulose, and 1 g/l CuSO4; insulation: polystyrene casings) were placed with their long axis parallel to B_0 to the left and right of the double pipe.

MR velocity mapping was performed using a pair of acquisitions, once without any fluid flows (reference scan) and once with the two flows at temperatures $T_{\text{flow 1}} = 21\,°\text{C}$ and $T_{\text{flow 2}} = 50\,°\text{C}$. The reference scan was used to correct for eddy currents in the flow measurement.

The evaluation of MRV and MRT data was conducted as described in subsection 6.2.

8.1.3 Comparative studies

External temperature sensors incorporated into the flow model are typically used to provide reference temperatures which are compared to PRF temperature data. Separate experiments were conducted outside the MR system to pointwise map the temperature distribution in two dimensions (2D). During these experiments the applied flow rates and fluid temperatures were the same as during the MR acquisition with $T_{\text{flow }1} = 21\,^{\circ}\text{C}$, and $T_{\text{flow }2} = 50\,^{\circ}\text{C}$.
Two different types of temperature sensors, a fiber optical probe and a thermocouple (TC), were used. The major difference between the sensors was that the TC could be bent into an L-shape. Therefore, the TC could enter flow 1 radially further upstream than the actual region of interest (indicated by a circled asterisk in Fig. 8.1b) was located, and its distal part (including the tip) could be aligned with the main flow direction. Such alignments can minimize possible distortions of the flow caused by the external sensor.

Measurements with the fiber optical probe were performed with model 1 (see subsection 7.1.1, fiber optical probe inlets) because it provided an inlet at the position marked with a circled asterisk in Fig. 8.1b. The probe (FOP$*$) was fed through a steel cannula preventing it from bending once it was inserted into flow 1. The position of the probe tip could be adjusted radially by moving the probe into or out of the inlet, and circumferentially by rotating the acrylic glass pipe, thus a 2D temperature map was obtained point-wise. A pause between probe adjustment and data acquisition was kept, so that the flow and temperature field could settle to stable conditions. Additional probes were positioned through the inlets $T_{1,\text{in}}$ and $\text{T}_{2,\text{in}}$. Temperature data was sampled for approximately 60 s (sampling rate: $\sim 150\,\text{ms}$) at each grid point (15 angular positions and $4-5$ radial positions) and averaged during post processing. The temperature differences ΔT were determined between $T_{1,\text{in}}$ and $\text{T}_{\text{FOP}*}$. Only data in the upper left quarter of the pipe was collected in this experiment because of symmetry properties of the double pipe.

Measurements with the TCs were performed with Type T TCs (copper-constantan junction, Temperatur Messelemente Hettstedt GmbH, Maintal, Germany) with a sheath diameter of 1 mm and a sheath length of 100 mm. The TCs were connected to a NI-SCC-TC02 module (National Instruments, Austin, Texas, USA) which comprises a built-in thermistor for cold-junction-compensation with an accuracy of ± 0.4 °C. The TC02 module was plugged into a carrier module NI-SC-2345, which was connected to a PXI-1031 DC system (embedded controller card NI PXI-8106). The temperature data was monitored and logged by a LabVIEW program. TCs were fed through the inlets $\text{T}_{1,\text{in}}$, $\text{T}_{2,\text{in}}$, and $\text{T}_{2,\text{out}}$. An elongated hole in the acrylic glass pipe located further upstream with respect to flow 1 and with respect to the location marked with a circled asterisk in Fig. 8.1b allowed to insert the L-shaped TC (TC$*$). TC$*$ entered the pipe radially before bending 90° so that the tip faced into the flow at the Z-position marked with a circled asterisk in Fig. 8.1b. Thus, the flow of flow 1 was not substantially distorted by the sensor. Temperature distributions were mapped pointwise at a radial position R of the TC$*$ head (adjustable moving the TC$*$ into or out of the inlet) and corresponding circumferential position Φ (adjustable by rotating the acrylic glass pipe). One set of data was acquired at $\Phi = 0^{\circ}$ and moving the TC$*$ radially in steps of 1 mm covering the range of 8 mm $\leq \text{R} \leq$ 23 mm. This kind of measurement was performed in total twice. Another measurement was conducted at R = 20 mm adjusting different angular positions in the range of -60° $\leq \Phi \leq$ 60° by circumferentially rotating the acrylic glass pipe in steps of 5°. Each pointwise temperature measurement was sampled

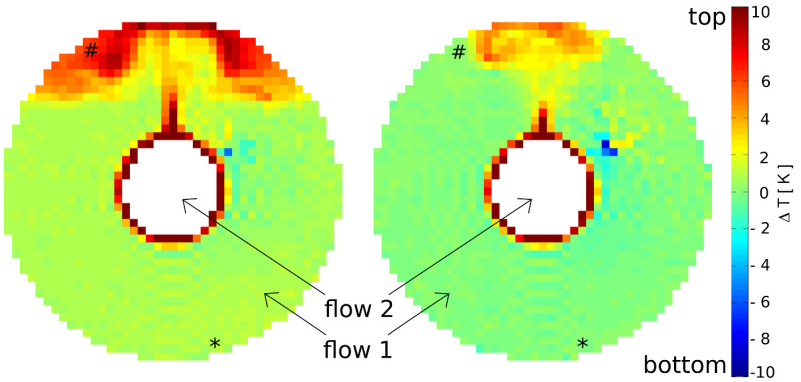

(a) $\overline{\Delta T}$ maps

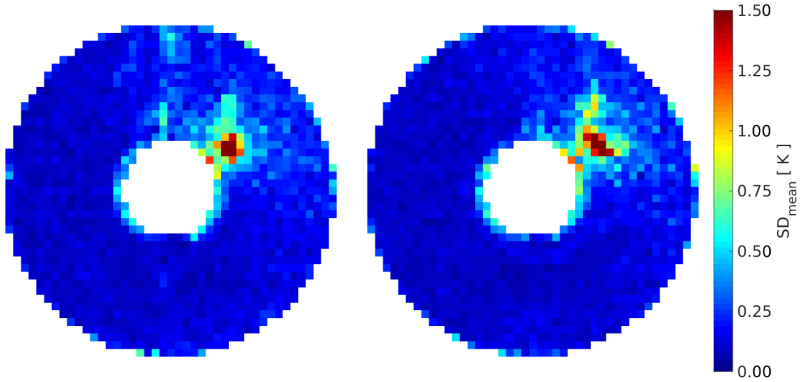

(b) Temperature uncertainty maps

Figure 8.2: Cross-sectional views of averaged PRF ΔT maps ($\overline{\Delta T}$ maps) and maps of the standard deviation of the mean are presented for flow 1 = 5 l/min (left row) and flow 1 = 10 l/min (right row). The experiments were performed with model 1. (Fig. 8.2a was adapted from the conference proceeding Buchenberg *et al.* [142].)

for approximately 60 s (sampling rate: $\sim$ 10 Hz). The values were averaged during post processing. Temperature differences were determined analogue to the experiment with FOP$*$.

8.2 Results

Fig. 8.2a shows cross-sectional views or transverse views (equal to X-Y planes) of PRF temperature phase maps (PRF ΔT maps) acquired with model 1. Ten transverse slices were averaged (the heat distribution was assumed constant over this distance). The first slice used for calculating the averaged maps was approximately 2 cm further upstream in flow 1 than the FOP inlets since these inlets disturbed the PRF ΔT maps (see pp. 69 ff.). Clearly visible is a temperature increase at the upper part of the outer pipe for both flow rates. However, the spatial temperature distribution depends strongly on the flow rate. Lower temperatures are seen if the flow rate is doubled as the induced heat is carried away more efficiently. In the major part of the cross section no temperature increase occurs. As depicted in Fig. 8.2b, the standard deviation of the mean is smaller than 0.4 K for the

	$\overline{\Delta T_{\mathrm{loc}}}$ [K]	
	flow 1 = 5 l/min	flow 1 = 10 l/min
FOP at #	6.5±0.3	0.3±0.3
FOP at $*$	-0.2±0.3	-0.1±0.3
MRI at #	6.35±0.15	0.22±0.07
MRI at $*$	0.92±0.13	0.02±0.08

Table 8.2: The temperature change measured at two locations in flow 1 (approximate position within the slice depicted by # and $*$ in Fig. 8.2a) simultaneously by the fiber optical probes and MRT (4 voxel average) are listed. Mean values at these positions ($\overline{\Delta T_{\mathrm{loc}}}$) and the corresponding standard deviations of the mean are presented. The experiments were performed with model 1. (This table 8.2 was taken from the conference proceeding Buchenberg *et al.* [142].)

vast majority of the voxels. An area with substantial higher uncertainty values is observed in the upper right quadrant. An exchange of the copper pipe and new assembling of the setup did not resolve this issue. Hence, this local increase of temperature uncertainties is most likely cased by the noise issue which can occur if precombined dicom phase data is used for the evaluation of temperature data (see subsection 6.2).
The temperature change measured by the FOPs at two locations in flow 1 (approximate position of the probe's tip within the slice is depicted by # and $*$ in Fig. 8.2a) and the average values from an ROI (consisting of 4 voxels) in the MRT data at these positions were determined and are listed in Tab. 8.2.
Cross-sectional views of PRF ΔT maps along the double pipe are presented in Figure 8.3 for all three cases studied with model 2. For the first case (considering $T_{\text{flow 1}} = T_{\text{flow 2}}$), a homogeneous distribution of ΔT inside flow 1 is clearly visible in Fig. 8.3a. The ΔT value determined from the fiber optical probe measurements (data logged during MR acquisitions) was $\Delta T_{FOP} = 9.9 \pm 0.2\,\mathrm{K}$. To estimate the uncertainty of the MR measurement the root mean square deviation (rmsd) between ΔT_{FOP} and ΔT of the MRT map was determined according to

$$\mathrm{rmsd} = \sqrt{\frac{\sum_{i=1}^{n}(\Delta T_{MRT,i} - \Delta T_{FOP})^2}{n}} = 0.5\ \mathrm{K}. \tag{8.1}$$

$\Delta T_{MRT,i}$ represents the temperature measured by MRT in the ith voxel, and n equals the total number of voxels measured with MRT within flow 1.
Fig. 8.3b shows ΔT distributions for the second case considering $T_{\text{flow 1}} < T_{\text{flow 2}}$. A vertical thin stripe of hot fluid appears above the copper pipe in these cross-sectional views. This structure is known as plume in literature [136, 141]. The hot fluid develops axis-symmetric pairs of hot spots as a kind of double lobe in the vicinity of the upper edge of the acrylic glass pipe since the acrylic glass pipe acts as a barrier. Starting at the left lower corner towards the upper right corner in Fig. 8.3b the hot spots move outwards as the fluid in the annulus is flowing along the hot copper tube.

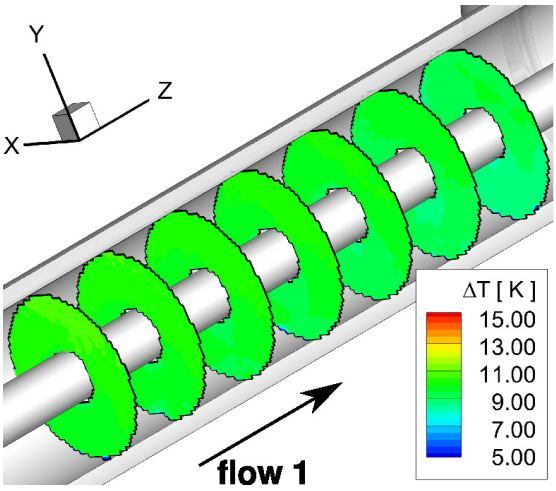

(a) $T_{\text{flow 1}} = T_{\text{flow 2}}$

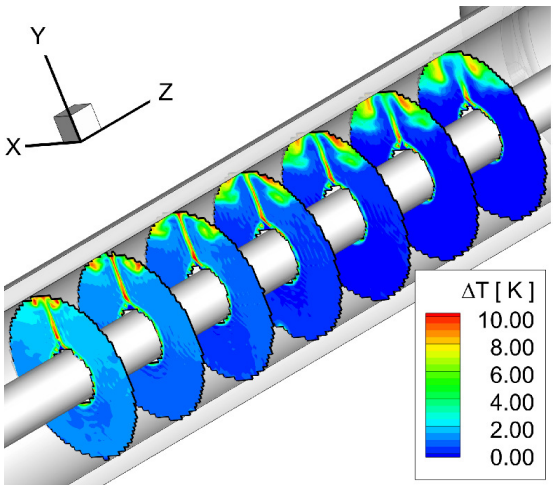

(b) $T_{\text{flow 1}} < T_{\text{flow 2}}$

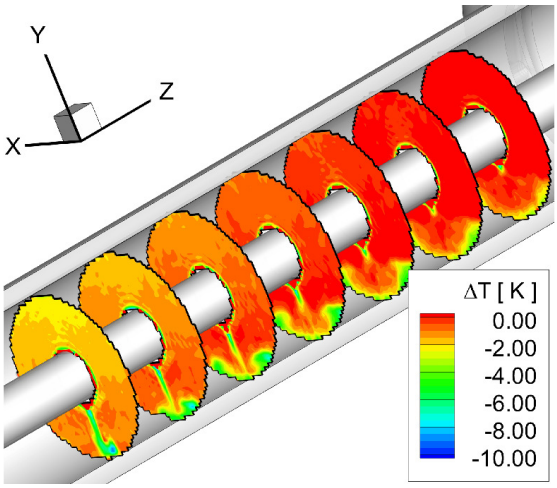

(c) $T_{\text{flow 1}} > T_{\text{flow 2}}$

Figure 8.3: PRF ΔT maps (transverse views) along the double pipe are presented for the three different cases studied. The first and last slice shown are separated by a distance equal to 150 mm. The experiments were performed with model 2. Note, distinct color scales are used for each individual figure. For orientation purposes the coordinate axes are shown. (Figures were adapted from the journal article Buchenberg *et al.* [133]. Visualization was performed together with the project partner using TecPlot software tools.)

The corresponding dimensionless numbers of the heated acquisition describing fluid mechanical as well as thermodynamical settings were determined by the project partner and are given as follows: Reynolds number = 1800, Rayleigh number = $1.9 \cdot 10^7$ and Richardson number = 0.85.

In Fig. 8.3c the ΔT distribution of the third case (considering $T_{\text{flow 1}} > T_{\text{flow 2}}$) appears mirrored compared to the second case (Fig. 8.3b). Similar characteristic structures are observable within flow 1 such as a plume and double lobes formed by cold fluid in this case. The extent of the lobes is slightly reduced compared to Fig. 8.3b. Note, the temperature

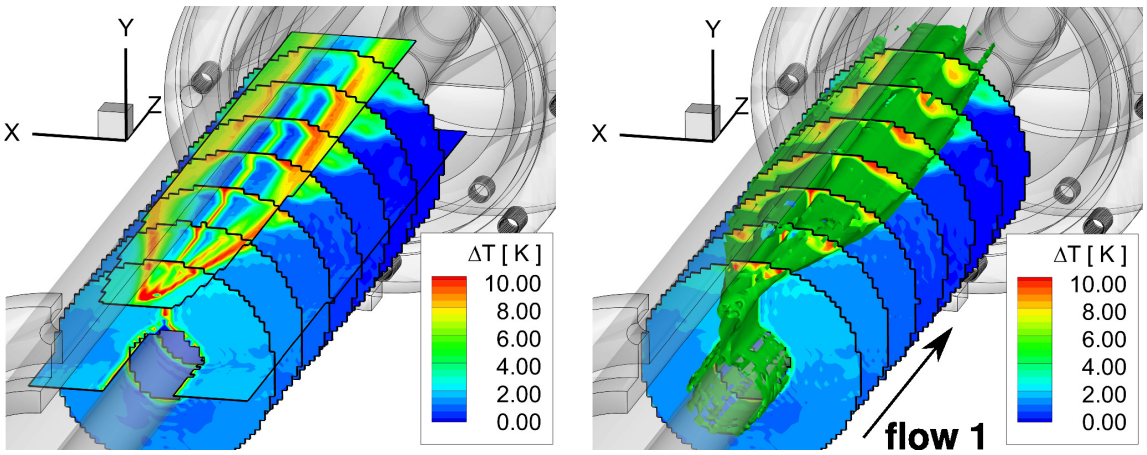

(a) Coronal view superimposed onto transverse views.

(b) Iso-temperature surface (dark green structure) shows the spatial distribution of ΔT = 5 K.

Figure 8.4: Further visualizations of PRF ΔT data indicate the 3D nature of the temperature and velocity fields for the second case (considering $T_{\text{flow 1}} < T_{\text{flow 2}}$). The experiments were performed with model 2. For orientation purposes the coordinate axes are shown. (Figures were adapted from the journal article Buchenberg *et al.* [133]. Visualization was performed together with the project partner using TecPlot software tools.)

difference between flow 1 and flow 2 was 22 K for the third case ($T_{\text{flow 1}} > T_{\text{flow 2}}$) and 29 K for the second case ($T_{\text{flow 1}} < T_{\text{flow 2}}$).
In all PRF ΔT maps (Figs. 8.3a, 8.3b, 8.3c) a small temperature gradient of approximately 1 K over the FOV along the Z axis is present. This temperature gradient cannot be explained by heat transfer from the surroundings or from flow 2, and thus, are expected to be artifacts arising from uncorrected higher order field drifts.
Since a 3D volume was covered by the measurement a variety of data visualization options are applicable to assess features of the temperature distribution and analyze them. For the second case a coronal view (equal to X-Z plane) and an iso-temperature surface with ΔT = 5 K superimposed onto the transverse slices are presented in Fig. 8.4. The location and extent of the plume as well as the formation and enlargement of the double lobes as the fluid passes along the hot copper pipe are clearly depicted.
Comparisons between data of the pointwise fiber optical probe measurement and the corresponding PRF thermometry data is shown in Figure 8.5. The structure of the side lobe is clearly depicted showing similar extensions in both measurements. ΔT values within the lobe are higher in the MR data than in the probe data and an additional hot spot at coordinate location (0.0,23.5) is visible only in the probe data.
The thermocouples can be introduced to the flow without substantially disturbing it. This allows a more quantitative comparison with the MR data to be performed. Comparisons between the pointwise measured TC data and the corresponding PRF data are shown in Figure 8.6. On the left of Fig. 8.6a and of Fig. 8.6b, a transverse view of the PRF ΔT map is presented. This slice corresponds to the Z-position marked by the symbol ⊛ in Fig. 8.1b.
In Fig. 8.6a (right chart), TC data measured at a fixed angle of zero and various radial positions is shown. The mean and standard deviation of the two separate TC measurements are depicted with grey and black circles and error bars, respectively. With respect to the

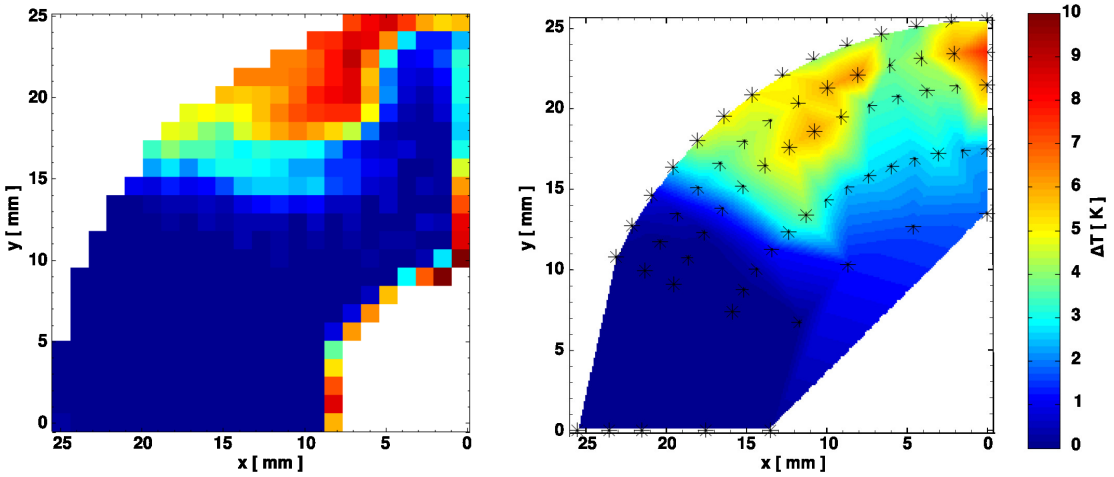

(a) PRF ΔT map **(b)** FOP data

Figure 8.5: Upper left quarter of ΔT maps (transverse views) are shown measured pointwise with a fiber optical probe and with MRT for the second case (considering $T_{\text{flow 1}} < T_{\text{flow 2}}$). The black stars depict the position of the tip of the FOP. Temperature values of the fiber optical probe were interpolated to depict the shape of the temperature distribution.

spatial resolution of the MR data, the zero angle data of the PRF temperature map can be related to either one of the two voxel columns indicated by purple triangles and lilac diamonds. Therefore, MR data of both columns is considered in the comparative study. Two sets of data, one MR data set and one TC data set, are found which match quite well. Similar curve progressions are observed between the MRT data in the left column (purple triangles) and the TC data of the second measurement as well as between the MRT data in the right column (lilac diamonds) and the TC data of the first measurement.
In Fig. 8.6b (right chart), TC data measured at a fixed radius of 20.0 mm and various angular positions is shown. Mean and standard deviation of the data are depicted with black circles and error bars, respectively. A characteristic w-shape is clearly captured with both temperature measurement techniques. The PRF data set which corresponds to a radius between 19.0 mm and 20.0 mm (lilac diamonds) is similar to the TC data. The PRF data set corresponding to a radius between 20.0 mm and 21.0 mm (purple triangles), however, shows higher values in particular in the side lobes ($\Phi \approx -25°$ and $+25°$). Both temperature measurement techniques detect a similar width of the w-shape and ΔT values of 0 K at angles of approximately $-55°$ as well as $+60°$. Furthermore, both techniques resolve a kink in the temperature curve of the right lobe at $\Phi \approx +35°$. Overall, the thermocouple measurements are not perfectly symmetric about $0°$. This could be related to positioning errors of the TC since MRV data showed a symmetric inlet flow (see streamwise velocity presented in Fig. 8.7 and in the thesis of the project partner [17]).
For all experiments, the temperature increase in the reference phantoms was within the accuracy of the fiber optical system and hence negligible.
Fig. 8.8a shows superpositions of PRF temperature distributions and velocity vector fields occurring inside a counter-current double pipe heat exchanger for the second case (considering $T_{\text{flow 1}} < T_{\text{flow 2}}$). The heated fluid raises to the top of the outer pipe in a localized thin structure and moves outwards at the top forming side lobes which are warmer than

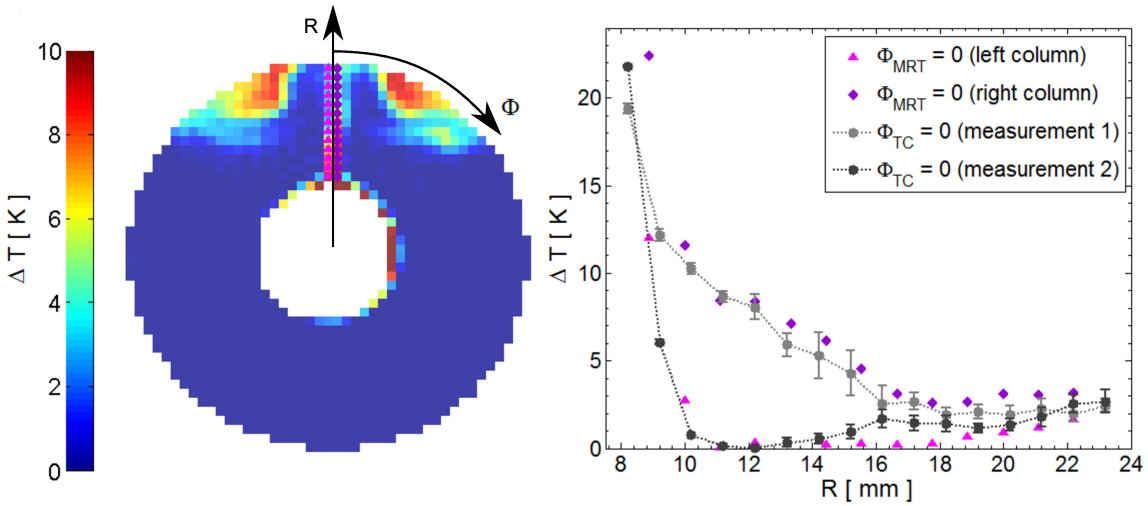

(a) Zero angle data of the PRF ΔT map is highlighted with purple triangles and lilac diamonds (left image). This MR data and the zero angle TC data (gray and black circles) from two separate measurements are depicted on the right.

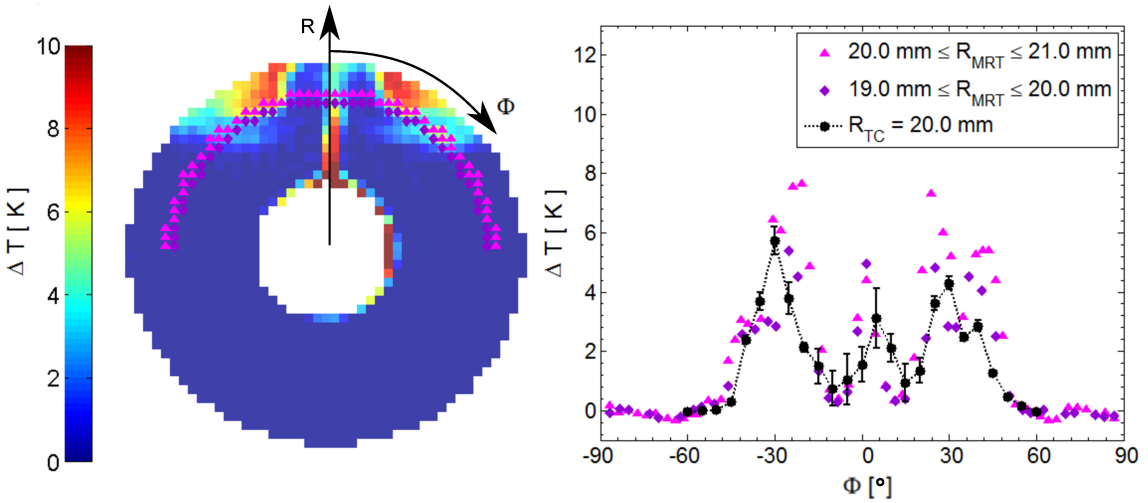

(b) PRF ΔT data corresponding to a radius $\mathrm{R_{MRT}}$ between 19.0 and 20.0 mm is highlighted with lilac diamonds. PRF ΔT data corresponding to a radius $\mathrm{R_{MRT}}$ between 20.0 and 21.0 mm is highlighted with purple triangles (left image). This MR data and the corresponding TC data (black circles) is depicted on the right.

Figure 8.6: PRF ΔT maps (transverse views) are shown on the left side for the second case (considering $T_{\mathrm{flow\ 1}} < T_{\mathrm{flow\ 2}}$). TC measurements performed at the same Z-position as the MR acquisition are presented on the right column together with the MR data voxel values highlighted with purple triangles and lilac diamonds in the PRF ΔT maps (left column). The mean and standard deviation of the TC data is presented. Dashed lines are added to aid visualization. (Figures were adapted from the journal article Buchenberg *et al.* [133].)

the surroundings. The velocity field clearly represents the natural convection flow due to the temperature increase within the fluid.
Besides the vector representation common approaches to visualize flow are based on tools called streamlines and pathlines. At one instant of time the velocity vectors are the tangent

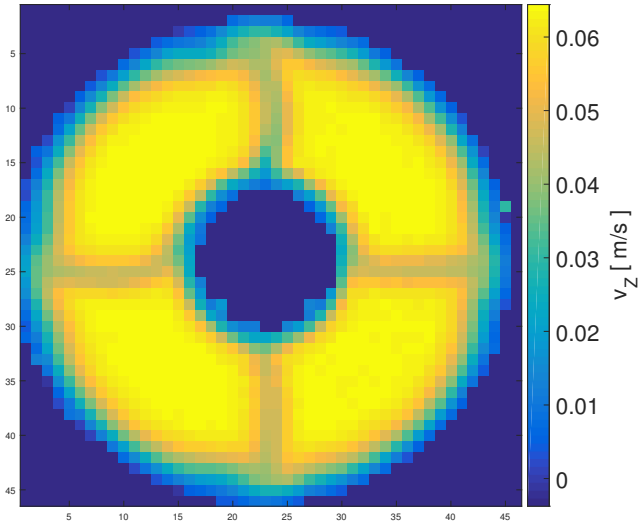

Figure 8.7: Velocity component v_Z of the inlet flow. The four quadrants are caused by struts built into the nozzle. Further details on the construction of the nozzle as well as on the components of the velocity field further upstream in flow 1 can be found in the thesis of the project partner [17].

vectors of every spatial point along a streamline [32]. The trace of a particle detected by a cloud chamber is an example for a pathline (time exposure of particles). Streamlines and pathlines represent the same curves for a steady flow e.g. present in the double pipe heat exchanger.
In Fig. 8.8b streamlines are depicted on top of the PRF temperature views. They start at the locations marked by an X and O. The distance between the bullets represents the velocity magnitude, and the color of the bullets represents ΔT. In areas with $\Delta T = 0\,\mathrm{K}$ only forced convection is present (represented by equally spaced bullets). Meanwhile in areas with $\Delta T > 0\,\mathrm{K}$ the particle follows a 3D trajectory. Its temperature and speed increase at the beginning (wider spaced bullets), and its speed is slower in the side lobe of the plume (densely packed bullets). The location of the particle remains similar as the forced convection exceeds the natural convection.

8.3 Discussion

This case study presents an MR compatible experimental setup which arose from a close collaboration between the project partner (responsible for the fluid mechanical and engineering contributions) and the author of this thesis covering the development of suitable MRI techniques. The setup provided a stable 3D temperature distribution within the fluid flow. It allowed a measurement of 3D velocity fields and 3D temperature fields within the fluid flow using phase contrast MRI methods. Since velocity as well as temperature were determined from the same parameter ,i.e. the phase of the MR images, it is essential to differentiate the individual contributions to the imaging phase in order to obtain accurate results. In this work, MRI methods were adjusted and established to meet this requirement providing accurate and precise measurements of both velocity and temperature fields in fluid flows.

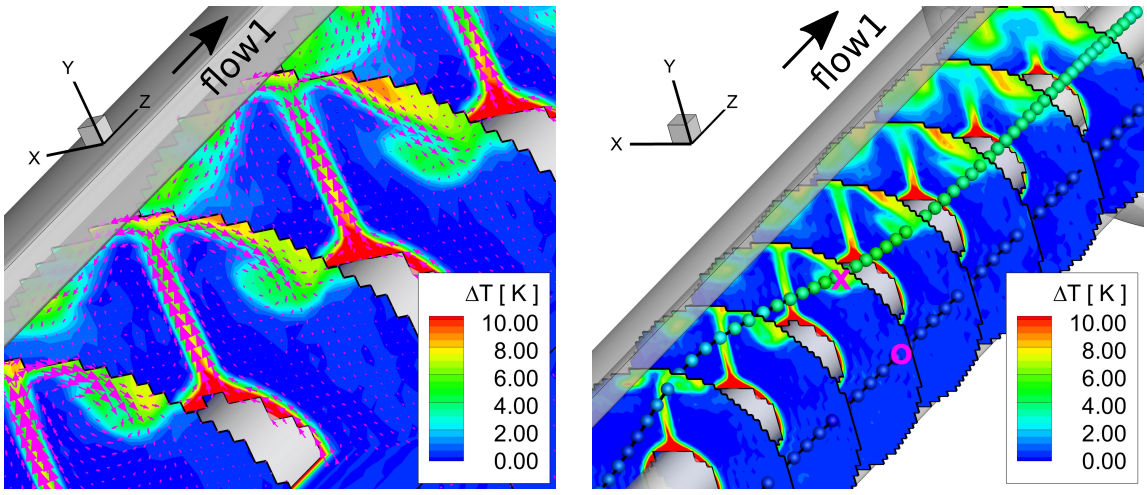

(a) PRF ΔT maps and velocity vector fields

(b) PRF ΔT maps and streamlines originating from the locations X and O

Figure 8.8: PRF ΔT maps, velocity vector fields and velocity streamlines are depicted for the second case (considering $T_{\text{flow 1}} < T_{\text{flow 2}}$). The distance between the different cross-sectional views is equal to 30 mm. The experiments were performed with model 2. (Figures were adapted from the conference proceeding Buchenberg *et al.* [143]. Visualization was performed by the project partner using TecPlot software tools.)

The flow model investigated in this case study was a counter-current double pipe heat exchanger. It was composed of two long concentric cylinders connected to separate flow circuits which could be supplied with different temperatures. The superposition of 3D temperature and velocity fields as illustrated in Fig. 8.8 depict the complexity of their interplay. The ability to quantitatively assess 3D distributions of temperature as well as velocity lays the foundation to open up a variety of applications and prospects for engineering communities (i.e. fluid mechanics community), for the medical physics community and many other fields of science.
A qualitative and quantitative comparison between the MRV data and the LDV data acquired in a separate measurement session revealed a good agreement (see thesis of the project partner [17], subsection 5.3.2.6 for details). LDV is a gold standard technique to determine velocities in fluid flows.
However, for the temperature acquisitions a full quantitative validation could not be achieved due to the difficulty of measuring 3D temperature distributions noninvasively in fluid flows with a different method than MRI. Thus, temperature sensors had to be inserted into the flow for pointwise mapping with the possibility of changing the flow distribution. A fiber optical probe and a thermocouple were incorporated into the flow in two different ways. In contrast to the fiber optical probe, the thermocouple could be introduced without substantially disturbing the flow, and thus a more quantitative comparison with the MR data could be performed.
Locally observed deviations of up to several Kelvin between ΔT determined once via fiber optical probes and once with MRT was assumed to arise mainly from local distortions of the flow due to the probe placement (i.e., FOP entered flow 1 perpendicular to the flow direction). In particular the subtle structure of the plume and the distributions of the heat

within the side lobes might be affected. Nevertheless, the extent of the pointwise mapped side lobe was qualitatively captured by the fiber optical probes.
The main issue with the thermocouple measurements was that their co-registration with the corresponding MR data was difficult. The tip of the thermocouple was positioned by adjusting its position radially and circumferential at the edge of the acrylic pipe. The accuracy of this positioning was approximately ± 0.5 mm radially and $\pm 1^\circ$ circumferentially. Furthermore, it was possible that the thermocouple twisted slightly such that its bent portion was not exactly aligned parallel to the Z-axis after it had been positioned. This lead to additional uncertainty in the position of the tip of the thermocouple. The area of the tip ($\sim 1\ \mathrm{mm}^2$) was comparable to the spatial resolution of the PRF temperature phase maps. Nonetheless, it was difficult to perform a quantitative comparison between individual voxels of the MRT data and individual points measured by the thermocouple since the fine features of the temperature distribution were similar in size to the positioning accuracy of the thermocouples and the resolution of the MRT maps.

Overall, temperature data measured with a thermocouple and by MRI agreed closely (Fig. 8.6), and thus providing evidence that the MRT values are correct. At the fixed circumferential position $\Phi = 0^\circ$ the two separate thermocouple measurements showed quite distinct ΔT values (Fig. 8.6a). Each of these measurements agreed closely with one of the two columns of the PRF ΔT data at $\Phi = 0^\circ$. This indicates that the two separate thermocouple measurements were made at slightly different angular positions corresponding approximately to the two highlighted lines of MR ΔT values.
Similarly, thermocouple measurements performed at a fixed radial position and varying circumferential positions agreed closely (Fig. 8.6b). Because of the spatial resolution of the PRF ΔT maps it was difficult to pick a single line of voxels matching exactly to the radius of the thermocouple measurements. Instead all voxels of the PRF ΔT map in the range of the radius between 19.0 mm and 21.0 mm were shown. Hence, the inaccuracies due to radial positioning of the thermocouples and additional twisting were accounted for. In particular for the range of the radius between 19.0 mm and 20.0 mm, the thermocouple data and PRF ΔT data were very similar.
The difficulty in validating the PRF ΔT measurements quantitatively can be seen for example at the circumferential position $\Phi = -30^\circ$. Two values, one at approximately $\Delta T = 3\,\mathrm{K}$ and the other at approximately $\Delta T = 6.5\,\mathrm{K}$, are depicted for the range enclosing the positioning uncertainty of the thermocouple tip. The thermocouple data is approximately $\Delta T = 5.8\,\mathrm{K}$ at this position.
Additional comparisons provided in the thesis of the project partner [17] (subsection 5.3.2.7; note, the x-axis representing Φ is reversed and the right lobe as well as left lobe are interchanged compared to this work) include MRT data of three separate measurement sessions and one additional fixed circumferential position $\Phi = 20^\circ$. MRT data and TC data revealed close agreements in particular for the data at fixed circumferential positions. For a fixed radial position and various circumferential positions the scattering between the three different MR data sets is similar to the scattering of the MR data presented in Fig. 8.6b for two different ranges of $\mathrm{R_{MRT}}$. This again demonstrates the difficulties with co-registration of the data since only minor scattering was observed between the three different MR data sets for the fixed circumferential position $\Phi = 0^\circ$.

Further evidence that the applied PRF MRT method accurately measures temperature was provided by simultaneously acquired MRT data and fiber optical probe data at two distinct locations within flow 1 (Tab. 8.2). Close agreement was observed for both sets of data.

Since sensor inlets disturbed the PRF ΔT maps locally, a stack of slices at a sufficient distance was chosen for the data comparison, which, in turn makes an exact quantitative comparisons between fiber optical probes and MR measurements difficult.
A further approach to add additional evidence for the accuracy of the MRT measurements was provided by the case with $T_{\text{flow1}} = T_{\text{flow2}}$ (Fig. 8.3a). In this case the temperature was constant throughout the entire volume. Furthermore, the flow field was quite simple, apart from acceleration present in the boundary layers next to the pipe walls. The PRF ΔT distribution was highly homogeneous besides a small slope along Z which may be artifacts arising from uncorrected higher order field drifts. The root mean square deviation between the actual ΔT_{FOP} and the ΔT of the MRT measurement across the whole volume was 0.5 K. Therefore, the PRF temperature phase mapping methods could measure the temperature accurately within 0.5 K in this simple flow field. The value of 0.5 K represents a superposition of errors in this flow situation originating from noise, susceptibility effects, displacement, acceleration, and experimental stability. The contribution of each of these sources of error will be different with different flow temperatures and in different flow models.
Furthermore, numerical studies and experimental investigations conducted with other modalities than MRI were performed in similar flow models as investigated in this work. They showed similar temperature distributions [136, 137, 193].
In the following subsection various sources of error are discussed, and how they are expected to change in the $T_{\text{flow1}} \neq T_{\text{flow2}}$ cases. This subsection also provides a framework considering the errors which could arise in other flow models.
The variety of possible error sources indicates that complex considerations are required to achieve accurate and precise velocity as well as temperature measurements with MRI. If the impact of geometry and materials are identified and the possible sources of error are minimized, the resultant flow model can be easily further modified to address other thermofluid questions. For example, the double pipe heat exchanger was extended to a more complex flow model called pin fin array heat exchanger. Generally, this work laid the foundation to gain knowledge on the MR perspective how to establish precise velocity and temperature measurements in fluid flows.

8.3.1 Possible sources of error

Noise

The uncertainty in the temperature phase change is inversely proportional to the SNR (Eq. (4.9)). For the case with $T_{\text{flow1}} = T_{\text{flow2}}$, the uncertainty arising from phase noise is determined in what follows. The SNR in NMR phased arrays was determined according to Constantinides $et\ al.$ [194]

$$\sigma_{\text{BG}} = \sqrt{\frac{\overline{M_{\text{BG}}^2}}{2L}} \tag{8.2}$$

$$A_{\text{ROI}} = \sqrt{\overline{M_{\text{ROI}}^2} - 2L\sigma_{\text{BG}}^2} \tag{8.3}$$

$$\text{SNR} = \frac{A}{\sigma_{\text{BG}}} \tag{8.4}$$

for sum-of-squares images (magnitude images). σ_{BG} and A_{ROI} denote the standard deviation of the background noise and the average signal intensity in the flow phantom, respectively. The ROI to determine σ_{BG} has to be selected in artifact-free areas in the background of the magnitude image. M_{BG} and M_{ROI} represent voxels of the background and of the region of interest within the flow phantom, respectively. Averaging is denoted with $\overline{\dots}$, and L is the number of coils.
The values obtained at temperatures T = 21 °C, and 31 °C were $\sigma_{\mathrm{BG},21\,^\circ\mathrm{C}} = \sigma_{\mathrm{BG},31\,^\circ\mathrm{C}} = 0.82$, $A_{\mathrm{ROI},21\,^\circ\mathrm{C}} = 131.94$, $A_{\mathrm{ROI},31\,^\circ\mathrm{C}} = 125.77$, $\mathrm{SNR}_{21\,^\circ\mathrm{C}} = 160.43$, and $\mathrm{SNR}_{31\,^\circ\mathrm{C}} = 153.02$. Note that the signal decreased by approximately 5% with increasing temperature. The corresponding uncertainty in the temperature phase (equation provided in reference [74] or see Eq. (4.9) neglecting $\sqrt{2}$) at temperatures T = 21 °C and 31 °C revealed $\sigma_{T,21\,^\circ\mathrm{C}} = \sigma_{T,31\,^\circ\mathrm{C}} = 0.04\,\mathrm{K}$. The uncertainty in the temperature phase difference images was obtained by Gaussian error propagation $\sigma_{\Delta\mathrm{T}} = \sqrt{\sigma_{T,21\,^\circ\mathrm{C}}^2 + \sigma_{T,31\,^\circ\mathrm{C}}^2} = 0.06\,\mathrm{K} \approx \sqrt{2}\,\sigma_{\mathrm{T}}$ in accordance with Eq. (4.9). $\sigma_{\Delta\mathrm{T}}$ was not expected to be substantially different between the different cases studied due to similar SNR values or even higher SNR values in the case of lower fluid temperatures. However, they will be different for other flow models and with other acquisition parameters.
The same SNR analysis was applied to the magnitude data of the MRV measurement revealing $\sigma_{\mathrm{BG}} = 1.71$, $A_{\mathrm{ROI}} = 159.83$, and $\mathrm{SNR} = 93.53$. The magnitude data used for this analysis was the averaged magnitude data of four acquisitions (three velocity encoding directions and the velocity reference). Thus, this SNR value had to be corrected by a factor of $1/2$ since the SNR of the averaged data is directly proportional to the SNR of a single acquisition according to $\mathrm{SNR}_{\mathrm{averaged}} \propto \sqrt{n}\,\mathrm{SNR}_{\mathrm{single}}$ [27] with n representing the number of acquisitions. Eq. (3.13) was adjusted accordingly leading to $\sigma_{\mathrm{v}} = 2\frac{\sqrt{2}}{SNR}\frac{v_{enc}}{\pi}$. An uncertainty in the velocity phase of $\sigma_v = 0.0005\,\mathrm{m/s}$ was determined for a $v_{enc} = 0.05\,\mathrm{m/s}$.
A much higher value of σ_v (by a factor of 28 larger) was reported by the project partner in reference [17] for a similar acquisition, however, with a $v_{enc} = 0.2\,\mathrm{m/s}$. The different v_{enc} values contribute a factor of 4. The remaining factor of 7 is likely to be caused by differently selected ROIs to calculate background noise. A value of $\sigma_{\mathrm{BG}} \approx 7$ in [17] lead to a low SNR value which in turn resulted in a comparatively high velocity phase noise. The velocity phase noise determined in this work seems to be in a reasonable order of magnitude. The method applied to determine SNR, and thus the velocity phase noise, is assumed to be a valid approach in the flow situation inside the double pipe heat exchanger. However, this approach to estimate the uncertainty of velocity measurements becomes more inaccurate with increasing Reynolds number of the flow because the noise is solely determined in the artifact-free background (considering thermal noise) neglecting contributions from the turbulent flow [195].

Susceptibility

The flow model placed into the homogeneous B_0 introduces local variations of this field because of susceptibility differences of materials. Thus, the proton resonance frequency changes locally. To avoid undesired artifacts in the MR image such as deformations of the object's shapes or signal voids, effects of the magnetic susceptibility on the MR image have to be considered carefully (see reference [34] for more details on this subject). For example, the shapes and the orientation of the objects with respect to B_0 [34, 67] as well as

susceptibility matching of the components is important for phantom designs.
In this work MRV as well as MRT were performed based on phase contrast methods. This involves a subtraction of two sets of phase data. Thus, local field variations have to remain unchanged between both data acquisitions to be removed by the phase subtraction. For this reason, the temperature of the experimental setup has to stay constant during an MRV acquisition. In contrast, MRT based on PRF temperature phase mapping requires two measurements which are performed at distinct temperatures. Temperature dependent changes of the susceptibility cause phase changes which are different for measurements conducted at different temperatures. This leads to errors in the PRF temperature phase maps. Therefore, the entire setup to perform MRT has to be designed more carefully than for MRV to minimize distortions arising from temperature dependent susceptibility effects. The temperature dependence of the susceptibility of pure water is known to be small compared with its temperature coefficient α_{water} [10] (see also p. 39). However, for fat the temperature dependence of the susceptibility is much larger than its temperature coefficient and almost similar in size to α_{water} (p. 39). Consequently, areas containing fat can only be used as reference to monitor field drifts if they do not change temperature. This is important to remember if field drifts are monitored via fat which is frequently the case in in vivo MR thermometry. For other materials data is often not available, however, a method presented by de Poorter [69] could be applied to determine their susceptibility change with temperature.
The flow model in this work was designed with a cylindrical shape oriented parallel to B_0. In particular, two cylinders (one put into the other) were used because a cylinder aligned with B_0 causes no distortion in the magnetic field outside the cylinder, while the field inside has a spatially invariant offset [34]. The case considering $T_{\mathrm{flow1}} = T_{\mathrm{flow2}}$ can be used to detect temperature dependent susceptibility changes. It would show a constant offset in the PRF temperature phase maps originating from temperature dependent susceptibility changes if they are substantial compared with the PRF shielding effect. However, the temperature of the PRF ΔT map was within 0.5 K of the temperature determined by the fiber optical probe. Therefore, the temperature dependent susceptibility changes do not have a strong effect on the temperature results of this flow model. This fact is not expected to change between the three cases investigated in this work ($T_{\mathrm{flow\ 1}} = T_{\mathrm{flow\ 2}}$, $T_{\mathrm{flow\ 1}} < T_{\mathrm{flow\ 2}}$, and $T_{\mathrm{flow\ 1}} > T_{\mathrm{flow\ 2}}$).
Whether temperature dependent susceptibilities play a substantial role in a specific flow model can be investigated with known temperature distributions. An alternative approach to determine the influence of temperature dependent susceptibilities is to measure the susceptibility change with temperature, the magnetic field resulting from a particular geometry can be simulated (as in [69]).
Another aspect to be considered with the double pipe setup was that air bubbles appeared at the hot copper surface causing local artifacts in the PRF ΔT map. To reduces the occurrence of this bubbles or avoid them from being generated, the fluid inside the copper pipe can be cooled instead of heated. Alternatively, the fluid outside the copper pipe could be degassed before it is used in MRT experiments.

Displacement

If spins move between the RF excitation and readout of the signal, MR images are corrupted. In this work, in-plane displacement was minimized by placing the phase encod-

ing gradient as close as possible to the readout gradient. A flow rate of 5 l/min reveals maximum flow velocities of approximately 0.1 m/s along Z (corresponding to readout direction). For the cases with $T_{\text{flow 1}} < T_{\text{flow 2}}$ and $T_{\text{flow 1}} > T_{\text{flow 2}}$ maximum velocities occur in the X and Y direction which are an order of magnitude smaller than along Z.
The time separation between phase encoding and the center of readout is 7 ms for the MRT acquisitions performed with TE = 20 ms. During this time, spins move less than the spatial resolution and a substantial corruption of the MR image due to in-plane displacement is not expected. In-plane displacement of spins is less for the MRV acquisitions than for the MRT acquisitions, and thus not assumed to be a relevant source of error.
Additionally, through-plane displacement errors are not expected to be substantial for the MRT or MRV acquisitions because of the very small velocities in this direction.
If the spins move through a temperature gradient or velocity gradient during TE, temperatures or velocities given in PRF temperature phase maps or velocity maps, represent an integral value of the temperatures or velocities experienced, rather than temperature or velocity at a single time point and spatial location. However, in the flow conditions investigated in this setup the velocity field and the temperature field are strongly coupled. Spins move in layers where the velocity changes slowly. Also the temperature only changes slowly due to heat conduction perpendicular to the flow field, not due to mixing of layers with different temperatures. Therefore, effects related to temperature gradients or velocity gradients are not important. In strongly turbulent flows where more mixing occurs, shorter readout times and echo times might be advantageous to account for these effects.

Acceleration

Acceleration compensation was not implemented in the sequence used in this work. Thus, acceleration of the spins can lead to phase errors degrading the accuracy of the measured velocity and temperature fields. The acceleration vector field of the flow can be determined by the total time derivative (also called material derivative) of the 3D velocity vector field $\vec{V}(\vec{r}_{\text{flow}}, t_{\text{flow}})$ which represents the speed and direction of particles at each spatial location $\vec{r}_{\text{flow}}$ and at each instant of time t_{flow}

$$\vec{V}(\vec{r}_{\text{flow}}, t_{\text{flow}}) = \begin{pmatrix} u(\vec{r}_{\text{flow}}, t_{\text{flow}}) \\ v(\vec{r}_{\text{flow}}, t_{\text{flow}}) \\ w(\vec{r}_{\text{flow}}, t_{\text{flow}}) \end{pmatrix} = \begin{pmatrix} u(x_{\text{flow}}, y_{\text{flow}}, z_{\text{flow}}, t_{\text{flow}}) \\ v(x_{\text{flow}}, y_{\text{flow}}, z_{\text{flow}}, t_{\text{flow}}) \\ w(x_{\text{flow}}, y_{\text{flow}}, z_{\text{flow}}, t_{\text{flow}}) \end{pmatrix} \tag{8.5}$$

The flow is steady if $\frac{\partial \vec{V}}{\partial t} = \vec{0}$ [32].
Starting with Eq. (8.5), the acceleration field is given by [196]

$$\vec{a}(\vec{r}_{\text{flow}}, t_{\text{flow}}) = \frac{d\vec{V}(\vec{r}_{\text{flow}}, t_{\text{flow}})}{dt} = \begin{pmatrix} \frac{\partial u}{\partial t} + u\frac{\partial u}{\partial x} + v\frac{\partial u}{\partial y} + w\frac{\partial u}{\partial z} \\ \frac{\partial v}{\partial t} + u\frac{\partial v}{\partial x} + v\frac{\partial v}{\partial y} + w\frac{\partial v}{\partial z} \\ \frac{\partial w}{\partial t} + u\frac{\partial w}{\partial x} + v\frac{\partial w}{\partial y} + w\frac{\partial w}{\partial z} \end{pmatrix} \tag{8.6}$$

$$= \underbrace{\frac{\partial \vec{V}}{\partial t}}_{\text{local acceleration}} + \underbrace{\left(\vec{V} \cdot \vec{\nabla}\right)\vec{V}}_{\text{convective acceleration}} . \tag{8.7}$$

Thus, the acceleration experienced by a particle in the fluid consists of two parts, one aris-

ing from a temporal varying velocity field at a fixed location (local acceleration), and one arising from a spatial varying velocity field (convective acceleration). The local acceleration vanishes in steady flows ($\frac{\partial \vec{V}}{\partial t} = \vec{0}$).
Acceleration maps were calculated from the MR velocity data acquired for the two cases: Case 1 with $T_{\text{flow 1}} < T_{\text{flow 2}}$ and case 2 with $T_{\text{flow 1}} > T_{\text{flow 2}}$. The maximum acceleration observed in the double pipe flow model is approximately $0.2\,\text{m/s}^2$ in both cases. This relatively small value can be referred to the low velocities in combination with the lack of obstruction to the flow.
No contributions from acceleration remain in phase difference maps if the acceleration fields are identical for the reference measurement ($T_{\text{flow 1}} = T_{\text{flow 2}}$) and the heated case ($T_{\text{flow 1}} < T_{\text{flow 2}}$) or the cooled case ($T_{\text{flow 1}} > T_{\text{flow 2}}$). No temperature gradient, and thus only forced convection is present for the reference measurement. Whereas, in the heated or cooled cases natural convection and forced convection occur leading to local acceleration. Hence, the corresponding phase due to acceleration changes, $\Phi_{\Delta\text{a}} = 1/2\,\gamma\,\Delta a\,M^2 = 0.02$, results in a temperature error of approximately 0.14 K. The second moment of the gradients M^2 is calculated according to $M^2 = \int_0^{\text{TE}} G(\tau)\tau^2\,\text{d}\tau$ (Eq. (3.7)). The gradient amplitudes and timing are determined with sequence simulations applying identical imaging parameters as during the actual MR data acquisition.
In a similar manner the phase error due to acceleration was estimated for the velocity data and revealed $\Phi_{\text{a}} = 1/2\,\gamma\,a\,\Delta M^2 = 0.07$ (note, the acceleration field is the same for both acquisitions, however the velocity encoding is different leading to an effective second moment ΔM^2). This phase translated into a velocity error of 0.0011 m/s using $v_{\text{error}} = \Phi_{\text{a}}\frac{v_{enc}}{\pi}$. Therefore, errors due to acceleration changes are assumed not to have an influence on the experimental results in this setup. However, in other flow models acceleration compensation could be necessary to be implemented in the sequence.

Experimental stability

Substantial temperature errors may arise from field drifts which can occur between acquisitions required to perform PRF temperature phase mapping. To track this drift there are various possibilities. Thermally insulated reference phantoms (used in this work) can be positioned in the vicinity of the flow model. Note that the separation between the references and the flow model has to be sufficiently large (approximately a few centimeters) otherwise the temperature maps are distorted by susceptibility artifacts. The inclusion of references requires the FOV to be enlarged prolonging scan time. Furthermore, because of the shape of the flow phantom, the references could be only included in X direction. This restricted the correction to 0-th order which left residual first or higher order offsets uncorrected. The temperature slope along the Z direction (see Fig. 8.3) is expected to arise due to an uncorrected first order field drift.
As proposed in Buchenberg *et al.* [133], the usage of non-insulated oil phantoms did not reveal the desired correction. Since the temperature dependent susceptibility of oil is in the same order as the temperature coefficient of water (p. 39), substantial phase changes were observed if the temperature of the oil changed. Therefore, oil references require isolation and cannot be placed closer to the flow phantom (to provide higher order field drift corrections) than the references used in this work.
Furthermore, the field drift could be monitored with field probes [83]. In this case the FOV has not to be enlarged. However, additional time is required to read the data of the field

probes (in the order of milliseconds per read-out of the field camera data) during MR data acquisition. This prolongs the total measurement time. Furthermore, field probes are sensitive to temperature changes requiring temperature monitoring and corresponding corrections. Recently, field probes with a temperature dependence of below 0.1 ppb/K were presented by Gross $et\ al.$ [197]. Field probes to monitor the field drift were tested with the double pipe heat exchanger setup in this work. During this experiment, however, the field drift remained unexpectedly small ($\sim 1\,K$), which is approximately the overall measurement uncertainty of MRT measurements. Since the field drift was in a similar order of magnitude as this uncertainty, a detailed analysis and comparison between temperature data corrected by field probe measurements and temperature data corrected by reference phantoms could not be performed. Moreover, the experiment could not be repeated since the field probe setup was only temporarily available. Future work on this subject is required particularly in complex flow models where a reasonable placement of reference phantoms is difficult to achieve without degrading MR images. In these cases field probes could represent a valuable approach for monitoring field drift.
Finally, spectroscopic methods could be used (as presented in chapter 10) to provide absolute temperature measurements with a single acquisition. However, its spatial resolution is typically in the order of a few millimeters. Hence, thin structures such as the plume inside the annulus of the double pipe heat exchanger are difficult to detect.
Highly unstable or rapidly fluctuating temperature distributions would be difficult to measure with PRF methods. In the presence of turbulent flow with integral time scales shorter than the velocity compensation gradients [5], residual phase distribution after the velocity compensation would lead to signal loss due to intra voxel dephasing (reduced $T2^*$).
Velocity measurements are typically affected by eddy currents. This source of error is assumed to be most relevant in MRV acquisitions of the double pipe flow model. Acquisitions performed at minimum possible TE revealed higher order distortions which could not be sufficiently corrected by post-processing. An increase of TE (i.e. prolonging gradient ramp up times and reducing gradient amplitudes) and a correction of eddy currents during post-processing could resolve this issue. Good agreements were found between MR velocity data and LDA data (see thesis of the project partner [17]). Due to the low velocities an increase of TE was feasible without introducing displacement errors. Additionally, as discussed before errors due to acceleration were not expected to be relevant in this setup. Furthermore, due to the laminar flow no relevant signal loss due to intra voxel dephasing was observed as it would occur in turbulent flows.
The discussion above about possible sources of error indicates, that in this flow model and with the imaging parameters applied the majority of the errors are small compared with the velocities or temperatures being measured. A better correction of the field drift can reduce the error of the temperature maps since the field drift is assumed to be the main error source contributing to the rmsd value of 0.5 K for the case with $T_{\mathrm{flow1}} = T_{\mathrm{flow2}}$.

Chapter 9

Pin fin array heat exchanger

The pin fin array heat exchanger is a more complex arrangement of copper tubes for heating or cooling than the latter discussed double pipe heat exchanger. However, the experiments of the double pipe heat exchanger contributed valuable input with respect to its design and the MR data acquisitions.

9.1 Methods

9.1.1 Flow model design

A staggered pin fin array heat exchanger was constructed by the project partner based on design rules to establish a benchmark case in CFD calculations [147]. A CAD drawing provided by the project partner and a picture of the pin fin array heat exchanger are shown in Fig. 9.1.
Results of experimental groundwork (subsections 7.1.1, 7.1.2), lessons learned from the double pipe heat exchanger experiments, and Schenck's review on susceptibility [34] were

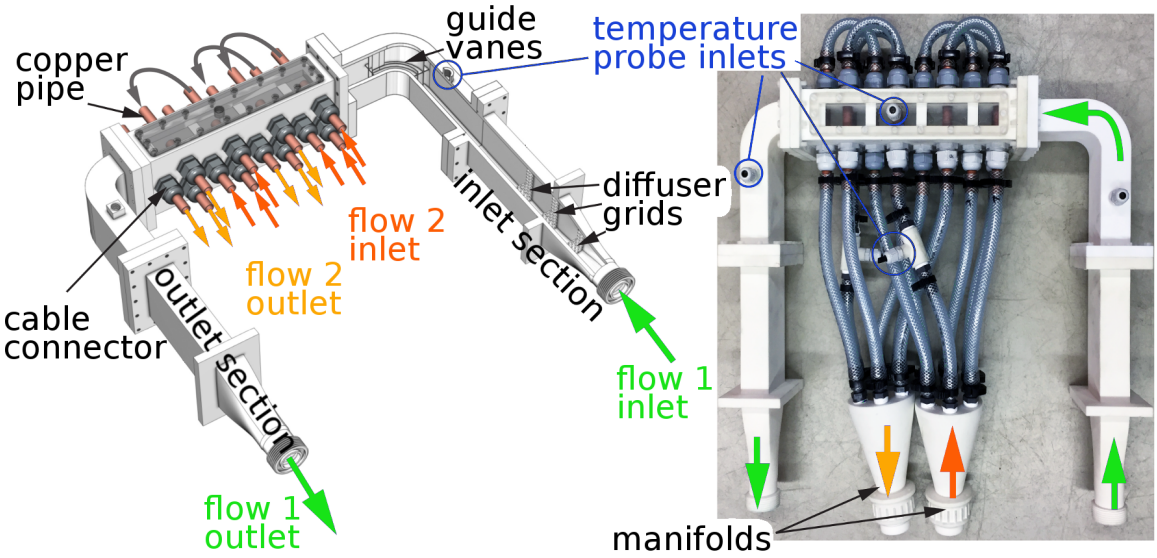

Figure 9.1: A CAD drawing and a picture (top view) of the pin fin flow model are shown.

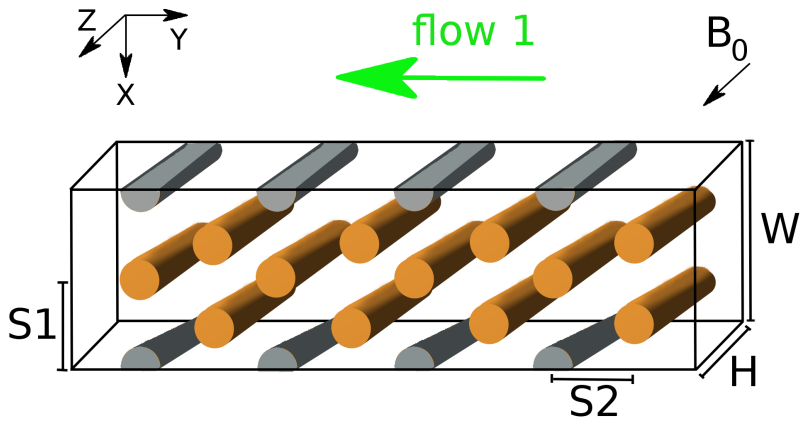

Figure 9.2: Schematics of the staggered pin fin heat exchanger with the copper pipes (orange) and the half-cylinders (grey) made from PA. The characteristic parameters are depicted (H: height, W: width, S1: cross streamwise pin distance, S2: streamwise pin distance). The orientation of the pin fin flow model with respect to B_0 and the direction of flow 1 is presented. The coordinate system used for the velocity components and acceleration components is shown.

considered to ensure MR compatibility of the model. Therefore, to minimize possible susceptibility issues copper pipes were aligned parallel to B_0. In total 12 copper pipes (full pins, ID = 10 mm, OD = 12 mm, length of these pipes = 150 mm) were arranged in a staggered manner forming 8 rows of pins (Fig. 9.2). Half-cylinders (half pins) made from PA had to be inserted at the bottom and top of the casing to achieve a staggered array. Hence, each row of pins was composed of either two full pins or one full pin and two half pins. The copper pipes were fixed into the casing and sealed off by cable connectors mated to the casing. The half pins were fixed to the surrounding casing made from PA (displayed in white in Fig. 9.1) using direct laser-sintering. The top wall of the casing consisted of an acrylic glass plate to allow optical access to check for air bubbles.
Overall, the casing established a rectangular flow channel with its length axis oriented perpendicular to B_0. Because of the limited amount of space in the MR scanner bore, bends at the inlet and outlet of the channel were required to redirect flow 1 by 90°. Inside the bend of the inlet, guide vanes were located to reduce the development of secondary flows. The distance between the beginning of the first row of pins and the end of the guide vanes was 80 mm.
The bend of the inlet was connected to an inlet section (see Fig. 9.1) which included a wide-angle diffuser at its very beginning. The diffuser comprised internal grids generating pressure loss and thus, preventing flow separation. The inlet section equals the outlet section which is connected to the downstream part of the pin fin casing.
The geometric dimensions of the staggered pin fin model were chosen according to the proposal of Benhamadouche *et al.* [147] with S1/OD = S2/OD = 2.5, W/OD = 5 and H/OD = 2.
Two separate closed flow circuits were established with this flow model. The casing contained flow 1 with its direction of flow oriented perpendicular to the length axis of the pins. Inside the copper pins flow 2 could provide heating or cooling of flow 1. To establish flow 2, the copper pipes were grouped into two groups (denoted 'flow 2 inlet'and 'flow 2

MR imaging parameters	MRV	MRT
TE/TR [ms]	6.1/9.1	20.0/29.1
flip angle [°]	25	25
pixel bandwidth [Hz/pixel]	455	120
spatial resolution [mm^3]	$1.0 \times 1.0 \times 3.0$	$1.0 \times 1.0 \times 3.0$
Phase encoding (PE) lines/slices	384/3	384/3
Read out direction	Y	Y
In plane PE direction	X	X
Slice direction	Z	Z
v_{enc} in plane/through plane [m/s]	0.2/0.1	—

Table 9.1: MR sequence parameters used for 2D MRV and 2D MRT acquisitions of the pin fin array heat exchanger. The total acquisition time of a MRV measurement (single slice, 3 directional velocity encoding) was around 14 seconds and of a MRT measurement (single slice, velocity compensated) was around 11 seconds.

outlet'). Flow 2 inlet and flow 2 outlet were split into two subgroups of three copper pins each. These subgroups were alternated as presented in Fig. 9.1.
A manifold (made from PA using laser-sintering) split flow 2 into six feed lines. Each of these lines was connected (via polyvinyl chloride (PVC) hoses) to one of the six copper pipes corresponding to flow 2 inlet. The pipes of flow 2 inlet were connected to the pipes of flow 2 outlet using PVC hoses. Thus, flow 2 passed in total twice through the pipes of the pin fin array. A second manifold collected all six lines of flow 2 outlet.
The flow apparatus as described in section 7.1.3 was used to provide flow 1 and flow 2 at the desired temperatures. Various inlets for the fiber optical probes were available (highlighted by the blue circles in Fig. 9.1) to allow temperature measurements at distinct locations during the MR acquisitions.

9.1.2 Experiments

2D MRV and 2D MRT were performed using the sequence described in 6.1. The imaging parameters applied for these measurements are summarized in Table 9.1. MR acquisitions were performed similarly as in the study of the double pipe heat exchanger. The case $T_{\text{flow 1}} < T_{\text{flow 2}}$ was not considered in this setup because of the air bubble generation at the hot surface of the copper tubes (see discussion about double pipe heat exchanger, 8.3.1) introducing additional air into the flow channel. After careful deaeration of the flow 1 circuit, some air still remained trapped at the half pins at the top of the pin fin array (visible as artifacts in PRF temperature phase maps, see results section 9.2).
PRF temperature phase mapping was conducted with two different pairs of acquisitions at different temperatures for flow 1 ($T_{\text{flow 1}}$) and flow 2 ($T_{\text{flow 2}}$).

1. Homogeneous spatial temperature distribution i.e., $T_{\text{flow 1}} = T_{\text{flow 2}}$. A reference acquisition with flow 1 and flow 2 both at room temperature (25 °C) and an acquisition with flow 1 and flow 2 both at a higher temperature (40 °C) were performed. Flow 2 was provided by the HC-pump (see section 7.1.3). Both pairs of acquisitions were

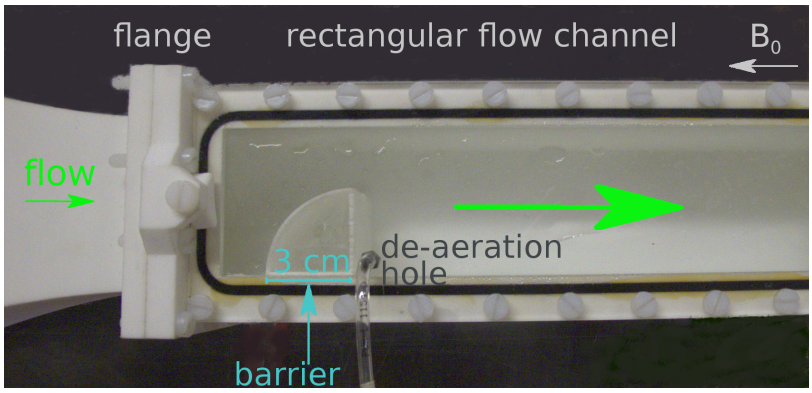

Figure 9.3: Picture of the rectangular flow channel. A barrier is placed inside the flow to cause acceleration. Only one closed flow circuit (flow 1 described in section 7.1.3) was established with this model. The fluid flow was from left to right once at a temperature of 22 °C (reference acquisition) and once at a temperature of 37 °C (heated acquisition). The resultant change in temperature was $\Delta T = 15\,\mathrm{K}$. A de-aeration hole behind the barrier was present to remove air bubbles. A flange was connecting the flow preparation section (not shown) to the flow channel.

performed with sequence gradient settings stretched and non-stretched. In total ten repetitions were acquired for each setting.

2. Inhomogeneous spatial temperature distribution i.e., $T_{\mathrm{flow\ 1}} > T_{\mathrm{flow\ 2}}$. A reference acquisition with flow 1 and flow 2 both at the same temperature (40°C) and an acquisition with flow 1 at a higher temperature than flow 2 ($T_{\mathrm{flow\ 1}} = 40\,°\mathrm{C}$, $T_{\mathrm{flow\ 2}} = 12\,°\mathrm{C}$) were performed. Flow 2 was provided by the immersion heater during the reference acquisition. Meanwhile, water at a low temperature was prepared and maintained by the HC-pump. After the reference acquisition was finished the immersion heater was removed and replaced by the HC-pump. This approach allowed the two acquisitions to be performed as closely together in time as possible. The acquisitions were performed with the stretched gradient settings only and repeated 50 times.

Homogeneous spatial temperature distributions (first pair of acquisitions) can be used to show that the applied PRF temperature mapping method is able to accurately and precisely measure temperature changes in fluid flows, and to detect possible areas suffering from artifacts. Additionally, they allow a comparison between acquisitions performed with different parameter settings (in this case, stretched and non-stretched gradients). The second pair of acquisitions (case with $T_{\mathrm{flow\ 1}} > T_{\mathrm{flow\ 2}}$) was performed to demonstrate that the applied PRF temperature mapping method is capable of measuring spatially inhomogeneous temperature distributions in fluid flows.
During the MR acquisitions the temperature distributions were assumed to remain constant.
The flow rate for flow 1 was held constant at 5.5 l/min, whereas, the flow rate for flow 2 was according to the maximum possible supply provided by the two Julabo systems during all MR acquisitions. Fiber optical probes were positioned into inlets (see Fig. 9.1) to measure the inlet temperature and outlet temperature of flow 1 ($T_{1,\mathrm{in}}$, $T_{1,\mathrm{out}}$), the temperature locally at the top of the pin fin array ($T_{1,\mathrm{top}}$), and the temperature of one of the

insulated reference phantoms.
The reference phantoms (same used as in the double pipe experiments) were included to correct for field drifts during post processing of the temperature data. They were placed with their long axis parallel to B_0 on top of the MR surface coil for two reasons: first, to minimize the distance between the pin fin array and the coil to yield higher SNR. Second, to ensure a sufficient separation between the flow model and the references since PRF temperature phase maps can be locally distorted if the distance between the model and the references is too small (see conference article Wassermann *et al.* [198], Fig.9).

MR velocity mapping was repeated ten times using a pair of acquisitions, once without any flows for reference and once with the two flows at temperatures $T_{\text{flow 1}} = 40\,^{\circ}\text{C}$ and $T_{\text{flow 2}} = 12\,^{\circ}\text{C}$, respectively. The reference scan was used to correct for eddy currents in the actual measurement.

Since the flow of this setup is more turbulent than in the double pipe setup, multiple acquisitions for data averaging were performed to increase SNR, and thus reducing the uncertainty of the temperature and velocity measurements. The evaluation of MRV data and MRT data was conducted as described in subsection 6.2.

Additionally, to examine the impact of acceleration on the PRF temperature phase maps, homogeneous temperature distributions were investigated in a separate experiment with

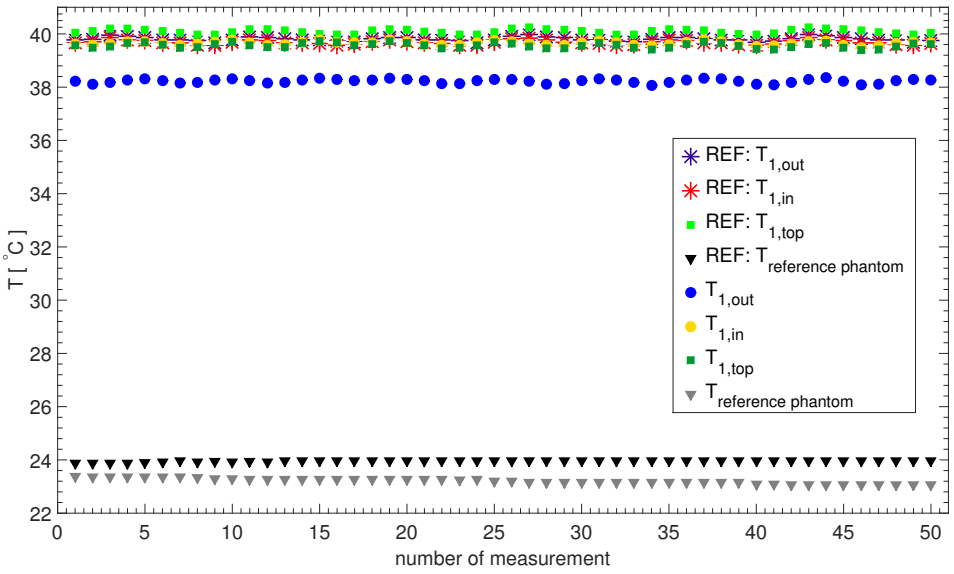

Figure 9.4: Averaged absolute temperature values of the fiber optical probes are depicted. They were measured at four distinct locations: inlet temperature and outlet temperature of flow 1 ($T_{1,\text{in}}$, $T_{1,\text{out}}$), the temperature locally at the top of the pin fin array ($T_{1,\text{top}}$), and the temperature of one of the reference phantoms. The FOP data was logged during the MR data acquisitions for the case with $T_{\text{flow 1}} > T_{\text{flow 2}}$. The MR acquisitions were repeated 50 times with flow 1 and flow 2 both at the same temperature (40°C) denoted REF, and with flow 1 at a higher temperature than flow 2 ($T_{\text{flow 1}} = 40\,^{\circ}\text{C}$, $T_{\text{flow 2}} = 12\,^{\circ}\text{C}$). The FOP data recorded per MR acquisition was averaged. Note, the standard deviation of the mean is below the marker size and thus, not shown.

an additional flow model (constructed by the project partner). It consisted of a rectangular flow channel and a barrier located inside the flow (Fig. 9.3). The barrier was a thin shell (made from PA using laser-sintering) with its shape equal to the quarter of a cylinder (OD=6 cm). The barrier was filled with the same fluid as used for MR imaging to minimize susceptibility issues. The flow rate (20 l/min) was four times as high as applied in the pin fin array to enhance possible acceleration effects at the barrier. The MR imaging parameters were similar as in the double pipe experiment, and MRT data evaluation was performed as described in the subsection 6.2.

9.2 Results

Fig. 9.4 shows absolute temperature values measured by the four FOPs. The FOP data was logged during 50 consecutive MR acquisitions. The flow apparatus provided excellent stable fluid temperatures for all repeated MR measurements.
Temperature changes (ΔT_{FOP}) obtained by the four FOPs are listed for all different cases investigated in Tab. 9.2. The temperature changes of the reference phantom were in the order of 1 K (Tab. 9.2). These changes were considered in the data evaluation of the PRF temperature phase maps.
As a measure for the accuracy the rmsd was calculated similarly as in the double pipe heat exchanger experiment (see Eq. (8.1)) between the FOP data and the MR temperature data. The mean of $T_{1,\mathrm{in}}$, $T_{1,\mathrm{out}}$, and $T_{1,\mathrm{top}}$ (see Tab. 9.2) was considered in the rmsd calculation. Therefore, ΔT_{FOP} was 15.079 K and 14.995 K for the stretched case and non-stretched case, respectively. MR data of the pin fin array was included from the first row of pins to the last row of pins. The rmsd of roughly 1 K was generally lower (up to $\sim 15\%$) for the stretched than the non-stretched gradient scheme (Tab. 9.3).
Fig. 9.5a and Fig. 9.5b show transverse views (equal to X-Y planes) of PRF temperature phase maps which were acquired with the stretched and non-stretched gradient scheme and averaged over 10 repetitions. Homogeneous spatial temperature distributions are clearly observed apart from the inflow and outflow sections of the pin fin array where the flanges were located (see Fig. 9.1).
For each slice depicted in Fig. 9.5a and Fig. 9.5b, ΔT values were averaged in cross-streamwise direction (equal to voxel columns). The resultant mean values are presented

ΔT_{FOP} [K] = $T_{40^\circ\mathrm{C}} - T_{25^\circ\mathrm{C\ or\ }12^\circ\mathrm{C}}$			
	$T_{\mathrm{flow\ 1}} = T_{\mathrm{flow\ 2}}$		$T_{\mathrm{flow\ 1}} > T_{\mathrm{flow\ 2}}$
	stretched	non-stretched	stretched
$T_{1,\mathrm{in}}$	14.975±0.011	14.892±0.006	0.040±0.003
$T_{1,\mathrm{out}}$	15.125±0.009	15.044±0.007	1.577±0.003
$T_{1,\mathrm{top}}$	15.136±0.011	15.049±0.007	0.527±0.004
$T_{\mathrm{reference\ phantom}}$	1.096±0.003	1.064±0.004	0.747±0.003

Table 9.2: Temperature changes of the fiber optical probes (mean± standard deviation of the mean) are listed. They were measured at the four distinct locations: inlet temperature and outlet temperature of flow 1 ($T_{1,\mathrm{in}}$, $T_{1,\mathrm{out}}$), the temperature locally at the top of the pin fin array ($T_{1,\mathrm{top}}$), and the temperature of one of the reference phantoms.

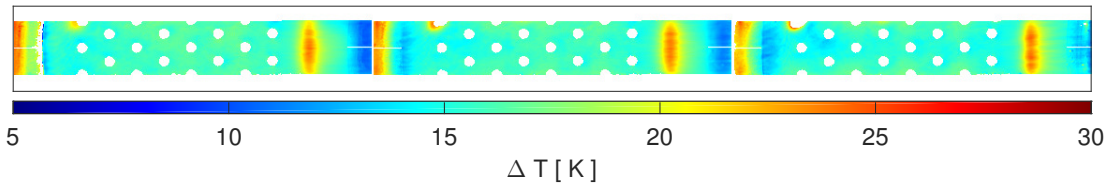

(a) $T_{\text{flow 1}} = T_{\text{flow 2}}$: stretched gradient scheme

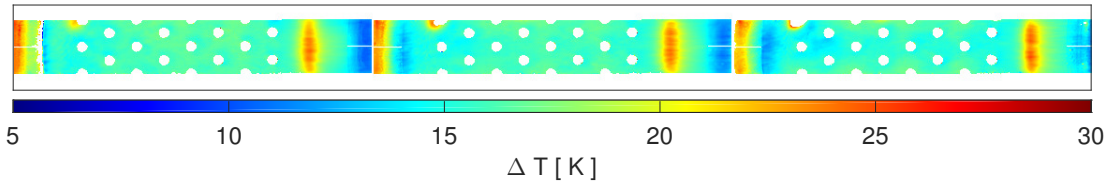

(b) $T_{\text{flow 1}} = T_{\text{flow 2}}$: non-stretched gradient scheme

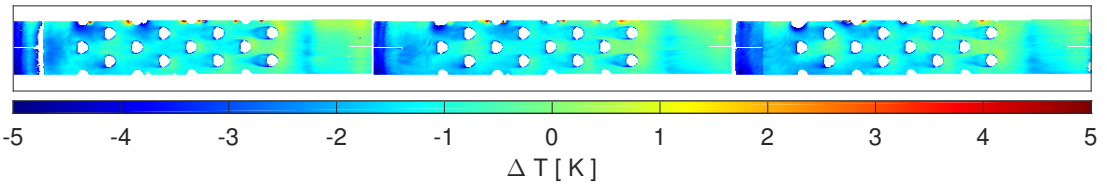

(c) $T_{\text{flow 1}} > T_{\text{flow 2}}$: stretched gradient scheme

Figure 9.5: Transverse PRF temperature phase maps are shown for all the different cases investigated. Three different slices (slice 1 to slice 3 from left to right) are depicted for each case acquired either with $T_{\text{flow 1}} = T_{\text{flow 2}}$ or $T_{\text{flow 1}} > T_{\text{flow 2}}$. The direction of flow 1 is from right to left (corresponding to negative Y). Note, different color scales are used.

in Fig. 9.6. The voxel number counts the voxel columns of a slice from left to right (i.e. voxel 1 corresponds to the very left side of a slice). At the central section of the pin fin array the temperature varies by ∼0.5 K, whereas towards the first row of pins (i.e. voxel 273 to 284) and last row of pins (i.e. voxels 70 to 81) the mean ΔT decreases. The locations of the 8 equidistant rows of pins can be detected in Fig. 9.6. In addition, substantial temperature changes are observed at the inflow and outflow sections of the pin fin array. These changes are assumed to be artifacts caused by susceptibility issues related to the flanges.
PRF temperature phase maps (three transverse slices) for the case with $T_{\text{flow 1}} > T_{\text{flow 2}}$ are

	rmsd$_{T_{\text{flow 1}}=T_{\text{flow 2}}}$ [K]	
	stretched	non-stretched
slice 1	1.09	1.28
slice 2	0.93	1.09
slice 3	0.86	0.96

Table 9.3: The rmsd values are listed for all slices which were acquired with the stretched and non-stretched gradient schemes and the case considering a homogeneous spatial temperature distribution.

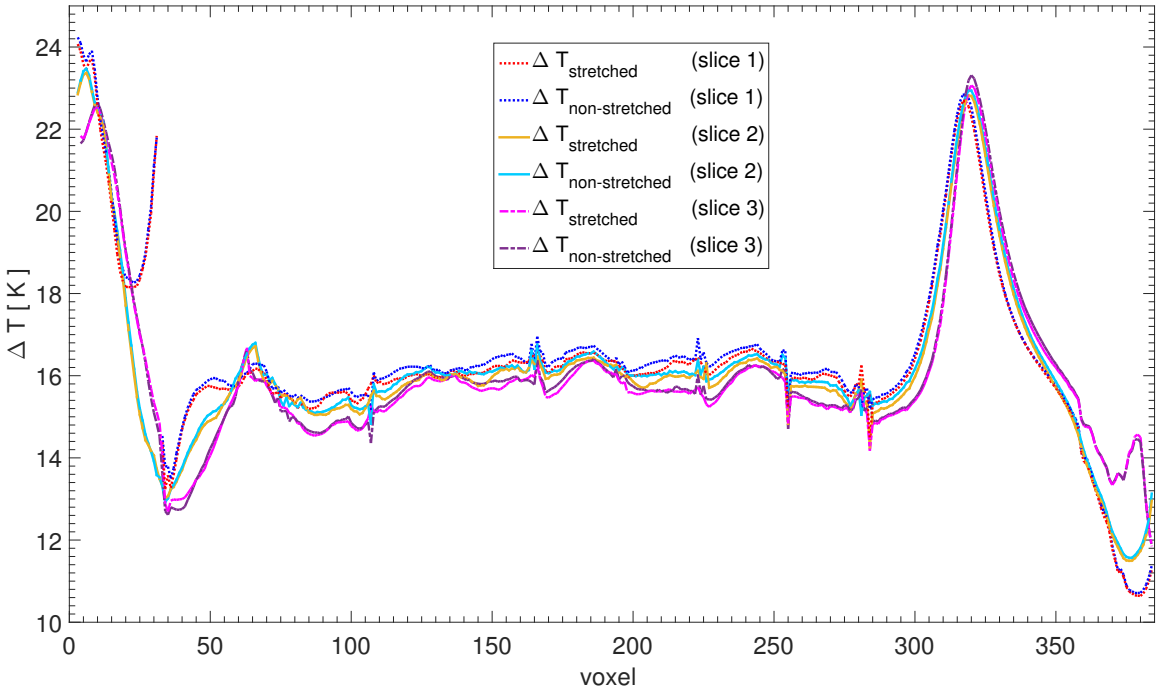

Figure 9.6: Homogeneous spatial temperature distribution: ΔT values were averaged in cross-streamwise direction and are depicted for all three slices acquired with the stretched and non-stretched gradient scheme, respectively. Error bars are not included for clarity reasons.

shown in Fig. 9.5c. An inhomogeneous spatial temperature distribution and a decrease of ΔT from right to left is observed in each slice. Again distortions due to the flanges are visible, however, less pronounced as in Figs. 9.5a and 9.5b.
To investigate the temperature changes in flow 1, mean ΔT values of voxel columns were calculated for each slice in a similar manner as for the homogeneous case before. Firstly, the middle of the pin fin array was considered to obtain Fig. 9.7a. It represents the average change in temperature primarily caused by the four centered full pins in streamwise direction of flow 1 (right to left). The location of the four full centered pins are indicated by the four equidistant minima at the voxel $\approx$ 250, 190, 130, and 70. An overall decrease of the mean ΔT is observed from $\sim 0\,\mathrm{K}$ (begin of first pin row at $\approx$ voxel 284) to $\sim -1.6\,\mathrm{K}$ (end of eighth pin row plus $\sim$1 cm at $\approx$ voxel 60). After the first central pin a clear decrease in temperature is observed. The decrease becomes less pronounced as further pins are passed. This could be related to mixing effects due to increased turbulence. Artifacts occur at voxels $\lesssim 60$ and $\gtrsim 290$ which may be caused by the flanges connecting the pin fin flow model to the bends.
Secondly, because of artifacts which occurred in the PRF temperature phase maps due to air bubbles at the top of the pin fin array, the lower half of the pin fin array was considered in the data evaluation presented in Fig. 9.7b. Similar as before, mean ΔT values in cross-streamwise direction were calculated for each slice. Because of the axial symmetry of the temperature distribution, the shape of the curve in Fig. 9.7b, should not be altered if the upper half of the pin fin array would have been also considered (prerequisite: temperature data is not corrupted by artifacts). In total eight equidistant minima (first at voxel$\approx$280,

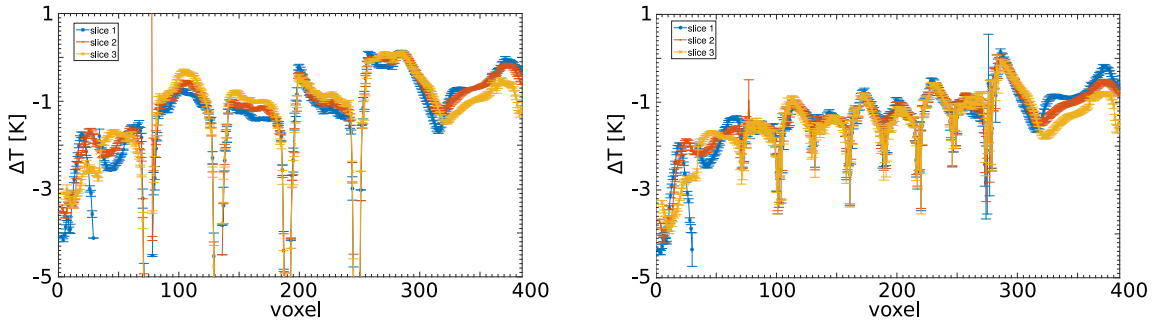

(a) Middle part **(b)** Lower half

Figure 9.7: Inhomogeneous spatial temperature distribution: ΔT values were averaged in cross-streamwise direction. The mean and the standard deviation of the mean are depicted for all three slices and (a) the middle part of the pin fin (section between two copper pipes), as well as (b) the lower half of the pin fin array. Voxel 284 corresponds to the beginning of pin row one, and voxel 70 corresponds to the end of pin row eight.

	$\overline{\Delta T}_{60,284}$ [K]
slice 1	-1.303±0.012
slice 2	-1.316±0.012
slice 3	-1.371±0.012

Table 9.4: The average changes in temperature are listed for the case with $T_{\text{flow 1}} > T_{\text{flow 2}}$ for all three acquired slices. The corresponding temperature decrease determined by the fiber optical probe between $T_{1,\text{in}}$ and $T_{1,\text{out}}$ was -1.537±0.004 K.

last at voxel≈70) are distinguishable which correspond to the eight rows of pins. An overall decrease of the mean ΔT by ~ -1.4 K, ~ -1.7 K, and ~ -1.8 K is observed (beginning of first pin row to about the end of eighth pin row which corresponds to the range of voxels between $\approx$ 284 and 60). As expected, rows containing two full pins lead to a substantially larger temperature change than the rows consisting only of a single full pin. The mean temperature decrease $\overline{\Delta T}_{60,284}$ was calculated for each slice individually and are listed in Tab. 9.4. All voxels located in the lower half of the pin fin array and in the voxel range from 60 to 284 were averaged.

Furthermore, to estimate the uncertainty of the PRF temperature measurements, the standard deviation of 50 consecutively acquired PRF temperature phase maps was determined (Fig. 9.8). For the majority of the data, the standard deviation is $\lesssim$0.5 K. However, it can be substantially larger in certain areas, as in the vicinity of air bubbles at the top of the pin fin array. To obtain the voxel-wise standard deviation of the mean, the standard deviation maps (Fig. 9.8) have to be multiplied by $1/\sqrt{50}$. Therefore, temperature uncertainties are up to $\lesssim$0.14 K. This approach provides a spatially resolved map of uncertainties, and thus accounts for local fluctuations e.g. due to turbulent flows.

Fig. 9.9 shows velocity magnitude maps and velocity vector fields for two distinct temperature settings. Clearly visible is the typical symmetric flow pattern around the pins and the approximately zero velocity at the back of the pins. In the zoomed vector image (Fig. 9.9d) two flow vortices with very small velocities are depicted at the back of the pins.

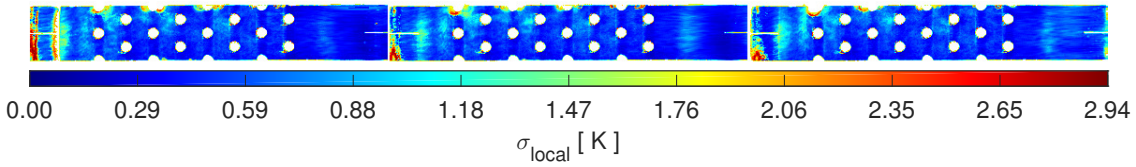

Figure 9.8: Inhomogeneous spatial temperature distribution: Voxel-wise standard deviation σ_{local} was calculated from 50 PRF temperature phase maps. Slice 1, slice 2, and slice 3 are shown from left to right.

Overall, velocities are very similar in magnitude and direction for the different temperature settings. The flow in this setup is mainly 2D and described by in plane (equal to X, Y) velocity components as shown in Fig. 9.10.
Due to the orientation of the pin fin array (length axis of pins $\parallel B_0$), gravitational force plays a role in inhomogeneous temperature distributions leading to temperature induced buoyancy forces. To estimate the influence of these forces, a Richardson number $Ri = 0.04$ of flow 1 was estimated by the project partner. This estimation suggests that temperature induced buoyancy forces on the flow pattern are negligible in this setup. The measured symmetric velocity fields, and thus acceleration fields support this result. In particular, the mean velocity values calculated for each vertical column and drawn along the direction of flow 1 (Fig. 9.11) depict clearly that the velocity component $\mathrm{v_x}$ (parallel to the gravitational force) is approximately 0 m/s which indicates that buoyancy forces are not important.
The *Re* numbers of flow 1 and flow 2 for the cooled acquisition with $T_{\mathrm{flow\ 1}} = 40\,^{\circ}\mathrm{C}$ and $T_{\mathrm{flow\ 2}} = 12\,^{\circ}\mathrm{C}$ are 3000 and 7200, respectively (determined by the project partner).

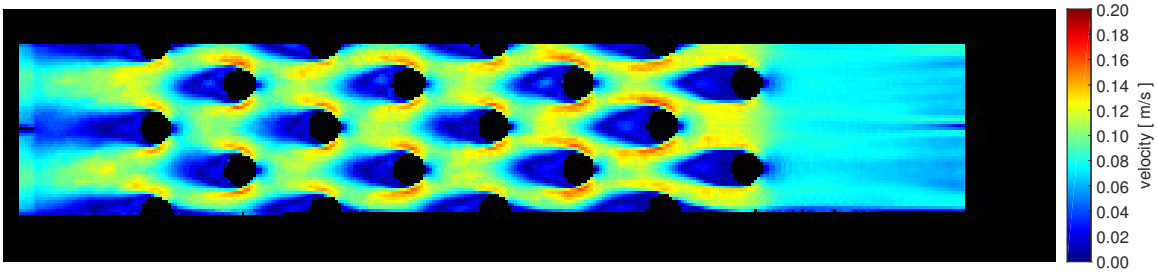

(a) Velocity magnitude at $T_{\text{flow }1} = 40\,^{\circ}\text{C}$, $T_{\text{flow }2} = 12\,^{\circ}\text{C}$

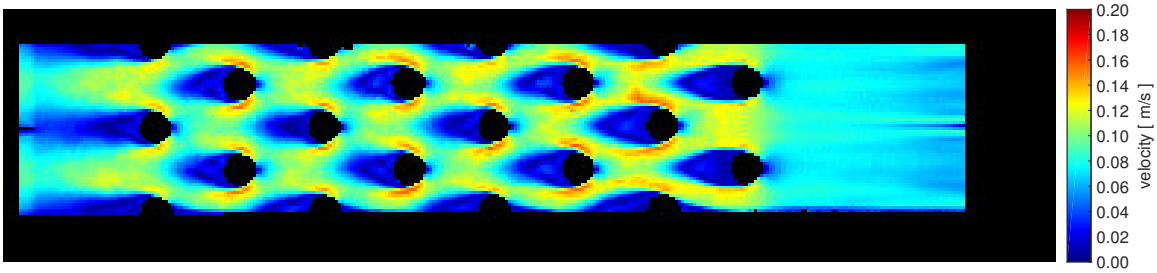

(b) Velocity magnitude at $T_{\text{flow }1} = 40\,^{\circ}\text{C}$, $T_{\text{flow }2} = 40\,^{\circ}\text{C}$

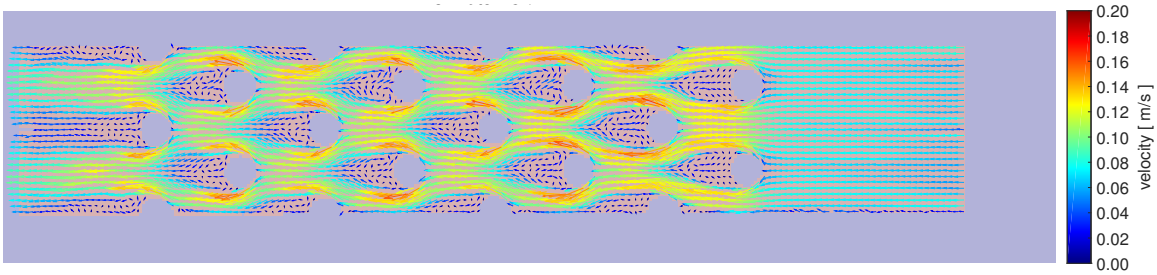

(c) Velocity vector field at $T_{\text{flow }1} = 40\,^{\circ}\text{C}$, $T_{\text{flow }2} = 12\,^{\circ}\text{C}$

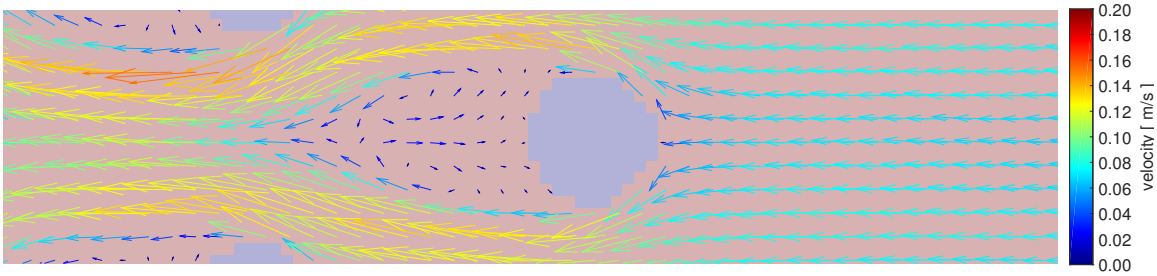

(d) Velocity vector field at $T_{\text{flow }1} = 40\,^{\circ}\text{C}$, $T_{\text{flow }2} = 12\,^{\circ}\text{C}$ (zoom to lower right part of Fig. 9.9c)

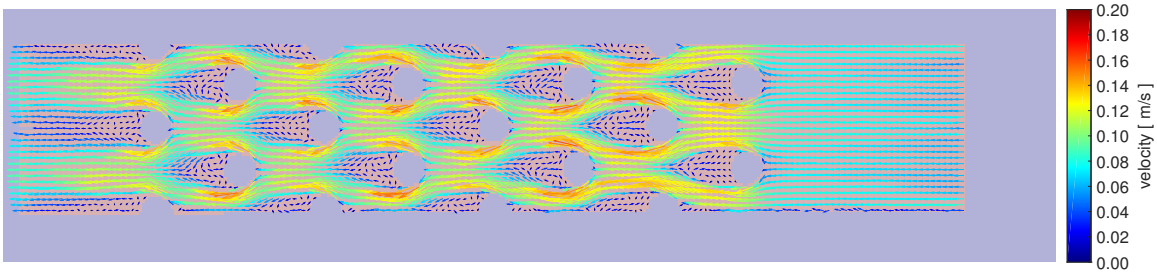

(e) Velocity vector field at $T_{\text{flow }1} = 40\,^{\circ}\text{C}$, $T_{\text{flow }2} = 40\,^{\circ}\text{C}$

Figure 9.9: The magnitude of the velocity and the velocity vector fields are shown for the case with $T_{\text{flow }1} > T_{\text{flow }2}$.

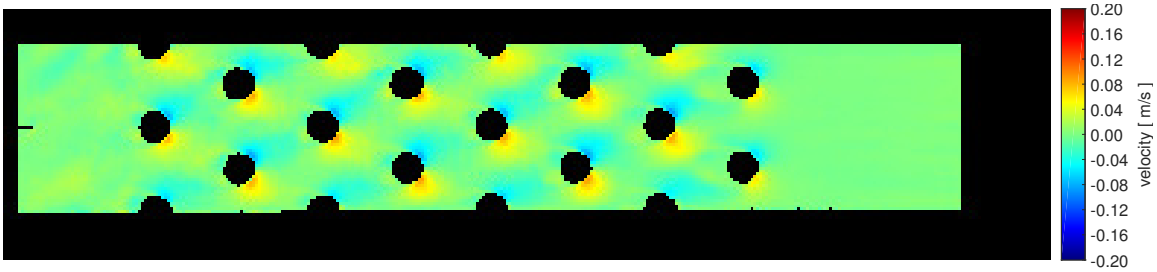

(a) Velocity v_{x} at $T_{\mathrm{flow}\ 1} = 40\,^{\circ}\mathrm{C}$, $T_{\mathrm{flow}\ 2} = 12\,^{\circ}\mathrm{C}$

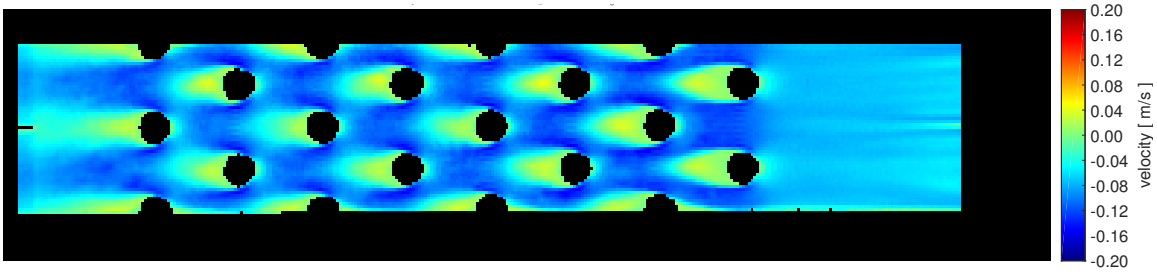

(b) Velocity v_{y} at $T_{\mathrm{flow}\ 1} = 40\,^{\circ}\mathrm{C}$, $T_{\mathrm{flow}\ 2} = 12\,^{\circ}\mathrm{C}$

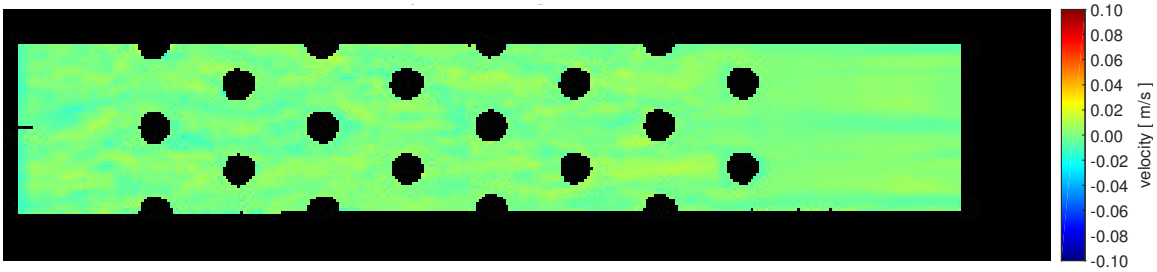

(c) Velocity v_{z} at $T_{\mathrm{flow}\ 1} = 40\,^{\circ}\mathrm{C}$, $T_{\mathrm{flow}\ 2} = 12\,^{\circ}\mathrm{C}$

Figure 9.10: The individual velocity components of one slice (velocity component maps) are depicted for the temperature setting with $T_{\mathrm{flow}\ 1} > T_{\mathrm{flow}\ 2}$. Note, the different colormap scale for the Z component.

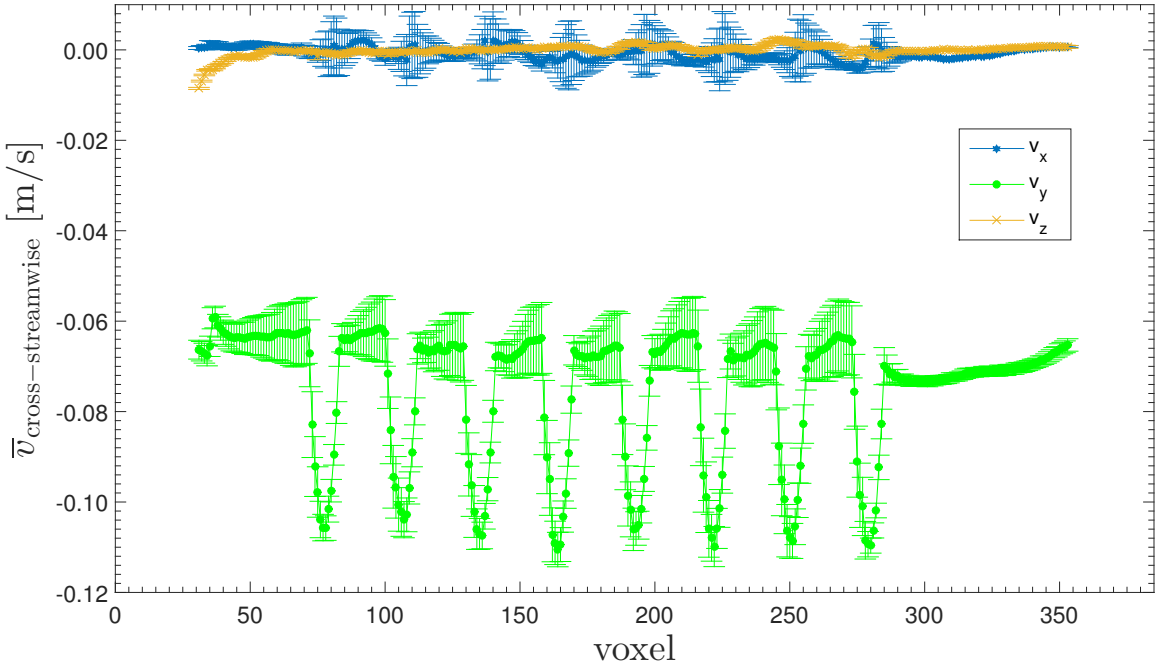

Figure 9.11: Mean velocity values of the velocity components v_x, v_y, v_z and the standard deviation of the mean were determined for each cross-streamwise column of voxels. The three slices acquired for each individual velocity component had been averaged before. The X axis here is identical to the X axis shown in Fig. 9.6 and Fig. 9.7. Therefore, voxel 284 corresponds to the beginning of pin row one, and voxel 70 corresponds the end of pin row eight.

Based on the velocity data, acceleration fields and magnitudes could be derived by applying Eq. (8.6) and are shown in Fig. 9.12. Additionally, individual components of the acceleration are shown for one temperature setting in Fig. 9.13. The fluid decelerates before the pin, and it is accelerated towards the side walls of the pin. As in the case of the velocity data, there are only minor differences in the acceleration which occurs inside flow 1 at temperature settings $T_{\text{flow 1}} = 40\,^{\circ}\text{C}$, $T_{\text{flow 2}} = 12\,^{\circ}$ or $T_{\text{flow 1}} = 40\,^{\circ}\text{C}$, $T_{\text{flow 2}} = 40\,^{\circ}$. Locally, acceleration differences are $\sim 0.8\,\text{m/s}^2$.
The measurements with an additional flow model, to analyze the impact of acceleration on the PRF temperature phase maps, revealed no relevant increase or decrease in temperature at the vicinity of the wall of the barrier (Fig. 9.14a) where high velocity gradients occurred (Fig. 9.14b). The rmsd at the barrier between the voxels outside and the average temperature inside the barrier ($\Delta T_{\text{barrier}} = 14.7171 \pm 0.0007\,\text{K}$) revealed 0.6 K. Furthermore, the PRF temperature phase data was normalized by T_{barrier}. ΔT values along a horizontal line crossing through the middle of the barrier are shown as red triangles in Fig. 9.14c. The average temperature inside the barrier was used for normalization to make the comparison independent of temperature offsets e.g. due to field drifts. Fig. 9.14c shows that normalized temperature values located inside and outside the barrier are close to 1. Hence, the forced convection flow and in particular the convective acceleration occurring at the barrier does not cause relevant artifacts in the PRF temperature phase maps. The increasing deviation towards decreasing voxel numbers in Fig. 9.14c is likely caused by air bubbles which were stuck to the wall of the flow channel. Furthermore, normalized PRF ΔT data acquired with the non-stretched gradient scheme is included in Fig.9.14c since this gradient scheme was expected to be less prone to acceleration effects. However, both gradient schemes perform similarly well.

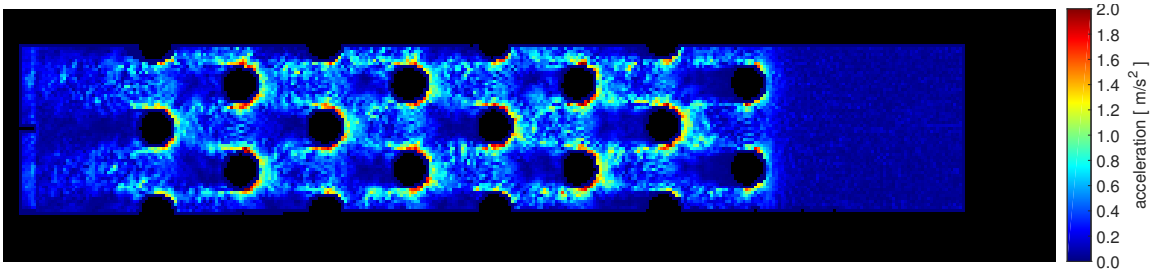

(a) Acceleration magnitude at $T_{\text{flow }1} = 40\,^{\circ}\text{C}$, $T_{\text{flow }2} = 12\,^{\circ}\text{C}$

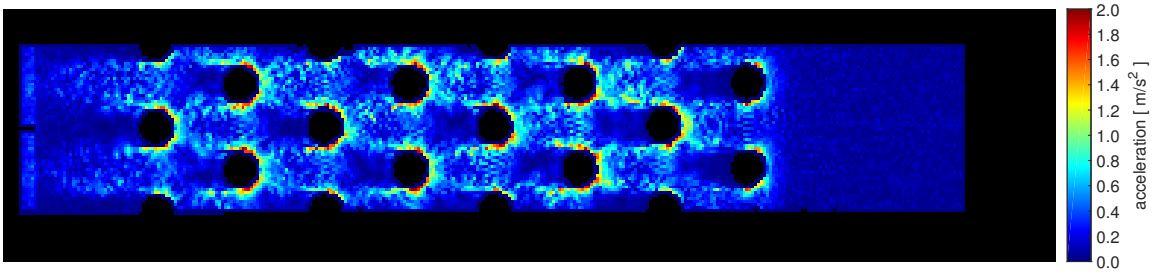

(b) Acceleration magnitude at $T_{\text{flow }1} = 40\,^{\circ}\text{C}$, $T_{\text{flow }2} = 40\,^{\circ}\text{C}$

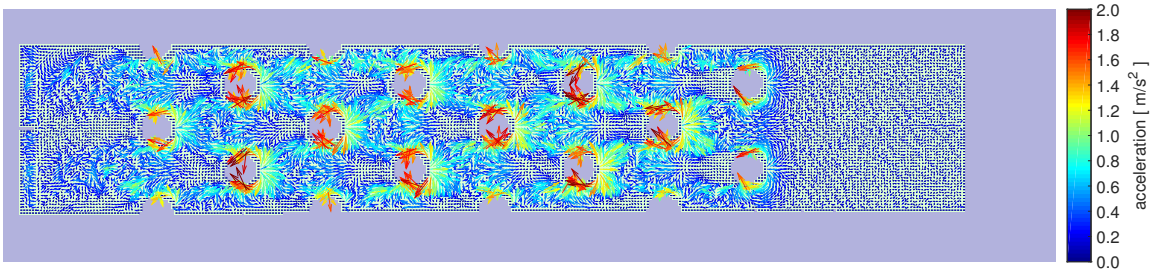

(c) Acceleration vector field at $T_{\text{flow }1} = 40\,^{\circ}\text{C}$, $T_{\text{flow }2} = 12\,^{\circ}\text{C}$

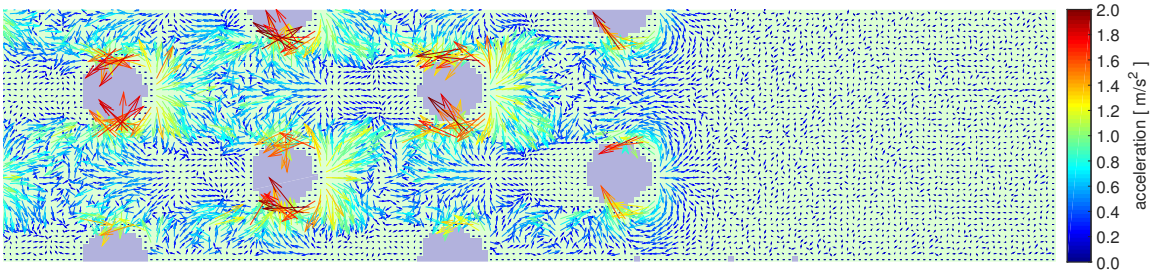

(d) Acceleration vector field at $T_{\text{flow }1} = 40\,^{\circ}\text{C}$, $T_{\text{flow }2} = 12\,^{\circ}\text{C}$ (zoom to lower right part of Fig. 9.12c)

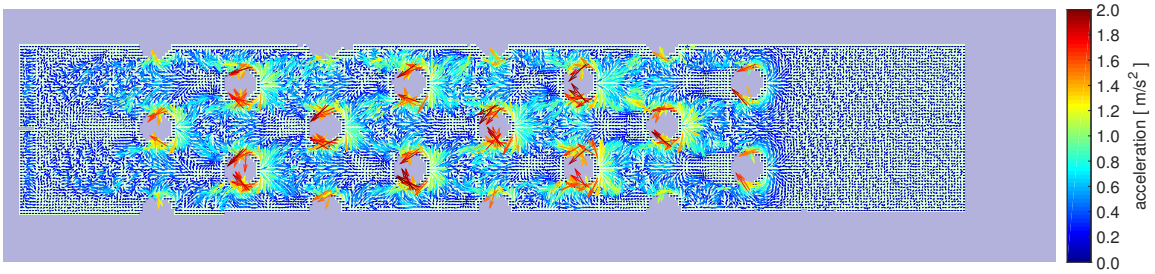

(e) Acceleration vector field at $T_{\text{flow }1} = 40\,^{\circ}\text{C}$, $T_{\text{flow }2} = 40\,^{\circ}\text{C}$

Figure 9.12: The magnitude of the acceleration and the acceleration vector fields are shown for the case with $T_{\text{flow }1} > T_{\text{flow }2}$.

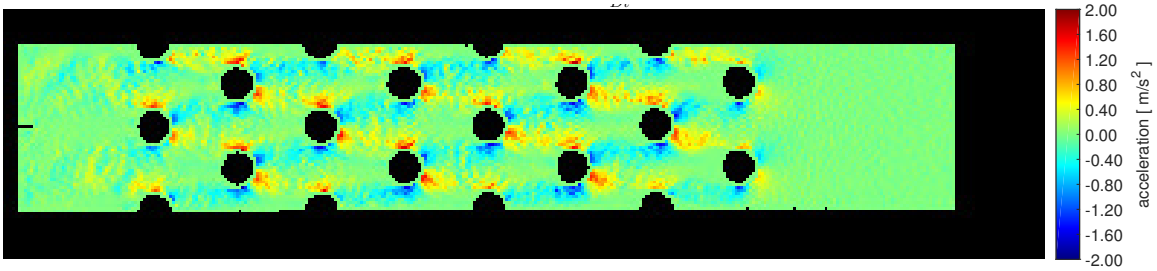

(a) Acceleration a_{x} at $T_{\mathrm{flow}\ 1} = 40\,^{\circ}\mathrm{C}$, $T_{\mathrm{flow}\ 2} = 12\,^{\circ}\mathrm{C}$

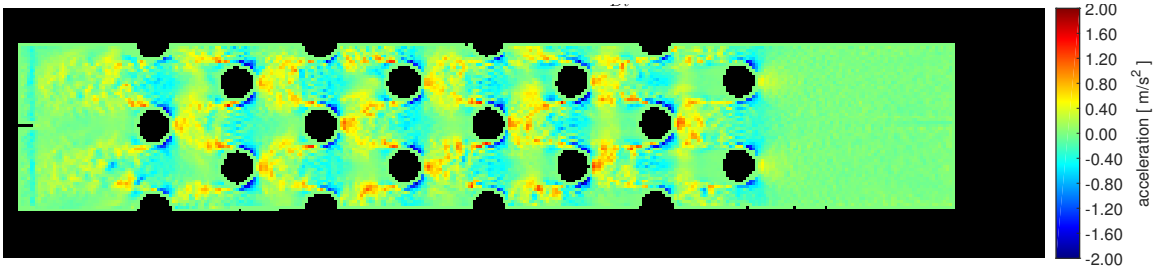

(b) Acceleration a_{y} at $T_{\mathrm{flow}\ 1} = 40\,^{\circ}\mathrm{C}$, $T_{\mathrm{flow}\ 2} = 12\,^{\circ}\mathrm{C}$

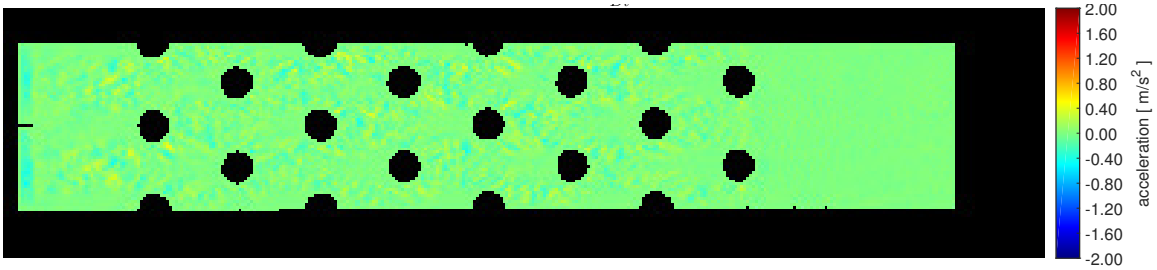

(c) Acceleration a_{z} at $T_{\mathrm{flow}\ 1} = 40\,^{\circ}\mathrm{C}$, $T_{\mathrm{flow}\ 2} = 12\,^{\circ}\mathrm{C}$

Figure 9.13: The individual acceleration components are depicted for one temperature setting with $T_{\mathrm{flow}\ 1} > T_{\mathrm{flow}\ 2}$.

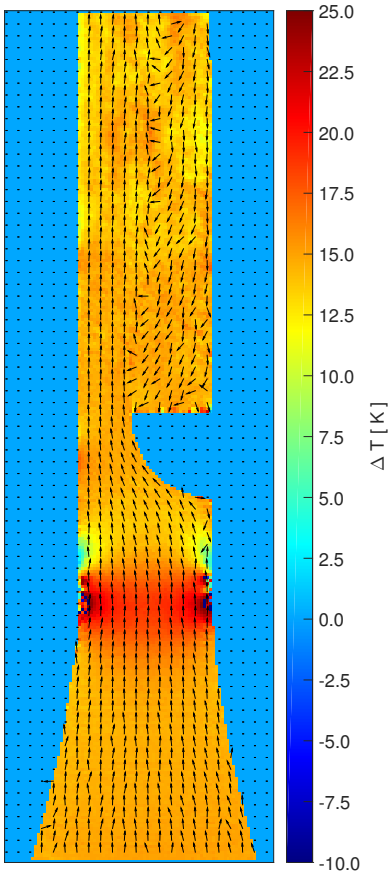

(a) PRF temperature phase map and velocity vector field

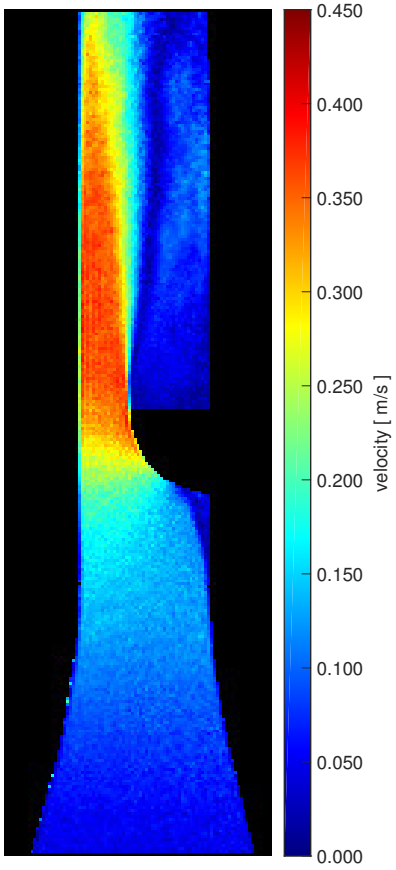

(b) Velocity magnitude map

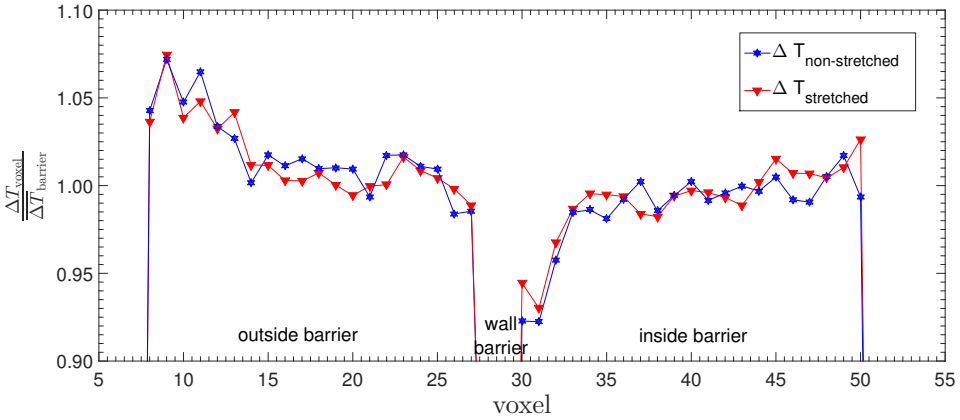

(c) Normalized ΔT along a horizontal line (left to right) cutting approximately through the middle of the barrier. Additionally, data of the non-stretched gradient scheme is depicted for comparison.

Figure 9.14: A superposition of the PRF temperature phase map and the corresponding velocity vector field is presented for the rectangular flow channel with a barrier located inside the flow. Additionally, a velocity magnitude map is shown. The direction of the forced convection flow is from bottom to top. The left side of e.g. the magnitude image corresponds to the top of the flow channel and the right side corresponds to the bottom of the flow channel. The location of the flange connecting the flow preparation section to the inflow section of the flow channel is clearly visible as artifact in the PRF temperature phase maps (red stripe).

9.3 Discussion

This case study presents a more complex MR compatible flow model than the counter current double pipe heat exchanger and was again developed in close cooperation with the fluid mechanical project partner. As in the case of the double pipe experiment velocity as well as temperature were determined from MR phase images. Thus, the MRI methods established for the double pipe setup to obtain accurate results were transferred to study the pin fin array. The entire experimental setup provided very stable experimental conditions to study the velocity as well as temperature fields.
The pin fin flow model provided an axial symmetric 2D temperature and velocity distribution since flow parallel to the pipes was small and buoyancy forces were found to be negligible. In contrast, the buoyancy forces played an essential role in developing 3D temperature and velocity fields in the double pipe flow model. Furthermore, the flow was more turbulent in the pin fin array compared to the double pipe heat exchanger (Reynolds number of the pin fin array with 3000 is about a factor of 1.7 larger). Hence, contributions due to acceleration might be of greater importance in this setup. For this reason, the two different gradient schemes implemented to acquire PRF temperature phase data were studied in this setup (case with $T_{\text{flow }1} = T_{\text{flow }2}$) since they were expected to be differently susceptible to acceleration errors. A summary about this comparison and major outcomes were already shown and discussed in section 6.1. Generally, the two gradient schemes revealed similar PRF temperature phase maps, however, the rmsd values for the non-stretched gradient scheme were higher than for the stretched gradient scheme (deviation up to 15%). The rmsd between the MR data and the fiber optical probes was in the order of 1 K. The major contribution to this error was expected to arise from insufficient first and higher order background phase errors since the position of the reference phantom allowed solely a constant offset correction.
Overall, the case considering $T_{\text{flow1}} = T_{\text{flow2}}$ (Figs. 9.5a and 9.5b) provides evidence of the accuracy of the MRT measurements since the PRF temperature distribution was highly homogeneous. The temperature changes in the pin fin flow model of this case could be accurately measured with $\lesssim 1$ K (see rmsd values of stretched gradient scheme in Tab. 9.3, and see also Fig. 9.6). This value included several errors originating from noise, susceptibility effects, displacement, acceleration, and field drifts and were discussed in detail for the pin fin flow model below. Additional evidence for the accuracy of the inhomogeneous maps is provided by the decrease of the mean ΔT values by approximately on average 1.6 K (Fig. 9.7, voxel ≈60 to voxel ≈285) which is in close agreement to the temperature decrease measured by the fiber optical probes (1.537±0.004 K). However, to determine the outlet temperature changes exactly, a complete homogeneous mixing of the temperatures is required. For this the connection due to the flange would need to be moved further away from the flow model to prolong the outlet channel where the mixing could take place and to avoid artifacts being induced in the PRF temperature phase maps.

9.3.1 Possible sources of error

The majority of possible error sources discussed in detail for the double pipe setup are of the same order of magnitude in this setup. Since the uncertainty on the temperature phase or velocity phase is indirectly proportional to the SNR, averaging was performed to account for possible reduction of SNR due to higher turbulent flow and also because of

the 2D instead of 3D data acquisition.
Temperature dependent susceptibility effects were observable at the flanges connecting the pin fin model to the bends. Whereas, no artifacts due to the flanges arose in MRV data (remember, both acquisitions to determine velocities are performed at the same temperature, p. 107). To avoid these kinds of image artifacts in PRF temperature phase mapping, connections to the flow model have to be designed differently or if possible moved far outside the region of interest. Additionally, structures where air can be trapped should be avoided in the design of flow models. To perform acquisitions with hot fluid passing though the copper pipes, the fluid providing flow 1 would need to be degased to avoid generation of air bubbles at the surface of the copper pipes.
Furthermore, errors due to spin displacement are still within the spacial resolution of the MR data, and thus not expected to contribute to substantial image distortions. Also in this setup, the motion of the spins follows layers with slowly varying velocities, and heat conduction across this layers is assumed to be of minor influence on the overall temperature distribution. Therefore, velocity or temperature averaging through spins traveling along steep temperature or velocity gradients within TE are not expected.
The estimation of acceleration differences revealed an up to four times larger value than in the case of the double pipe setup leading to an estimated temperature error of $\sim 0.56\,\mathrm{K}$. This error value would transform to values depicted at 1.04 or 0.96 in the normalized plot (Fig. 9.14c). However, values determined from temperature data acquired at even a four times larger flow rate were close to 1 (range within 0.995 and 1.02) and thus, the contribution of acceleration errors on the PRF temperature phase maps is expected to be negligible in this setup. The same applies for the MRV data since the velocity error related to acceleration was estimated to be in the order of $\sim 0.003\,\mathrm{m/s}$ (derived in a similar manner as described in subsection 8.3.1 of the double pipe setup). A shorter TE (reducing acceleration effects) could be applied in the MRV acquisition of the pin fin flow model since no severe higher order distortions occurred as in the case of the double pipe heat exchanger (see subsections 6.1 and 8.3.1). To correct for eddy currents an additional acquisition without any flows was used since the distribution of the reference phantoms would not allow for first order corrections.
As in the case of the double pipe heat exchanger, the field drift is expected to contribute substantially to the overall uncertainty of the PRF temperature phase maps since other sources of error were found to be small compared to the values measured. In particular since the reference phantoms could only be placed on top of the pin fin setup, the zeroth order correction became less reliable. However, the half pins could be designed in a similar manner as the obstruction in the flow model (Fig. 9.3) consisting of a thin shell and the inside filled with the same fluid as used for the MR measurements. Thereby, the reference phantoms would be integrated into the setup and allow monitoring of the field drift at various locations along the flow model. Of major importance, however, is that the temperature change at each of these phantoms need to be known. Thus, this would be only practical for the case investigating homogeneous temperature distributions with known temperature changes monitored by the fiber optical probes. For the inhomogeneously heated case, the temperature of flow 2 inside the copper tubes could be used for reference if monitored with fiber optical probes and if the copper pipes are replaced by ceramic pipes (pp. 67 ff.). Additionally, fluctuations are likely to occur in the flow of the pin fin array contributing to the overall uncertainty. To account for this, standard deviation maps of the PRF temperature phase data were determined to estimate the local uncertainty in

the temperature data. In a similar way a spatially resolved uncertainty map of the velocity data could be determined to obtain an estimate on the measurement uncertainty in higher turbulent flows (see also Bruschewski $et\ al.$[195]).

Chapter 10

Free convection inside a horizontal cylinder

In addition to PRF temperature phase mapping another approach was investigated in this work to monitor temperature distributions by MRI. It was based on PRF spectroscopy and applied on a free convection flow inside a horizontal cylinder. PRF spectroscopy allows for the measurement of absolute temperatures, and thus does not require a pair of acquisitions in order to calculate the phase differences. Furthermore, reference phantoms to monitor field drifts between the two acquisitions are not required.

10.1 Methods

10.1.1 Flow model design

The flow model was constructed by the project partner. It consists of a closed cylinder (referred to as a cell; ID = 80 mm, length of the cylinder = 80 mm) made of acrylic glass (Figs. 10.1a and 10.1c). The cell can be heated or cooled via two separate additional cylindrical cavities attached to each end of the cell. Each cavity is part of a closed flow circuit. Therefore, two separate closed flow circuits (denoted flow 1 and flow 2) provide the possibility of heating or cooling the cell. The fluid (in this case, water) of flow 1 as well as of flow 2 enters the cavities through the inlets and leaves them through the outlets. The inlet and outlet connections were made from PA using direct laser-sintering. The temperature of flow 1 and flow 2 are monitored at the center of the cylindrical cavities by temperature sensors.

The cell contained a 20 mM solution of DSS (4,4-dimethyl-4-silapentane-1-sulfonic acid) and double distilled water. Copper sulfate (1 g/l) was added to improve SNR for phase mapping methods such as MRV, in the case that such experiments are performed in future studies. The spectra of this solution provided two predominant peaks: one corresponding to water and one corresponding to DSS (Fig. 10.2). DSS is frequently used in NMR spectroscopy as a water-soluble NMR reference compound with a very small temperature-dependent chemical shift dependence [199, 200]. It is therefore assumed that the temperature-dependent chemical shift of this solution is dominated only by the shift of the water signal peak.

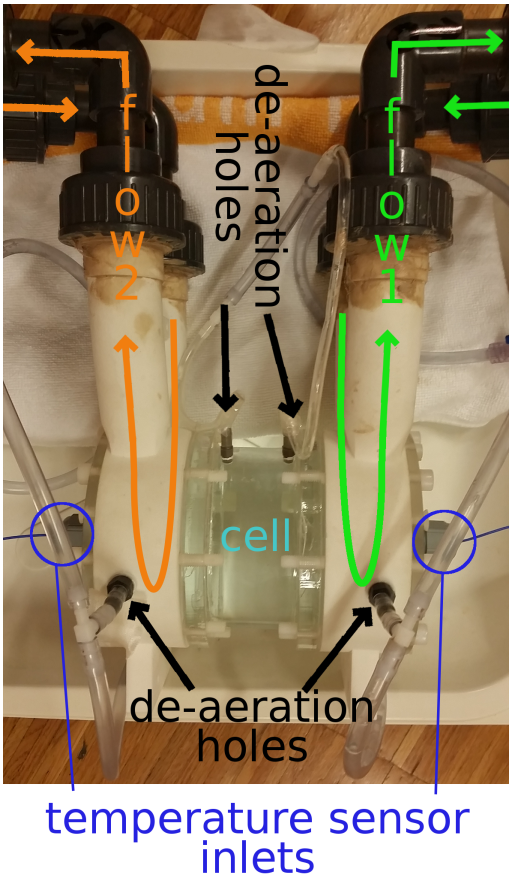

(a) Picture showing the main parts and features (top view)

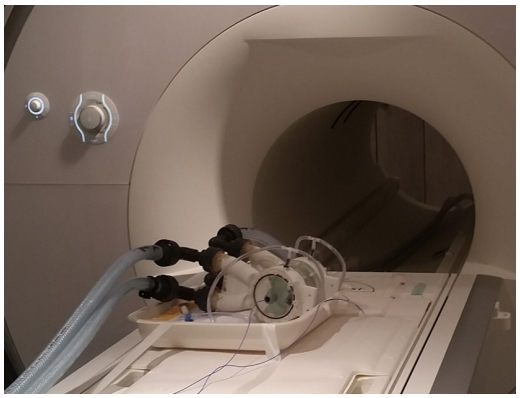

(b) Cylindrical flow model and its positioning on the table of the MR system

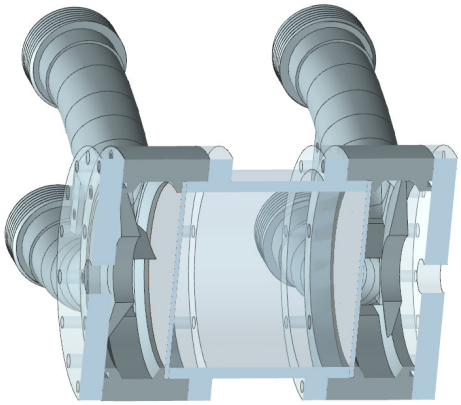

(c) 3D CAD drawing cut along the long axis of the cylinder

Figure 10.1: Various views of the cylindrical flow model are depicted. Fiber optical probes were inserted into the two inlets to measure the temperature of flow 1 ($T_{\text{flow 1}}$) and flow 2 ($T_{\text{flow 2}}$) at each side of the cell. The long axis of the cylinder was aligned parallel to B_0. CAD drawing was provided by the project partner.

10.1.2 Experiments

Chemical shift imaging (CSI) was performed using a stimulated echo acquisition mode (STEAM) sequence [201] with the applied CSI imaging parameters summarized in Table 10.1. The STEAM sequence was used instead of a point-resolved spectroscopy (PRESS) sequence [202] since it is less susceptible to chemical shift displacement artifacts due to the larger bandwidth of $90°$ RF pulses compared to $180°$ RF pulses.
Spectroscopy was performed with two different temperature settings for flow 1 ($T_{\text{flow 1}}$) and flow 2 ($T_{\text{flow 2}}$).

1. Homogeneous spatial temperature distribution i.e., $T_{\text{flow 1}} = T_{\text{flow 2}}$. A CSI acquisition with flow 1 and flow 2 both at 25.2 °C was conducted. Flow 1 and flow 2 were generated by the immersion heater and the HC-pump, respectively (see section 7.1.3 for specifications of the pumps).

CSI parameters	MRT
TE/TR/TM (mixing time) [ms]	20.0/1430.0/10.0
flip angle [°]	90
bandwidth [Hz]	1801.8
nominal spectral resolution [Hz]	0.9
nominal spatial resolution [mm^3]	$3.1 \times 3.1 \times 10.0$
CSI matrix	$32 \times 32 \times 1$
CSI slice orientation	transverse
water suppression	weak

Table 10.1: MR sequence parameters used for 2D MRT acquisitions of the cylindrical flow model. The total acquisition time of one CSI measurement was approximately 17 minutes.

2. Inhomogeneous spatial temperature distribution i.e., $T_{\text{flow 1}} > T_{\text{flow 2}}$. A CSI acquisition with flow 1 at a higher temperature than flow 2 ($T_{\text{flow 1}} = 30\,°\text{C}$, $T_{\text{flow 2}} = 15\,°\text{C}$) was conducted twice to check for reproducibility. As in the homogeneous case, flow 1 and flow 2 were generated by the immersion heater and the HC-pump, respectively.

The homogeneous spatial temperature distribution was applied to determine the equation for converting the temperature-dependent chemical shift into absolute temperatures (Eq. (4.5)). The second experiment (case with $T_{\text{flow 1}} > T_{\text{flow 2}}$) was performed to show that the

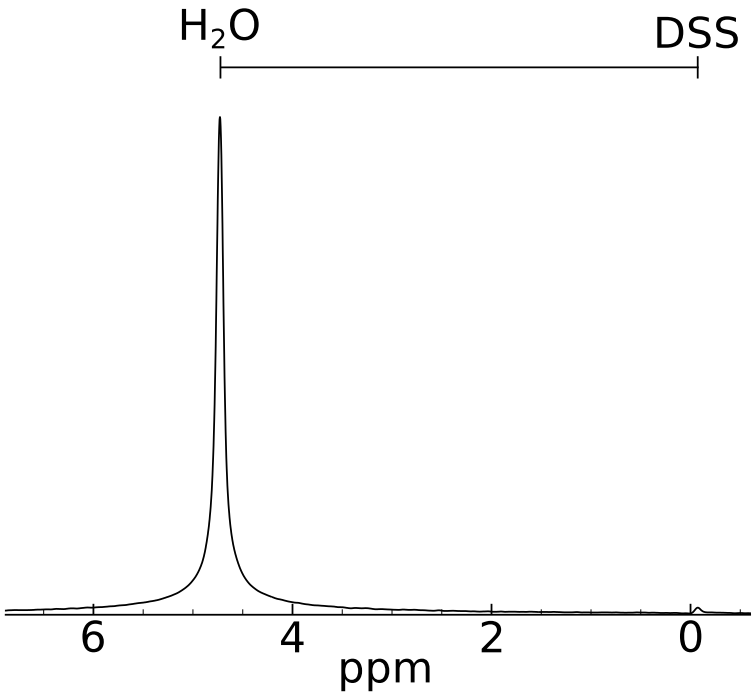

Figure 10.2: Example of a spectrum of one voxel acquired at a temperature of 25.2 °C. Clearly visible are the two separate peaks of water and DSS. The separation between both peaks (distance from maximum to maximum) is dependent on temperature.

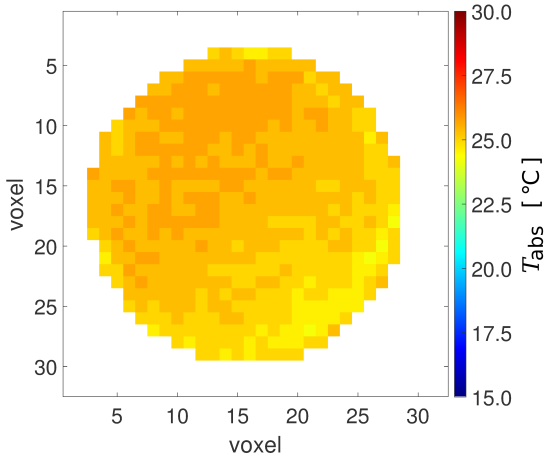

Figure 10.3: The 2D spatial temperature distribution is shown for the case with $T_{\text{flow 1}} = T_{\text{flow 2}}$ at the center of the cylindrical flow model.

applied PRF spectroscopy method is capable of measuring spatially inhomogeneous, 2D temperature distributions in fluid flow. The 2D temperature distribution was assumed to remain constant during the MR data acquisition.
The flow rate for flow 1 and flow 2 was according to the maximum possible supply provided by the two Julabo systems during all CSI acquisitions. Fiber optic probes were positioned into the inlets to measure $T_{\text{flow 1}}$ and $T_{\text{flow 2}}$. Since absolute temperature values were considered in the experiments, it was of high importance to account for the B_0 dependency of these probes (see section 7.2).
The spectroscopy data was evaluated using an in-house built software tool. The magnitude of the spectra were evaluated to avoid sensitivity to phase errors (see subsection 1.6). The water peak and the DSS peak were clearly non-overlapping and distinct (Fig. 10.2). The chemical shift between the two maxima of the peaks was determined to evaluate temperature. Zero filling was applied to the data to increase the nominal spectral resolution (by a factor of two) for a more accurate determination of the maxima of the peaks.

10.2 Results

The case with the homogeneous spatial temperature distribution was studied to determine the relationship between the chemical shift difference $\sigma_{\text{water,DSS}}$ of the two spectra peaks and temperature. In a central transverse slice the average chemical shift of all voxels in the cell was determined to be 4.80130 ± 0.00013 ppm at a temperature of $T_{\text{flow 1}} = T_{\text{flow 2}} = 25.27 \pm 0.07\,^{\circ}\text{C}$ (average temperature measured by the fiber optic probes $\pm$ standard deviation of the mean). With the value of α determined in subsection 7.1.2, the temperature dependent chemical shift offset was determined according to

$$4.80130\ [\text{ppm}] = -0.009706\ [\text{ppm}/^{\circ}\text{C}] \cdot 25.27\ [^{\circ}\text{C}] + \text{offset}\ [\text{ppm}]. \tag{10.1}$$

Thus, the temperature dependency of the chemical shift was

$$\sigma_{\text{water,DSS}}\ [\text{ppm}] = -(0.009706 \pm 0.000014)[\text{ppm}/^{\circ}\text{C}]\ T_{\text{abs}} + (5.0466 \pm 0.0008)\ [\text{ppm}]. \tag{10.2}$$

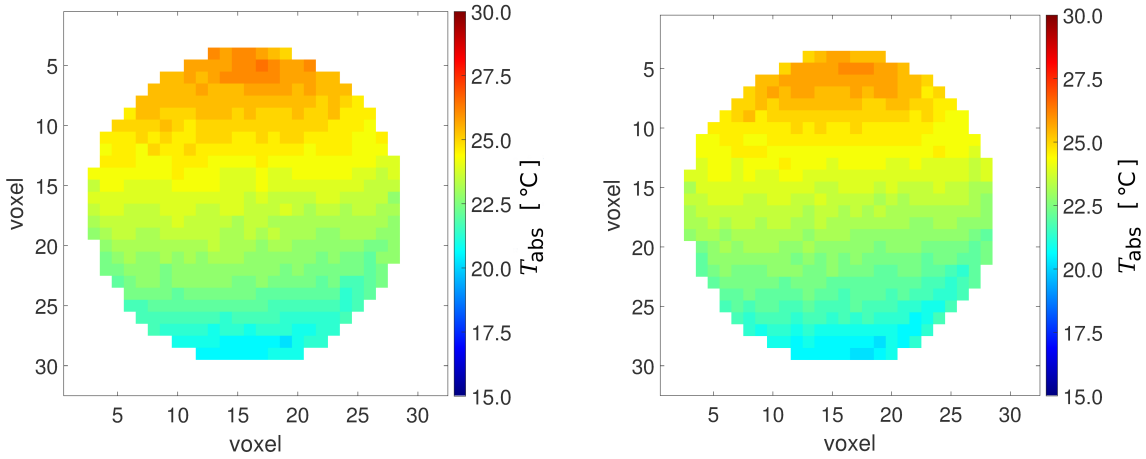

(a) Central slice (first acquisition) **(b)** Central slice (second acquisition)

Figure 10.4: Absolute temperature maps (transverse views) are shown for the case with $T_{\text{flow 1}} > T_{\text{flow 2}}$. They were acquired consecutively at the center of the cylindrical flow model.

Note that, for simplification and since solely temperatures of the fluid above $0\,°\text{C}$ were considered the temperature scale °C instead of Kelvin was considered to obtain Eq. (10.2). Thus, T_{abs} has to also be in units of °C.
For comparison, similar CSI measurements performed with a 10 mM solution of DSS and double distilled water revealed $\sigma_{\text{water,DSS}}\ [\text{ppm}] = -(0.0100 \pm 0.0003)[\text{ppm}/°\text{C}]\ T_{\text{abs}} + (5.049 \pm 0.007)\ [\text{ppm}]$. Eq. (10.2) can be rearranged such that T_{abs} is obtained for each voxel for a given $\sigma_{\text{water,DSS}}$ (similar to Eq. (4.5)).
Fig. 10.3 shows the spatial temperature distribution of the CSI data acquired with $T_{\text{flow 1}} = T_{\text{flow 2}} = 25.27 \pm 0.07\,°\text{C}$. The distribution is quite homogeneous with a small slope from top left to bottom right. The variations, however, are of the order of the error arising from the nominal spectral resolution of the data acquisition. This resolution sets the lower boundary on the accuracy of the temperature measurements and thus, the temperature can not be determined better than $\pm 0.8°\text{C}$ (determined with $\frac{1}{0.009706}[°\text{C}/\text{ppm}] \cdot \frac{0.9\ [\text{Hz}]}{123.19499\ [\text{MHz}]}$).
The case with $T_{\text{flow 1}} > T_{\text{flow 2}}$ was studied at the center of the cylindrical flow model and used for comparison of fiber optical probe temperatures and CSI data. The consecutively acquired 2D temperature maps at the central position (Figs. 10.4a and 10.4b) depict a warmer fluid at the top than at the bottom, as expected, because of the existing free convection flow inside the cell. A slightly more pronounced top-bottom asymmetry of the temperature profile is observed for the first acquired data (Fig. 10.4a) than for the second data set (Fig. 10.4b) indicating that the first acquisition might have been performed before a stable temperature distribution was reached. Central temperature gradients from top to bottom as well as from left to right are presented in Fig. 10.5. The vertical temperature gradients are approximately linear, whereas, the horizontal ones are equal to ≈ 0. Hence, a constant average temperature of approximately $23.5\,°\text{C}$ occurs along the horizontal symmetry axis. The average temperature along the horizontal symmetry axis is expected to be equal to $0.5 \cdot (T_{\text{flow 1}} + T_{\text{flow 2}})$ corresponding to a temperature of $22.4 \pm 0.3\,°\text{C}$ according to the fiber optical probes with $T_{\text{flow 1}} = 30.0 \pm 0.2\,°\text{C}$ and $T_{\text{flow 2}} = 14.7 \pm 0.2\,°\text{C}$ (temperatures

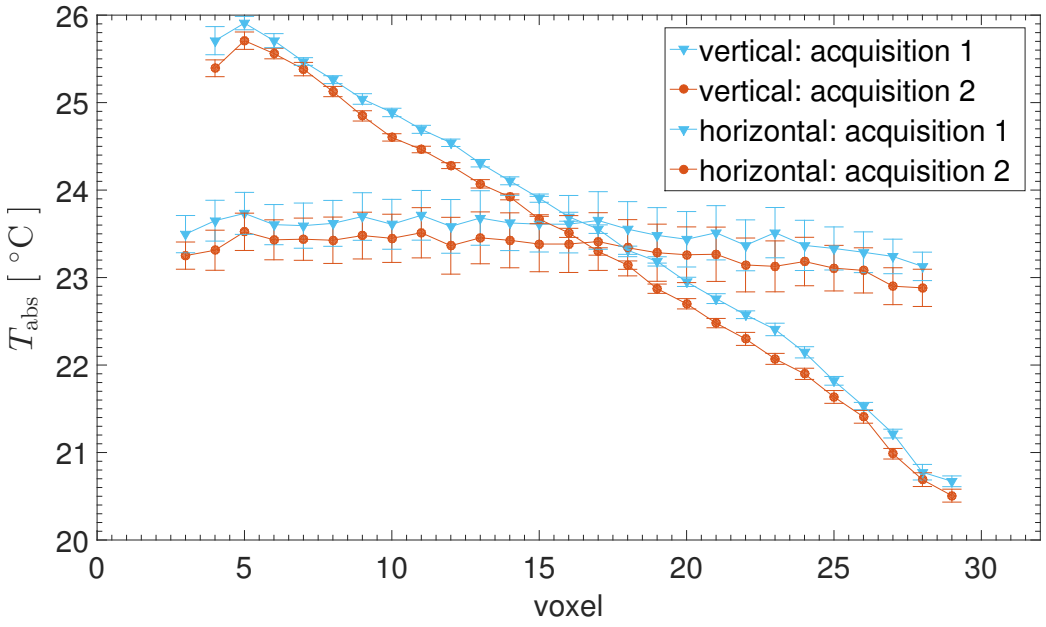

Figure 10.5: Average temperature gradients occurring from top to bottom (denoted with vertical) and from left to right (denoted with horizontal) are shown for the case with $T_{\text{flow 1}} > T_{\text{flow 2}}$. The mean and standard deviation of the mean is depicted by averaging voxels inside the cell either along a horizontal line (to obtain the vertical temperature gradient) or a vertical line (to obtain the horizontal temperature gradient).

measured by the fiber optical probes remained constant during all acquisitions).
In addition to the central slice, CSI slices positioned approximately 1 cm away from the cold and hot side of the cylindrical flow model were acquired and are shown in Fig. 10.6. The spectral peaks were corrupted at locally connected voxels of the 2D cross-section and showed two or even multiple maxima per peak. This results in erroneous chemical shift and temperature determination.

10.3 Discussion

This study presents an MR-compatible flow model that provides a natural convection flow if the two sides enclosing the cell are at different temperatures. It was developed in close cooperation between the project partner who focussed on the fluid mechanical questions, while this work addressed the MR aspect. This flow model was particularly suited for the application and testing of NMR spectrocopic methods for temperature mapping in fluid flows because it offers the ability to generate slow natural convection flow in a closed cavity of a given size. Slow flow in combination with slowly spatially varying temperature gradients are required in order to minimize temperature averaging in one voxel, since voxel sizes are typically in the order of 2-3 mm for NMR acquisitions. Spatial encoding of the CSI data occurs within 30 ms and displacement errors caused by the slow flow are not expected to be substantial compared to the CSI spatial resolution. Furthermore, a long read out time (approximately 1.1 seconds in this work) is required for CSI data acquisition to achieve an acceptable nominal spectral resolution, and thus, acceptable temperature

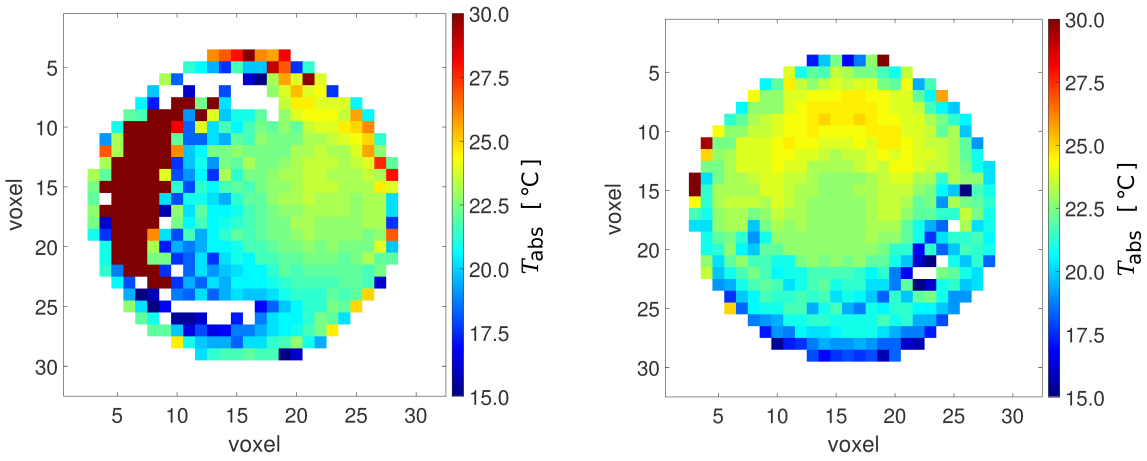

(a) Slice towards cold side **(b)** Slice towards hot side

Figure 10.6: Absolute temperature maps (transverse views) are shown for the case with $T_{\text{flow 1}} > T_{\text{flow 2}}$. They were acquired for slices positioned more closely towards the cold and hot side, respectively. White colored voxels inside the cell correspond to temperatures $\leq 15°C$.

accuracy. Hence, spatially encoded fluid flows have to remain within the region where the signal can be detected completely. This is the case in a closed cavity as used in this work.

The case with $T_{\text{flow 1}} = T_{\text{flow 2}}$ was used to obtain the conversion of the temperature-dependent chemical shift to temperature. The determined conversion equation was similar to the one obtained for pure water. The value of 0.0100 ± 0.0003 for pure water agrees excellently with literature values (see section 4.1), which provides evidence that the experimental procedure applied in this work yielded correct results. The copper sulfate added to the flow model caused only small alterations of the temperature coefficient (approximately 3%) as well as that of the chemical shift offset (approximately $\ll$1%) if compared to pure water. Furthermore, the case with homogeneous 2D spatial temperature distribution offered the possibility to check for distortions which may occur locally, and for example corrupt the water peaks such that two maxima appear per peak. Thus, problems arising from components of the setup such as the choice or shape of the materials may be detected and eliminated in this way. However, no severe distortions of the spectra were observed in the case with $T_{\text{flow 1}} = T_{\text{flow 2}}$ acquired at the center of the cylindrical flow model. Additionally, comparing the spectra of the case with $T_{\text{flow 1}} = T_{\text{flow 2}}$ to the spectra of the case obtained with $T_{\text{flow 1}} > T_{\text{flow 2}}$ may help to detect heat-and flow-related issues. For example the FWHM of the water peaks and the DSS peaks was determined for both cases. On average, a small increase of the FWHM of both peaks (approximately 4%) for the inhomogeneously heated case was observed which might be due to the intra-voxel temperature gradients.

For the inhomogeneously heated case, the cross-sectional stable temperature profile showed a symmetric profile at the center of the Cylindrical flow model. This heat distribution was expected due to the free convection flow in this kind of heating and assuming that the energy exchange between the cylindrical flow model and its surrounding air is negligible. Furthermore, since the central cross-sectional slice was considered, the average

temperature along the horizontal central line of the 2D slice can be compared with the average temperature of the fiber optical probes. The average temperature of the fiber optical probes agrees well with the average temperature along the horizontal central line (within approximately 1 °C). This comparison gives evidence that the NMR spectrocopy methods are reliable. The observed constant offset towards higher temperature could be related to an overestimation of the temperature inside the cell during the calibration acquisition (case with $T_{\text{flow 1}} = T_{\text{flow 2}}$). The calibration acquisition might be performed before a stable homogeneous temperature distribution was achieved.

The cross-sectional stable temperature profiles measured in the vicinity of the hot and cold side attached to the cylindrical flow model showed severe distortions of the water as well as of the DSS peaks affecting larger areas. The distortions were considered to be most likely because of B_0 inhomogeneities in combination with the weak water suppression. At the vicinity of the hot and cold side of the flow model B_0 inhomogeneities are likely to occur because of the geometric complexity which no longer offers a cylindrical symmetry. Careful shimming might reduce these distortions of the spectra. Furthermore, measurements at these locations with $T_{\text{flow 1}} = T_{\text{flow 2}}$ might help to clarify the origin of the distortions.

Overall, NMR spectrocopy could be applied in order to measure 2D temperature profiles with an accuracy of approximately ± 1 °C in free convection flow at the central section of the cylindrical flow model. The absence of additional reference phantoms to monitor field drifts was beneficial due to the reduction in the complexity of the setup, and thus susceptibility related issues could be reduced. However, major shortcomings of this temperature mapping technique were the considerably long acquisitions times (2D slice: $\sim$17 min versus $\sim$11 s) and the poor spatial resolution (factor of three difference in the presented measurements) compared to PRF temperature mapping. Nonetheless, NMR spectroscopy can be useful for the determination of temperature coefficients, since for this method field drifts are not relevant. In contrast, field drifts were considered to be the main source of uncertainty in the PRF temperature maps, and thus affect the temperature coefficient measurements as presented by Peter *et al.* [77]. Furthermore, temperature errors might be more easily identified in the spectra of NMR spectroscopy than in the phase images of the PRF temperature phase mapping method.

The focus of the study performed was to investigate the feasibility of measuring temperature using PRF spectroscopy in fluid flow. As of yet however, PRF temperature phase mapping for comparison was not performed because unlike PRF spectroscopy, this method requires insulated reference phantoms to be placed next to the flow model. In doing so, this may have affected the spectroscopic results, leading to a loss of accuracy. As a next step, PRF temperature phase mapping will be performed and compared to the PRF spectroscopy results in order to analyze the potential sources of error in the two methods.

Part IV

Summary and Outlook

The feasibility of measuring reliably high spatially resolved 2D and 3D temperature distributions in the same measurement session like velocity fields in fluid flows using MRI was demonstrated in this thesis. MRT data acquisition strategies were developed and successfully implemented to provide accurate and precise results.
These required modifications of the MR imaging sequence in addition to thorough adjustments of imaging parameters to minimize systematic measurement errors. In particular, phase contrast methods use phase accumulation to measure velocity by the motion along a magnetic field gradient. However, changes in temperature or susceptibility also manifest as phase variations, and therefore confound any desired velocity measurement. To prevent these errors, the temperature was kept constant during MRV measurements and for MRT measurements a velocity compensation was implemented.
To account for magnetic field inhomogeneities, a careful examination and selection of materials was done. Flow model designs which revealed on the one hand accurate and precise velocity maps can on the other hand cause severely distorted PRF temperature phase maps. The distribution can be due to temperature dependent changes of susceptibilities between the reference acquisition and the actually heated or cooled acquisition. This made it necessary to thoroughly investigate possible artifacts that could affect MRT measurements. The studies lead to a set of design rules that allow measurement of temperature fields in a variety of flow scenarios, thereby demonstrating that MRT has potential as a tool for fluid engineering.
To establish heating or cooling, copper pipes have been incorporated into thermofluid models. To the author's knowledge, such thermofluid models are investigated for the first time using MRT and MRV. Metal components were positioned next to the region of interest in the field of view without causing substantial measurement errors (if certain precautions concerning shapes and orientation were considered). As previously stated, copper is important for the flow models because of its high thermal conductivity and because of its good susceptibility matching to the measurement fluid. Furthermore, copper pipes prevent artifacts in the MR data which could arise from the flow inside the pipes. It was clearly shown that sensor inlets can cause substantial temperature errors in the PRF temperature phase maps. Therefore, the placement of temperature sensors for reference through inlets has to be selected with care. Moreover, as presented in this thesis, the temperature measurement system used to provide the reference temperature has to be checked for possible magnetic field dependencies of the temperature results. This will be especially important if these sensors are placed into strong static magnetic fields.
Further main tasks of this thesis were first, the selection of an appropriate temperature sensitive MR parameter which is applicable in fluid flows and second, the corresponding individual post processing of the temperature data. The MRT method based on phase contrast was selected, since it is known that this method is capable of precisely measuring small changes in temperature in static applications. In this thesis, PRF temperature mapping was successfully extended in order to acquire high spatially resolved temperature distributions in fluid flows as demonstrated in various thermofluid flow models. Accurate and precise acquisition of 3D velocity and temperature fields inside the double pipe heat exchanger showed 3D temperature maps with unprecedented detail and also demonstrated the coupling of these two fields. Moreover, measurements of 2D velocity and temperature fields inside a pin fin array heat exchanger demonstrated that the established method can be used in more complex models.
Compared to PRF spectroscopy, PRF temperature phase mapping provided a higher spa-

tial resolution within a substantial shorter measurement time. The high spatial resolution is important in order to resolve small features such as the thin structure of the plume inside the annulus of the double pipe heat exchanger. A 2D temperature map in free convection flow acquired with PRF spectroscopy represents a possible alternative method that could be used for a different set of engineering scenarios.
In conclusion, the case studies presented in this thesis clearly show that MRI excellently extends the possible conventional experimental temperature and velocity measurement tools, which are applicable to engineers and many other fields of science.
Regarding post processing, the quality of the temperature maps was substantially improved by considering single coil phase data. The data acquisition was performed with multiple receiver coils to yield a higher signal to noise ratio. Furthermore, the correction of field drifts was essential to obtain accurate temperature results, since they were a major source of error, corrupting the PRF temperature maps acquired in this thesis. Insulated reference phantoms positioned in the vicinity of the flow models to estimate these drifts worked well as the accurate temperature results indicate. Additionally, also other possibilities to detect field drifts were tested and were discussed in this thesis with respect to their advantages and challenges compared to the approach used.
The flow models covered in this thesis establish important foundations in order to address more complex questions in the fields of fluid mechanics and thermodynamics. However, exchanging the flow model also requires a thorough consideration of the MR imaging parameters and flow parameters to ensure that possible sources of error are minimized with respect to the underlying velocity or temperature distribution. For example, the sensitivity to temperature changes increases with a longer echo time. However, a longer echo time increases the sensitivity to displacement artifacts or acceleration induced phase errors. An increase of the signal to noise ratio can be achieved by using a lower bandwidth of the receiver. This may lead to displacement errors. Acceleration compensation is not currently included in the MR imaging sequence applied in this thesis. Nonetheless, in some circumstances it could be important to compensate for higher orders of motion. As presented in this thesis, the imaging parameters represent a general trade-off between these various effects.
The application of the developments in this thesis were in the context of engineering. Nevertheless, there are also possible medical applications. For example, a better estimate of the thermal dose during thermal interventions is desirable to ensure an efficient treatment of a tumor while leaving surrounding healthy tissue unaffected. The heat transport via blood flow is of great interest in the vicinity of large blood vessels, and flow models could be designed to address this question using MRV and MRT.
Since velocity and temperature fields are closely coupled for a vast majority of cases in fluid flows, the ability to measure both quantities is of great interest. It especially improves the understanding of processes involving heat transfer. Currently no other common measurement technique exists which could non-invasively measure 3D temperature and velocity distributions with comparable performance and speed. Therefore, the results of this thesis open up the possibility to gain new insights into fundamental heat transfer phenomena.

Publications

Journal articles

E. S. M. Ali, **W. Buchenberg**, and D. W. O. Rogers, Sci—Fri PM: Dosimetry—05: Megavoltage electron backscatter: EGSnrc results versus 21 experiments, Med. Phys. **41**, 27 (2014);

W. B. Buchenberg, T. Dadakova, J. Groebner, M. Bock, and B. Jung, Comparison of two fiber-optical temperature measurement systems in magnetic fields up to 9.4 Tesla, Magnetic Resonance in Medicine **73**, 2047 (2015).

W. B. Buchenberg, W. Mader, G. Hoppe, R. Lorenz, M. Menza, M. Büchert, J. Timmer, and B. Jung, In vitro study to simulate the intracardiac magnetohydrodynamic effect, Magnetic Resonance in Medicine **74**, 850 (2015).

B. Jung, C. Müller,**W. Buchenberg**, M. Ith, D. Reineke, F. Beyersdorf, and C. Benk, Investigation of hemodynamics in an in vitro system simulating left ventricular support through the right subclavian artery using 4-dimensional flow magnetic resonance imaging, The Journal of Thoracic and Cardiovascular Surgery **150**, 200 (2015).

W. B. Buchenberg, F. Wassermann, S. Grundmann, B. Jung, and R. Simpson, Acquisition of 3D temperature distributions in fluid flow using proton resonance frequency thermometry, Magnetic Resonance in Medicine **76**, 145 (2016).

M. Bruschewski, D. Freudenhammer, **W. B. Buchenberg**, H.-P. Schiffer, and S. Grundmann, Estimation of the measurement uncertainty in magnetic resonance velocimetry based on statistical models, Experiments in Fluids **57** (2016).

Conference proceedings

W. B. Buchenberg, M. Markl, S. Bauer, J. Bock, R. Lorenz, and B. A. Jung, Dual VENC phase contrast MRI for simultaneous assessment of blood flow and cardiac motion, in Proc. Intl. Soc. Mag. Reson. Med., page 3303, Montreal, Canada, 2011.

W. B. Buchenberg, S. Gruhlke, J. Maclaren, M. Markl, A. Bongers, J. Jenne, M. Zaitsev, and B. Jung, Development of a hybrid MR-US system for the assessment of cardiac function

during free breathing, in Proc. Intl. Soc. Mag. Reson. Med., page 0085, Melbourne, Australia, 2012.

W. B. Buchenberg, G. Hoppe, R. Lorenz, W. Mader, P. Laudy, C. Bieneck, and B. Jung, Experimental study of the magnetohydrodynamic (MHD) effect with respect to intracardiac ECG signals, in Proc. of CARDIOTECHNIX 2013, pages 1–2, Vilamoura, Algarve, Portugal, 2013.

W. B. Buchenberg, R. Lorenz, P. Laudy, W. Mader, C. Bienek, and B. Jung, An Experimental setup to simulate the magnetohydrodynamic (MHD)-effect with respect to intra cardiac ECG signals, in Proc. Intl. Soc. Mag. Reson. Med., page 0477, Salt Lake City, Utah, USA, 2013.

S. Littin, M. Zaitsev, **W. B. Buchenberg**, A. M. Welz, H. Weber, F. Jia, F. Testud, D. Gallichan, J. Hennig, and W. R. T. Witschey, Zoomed cardiac CINE-MRI using nonlinear phase preparation, in Proc. Intl. Soc. Mag. Reson. Med., page 0428, Milan, Italy, 2014.

C. Müller, **W. B. Buchenberg**, C. Benk, R. Lorenz, S. Berner, and B. Jung, Investigation of a ventricular assist device (VAD) in an in vitro model system using 4D-phase contrast MRI, in Proc. Intl. Soc. Mag. Reson. Med., page 0505, Milan, Italy, 2014.

F. Wassermann, **W. B. Buchenberg**, R. Simpson, B. Jung, and S. Grundmann, Applying Magnetic Resonance Thermometry to engineering flows, in 17th International Symposium on Applications of Laser Techniques to Fluid Mechanics, pages 1–14, Lisbon, Portugal, 2014.

W. B. Buchenberg, F. Wassermann, S. Grundmann, B. Jung, and R. Simpson, MR thermometry in in-vitro flows, in Proc. Intl. Soc. Mag. Reson. Med., page 4053, Toronto, Canada, 2015.

F. Wassermann, **W. B. Buchenberg**, B. Jung, R. Simpson, C. Tropea and S. Grundmann, MRI Techniques for Thermofluids Engineering, GDCh FGMR 37th Annual Meeting 2015, Darmstadt, Germany

W. B. Buchenberg, F. Wassermann, S. Grundmann, J. Hennig, and B. Jung, Simultaneous 3D velocity and temperature mapping in fluid flow using MRI, in Proc. Intl. Soc. Mag. Reson. Med., page 2605, Singapore, 2016.

D. Freudenhammer, G. Rehs, **W. B. Buchenberg**, J. Hennig, C. Tropea, and S. Grundmann, Phase-averaged MRV measurements of the von Kármán vortex of a confined cylinder, in 18th International Symposium on the Application of Laser and Imaging Techniques to Fluid Mechanics, pages 1-13, Lisbon, Portugal, 2016

Bibliography

[1] E. M. Haacke, D. Li, and S. Kaushikkar, Cardiac MR imaging: principles and techniques, Top Magn Reson Imaging **7**, 200 (1995).

[2] B. Jung, *Neue kernspintomographische Techniken für funktionelle Untersuchungen des Herzmuskels*, PhD thesis, Albert-Ludwigs-University, Freiburg, 2005.

[3] M. Markl, A. Frydrychowicz, S. Kozerke, M. Hope, and O. Wieben, 4d flow MRI, J. Magn. Reson. Imaging **36**, 1015 (2012).

[4] C. J. Elkins, M. Markl, A. Iyengar, R. Wicker, and J. K. Eaton, Full-field velocity and temperature measurements using magnetic resonance imaging in turbulent complex internal flows, International Journal of Heat and Fluid Flow **25**, 702 (2004).

[5] C. J. Elkins, M. T. Alley, L. Saetran, and J. K. Eaton, Three-dimensional magnetic resonance velocimetry measurements of turbulence quantities in complex flow, Experiments in Fluids **46**, 285 (2009).

[6] M. J. Benson, C. J. Elkins, and J. K. Eaton, Measurements of 3d velocity and scalar field for a film-cooled airfoil trailing edge, Experiments in Fluids **51**, 443 (2011).

[7] S. Grundmann, F. Wassermann, R. Lorenz, B. Jung, and C. Tropea, Experimental investigation of helical structures in swirling flows, International Journal of Heat and Fluid Flow **37**, 51 (2012).

[8] F. Wassermann, D. Hecker, B. Jung, M. Markl, A. Seifert, and S. Grundmann, Phase-locked 3d3c-MRV measurements in a bi-stable fluidic oscillator, Exp Fluids **54**, 1 (2013).

[9] D. Freudenhammer, E. Baum, B. Peterson, B. Böhm, B. Jung, and S. Grundmann, Volumetric intake flow measurements of an IC engine using magnetic resonance velocimetry, Experiments in Fluids **55** (2014).

[10] V. Rieke and K. Butts Pauly, MR thermometry, J. Magn. Reson. Imaging **27**, 376 (2008).

[11] D. Germain, P. Chevallier, A. Laurent, and H. Saint-Jalmes, MR monitoring of tumour thermal therapy, MAGMA **13**, 47 (2001).

[12] B. Quesson, J. A. de Zwart, and C. T. Moonen, Magnetic resonance temperature imaging for guidance of thermotherapy, J. Magn. Reson. Imaging **12**, 525 (2000).

[13] B. T. Svedin, A. Payne, and D. L. Parker, Respiration artifact correction in three-dimensional proton resonance frequency MR thermometry using phase navigators: 3d PRF Respiration Correction, Magnetic Resonance in Medicine **76**, 206 (2016).

[14] L. Sun and L. D. Hall, An experimental solution of the graetz problem in heat exchangers, International Communications in Heat and Mass Transfer **28**, 461 (2001).

[15] C. J. Elkins and M. T. Alley, Magnetic resonance velocimetry: applications of magnetic resonance imaging in the measurement of fluid motion, Exp Fluids **43**, 823 (2007).

[16] K. Ogawa, M. Tobo, N. Iriguchi, S. Hirai, and K. Okazaki, Simultaneous measurement of temperature and velocity maps by inversion recovery tagging method, Magnetic Resonance Imaging **18**, 209 (2000).

[17] F. Wassermann, *Magnetic Resonance Imaging Techniques for Thermofluid Applications*, Dissertation, Technische Universität, Darmstadt, 2015.

[18] F. Bloch, Nuclear Induction, Phys. Rev. **70**, 460 (1946).

[19] E. M. Purcell, H. C. Torrey, and R. V. Pound, Resonance Absorption by Nuclear Magnetic Moments in a Solid, Phys. Rev. **69**, 37 (1946).

[20] P. A. Rinck, A. Bjørnerud, and European Magnetic Resonance Forum, *Magnetic resonance in medicine: the basic textbook of the European Magnetic Resonance Forum*, Blackwell Wissenschafts-Verl, Berlin, 4th, completely revised ed edition, 2001.

[21] R. Damadian, Tumor Detection by Nuclear Magnetic Resonance, Science **171**, 1151 (1971).

[22] P. C. Lauterbur, Image Formation by Induced Local Interactions: Examples Employing Nuclear Magnetic Resonance, Nature **242**, 190 (1973).

[23] P. Mansfield and P. K. Grannell, NMR 'diffraction' in solids?, J. Phys. C: Solid State Phys. **6**, L422 (1973).

[24] W. S. Hinshaw, P. A. Bottomley, and G. N. Holland, Radiographic thin-section image of the human wrist by nuclear magnetic resonance, Nature **270**, 722 (1977).

[25] S. J. Schmidt, X. Sun, and J. B. Litchfield, Applications of magnetic resonance imaging in food science, Crit Rev Food Sci Nutr **36**, 357 (1996).

[26] B. Hills, *Magnetic resonance imaging in food science*, Wiley, New York, 1998.

[27] M. H. Levitt, *Spin dynamics: basics of nuclear magnetic resonance*, John Wiley & Sons, Chichester ; New York, 2001.

[28] E. M. Haacke, *Magnetic resonance imaging: physical principles and sequence design*, Wiley, New York, 1999.

[29] Z.-P. Liang and P. C. Lauterbur, *Principles of magnetic resonance imaging: a signal processing perspective*, IEEE Press series in biomedical engineering, SPIE Optical Engineering Press ; IEEE Press, Bellingham, Wash. : New York, 2000.

[30] J. J. Sakurai and S. F. Tuan, *Modern quantum mechanics*, Addison-Wesley Pub. Co, Reading, Mass, rev. ed edition, 1994.

[31] D. Halliday, R. Resnick, J. Walker, and S. W. Koch, *Physik*, Wiley-VCH, Weinheim, 1. korr. nachdr edition, 2005.

[32] C. Gerthsen and D. Meschede, *Gerthsen Physik; "die ganze Physik zum 21. Jahrhundert"*, Springer-Lehrbuch, Springer, Berlin, 22., völlig neu bearb. aufl edition, 2004.

[33] P. Mansfield and P. G. Morris, *NMR imaging in biomedicine*, Number 2 in Advances in magnetic resonance, Academic Press, New York, 1982.

[34] J. F. Schenck, The role of magnetic susceptibility in magnetic resonance imaging: MRI magnetic compatibility of the first and second kinds, Medical Physics **23**, 815 (1996).

[35] L. G. Hanson, Is quantum mechanics necessary for understanding magnetic resonance?, Concepts Magn. Reson. **32A**, 329 (2008).

[36] M. A. Bernstein, K. F. King, and Z. J. Zhou, *Handbook of MRI pulse sequences*, Academic Press, Amsterdam ; Boston, 2004.

[37] R. A. De Graaf, *In vivo NMR spectroscopy: principles and techniques*, John Wiley & Sons, Chichester, West Sussex, England ; Hoboken, NJ, 2nd ed edition, 2007.

[38] A. G. Marshall and F. R. Verdun, *Fourier transforms in NMR, optical, and mass spectrometry: a user's handbook*, Elsevier, Amsterdam, 1990.

[39] E. L. Hahn, Spin Echoes, Phys. Rev. **80**, 580 (1950).

[40] R. R. Ernst and W. A. Anderson, Application of Fourier Transform Spectroscopy to Magnetic Resonance, Review of Scientific Instruments **37**, 93 (1966).

[41] H. Y. Carr and E. M. Purcell, Effects of Diffusion on Free Precession in Nuclear Magnetic Resonance Experiments, Phys. Rev. **94**, 630 (1954).

[42] G. Suryan, Nuclear resonance in flowing liquids, Proc. Indian Acad. Sci. (Math. Sci.) **33**, 107 (1951).

[43] R. L. Bowman and V. Kudravcev, Blood Flowmeter Utilizing Nuclear Magnetic Resonance, IRE Transactions on Medical Electronics **ME-6**, 267 (1959).

[44] J. R. Singer, Blood Flow Rates by Nuclear Magnetic Resonance Measurements, Science **130**, 1652 (1959).

[45] E. L. Hahn, Detection of sea-water motion by nuclear precession, J. Geophys. Res. **65**, 776 (1960).

[46] P. R. Moran, A flow velocity zeugmatographic interlace for NMR imaging in humans, Magnetic Resonance Imaging **1**, 197 (1982).

[47] O. C. Morse and J. R. Singer, Blood Velocity Measurements in Intact Subjects, Science **170**, 440 (1970).

[48] E. A. Zerhouni, D. M. Parish, W. J. Rogers, A. Yang, and E. P. Shapiro, Human heart: tagging with MR imaging–a method for noninvasive assessment of myocardial motion, Radiology **169**, 59 (1988).

[49] N. J. Pelc, F. G. Sommer, K. C. Li, T. J. Brosnan, R. J. Herfkens, and D. R. Enzmann, Quantitative magnetic resonance flow imaging, Magn Reson Q **10**, 125 (1994).

[50] H. Gudbjartsson and S. Patz, The Rician Distribution of Noisy MRI Data, Magn Reson Med **34**, 910 (1995).

[51] N. J. Pelc, M. A. Bernstein, A. Shimakawa, and G. H. Glover, Encoding strategies for three-direction phase-contrast MR imaging of flow, J. Magn. Reson. Imaging **1**, 405 (1991).

[52] K. M. Johnson and M. Markl, Improved SNR in phase contrast velocimetry with five-point balanced flow encoding, Magn. Reson. Med. **63**, 349 (2010).

[53] P. D. Gatehouse, J. Keegan, L. A. Crowe, S. Masood, R. H. Mohiaddin, K.-F. Kreitner, and D. N. Firmin, Applications of phase-contrast flow and velocity imaging in cardiovascular MRI, Eur Radiol **15**, 2172 (2005).

[54] M. D. Hope, T. Sedlic, and P. Dyverfeldt, Cardiothoracic Magnetic Resonance Flow Imaging, Journal of Thoracic Imaging **28**, 217 (2013).

[55] M. Markl, S. Schnell, and A. J. Barker, 4d Flow Imaging: Current Status to Future Clinical Applications, Current Cardiology Reports **16** (2014).

[56] J. R. Cebral, P. J. Yim, R. Löhner, O. Soto, and P. L. Choyke, Blood Flow Modeling in Carotid Arteries with Computational Fluid Dynamics and MR Imaging, Academic Radiology **9**, 1286 (2002).

[57] L. Hall and T. Carpenter, Magnetic resonance imaging: A new window into industrial processing, Magnetic Resonance Imaging **10**, 713 (1992).

[58] J. R. Singer, Nuclear magnetic resonance measurements of jet fuel, NASA contract No. NAS8-1581 .

[59] R. E. Goldstein and J.-W. van de Meent, A physical perspective on cytoplasmic streaming, Interface Focus **5**, 20150030 (2015).

[60] W. Small, E. Gjersing, J. L. Herberg, T. S. Wilson, and D. J. Maitland, Magnetic resonance flow velocity and temperature mapping of a shape memory polymer foam device, BioMedical Engineering OnLine **8**, 42 (2009).

[61] Y. Ishihara, A. Calderon, H. Watanabe, K. Okamoto, Y. Suzuki, K. Kuroda, and Y. Suzuki, A precise and fast temperature mapping using water proton chemical shift, Magn. Reson. Med. **34**, 814 (1995).

[62] D. L. Parker, Applications of NMR Imaging in Hyperthermia: An Evaluation of the Potential for Localized Tissue Heating and Noninvasive Temperature Monitoring, IEEE Transactions on Biomedical Engineering **BME-31**, 161 (1984).

[63] J. Chen, B. L. Daniel, and K. B. Pauly, Investigation of proton density for measuring tissue temperature, J. Magn. Reson. Imaging **23**, 430 (2006).

[64] D. Le Bihan, J. Delannoy, and R. L. Levin, Temperature mapping with MR imaging of molecular diffusion: application to hyperthermia., Radiology **171**, 853 (1989).

[65] R. M. Henkelman, G. J. Stanisz, and S. J. Graham, Magnetization transfer in MRI: a review, NMR Biomed **14**, 57 (2001).

[66] J. C. Hindman, Proton Resonance Shift of Water in the Gas and Liquid States, The Journal of Chemical Physics **44**, 4582 (1966).

[67] R. D. Peters, R. S. Hinks, and R. M. Henkelman, Heat-source orientation and geometry dependence in proton-resonance frequency shift magnetic resonance thermometry, Magn. Reson. Med. **41**, 909 (1999).

[68] R. Samson, J. Thornton, M. McLean, S. Williams, and P. Tofts, 1h-MRS internal thermometry in test-objects (phantoms) to within 0.1 K for quality assurance in long-term quantitative MR studies, NMR Biomed. **19**, 560 (2006).

[69] J. D. Poorter, Noninvasive MRI thermometry with the proton resonance frequency method: Study of susceptibility effects, Magn. Reson. Med. **34**, 359 (1995).

[70] R. Stollberger, P. W. Ascher, D. Huber, W. Renhart, H. Radner, and F. Ebner, Temperature monitoring of interstitial thermal tissue coagulation using MR phase images, J. Magn. Reson. Imaging **8**, 188 (1998).

[71] W. Wlodarczyk, R. Boroschewski, M. Hentschel, P. Wust, G. Mönich, and R. Felix, Three-dimensional monitoring of small temperature changes for therapeutic hyperthermia using MR, J. Magn. Reson. Imaging **8**, 165 (1998).

[72] W. Wlodarczyk, M. Hentschel, P. Wust, R. Noeske, N. Hosten, H. Rinneberg, and Roland Felix, Comparison of four magnetic resonance methods for mapping small temperature changes, Phys. Med. Biol. **44**, 607 (1999).

[73] K. Kuroda, Non-invasive MR thermography using the water proton chemical shift, International Journal of Hyperthermia **21**, 547 (2005).

[74] V. Rieke, K. K. Vigen, G. Sommer, B. L. Daniel, J. M. Pauly, and K. Butts, Referenceless PRF shift thermometry, Magn. Reson. Med. **51**, 1223 (2004).

[75] J. S. Philo and W. M. Fairbank, Temperature dependence of the diamagnetism of water, The Journal of Chemical Physics **72**, 4429 (1980).

[76] M. N. Streicher, A. Schäfer, E. Reimer, B. Dhital, R. Trampel, D. Ivanov, and R. Turner, Effects of air susceptibility on proton resonance frequency MR thermometry, Magnetic Resonance Materials in Physics, Biology and Medicine **25**, 41 (2012).

[77] R. T. D. Peters, R. S. Hinks, and R. M. Henkelman, Ex vivo tissue-type independence in proton-resonance frequency shift MR thermometry, Magn. Reson. Med. **40**, 454 (1998).

[78] R. D. Peters and R. M. Henkelman, Proton-resonance frequency shift MR thermometry is affected by changes in the electrical conductivity of tissue, Magn. Reson. Med. **43**, 62 (2000).

[79] P. A. Bottomley and E. R. Andrew, RF magnetic field penetration, phase shift and power dissipation in biological tissue: implications for NMR imaging, Phys. Med. Biol. **23**, 630 (1978).

[80] J. D. Poorter, C. Dewagter, Y. Dedeene, C. Thomsen, F. Stahlberg, and E. Achten, The Proton-Resonance-Frequency-Shift Method Compared with Molecular Diffusion for Quantitative Measurement of Two-Dimensional Time-Dependent Temperature Distribution in a Phantom, Journal of Magnetic Resonance, Series B **103**, 234 (1994).

[81] J. D. Poorter, C. D. Wagter, Y. D. Deene, C. Thomsen, F. Ståhlberg, and E. Achten, Noninvasive MRI Thermometry with the Proton Resonance Frequency (PRF) Method: In Vivo Results in Human Muscle, Magn. Reson. Med. **33**, 74 (1995).

[82] S. Sinha, T. Oshiro, U. Sinha, and R. Lufkin, Phase imaging on a .2-T MR scanner: Application to temperature monitoring during ablation procedures, J. Magn. Reson. Imaging **7**, 918 (1997).

[83] C. Barmet, N. D. Zanche, and K. P. Pruessmann, Spatiotemporal magnetic field monitoring for MR, Magn. Reson. Med. **60**, 187 (2008).

[84] V. O. Boer, T. v. d. Velden, M. Kohler, C. Moonen, D. W. Klomp, and C. Bos, Field drift compensation for MR thermometry using independent field probe measurements, in *Proc. Intl. Soc. Mag. Reson. Med. 22*, volume 22, page 3712, Milan, Italy, 2014.

[85] N. Bloembergen, E. M. Purcell, and R. V. Pound, Relaxation Effects in Nuclear Magnetic Resonance Absorption, Phys. Rev. **73**, 679 (1948).

[86] T. R. Nelson and S. M. Tung, Temperature dependence of proton relaxation times in vitro, Magnetic Resonance Imaging **5**, 189 (1987).

[87] P. T. Vesanen, K. C. J. Zevenhoven, J. O. Nieminen, J. Dabek, L. T. Parkkonen, and R. J. Ilmoniemi, Temperature dependence of relaxation times and temperature mapping in ultra-low-field MRI, J. Magn. Reson. **235**, 50 (2013).

[88] P. Jezzard, T. A. Carpenter, L. D. Hall, N. J. Clayden, and P. Jackson, Temperature mapping in solid polymers using the temperature dependence of NMR relaxation times, J. Polym. Sci. B Polym. Phys. **30**, 1423 (1992).

[89] K. P. Nott, L. D. Halla, J. R. Bows, M. Hale, and M. L. Patrick, MRI phase mapping of temperature distributions induced in food by microwave heating, Magnetic Resonance Imaging **18**, 69 (2000).

[90] P. A. Bottomley, T. H. Foster, R. E. Argersinger, and L. M. Pfeifer, A review of normal tissue hydrogen NMR relaxation times and relaxation mechanisms from 1–100 MHz: Dependence on tissue type, NMR frequency, temperature, species, excision, and age, Medical Physics **11**, 425 (1984).

[91] S. Meiboom and D. Gill, Modified spin-echo method for measuring nuclear relaxation times, Review of Scientific Instruments **29**, 688 (1958).

[92] A. Abragam, *The Principles of Nuclear Magnetism*, Clarendon Press, 1961.

[93] E. O. Stejskal and J. E. Tanner, Spin diffusion measurements: spin echoes in the presence of a time-dependent field gradient, The Journal of Chemical Physics **42**, 288 (1965).

[94] I. R. Young, J. W. Hand, A. Oatridge, and M. V. Prior, Modeling and observation of temperature changes in Vivo using MRI, Magn. Reson. Med. **32**, 358 (1994).

[95] S. D. Wolff and R. S. Balaban, Magnetization transfer contrast (MTC) and tissue water proton relaxation in vivo, Magn. Reson. Med. **10**, 135 (1989).

[96] R. de Boer, Magnetization transfer contrast. Part 1: MR Physics, in *Philips Medical Systems MedicaMundi*, volume 40 of *Philips Medical Systems MedicaMundi*, pages 64–73, Medica Mundi, Best, the Netherlands, 1995.

[97] L. H. Lindner, H. M. Reinl, M. Schlemmer, R. Stahl, and M. Peller, Paramagnetic thermosensitive liposomes for MR-thermometry, International Journal of Hyperthermia **21**, 575 (2005).

[98] S. K. Hekmatyar, R. M. Kerkhoff, S. K. Pakin, P. Hopewell, and N. Bansal, Noninvasive thermometry using hyperfine-shifted MR signals from paramagnetic lanthanide complexes, International Journal of Hyperthermia **21**, 561 (2005).

[99] S. Hekmatyar, P. Hopewell, S. K. Pakin, A. Babsky, and N. Bansal, Noninvasive MR thermometry using paramagnetic lanthanide complexes of 1,4,7,10-tetraazacyclododecane-alpha,alpha',alpha'',alpha'''-tetramethyl-1,4,7,10-tetraacetic acid ($DOTMA^{4-}$), Magnetic Resonance in Medicine **53**, 294 (2005).

[100] D. Coman, H. K. Trubel, R. E. Rycyna, and F. Hyder, Brain temperature and pH measured by ^{1}H chemical shift imaging of a thulium agent, NMR in Biomedicine **22**, 229 (2009).

[101] D. E. Woessner, S. Zhang, M. E. Merritt, and A. D. Sherry, Numerical solution of the Bloch equations provides insights into the optimum design of PARACEST agents for MRI, Magn. Reson. Med. **53**, 790 (2005).

[102] S. Zhang, C. R. Malloy, and A. D. Sherry, MRI Thermometry Based on PARACEST Agents, J. Am. Chem. Soc. **127**, 17572 (2005).

[103] R. N. Muller, L. Vander Elst, and S. Laurent, Spin Transition Molecular Materials: Intelligent Contrast Agents for Magnetic Resonance Imaging, J. Am. Chem. Soc. **125**, 8405 (2003).

[104] F. Settecase, M. S. Sussman, and T. P. L. Roberts, A new temperature-sensitive contrast mechanism for MRI: Curie temperature transition-based imaging, Contrast Media Mol Imaging **2**, 50 (2007).

[105] D. L. Parker, V. Smith, P. Sheldon, L. E. Crooks, and L. Fussell, Temperature distribution measurements in two-dimensional NMR imaging, Medical Physics **10**, 321 (1983).

[106] J. R. Zimmerman and W. E. Brittin, Nuclear Magnetic Resonance Studies in Multiple Phase Systems: Lifetime of a Water Molecule in an Adsorbing Phase on Silica Gel, J. Phys. Chem. **61**, 1328 (1957).

[107] J. H. Simpson and H. Y. Carr, Diffusion and Nuclear Spin Relaxation in Water, Phys. Rev. **111**, 1201 (1958).

[108] W. G. Schneider, H. J. Bernstein, and J. A. Pople, Proton Magnetic Resonance Chemical Shift of Free (Gaseous) and Associated (Liquid) Hydride Molecules, The Journal of Chemical Physics **28**, 601 (1958).

[109] H. Cline, R. Mallozzi, Z. Li, G. McKinnon, and W. Barber, Radiofrequency power deposition utilizing thermal imaging, Magn. Reson. Med. **51**, 1129 (2004).

[110] D. H. Gultekin and L. Moeller, NMR imaging of cell phone radiation absorption in brain tissue, Proceedings of the National Academy of Sciences **110**, 58 (2013).

[111] L. Alon, C. M. Deniz, R. Brown, D. K. Sodickson, and Y. Zhu, Method for in situ characterization of radiofrequency heating in parallel transmit MRI, Magn Reson Med **69**, 1457 (2013).

[112] L. Alon, G. Y. Cho, X. Yang, Y. Zhu, D. K. Sodickson, and C. M. Deniz, RF-emission device safety testing using MRI, in *2013 IEEE Antennas and Propagation Society International Symposium (APSURSI)*, pages 718–719, IEEE, 2013.

[113] L. Alon, G. Y. Cho, X. Yang, D. K. Sodickson, and C. M. Deniz, A method for safety testing of radiofrequency/microwave-emitting devices using MRI, Magn. Reson. Med. **74**, 1397 (2015).

[114] L. D. Hall and S. L. Talagala, Mapping of pH and temperature distribution using chemical-shift-resolved tomography, Journal of Magnetic Resonance (1969) **65**, 501 (1985).

[115] N. W. Lutz, A. C. Kuesel, and W. E. Hull, A 1h-NMR method for determining temperature in cell culture perfusion systems, Magn. Reson. Med. **29**, 113 (1993).

[116] R. D. Farrant, J. C. Lindon, and J. K. Nicholson, Internal temperature calibration for1h NMR spectroscopy studies of blood plasma and other biofluids, NMR in Biomedicine **7**, 243 (1994).

[117] M. E. Lacey, A. G. Webb, and J. V. Sweedler, On-Line Temperature Monitoring in a Capillary Electrochromatography Frit Using Microcoil NMR, Anal. Chem. **74**, 4583 (2002).

[118] K. Knoerzer, M. Regier, E. Hardy, H. Schuchmann, and H. Schubert, Simultaneous microwave heating and three-dimensional MRI temperature mapping, Innovative Food Science & Emerging Technologies **10**, 537 (2009).

[119] F. Mariette, G. Collewet, A. Davenel, T. Lucas, and M. Musse, Quantitative MRI in Food Science & Food Engineering, in *Encyclopedia of Magnetic Resonance*, edited by R. K. Harris, John Wiley & Sons, Ltd, Chichester, UK, 2012.

[120] X. Ye, R. Ruan, P. Chen, K. Chang, K. Ning, I. A. Taub, and C. Doona, Accurate and fast temperature mapping during ohmic heating using proton resonance frequency shift MRI thermometry, Journal of Food Engineering **59**, 143 (2003).

[121] G. J. Hulbert, J. B. Litchfield, and S. J. Schmidt, Temperature Mapping in Carrot Using T1 Weighted Magnetic Resonance Imaging, Journal of Food Science **60**, 780 (1995).

[122] G. J. Hulbert, J. Litchfield, and S. J. Schmidt, Determination of convective heat transfer coefficients using 2d MRI temperature mapping and finite element modeling, Journal of Food Engineering **34**, 193 (1997).

[123] X. Sun, S. J. Schmidt, and J. B. Litchfield, Temperature mapping in a potato using half Fourier transform MRI of diffusion, Journal of Food Process Engineering **17**, 423 (1994).

[124] C. Tropea, *Springer Handbook of Experimental Fluid Mechanics*, Springer Berlin, Berlin, 2009.

[125] P. R. N. Childs, J. R. Greenwood, and C. A. Long, Review of temperature measurement, Review of Scientific Instruments **71**, 2959 (2000).

[126] S. Minn Khine, T. Houra, and M. Tagawa, Heat-conduction error of temperature sensors in a fluid flow with nonuniform and unsteady temperature distribution, Review of Scientific Instruments **84**, 044902 (2013).

[127] D. Dabiri, Digital particle image thermometry/velocimetry: a review, Experiments in Fluids **46**, 191 (2009).

[128] R. Segura, M. Rossi, C. Cierpka, and C. J. Kähler, Volumetric time resolved measurements of temperature and velocity in microscopic flows using thermo-liquid crystals (tlcs), in *17th International Symposium on Applications of Laser Techniques to Fluid Mechanics, Lisbon, Portugal*, pages 1–14, Lisbon, Portugal, 2014.

[129] F. M. White, *Viscous fluid flow*, McGraw-Hill series in mechanical engineering, McGraw-Hill, New York, 2nd ed edition, 1991.

[130] P. Stephan, K. Schaber, K. Stephan, and F. Mayinger, *Thermodynamik*, Springer-Lehrbuch, Springer Berlin Heidelberg, Berlin, Heidelberg, 2013.

[131] H. K. Dawood, H. A. Mohammed, N. A. Che Sidik, K. M. Munisamy, and M. A. Wahid, Forced, natural and mixed-convection heat transfer and fluid flow in annulus: A review, International Communications in Heat and Mass Transfer **62**, 45 (2015).

[132] VDI-Gesellschaft Verfahrenstechnik und Chemieingenieurwesen, *VDI heat atlas*, VDI-buch, Springer, Berlin ; New York, 2nd ed edition, 2010.

[133] W. B. Buchenberg, F. Wassermann, S. Grundmann, B. Jung, and R. Simpson, Acquisition of 3d temperature distributions in fluid flow using proton resonance frequency thermometry, Magnetic Resonance in Medicine **76**, 145 (2016).

[134] P. Miller, J. J. Byrnes, and D. M. Benforado, Heat transfer to water in an annulus, AIChE J. **1**, 501 (1955).

[135] K. Avila, D. Moxey, A. de Lozar, M. Avila, D. Barkley, and B. Hof, The Onset of Turbulence in Pipe Flow, Science **333**, 192 (2011).

[136] M. Van Dyke, *An album of fluid motion*, Parabolic Press, Stanford, Calif, 12. printing edition, 2008.

[137] H. Togun, T. Abdulrazzaq, S. N. Kazi, A. Badarudin, A. A. H. Kadhum, and E. Sadeghinezhad, A review of studies on forced, natural and mixed heat transfer to fluid and nanofluid flow in an annular passage, Renewable and Sustainable Energy Reviews **39**, 835 (2014).

[138] N. Hattori and S. Kotake, Combined Free and Forced-Convection Heat-Transfer for Fully-Developed Laminar Flow in Horizontal Tubes (Experiments), Bulletin of JSME **21**, 861 (1978).

[139] A. O. Nieckele and S. V. Patankar, Laminar Mixed Convection in a Concentric Annulus With Horizontal Axis, J. Heat Transfer **107**, 902 (1985).

[140] K. Zerari, M. Afrid, and D. Groulx, Forced and mixed convection in the annulus between two horizontal confocal elliptical cylinders, International Journal of Thermal Sciences **74**, 126 (2013).

[141] F. P. Incropera, D. P. DeWitt, T. L. Bergman, and A. S. Lavine, *Fundamentals of heat and mass transfer*, John Wiley, Hoboken, NJ, 6th ed edition, 2007.

[142] W. B. Buchenberg, F. Wassermann, S. Grundmann, B. Jung, and R. Simpson, MR thermometry in in-vitro flows, in *Proc. Intl. Soc. Mag. Reson. Med.*, page 4053, Toronto, Canada, 2015.

[143] W. B. Buchenberg, F. Wassermann, S. Grundmann, J. Hennig, and B. Jung, Simultaneous 3d velocity and temperature mapping in fluid flow using MRI, in *Proc. Intl. Soc. Mag. Reson. Med.*, page 2605, Singapore, 2016.

[144] M. Tahat, Z. H. Kodah, B. A. Jarrah, and S. D. Probert, Heat transfers from pin-fin arrays experiencing forced convection, Applied Energy **67**, 419 (2000).

[145] A. I. Zografos and J. Edward Sunderland, Natural convection from pin fin arrays, Experimental Thermal and Fluid Science **3**, 440 (1990).

[146] J. Armstrong and D. Winstanley, A Review of Staggered Array Pin Fin Heat Transfer for Turbine Cooling Applications, J. Turbomach **110**, 94 (1988).

[147] S. Benhamadouche, R. Howard, and R. Manceau, Case 15.2, in *15th ERCOFTAC-SIG15/IAHR Workshop*, 2011.

[148] F. E. Ames, L. A. Dvorak, and M. J. Morrow, Turbulent Augmentation of Internal Convection Over Pins in Staggered Pin Fin Arrays, in *Turbo Expo 2004*, volume 3, pages 787–796, ASME, 2004.

[149] F. E. Ames and L. A. Dvorak, Turbulent Transport in Pin Fin Arrays: Experimental Data and Predictions, Journal of Turbomachinery **128**, 71 (2006).

[150] F. E. Ames, C. A. Nordquist, and L. A. Klennert, Endwall Heat Transfer Measurements in a Staggered Pin Fin Array With an Adiabatic Pin, page 423 (2007).

[151] D. E. Metzger and S. W. Haley, Heat Transfer Experiments and Flow Visualization for Arrays of Short Pin Fins, page V004T09A007 (1982).

[152] F. Wassermann and S. Grundmann, Flow visualization of a staggered pin fin array using Magnetic Resonance Velocimetry, in *15th ERCOFTAC-SIG15/IAHR Workshop*, Chatou, France, 2011.

[153] W. R. Martini, Natural convection inside a horizontal cylinder, AIChE Journal **6**, 251 (1960).

[154] I. Mercader, O. Batiste, L. Ramírez-Piscina, X. Ruiz, S. Rüdiger, and J. Casademunt, Bifurcations and chaos in single-roll natural convection with low Prandtl number, Physics of Fluids **17**, 104108 (2005).

[155] G. De Vahl Davis, Natural convection of air in a square cavity: A bench mark numerical solution, International Journal for Numerical Methods in Fluids **3**, 249 (1983).

[156] N. Markatos and K. Pericleous, Laminar and turbulent natural convection in an enclosed cavity, International Journal of Heat and Mass Transfer **27**, 755 (1984).

[157] S. Wakitani, Numerical Study of Three-Dimensional Oscillatory Natural Convection at Low Prandtl Number in Rectangular Enclosures, Journal of Heat Transfer **123**, 77 (2001).

[158] H. Dixit and V. Babu, Simulation of high Rayleigh number natural convection in a square cavity using the lattice Boltzmann method, International Journal of Heat and Mass Transfer **49**, 727 (2006).

[159] F. Staehle, *Entwicklung und Analyse von Methoden zur Untersuchung der Herzwandbewegung mit MRT*, Dissertation, Albert-Ludwigs-Universität, Freiburg, 2009.

[160] M. A. Griswold, P. M. Jakob, R. M. Heidemann, M. Nittka, V. Jellus, J. Wang, B. Kiefer, and A. Haase, Generalized autocalibrating partially parallel acquisitions (GRAPPA), Magnetic Resonance in Medicine **47**, 1202 (2002).

[161] F. Testud and M. Zaitsev, B0 Field Monitoring by Air-Matched Phantoms, in *Proc. Intl. Soc. Mag. Reson. Med.*, page 2791, Honolulu, Hawaii, USA, 2009.

[162] J. Gellermann, W. Wlodarczyk, A. Feussner, H. Fähling, J. Nadobny, B. Hildebrandt, R. Felix, and P. Wust, Methods and potentials of magnetic resonance imaging for monitoring radiofrequency hyperthermia in a hybrid system, International Journal of Hyperthermia **21**, 497 (2005).

[163] W. B. Buchenberg, T. Dadakova, J. Groebner, M. Bock, and B. Jung, Comparison of two fiber-optical temperature measurement systems in magnetic fields up to 9.4 Tesla, Magn Reson Med **73**, 2047 (2015).

[164] V. Runge, J. Clanton, C. Lukehart, C. Partain, and A. James, Paramagnetic agents for contrast-enhanced NMR imaging: a review, American Journal of Roentgenology **141**, 1209 (1983).

[165] C. P. Slichter, *Principles of magnetic resonance*, Number 1 in Springer series in solid-state sciences, Springer, Berlin ; New York, 3rd enl. and updated ed edition, 1996.

[166] M. D. Mitchell, H. L. Kundel, L. Axel, and P. M. Joseph, Agarose as a tissue equivalent phantom material for NMR imaging, Magnetic Resonance Imaging **4**, 263 (1986).

[167] A. Kolin, An Alternating Field Induction Flow Meter of High Sensitivity, Review of Scientific Instruments **16**, 109 (1945).

[168] T. Togawa, O. Okai, and M. Oshima, Observation of blood flow E.M.F. in externally applied strong magnetic field by surface electrodes, Medical & Biological Engineering **5**, 169 (1967).

[169] T. S. Tenforde, Magnetically induced electric fields and currents in the circulatory system, Progress in Biophysics and Molecular Biology **87**, 279 (2005).

[170] D. Abi Abdallah, A. Drochon, V. Robin, and O. Fokapu, Effects of static magnetic field exposure on blood flow, The European Physical Journal Applied Physics **45**, 11301 (2009).

[171] K. W. Naegeli, Ueber oligodynamische Erscheinungen in lebenden Zellen., Neue Denk-schriften der schweizerischen naturforschenden Gesellschaft **33-34**, 1 (1893).

[172] G. F. Johnson, The Early History of Copper Fungicides, Agricultural History Society **9**, 67 (1935).

[173] R. B. Thurman, C. P. Gerba, and G. Bitton, The molecular mechanisms of copper and silver ion disinfection of bacteria and viruses, Critical Reviews in Environmental Control **18**, 295 (1989).

[174] Y. Kinouchi, H. Yamaguchi, and T. Tenforde, Theoretical analysis of magnetic field interactions with aortic blood flow, Bioelectromagnetics **17**, 21 (1996).

[175] M. Fernandez-Seara and F. Wehrli, Postprocessing technique to correct for background gradients in image-based R*2 measurements, Magnetic Resonance in Medicine **44**, 358 (2000).

[176] D. Hernando, K. K. Vigen, A. Shimakawa, and S. B. Reeder, R 2* mapping in the presence of macroscopic B0 field variations, Magnetic Resonance in Medicine **68**, 830 (2012).

[177] U. Roland, C. P. Renschen, D. Lippik, F. Stallmach, and F. Holzer, A New Fiber Optical Thermometer and Its Application for Process Control in Strong Electric, Magnetic, and Electromagnetic Fields, Sensor Letters **1**, 93 (2003).

[178] J. Groebner, M. Berger, W. Semmler, and J. Rauschenberg, Influence from static magnetic fields on fiber-optical temperature probes - effects on safety measurements at 7T, in *In Proceedings of the 20th Annual Meeting of ISMRM*, page 2705, Melbourne, Australia, 2012.

[179] S. W. Harun, M. Yasin, H. A. Rahman, H. Arof, and H. Ahmad, Fiber Optic Temperature Sensors, in *Optical Fiber Communications and Devices*, edited by D. M. Yasin, InTech, 2012.

[180] M. McSherry, C. Fitzpatrick, and E. Lewis, Review of luminescent based fibre optic temperature sensors, Sensor Review **25**, 56 (2005).

[181] H. Y. Choi, K. S. Park, S. J. Park, U.-C. Paek, B. H. Lee, and E. S. Choi, Miniature fiber-optic high temperature sensor based on a hybrid structured Fabry–Perot interferometer, Optics Letters **33**, 2455 (2008).

[182] K. Han, Y. Lee, J. Kwon, S. Roh, J. Jung, and B. Lee, Simultaneous Measurement of Strain and Temperature Incorporating a Long-Period Fiber Grating Inscribed on a Polarization-Maintaining Fiber, IEEE Photonics Technology Letters **16**, 2114 (2004).

[183] K. Kyuma, Shuichi Tai, T. Sawada, and M. Nunoshita, Fiber-Optic Instrument for Temperature Measurement, IEEE Transactions on Microwave Theory and Techniques **30**, 522 (1982).

[184] J. S. Blakemore, Semiconducting and other major properties of gallium arsenide, Journal of Applied Physics **53**, R123 (1982).

[185] Y. Varshni, Temperature dependence of the energy gap in semiconductors, Physica **34**, 149 (1967).

[186] M. B. Panish, Temperature Dependence of the Energy Gap in GaAs and GaP, Journal of Applied Physics **40**, 163 (1969).

[187] C. D. Thurmond, The Standard Thermodynamic Functions for the Formation of Electrons and Holes in Ge, Si, GaAs, and GaP, Journal of The Electrochemical Society **122**, 1133 (1975).

[188] ASTM F 2182 – 02a, Standard test method for measurement of radio frequency induced heating near passive implants during magnetic resonance imaging, pages 1–8, 2002.

[189] S. A. Sapareto and W. C. Dewey, Thermal dose determination in cancer therapy, Int J Radiat Oncol Biol Phys. **10**, 787 (1984).

[190] V. Y. Aleshkin and N. V. Zakrevskiĭ, Optical band gap width in GaAs in megagauss magnetic fields, Physics of the Solid State **49**, 634 (2007).

[191] R. Gallagher and W. Corak, A Metal-Oxide-Semiconductor (MOS) Hall element, Solid-State Electronics **9**, 571 (1966).

[192] R. Mehta, The aerodynamic design of blower tunnels with wide-angle diffusers, Progress in Aerospace Sciences **18**, 59 (1979).

[193] X. Yuan, F. Tavakkoli, and K. Vafai, Analysis of Natural Convection in Horizontal Concentric Annuli of Varying Inner Shape, Numerical Heat Transfer, Part A: Applications **68**, 1155 (2015).

[194] C. D. Constantinides, E. Atalar, and E. R. McVeigh, Signal-to-noise measurements in magnitude images from NMR phased arrays, Magn. Reson. Med. **38**, 852 (1997).

[195] M. Bruschewski, D. Freudenhammer, W. B. Buchenberg, H.-P. Schiffer, and S. Grundmann, Estimation of the measurement uncertainty in magnetic resonance velocimetry based on statistical models, Experiments in Fluids **57** (2016).

[196] E. W. Weisstein, Convective Acceleration, From *MathWorld*–A Wolfram Web Resource. http://mathworld.wolfram.com/ConvectiveAcceleration.html .

[197] S. Gross, C. Barmet, and K. P. Pruessmann, Sub-ppb/K temperature drift of NMR field probes using intrinsic magnetostatic compensation, in *Proc. Intl. Soc. Mag. Reson. Med.*, page 1838, Toronto, Canada, 2015.

[198] F. Wassermann, W. B. Buchenberg, R. Simpson, B. Jung, and S. Grundmann, Applying Magnetic Resonance Thermometry to Engineering Flows, in *17th International Symposium on Applications of Laser Techniques to Fluid Mechanics*, pages 1–14, Lisbon, Portugal, 2014.

[199] B. P. Cross and T. Schleich, Temperature dependence of the chemical shifts of commonly employed proton n.m.r. reference compounds, Org. Magn. Reson. **10**, 82 (1977).

[200] R. E. Hoffman, Standardization of chemical shifts of TMS and solvent signals in NMR solvents, Magnetic Resonance in Chemistry **44**, 606 (2006).

[201] J. Frahm, K.-D. Merboldt, and W. Hänicke, Localized proton spectroscopy using stimulated echoes, Journal of Magnetic Resonance (1969) **72**, 502 (1987).

[202] P. A. Bottomley, Spatial Localization in NMR Spectroscopy in Vivo, Annals of the New York Academy of Sciences **508**, 333 (1987).

Acknowledgements

First of all I like to thank Prof. J. Hennig for providing all the ingredients to make this thesis possible in a motivating working atmosphere.
Many thanks to Bernd Jung and Sven Grundmann for setting up the grant which opened the possibilities to establish a very interesting and productive collaboration between the people from Darmstadt and myself. Thank you Florian Wassermann, Martin Bruschewski, and Daniel Freudenhammer for the enthusiastic atmosphere during the measurements which was substantial to survive very long days of measuring. I am also grateful for the fruitful discussions providing views into a different, however, very exciting field of science.
I would like to thank all people who gave me a helping hand (two of mine were sometimes not enough to ensure no flooding of the MR system) with the numerous pipes and pumps which had to be connected for certain setups or who were involved in fruitful discussions. In particular to mention here are Robin Simpson, Tetiana Dadakova, Thomas Lange, Jochen Leupold, Marius Menza, and Frederik Testud.
Many thanks to all colleagues and former colleagues (spread all over the world) for the great working atmosphere and the challenging sport or delicious cooking activities.
Moreover, I would like to thank people of the workshop at the neurocenter of the University Medical Center Freiburg for assistance with the construction of phantoms.
There is a world outside MRI. Many thanks to all friends and to my family for supporting me during all these years. In particular to my husband, I like to say thank you that you are there giving me any support I could think of.
And last but not least, I will definitively remember:
“a watched pot never boils.” (proverb of Benjamin Franklin)

Typeset November 28, 2016